Modeling and Simulation of Submerged Solar PV with an Efficient Energy Storage System Integrated with Wind-Fed Offshore Microgrid

THESIS

Submitted in partial fulfillment

of the requirement for the degree of

DOCTOR OF PHILOSOPHY

by

CHALLA SANTHI DURGANJALI

ID No. 2018PHXF0021H

Under the Supervision of

Prof. SUDHA RADHIKA

and

Under the Co-Supervision of

Prof. SANKET GOEL

Dr. PONNALAGU R. N

BITS Pilani
Pilani | Dubai | Goa | Hyderabad

Birla Institute of Technology and Science, Pilani

2023

BIRLA INSTITUTE OF TECHNOLOGY AND SCIENCE, PILANI

CERTIFICATE

This is to certify that the thesis entitled **Modeling and Simulation of Submerged Solar PV with an Efficient Energy Storage System Integrated with Wind-Fed Offshore Microgrid** and submitted by **Challa Santhi Durganjali**, ID. No. **2018PHXF0021H** for award of **Ph.D.** of the Institute embodies original work done by her under my supervision.

Signature of the Supervisor:

Name in capital letters: Prof. SUDHA RADHIKA

Designation: Associate Professor

       Department of Electrical and Electronics Engineering

       BITS Pilani- Hyderabad Campus, India - 500078

Date: 02-05-2023

Signature of the Co-supervisor:

Name in capital letters: Prof. SANKET GOEL

Designation: Professor

       Department of Electrical and Electronics Engineering

       BITS Pilani- Hyderabad Campus, India - 500078

Date: 03-05-2023

Signature of the Co-supervisor:

Name in capital letters: Dr. PONNALAGU R.N

Designation: Assistant Professor

       Department of Electrical and Electronics Engineering

       BITS Pilani- Hyderabad Campus, India – 500078

Date: 04-05-2023

DECLARATION OF AUTHORSHIP

I, CHALLA SANTHI DURGANJALI, ID No. 2018PHXF0021H declare that this thesis titled, "Modeling and Simulation of Submerged Solar PV with an Efficient Energy Storage System Integrated with Wind-Fed Offshore Microgrid" and the work presented therein are my own. I confirm:

• This work was done solely or mainly while in candidature for a Ph.D.

degree at this University.

• Any section of this doctoral thesis has previously been submitted for a

degree or other qualification at this university or any other institution;

this has been made abundantly clear.

• Where I have consulted the published work of others, this is always clearly

attributed.

• Where I have quoted from the work of others, the source is always given.

Except for such quotations, this thesis is entirely my work.

• I have acknowledged all main sources of help.

• The thesis is based on work done by myself jointly with others; I have

clarified exactly what I have done and contributed myself.

Signed: Sd/- Santhi Durganjali Challa
_____

Date: 08- 09 -2023
_____

"Discovering new frontiers of knowledge through rigorous inquiry and innovation takes time but gives effective output useful for the community"

Santhi Durganjali Challa

ACKNOWLEDGEMENTS

ABSTRACT

The future potential of offshore microgrid systems as a means of meeting the energy needs of remote and offshore installations is explored with the design and simulation of an offshore microgrid system that integrates Submerged Solar Photovoltaics (SSPV) and Wind Energy Conversion System (WECS) with Energy Efficient Storage System (EESS) to meet the electricity demand of a remote island. The system is designed to minimize the use of fossil fuels and carbon emissions while ensuring a stable and continuous power supply with the Renewable Energy Sources (RES). As the world moves towards renewable resources to meet the heaping power demand, the dependence on Photo Voltaic (PV) panel-based power generation has globally touched 1000TWh in 2021. In the current scenario of power crisis, solar photovoltaic (PV) power generation systems are favored as a long-endurance source of power for many of the applications like local utility grid connection, battery storage, backup generator power, small home applications and hybrid power systems. But the effect of temperature on PV cells drastically reduces their efficiency.

As a betterment to this problem, solar panel cooling technology using a variety of cooling liquids are existing. However, one of the cheaper solutions to the said problem is, using the PV cells in the underwater environment. Several studies are being done in this area during the past few decades and it is one of the emerging areas in the renewable energy sector. The solar irradiation above the earth's surface is a mix of the entire solar spectrum, whereas, inside the water, different irradiations will be absorbed at different depths. When light passes through the atmosphere, it scatters, but while passing through a liquid like water it gets absorbed too. Rather than having a proportional dependence with wavelength, water chooses to absorb ultraviolet light, infrared light, and red visible light whereas the light wavelengths for deepest blues have the more probability of getting re-emitted back and reflected out in water.

The sun's filtered spectrum in underwater is biased toward the green/blue portion of the spectrum with useful power to harvest at different depths. This thesis mainly focuses on detailing the different technologies available, by decreasing the surface temperature of the cells, to improve the PV cells efficiency. It also emphasizes on the recent developed technology of using solar panels in the underwater environment SSPV for improved efficiency. Further, the mathematical and Multiphysics modelling of the SSPV is required.

These SSPV panels made up of different materials, such as Germanium (Ge), Silicon (Si), Indium Phosphide (InP), and Gallium Arsenide (GaAs), work in wider applications ranging from earth to space. But in real-time environmental conditions, these materials exhibit only 11 to 15 % efficiency, mainly due to thermal loss and exposure to variable irradiation and temperature conditions. Thus, in the current research, the PV cell/panel is modeled in an experimentally validated Multiphysics environment at temperatures from $-45\ ^0C$ to $+51\ ^0C$ using Ge, Si, InP, and GaAs as materials from earth surface to submerged condition.

The efficiency of the PV cell/panel is estimated in the current research based on the thermal losses within the material, the width of the bandgap, and the thickness of the cell. To analyze the thermal losses, joule heat generation of PV cell/panels made of all different materials is obtained. It is observed that at ambient temperature, although the GaAs and InP have an energy bandgap of 1.42eV and 1.34eV, respectively, the joule heating effect is minimum (3.95 KW/m^3- InP, 5.05 KW/m^3- GaAs) when compared to Si (61 KW/m^3) and Ge (234 KW/m^3). But InP showed lower efficiency due to the thickness of the cell, which prevents the penetration of photons deeper into the inner layers. Further, in this research, the effect of real-time temperature conditions is obtained for all the PV panels by modeling them at -45 ^0C, 0 ^0C, 25 ^0C, and 51 ^0C.

Parameters such as short circuit current (I_{sc}), open circuit voltage (V_{oc}), Fill Factor (FF), and maximum power (P_{max}) are enumerated along with the efficiency. Similarly, for SSPV the GaAs is providing more efficiency compared to Si at different water depths till 1 m with 0.2 cm variations. For a faster parametric analysis at all possible real-time temperature conditions in Indian climatic scenario, in this research, an ML based prediction model is developed using Kernel Ridge Regression (KRR), Polynomial Regression (PR), Linear Regression (LR), and Support Vector Regression (SVR). It is observed that, the KRR algorithm can give faster (in few seconds), effective, and error-free prediction (92.23 % of accuracy). The prediction results are validated with the Multiphysics environment, data sheet, and experimental data.

In the past few decades, it has been observed that RES like solar PV cells coupled with a grid is a potential option for fulfilling the fast-growing load demand. However, the intermittent nature of Renewable Energy Resources (RER) limits the performance of RES and prevents it from being properly utilized. This results in power quality issues and grid system instability. To address this issue, it is a common practice to combine RES with

effective energy storage technologies, including the latest storage system based on Lithium-Ion Batteries (LIB) and Super Capacitors (SC). However, the fast charging of LIB and slow discharging of SC are still debatable. Time taken for charging LIB is usually sky-high that the Cost of Energy (CoE) becomes unprofitable. On the other side, although the charging of SC is faster, but undergoes quick discharging. Hence, in this paper, a cutting-edge model of LIB, i.e., an extreme Fast Charging LIB (FCLIB) is developed, where LIB is integrated with fast charging SC. This reduces the charging time of storage systems in comparison with conventional systems.

In the current thesis, six alternative topologies of FCLIB are developed and analyzed for CoE estimation, using real commercial load profiles and resource data. It is observed that the proposed FCLIB with the best topology is achieving 80 % of its State of Charge (SoC) in 5.84 min and 100 % of SoC in 13.5 min. The Optimized Electric Renewable Model (OERM) was employed to analyze the techno-economic analysis of the proposed FCLIB. It is estimated that the proposed topology of FCLIB has a CoE of 0.32$/kWh with fast charging, which is approximately equal to the CoE of a conventional slow charging LIB (estimated as 0.33$/kWh). Thus, the designed FCLIB provides an optimal storage solution for RES to overcome the intermittent nature of RER to meet the load demand.

The RER also include WECS with the conversion of wind speed into electricity. The WECS is the combination of wind turbine and Doubly Fed Induction Generator (DFIG). The WECS at offshore environment is exposed to harmful wind speeds which causes damage to wind turbine and DFIG. The DFIG exhibits stator and rotor faults where as finding the rotor fault like Broken Rotor Bar (BRB) by visually is difficult. So, the current signature analysis of the stator currents with/without the BRB fault by making DFIG as faulty and healthy is required. The DFIG with/without BRB fault is modeled in software and in experiment set-up to find the stator current variations with different percentage of faults (0%, 25%, 50% and 75%) and the load is also considered at no-load, half load and 1/4th load conditions.

The stator current data is collected from experimental set up via Data Acquisition (DAQ) system and from the obtained data, the features are extracted using five AI/ML techniques like Decision Trees (DT), Random Forest (RF), Logistics Regression (LR), Support Vector Machine (SVM)and K Nearest Neighbors (KNN). With the best

hyperparameters, the KNN gave 96 % accuracy making efficient prediction. The DFIG is then integrated with the SSPV, and EESS system to create an offshore microgrid in simulation and experimental model. The performance of the offshore microgrid is measured and obtained stable voltage and current performance with/without the fault consideration because of the control strategies.

CONTENTS

LIST OF TABLES

LIST OF FIGURES

NOMENCLATURE

List of Abbreviations

PV	Photo Voltaic
RER	Renewable Energy Resources
Ge	Germanium
Si	Silicon
InP	Indium Phosphide
GaAs	Gallium Arsenide
I$_{sc}$	Short circuit current
V$_{oc}$	Open circuit voltage
FF	Fill Factor
P$_{max}$	Maximum power
PR	Polynomial Regression
LR	Linear Regression
SVR	Support Vector Regression
KRR	Kernel Ridge Regression
CPV	Concentrated PV
STC	Standard Test Conditions
AI	Artificial Intelligence
SVM	Support Vector Machine
RBF	Radial Basis Function
RMSE	Root Mean Square Error
NISE	National Institute of Solar Energy
ML	Machine Learning
DL	Deep Learning
MSE	Mean Square Error
MAE	Mean Absolute Error
MAPE	Mean Absolute Percentage Error
FVDM	Finite Volume Discretization Method
SRH	Shockley-Read-Hall
SSPV	Submerged Solar Photovoltaic

LIB	Li-Ion Battery
SC	Supercapacitor
FCLIB	Fast Charging Li-Ion Battery
WECS	Wind Energy Conversion System
DFIG	Doubly Fed Induction Generator
ESS	Energy storage system
EESS	Energy Efficient Storage System
TSSPDCL	Telangana State Southern Power Distribution Company Limited
SOC	State of Charge
DOD	Depth of Discharge
PMSG	permanent Magnet Synchronous Generator
IM	Induction Machine
BRB	Broken Rotor Bar
LIC	Li-Ion Capacitor
SITF	Stator Inter Turn Fault
DT	Decision Tree
KNN	K Nearest Neighbors
PCC	Point of Common Coupling
HESS	Hybrid Energy Storage System
ANN	Artificial Neural Network
PERT	Passivated Emitter and Rear Cell Technology
HJ	Hetero Junction
FPV	Floating Photovoltaics
PCM	Phase Change Material

List of Symbols

I_{ph}	Photon current(A)
I_{sc}	Short circuit current(A)
I_d	Diode current (A)
K_i	Short circuit constant of cell at 25 ^{0}C and 1000 W/m^2 (0.0032)

T_{op}	Operating temperature
T_{ref}	Nominal temperature (273.15 K)
λ	Solar irradiation (W/m^2)
q	Electron charge (C) (1.6*10^{-19} C)
V_{oc}	Opencircuit voltage (V)
n	Ideality factor of the diode (1.5)
K	Boltzmann's constant (1.38 * 10^{-23})
E_{go}	Band gap energy of the semiconductor (eV) (1.12 eV)
N_s	Number of cells connected in series
N_p	Number of cells connected in parallel
R_s	Series resistance (Ω) (0.18 Ω)
R_{sh}	Shunt resistance (Ω) (360.002 Ω)
V_T	Diode thermal voltage (V)
V_m	Maximum Voltage (V)
I_m	Maximum Current
S	Cell area (m^2)
P_m	Maximum power (W)
R^2-Score	Coefficient of determination
$\overrightarrow{H_{opt}}$	Magnetic field vector
$\overrightarrow{E_{opt}}$	Electric field vector
v	Frequency
ε_r	Relative permittivity
ε_0	Permittivity of free space
S(v)	Spectral density of the AM 1.5G solar spectrum
h	Plank's constant
Q	Charge density
G	Irradiation distribution with spectrum wavelength
J_n and J_p	Current densities of electrons and holes
$\mu_{n(p)}$	Mobility of electrons (holes)
$n_f(p_f)$	Free electron (hole) concentration
$n_t(p_t)$	Electron (hole) trapped concentration
$R_n(R_p)$	Recombination rate of electron (hole)
$D_n(D_p)$	Electron (hole) impact ionization

s	Semi-conductor material thermal conductivity [W/(m*K)]
ρ_p	Density
C_p	Specific heat of material [J/(kg*K)]
Q	Generation of heat rate
U_{Aug}	Auger recombination rate
U_{SRH}	Shokley-Read-Hall recombination rate
E_g	Band gap of semi-conductor material
J	Conducting current density in the cell
I_{max}	Maximum current (A)
V_{max}	Voltage (V)
T	Temperature (T)
V	Voltage (V)
I	Current (A)
P	Power (W)
$w_0, w_1, w_2 \dots$	Weights
w	Weight vector
C	Regularization parameter
ε	Insensitive loss function
b_0	Bias

CHAPTER 1

INTRODCUTION

1.1   Background and Motivation

The global population increase is leading to an increased reliance on fossil fuels that release greenhouse gases [1], [2]. Future power and energy requirements in the world are at risk due to the potential shortage of fossil fuels. According to recent research, the existing reserves of natural gas and oil are anticipated to deplete within the next 40 and 70 years, respectively [3]. This intensifies the already ominous effects of climate change, prompting urgent action to reduce greenhouse gas emissions. So, finding the alternative energy sources to meet the energy and power demand is usage of renewable energy resources (RER) by achieving the goal of net zero emissions with effective storage solutions [4]. The increased use of RER in remote areas highly relies on the microgrid development as a solution for the reliable integration.

The marine/earth environment provides numerous RER, in the form of thermal, wind, tidal, solar energy etc., which if efficiently tapped can be used for many on shore and off-shore applications. Among these resources, wind and solar resources for power production are in most demand with more emerging infrastructure and storage technologies [5], [6]. The fundamental qualities of solar energy are geometric depth below the surface of water, light wavelength, photon travel polar angle, optical depth below the surface of water, polar angle cosine, solid angle, photon travel azimuthal angle, and scattering angle. The solar energy can be converted into electrical energy by using semiconductor device called Photovoltaic (PV) cells and being in use from 1839, when French scientist E. Becquerel [7] while experimenting on an electrolytic cell, discovered the PV effect. The PV cells are further improved and classified depending on the cell technology, type of top layer, and number of junctions as 1st, 2nd and 3^{rd}generation solar cells. The PV cells of different materials are considered but Silicon (Si) solar cells are the most commercialized PV cells [8]–[13].

The mounting of PV cells is of two ways one is earth/roof-top, and other is water-based mounting. The earth/roof-top mounting is emerged in the world more in terms of research, commercial utilization and implementation [13]. The PV cell efficiency is limited

and is ranging between 15% to 20% due to the Shockley-Read-Hall (SRH) recombination, bandgap, type of material, irradiation intensity, and temperature conditions [14]–[19].

To improve the efficiency of solar cells, cooling techniques and water-based mounting are implemented. The cooling techniques are again classified as active, passive, nano-fluid and thermo electric cooling technologies and the water-based mounting includes floating PV and submerged PV [20]–[25]. Figure 1.1 shows the co-occurrence of photovoltaic system three major clusters, cooling, materials, and sustainable development with network visualization from Scopus database and the Figure 1.2 shows the state of the art of the PV cell research overlay visualization from Scopus database from 2012 to 2023.

Figure 1.1 The co-occurrence of PV system clusters with network visualization from Scopus database (made in VOS viewer)

Present days research focus is on water based floating/submerged solar mounting cells is upcoming as the land required for earth mounted solar cells is more and also to improve efficiency of solar cells [24], [26]–[32]. Remarkably, despite the challenging weather conditions in which the experiment is conducted [23], [33], the PV panels displayed an impressive average maximum efficiency of 21.6% in an underwater (UW) environment, with various parameter variations. An analysis of the UW environment is presented in [34], which highlights the significant advantages of organic photovoltaic (OPV) for UW operation. The hydro-optical characteristics of water and the solar cell performance at different conditions are explored in [35]–[37].

The captured energy from earth/water based mounting PV needs to be stored efficiently to have reliable power supply to the load which ensures sustainability called as energy storage systems (ESS).

Figure 1.2 The state of the art of the PV cell research overlay visualization from Scopus database (made in VOS viewer)

The ESS are classified as superconducting magnetic energy storage, battery and hybrid ESS where the power obtained from all various RERs can be stored and delivered effectively to the load as per the demand. Wang *et al* in 2014 [38], proposed a 1-MW grid-connected solar PV power plant and a power smoothing strategy. A vanadium redox battery and a super capacitor bank composed Hybrid Energy Storage System (HESS) is used to smooth the fluctuating power output of the PV. The PV plant is modeled using MATLAB/SIMULINK and PLECS software environment including the HESS.

A novel grid ESS is proposed in [39], where the battery charging and discharging are carried out for large-scale PV systems through an AC voltage regulator which is connected in series to the line. For this system, a high-power application with cascaded H-Bridge based PV - inverter is selected. A review on hybrid EESS for renewable applications are suggested by different researchers with different combinations of Efficient Energy Storage System (EESS) [40]–[43].

In recent times, the requirement for fast charging is emerging and the implementations of different control topologies are increased at converter side. As the ESS evolves, the utilization of EESS are required for integrating with RERs which is the combination of the different sources called as microgrid [39]. PV alone and ESS storage are not sufficient to meet the load demand. So, the wind energy can also be utilized further to form a microgrid. In micro-grids, the most utilized combination of renewable resources is solar and wind energy [44]–[46]. Micro-grid integration, involves integrating a solar panel, and battery system with wind turbine.

The integration of RER exhibits different harmonic production, impedance mismatch problems [47]–[50]. When wind energy alone considered it exhibits different levels of stator and rotor failure conditions with varied wind flows on wind Energy Conversion System (WECS) [51], [52]. The diagnosis of the fault in WECS require signature analysis and the condition monitoring of the DFIG with the use of different sensing elements [53].It is important to note that while RERs and EESS hold great potential for providing a reliable power supply, there are still numerous challenges and barriers that need to be addressed [54], [55]. These obstacles are the focus of much research and effort, with significant consideration being given to develop, strengthen, and identify enablers to conquer the barriers [56], [57]. Figure 1.3 categorizes the main barriers to deploy RER which include technical, economic, institutional and social factors [58]–[60].
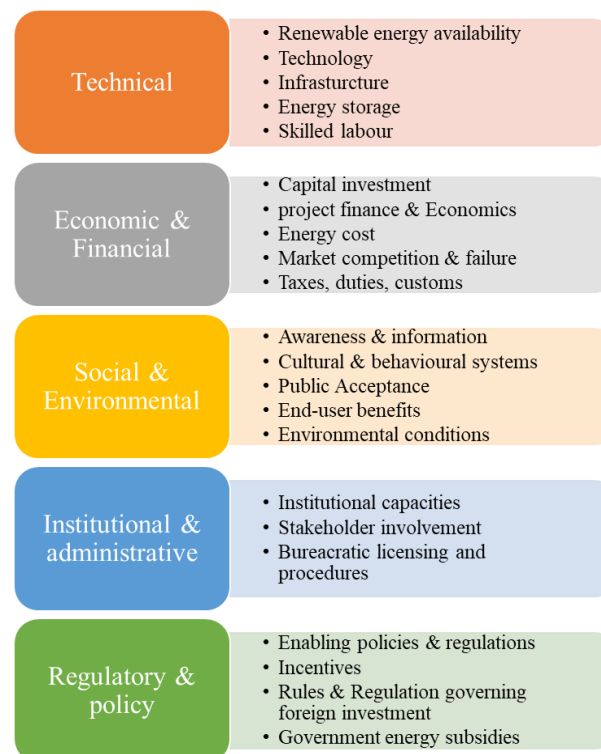
Figure 1.3 Categorization of the main barriers to deploy RER [2]

1.2   Aim and Scope

The increasing demand for energy and the need to reduce carbon emissions has led to the development of RER such as PV and wind energy. Offshore microgrid systems have the potential to integrate these renewable resources and provide a reliable and sustainable energy supply to remote areas [61].The microgrids can perform both in standalone and grid-connected modes [62]. The RERs include PV and the development of PV at offshore conditions is a major concern. The irradiation above the earth surface is mix of entire solar spectrum but inside the water the solar irradiance will be absorbed at different depths. In the ocean water depths, the scattering physics is a little different. The primary role of the atmosphere is to scatter light when light passes through it, but water primarily absorbs light rather than scattering. Water molecules, prefers the wavelengths absorb, rather than having a straight forward wavelength dependence, it can easily absorb infrared, ultraviolet, and red visible light. Heading down a little deeper, the orange light goes away, too. The green, violet, and yellow gets disappeared further deeper. On heading down to depths of multiple Kms in water, finally the blue light disappears as well, although it's the last to do so. All the other wavelengths get absorbed hence the deepest ocean depths appear dark deep blue.
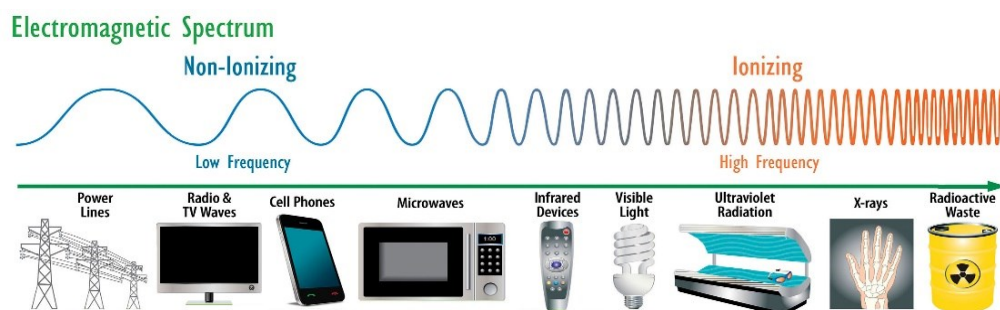
Figure 1.4 Electromagnetic spectrum(courtesy to [UTAH department of environmental quality](#))

The deepest blues, unique among all the light wavelengths in water, have the maximum possibility of getting re-emitted back and reflected. PV cells are favored as a long-endurance power source for many of the applications like local utility grid connection, battery storage, backup generator power, small home applications and connecting as a hybrid power system. In submerged conditions, there is solar power to harvest and use at water depth of 9.1 m. The filtered spectrum of the sun under water (UW) is biased toward the blue/green portion of the spectrum, and thus, higher bandgap cells, such as InGaP, perform much better than conventional silicon cells [63].

The different parameters variation of a PV panel in an UW environment, with an average of about 15.6% maximum efficiency, for which the experiment is performed [23] at remarkable weather conditions. In [34], an analysis of the submerged solar PV (SSPV) environment is presented which highlights the significant advantages of organic photovoltaic (OPV) for UW operation. The hydro-optical characteristics of water and the PV performance at different conditions are explored [35]–[37]. Designing of mathematical and Multiphysics modeling of the SSPV is one of the aims of this research.

Tina et.al [64], presented a review about the applications of Machine Learning (ML) techniques in different fields of PV. ML-based models are mostly proposed for the field of PV production forecasting. Berny Carrera and Kwanho Kim [65], presented linear regression (LR) and Polynomial Regression (PR) with different ANN techniques for 36Hrs prediction of PV power production with weather forecast and observations. A review based on Deep Learning (DL) techniques to forecast different cell technologies and utilization of them for the prediction of PV power is available in [66]–[68] and solar irradiance in [69], [70]. The Mean Square Error (MSE), RMSE, Mean Absolute Error (MAE) and Mean Absolute Percentage Error (MAPE) are considered as metrics and measured to find accuracy.

The design of HESS is considered in many of the research works to store the energy captured from RERs. The HESS is the combination of battery, pumped hydro storage and capacitors. In most of the cases, the demand for energy varies from day to day, and from season to time. Moreover, between day and night there is a major difference in the peak to valley [71]. Therefore, the generated power needs to be stored and available energy is provided during peak loads by peak shaving and load leveling [72]. Utilities are shifted to utilize RER to meet the rapidly increasing load demand. However, due to intermittent nature of these RER, the grid may experience instability and power quality issues [73] like harmonic distortion, phase unbalance and voltage drop. This significant increases in demand for RER, as well as the intermittent nature of RER, has promoted and necessitated the development of electrical ESS [74], [75]. The ESS like batteries and SC can effectively store renewable energy generated [76], [77] and deliver energy to the load demand during peak leveling.

Offshore microgrid systems with PV and WECS integration face various challenges. One of the primary challenges is the harsh environment, which can damage the components and affect system performance [78].The importance of reliability analysis for offshore WECS has increased with the development of offshore wind power generation, as

these systems operate in harsh conditions and exhibit complex behaviors that can have significant negative impacts [51], [52]. It is therefore crucial to thoroughly analyze the reliability of offshore wind turbines to ensure their safe and efficient operation. In [79], The WECS typically consists of wind turbines, generators, and a control system are explained and the failures are incorporated with fault tree analysis. Offshore, the wind blows at higher speeds and rotates the turbine blades which rotates the generator rotor via the gearbox. The Doubly-Fed Induction Generators (DFIG) are mostly preferred generators for offshore WECS due to higher wind speeds. The DFIG exhibit faults in the stator and rotor construction, like Broken Rotor Bar (BRB), Stator Inter Turn Faults (SITF), line faults etc.,[78], [80].

The DFIG exhibits almost 9-10 % of BRB fault while used as industrial machines and in the offshore environment, it is double the fault on land. The diagnosis of the incipient BRB fault in the WECS is the major concern to increase the reliability of the offshore micro-grid system [81], [82]. Different fault detection techniques in the experimental condition and with signature analysis are performed via Deep learning techniques using Convolution Neural Networks are performed with IR images, voltage, and frequency variation detection [82]–[87].

1.3   Research Gaps Identified

In order to study the physics of PV cell/panel, mathematical, and Multiphysics modeling of PV cell/panel is needed where all the PV parameter variations can be observed. In such case the modeled PV cell has to perform similar to the commercially available cell, and can be utilized further for different material coatings and environmental conditions. Similarly, the analysis of SSPV performance at different intervals of temperatures with standard irradiation in mathematical and Multiphysics environment is needed. But Multiphysics modeling requires large time for computations and the time can be reduced by predicting PV and SSPV performance using AI based ML prediction techniques in less time.

In order to overcome the variable power distribution, voltage and frequency instability, fast charging of Li-ion Battery (LIB) with Supercapacitor (SC) is the need of the hour. On the other hand, due to its RER high initial cost, there is an argument on the extensive and efficient utilization of LIBs and SCs. Hence, the techno-economic analysis and characteristics of LIB and SC are needed to be investigated for finding economically feasible fast charging technology [88]–[91]. Hence, designing of fast charging Li-ion

battery with the best identified characteristics such as life cycles, charge/discharge time, internal resistance and power/energy densities of both LIB and SC is needed.

The intermittent nature of PV leads to insufficient energy supply to the load demand even after integrating with the EESS. Hence, addition of high energy source like wind is required. So, with techno-economic analysis of integrated PV and EESS, the WECS is combined forming a small scale microgrid. The importance of reliability analysis for offshore microgrid with the detection of WECS failures is more important. The design of offshore microgrid with the integration of SSPV, EESS with WECS need to be considered with/without BRB fault consideration (healthy, unhealthy) via mathematical modeling, and experimental setup of DFIG. From the literature, the research objectives framed for offshore microgrid design with the below research gaps:

- ✓ The mathematical/ Multiphysics modelling of SSPV cell/panel under different depths of water and prediction of SSPV performance at more depths via AI/ML techniques are not implemented
- ✓ Mathematical modelling of a suitable EESS with the fast charging of LIB (FCLIB) and slow discharging of SC.
- ✓ Integrating SSPV with EESS by creating offshore microgrid and its techno-economic analysis and modelling of WECS and integrating with the combined SSPV and EESS model.
- ✓ Mathematical modelling of offshore WECS with the consideration of DFIG BRB fault and its condition monitoring by using AI/ML techniques and integrating with the SSPV and EESS.

1.4   Objectives of the Research

The objectives of the proposed research work are shown in Figure 1.5 include:
- ➢ Mathematical simulation and Multiphysics modelling of PV at cell/ panel level, and SSPV and validation of PV using I-V and P-V performance characteristics. The PV cell performance characteristics will be obtained with different temperatures, irradiation conditions and material variations using COMSOL Multiphysics modeling. Validation of modeling with the experimental values, and data sheet. Implementation of AI/ML techniques for the prediction of PV cell performance with different materials at different levels of water depths, and temperatures.

➢ Numerical modeling of EESS with the integration of fast charging LIB (FCLIB) and slow discharging SC. As the energy from the RER is intermittent, it has to be stored efficiently and effectively hence, the design of different topologies of FCLIB is simulated with the respective charging and discharging times plots at different internal resistance variations and temperature variations.

➢ Techno-economic analysis of off-shore micro-grid system with the integration of submerged PV system and EESS in Homer-Pro software for validation considering load demand. The offshore microgrid is further extended with the integration of WECS in simulation to provide continuous reliable power supply to the load demand.

➢ Simulation of WECS with BRB faults and integrating with the off-shore micro-grid system modeled using MATLAB/SIMULINK. Experimental set-up of offshore microgrid system with the integration of SSPV, EESS and WECS is developed with the DFIG BRB fault. For acquiring the healthy/faulty data of DFIG Hardware In-Loop (HIL) is considered and for Condition monitoring of DFIG with performance prediction and validation AI/ML techniques are implemented.

Phase 1
- Comprehensive literature survey.
- Identification of gaps in the literature and development of suitable methodology.

Phase 2
- Designing Solar PV cell
- Designing SSPV model
- AI/ML techniques implementation for performance prediction

Phase 3
- Mathematical/Multiphysics modelling of LIB and mathematical modeling of SC
- LIB design, SC design and parameter variations, and FCLIB capability

Phase 4
- Integration of SSPV and EESS connected in grid mode
- Techno-economic analysis of the integrated offshore microgrid

Phase 5
- Mathematical modeling of WECS with the DFIG with/without BRB fault modeling
- Modelling of offshore Microgrid system by integrating wind Energy System with SSPV and ESS

Phase 6
- Finding the results and making conclusion
- Future Scope (based on observed results, and challenges)

Figure 1.5 Different phases of objective research

9

1.5 Organization of the Research

There are seven chapters in total based on the research objectives and they are outlined as follows:

Chapter 1: This chapter gives a brief discussion about the background of research and the main scope of the work. The research motivation, Gaps identified, objectives and the organization of research are included in this chapter.

Chapter 2: This chapter presents an extensive literature survey on the earlier work which lead to SSPV design. The reasons for the decrease in PV efficiency are discussed and methods used to improve it are also discussed in this chapter.

Chapter 3: The modeling and simulation of SSPV is implemented in this chapter. This chapter details the numerical and Multiphysics modeling of SSPV panel and performance characteristics plotting at different levels of water depth and material variations. Firstly, the mathematical, Multiphysics modeling of PV at cell/ panel level and validation of PV with performance characteristics different temperature, irradiation conditions and material variations is presented. Then validation of modeling with the experimental values, and data sheet are observed and emerging into SSPV design is also presented. AI/ML techniques for the prediction of PV/ SSPV performance with different materials at different levels of water depths, and temperatures is also presented in this chapter.

Chapter 4: This chapter has presented storage of the energy received form the SSPV design, where the design of LIB and SC are presented. Multiphysics modeling of LIB with different materials, temperature and C-rates with the data sheet validation of model. The mathematical modeling of LIB and SC considering equivalent circuits with charge/discharge characteristics at different C-ratings. Numerical modeling of EESS with the integration of fast charging LIB and slow discharging SC is discussed in this chapter. Design of different topologies of EESS with their respective charging and discharging times at different internal resistance variations is also presented in this chapter.

Chapter 5: This chapter briefs the integration of SSPV with EESS with the use of HOMER-Pro software and presents the techno-economic analysis of the offshore microgrid. The present net cost (PNC) analysis is also presented in comparison with commercial equipment and is included in this chapter. The simulation design of WECS with the turbine and DFIG system is also discussed in this chapter and the integration to the SSPV and EESS is also explained.

Chapter 6: The harsh environment at offshore conditions creates faults in the WECS so here BRB fault of DFIG is considered. The WECS with/without the BRB fault of DFIG is modeled and integrated with the designed off-shore microgrid system. The performance of the total offshore microgrid is measured both in modeling and experimental set up. Acquired the healthy/faulty data from experimental DFIG system with the sensors via data acquisition (DAQ) and implemented AI/ML techniques for Condition monitoring of DFIG with performance prediction.

Chapter 7: Eventually, this chapter has concluded the thesis work and gives insight into the future scope. Also, it includes the limitations of the current thesis work.

Every chapter starts with an introduction, ends with a summary of the chapter, and addresses the reason for the next chapter.

CHAPTER 2

EVOLUTION OF THE PERFORMANCE OF SOLAR PHOTOVOLTAIC SYSTEMS IN THE SUBMERGED ENVIRONMENT

2.1   Introduction

The World's energy needs and future energy supply are under risk because of the scarcity of fossil fuels. Many researchers predicted that the current reserves of natural gas and oil diminish within 70 and 40 years respectively. Also, the carbon emissions are increasing at a rate more than 3% per year, increasing the amount of fossil fuels like carbon monoxide and carbon dioxide gases in the atmosphere [92]. Here is a great need to utilize energy resources that are renewable in nature to meet the current energy demand. The energy resources like solar, wind, tidal, geothermal etc., are the RERs and among them solar energy plays a major role and it contributes to 70 % of the total energy. The utilization of solar energy begun in the era of 7th century B.C and it is used for different applications but the conversion of solar energy into electricity begun after the discovery of PV effect.

In 1839, French scientist Becquerel [7] while experimenting on an electrolytic cell, discovered the PV effect. He found that solar energy can be captured by a semiconductor device through the PV effect and the device was thus named as PV cell. Significant research on various semiconductor materials were performed for observing PV effect, in 1948, June 15, Bell telephone laboratories patented "Light-Sensitive Electric Device Including Silicon". This achievement initiated the usage of silicon solar cells. Silicon solar cells have higher conversion efficiencies ranging between 15 to 18 % compared to other PV materials [15].

Essig et al, in the year, 2015, [93], proved that the silicon cell efficiency can be raised to 30 % by decreasing the surface temperature of silicon PV cell using a mechanism to cool the cell surface. As such, most commercialized solar cells are made up of silicon materials and water is utilized as a cooling liquid to decrease surface temperature and acquire higher efficiency from the solar cell. Water is preferred as a cooling agent because

of its non-toxicity, stability, high heat transfer capacity, low cost, and abundant availability.

Mauddi *et al.,* in the year 1991*,* stated that the solar cell spectral response matches with the absorption coefficient of the sunlight in water [94]. As 71% of the total surface of earth is covered with water and of which 96.5% is contributed by oceans [95], the marine or ocean environment provides number of RERs, such tidal energy, thermal energy, wind energy, light energy, etc., These renewable energy resources, if efficiently tapped, can be used for many onshore and off-shore applications [26]. In this chapter, the solar PV cells and SSPV[1] cells design consideration are explained in detail for efficiency improvement. The ocean environments and its irradiation variation in different depths of water are also detailed.

2.2 A Review on Performance Analysis of Solar PV Cell

As mentioned in the section 2.1, Becquerel [7] found in the year 1839 that solar energy can be captured by a semiconductor device through the PV effect forming the solar cells. The collection of solar cells arranged into a framework, known as a solar panel or PV panel. Wurfel in the year 2007 reported in his book [96] that, when photons fall on the PV cells surface, the energy of photon will undergo three main processes:

1. **The absorption of the incident radiation energy:** As photons fall over solar cell, all photons aren't absorbed by the cell. Photons that have sufficient energy to move it from valence band to the conduction band by excitation of an electron and cause the current to flow, will be absorbed. Any photon with lesser energy than the energy of bandgap will not be absorbed by the photovoltaic cells and cannot excite the electrons, it will be either transmitted or reflected.

2. **The hole-electron pair thermalization:** In thermalization, the heat energy from sun is converted to chemical energy through the heating process of electrons and holes causes bombarding and creating electron-hole pairs at the P-N junction.

3. **Energy Conversion:** The conversion into electrical energy from chemical energy is known as energy conversion, where holes are moved to P-type and electrons are moved

---

[1]C. S. Durganjali, S. Radhika, R. N. Ponnalagu, and S. Goel, "A Study on the Performance of Solar Photovoltaic Systems in the Underwater Environment," in *Microelectronics and Signal Processing*, CRC Press, 2021, pp. 203–226.

to N-type and get segregated. When these two ends are connected through an external circuit we can see movement of electrons and the obtained current is known as PV current.

If irradiation falls on a solar cell surface, the PV current can be observed and the maximum current obtained from a solar cell depends on its type of construction. The solar cell construction depends on cell technology, type of top layer and number of junctions in the solar cell. Based on all the above-mentioned parameters, the solar PV cells are classified again as shown in Figure 2.1.

2.2.1 Classification of Solar PV Cells
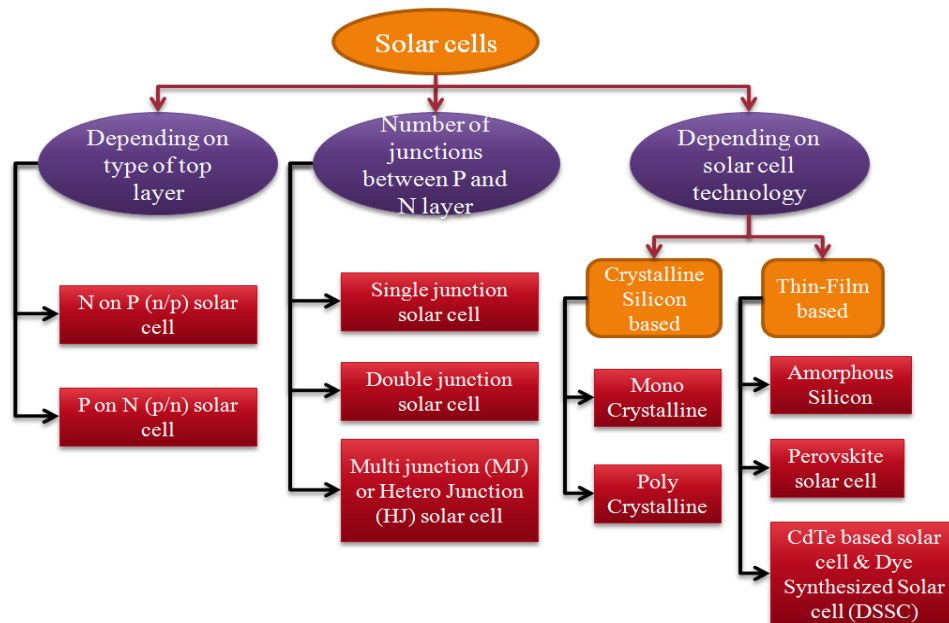
Figure 2.1 Classification of solar PV cells

2.2.2 PV Cell Characteristics

The performance of solar cells can be estimated from its electrical and thermal characteristics. The electrical characteristics include I-V and P-V (Power- "P", Current- "I" and Voltage- "V") characteristics through which the PV cell efficiency can be deliberated. From the I-V characteristics, the open circuit voltage (V_{oc}) and short circuit current (I_{sc}) are noted. From P-V characteristics, the maximum output power (P_{max}) from the PV cell can be obtained, from which the PV cell efficiency can be calculated. Irradiation from the sun is the source for a solar cell and temperature is an element that affects the performance of PV cells. Depending on irradiation, temperature and type of cell materials, the analysis of PV cell performance is further carried-out.

2.2.2.1 Irradiation dependence on PV cell characteristics

When the irradiation intensity on a PV cell increases, I_{sc} will increase and vice versa. But V_{oc} of solar cells will mostly remain constant irrespective of radiation. As intensity of radiation varies, depending on the electrons and holes' generation rate, the current output from the PV cell varies which in turn varies the power output. In general, with the surge in irradiation, the solar cell's I_{sc} escalates, because of this the power production also increases. At maximum irradiation point ($1000W/m^2$) and 25^0C temperature conditions i.e., at the standard test conditions (STC), it's possible to enhance the power produced from the PV cell.

The V_{oc} of the cell is constant and depends on the material used. To obtain a large V_{oc}, the solar cells are connected in parallel and series. If the irradiation that falls over a solar cell is continuous, then temperature on the top of the solar cell increases even though the environmental temperature is less. Werner Luft [12] compared experimentally, the performance of 5-grid and 13-grid silicon (Si) and gallium arsenide (GaAs) solar cells at different temperature ranging from $30\ ^0C$ to $150\ ^0C$ and radiation intensities ranging from $0.07\ W/cm^2$ to $2.8\ W/cm^2$ and concluded that, compared to GaAs solar cells, the 3-grid silicon solar cell showed a better performance.

2.2.2.2 Temperature dependence on the PV cell characteristics

Performance of a PV cell under different temperature and irradiation conditions will vary depending on the cell type. For example, an anomalous behavior is observed at less temperatures in the "N on P" cells; namely, the V_{oc} becomes nearly self-reliant of temperature beneath a transition temperature depending on the sunlight intensity. Smith *et al.* [97] explained the working of "N-on-P" solar cell and its characteristics when it is used in a spacecraft application. Kennerud [98] experimentally determined the values of V_{oc}, I_{sc}, and P_{max} for "N on P" and "P on N" silicon solar cells from $-177\ ^0C$ to $+50\ ^0C$ temperature ranges under equivalent sunlight intensity of $58\ mW/cm^2$ and the I-V characteristics are shown in Figure 2.2 (a) and 2.2 (b) respectively. It is detected from the I-V characteristics that V_{oc} lessens in a linear fashion with temperature, while I_{sc} increases.

a.   b.
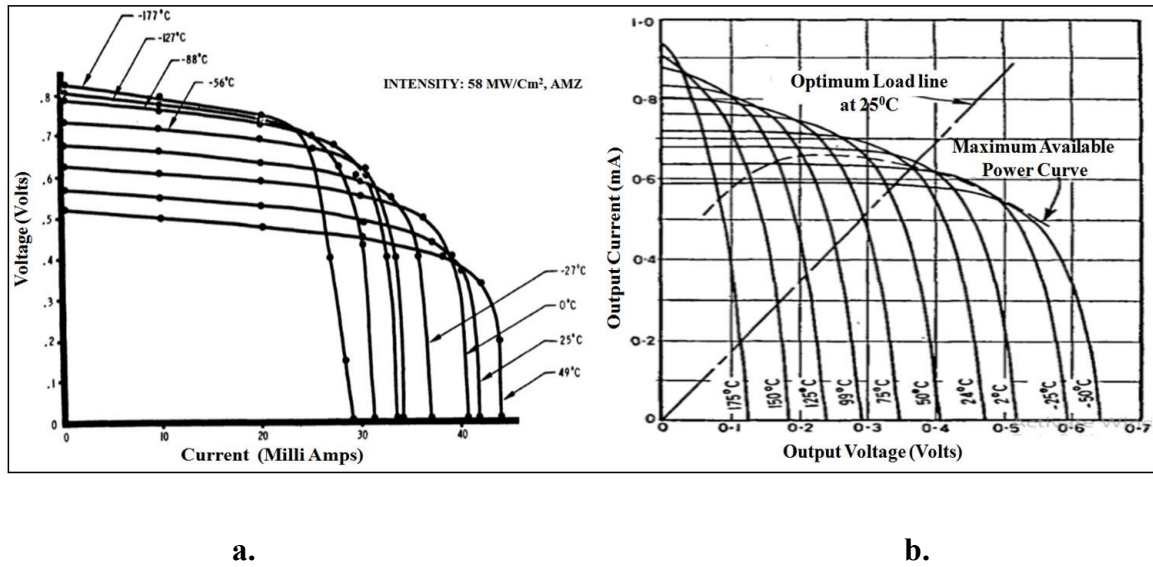
Figure 2.2 (a) I-V characteristics of silicon "N on P" solar cell and (b) I-V characteristics of "P on N" silicon solar cell at temperatures ranging from -177 ^{0}C to +50 ^{0}C [98], [99]

Durganjali *et al.* [100][2] made a mathematical modelling of a solar cell which will work in both positive and negative temperature conditions. It is perceived that performance of a PV cell with the varying temperature (-45^{0}C to +50^{0}C) levels and at different irradiations (600W/m^2, 1000W/m^2 and 200W/m^2) is analyzed and at 600W/m^2 the I-V and P-V characteristics analysis is shown in Figure 2.3 (a) and 2.3 (b).

The research is concentrated around PV cells performance during different temperatures. The electrical parameters include P_{max}, V_{oc} and I_{sc} are measured at greater than the absolute zero Kelvin temperature. The preferred test conditions (STC), top and truncated temperatures recorded in India, are taken into consideration for PV cell performance comparison. The electrical parameters under different irradiation and temperature variations are obtained from simulations in MATLAB/SIMULINK. As the temperature increases, the efficiency, P_{max}, V_{oc} falls and I_{sc} increases simultaneously. Similarly, as the material changes, the PV cell efficiency also changes due to the bandgap variation of the material utilised.

---

[2] C. S. Durganjali and R. Sudha, "PV Cell Performance with Varying Temperature Levels," *2019 Glob. Conf. Adv. Technol. GCAT 2019*, pp. 1–5, 2019, doi: 10.1109/GCAT47503.2019.8978302.

a)

b)
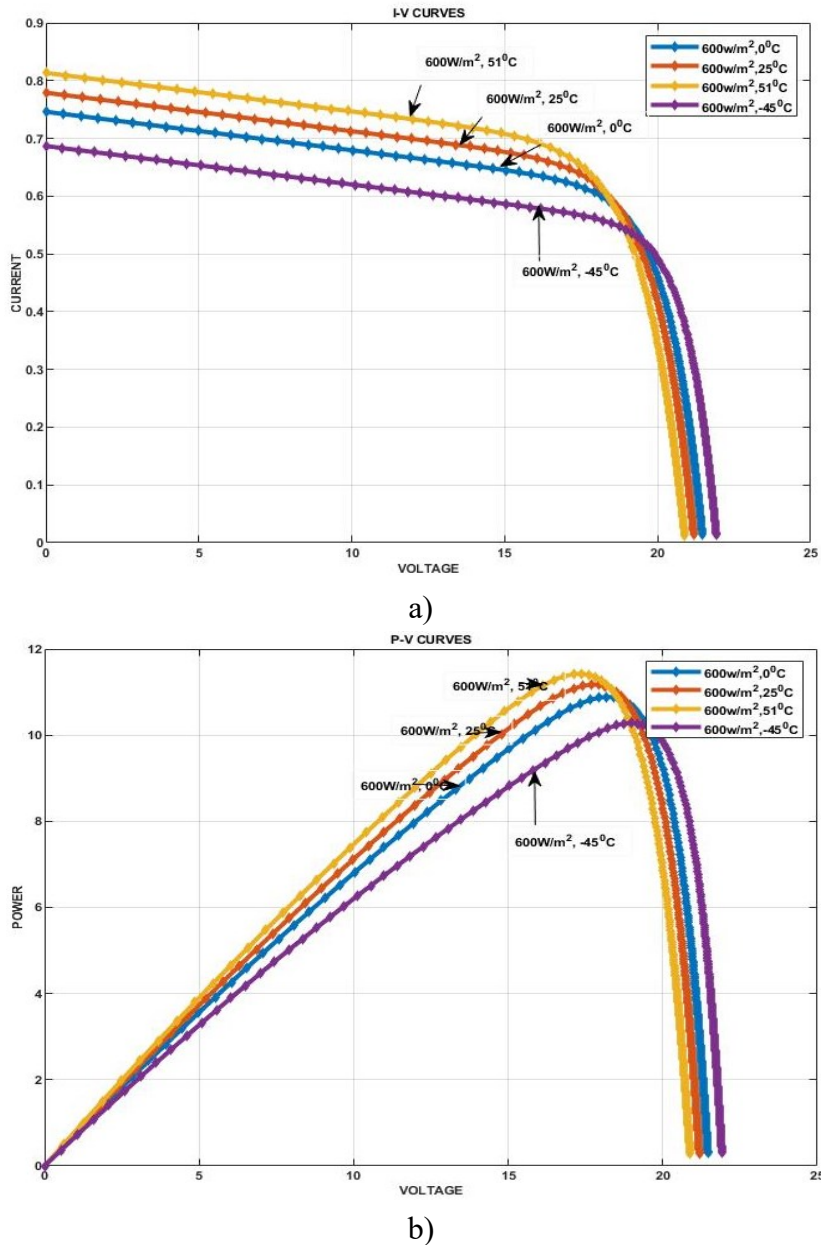
Figure 2.3 (a) I-V and (b) P-V characteristics of solar cell at 600W/m² for four different temperatures such as -45 ⁰C, 0 ⁰C, 25 ⁰C and 51 ⁰C

2.2.2.3 Material dependence on PV cell characteristics

The material utilised for the construction of solar cells plays a vital role. Different materials used for making solar cells are: Silicon (Si), copper indium gallium selenide (CIGS), Germanium (Ge), Gallium Arsenide (GaAs), thin-film solar cells, Cadmium Telluride (CdTe) etc. The majority of solar cells are fabricated using silicon as material and the efficiency of commercialised Silicon solar cells are 15 to 21 % and the experimental solar cells have more than 20 % and reach up to 30 % of conversion efficiency and is described in detail in the section 2.2.3.

Solar cell conversion rate or efficiency, refers to the rate of conversion of the inward flow of solar energy into the electrical power. Typically, the commercialised solar panels operate in the range of 15-21 % [15] of efficiency. Experiments are going on to improve the cell efficiency with different types of fabrications. In that Metal Wrap Through (MWT), Upgraded Metallurgical Grade (UMG), Passivated Emitter Rear and Totally diffused Rear-Junction (PERT_RJ) and Passivated emitter and rear solar cells (PERC) are reaching conversion or quantum efficiency of up to 30 % but these are not commercialised yet. Some of the fabrications and inventions made by different researchers are explained below with their respective efficiencies also listed in Table 2.1.

Table 2.1 List of different silicon solar cells and their efficiencies

Type of Silicon (Si) solar cell	Conversion Efficiency
Triple Junction-High Frequency	11 to 12 % [14]
MWT	19 to 19.6 % [101]
Bifacial N-type solar cell	> 20 % [102]
PERC Solar cell	20 % [103]
Boron-doped p-type mono-crystalline Cz silicon wafers	20 to 21 % [104]
Selective FSF n-type rear-junction laser-doped solar cells	20 to 21 % [11]
p-type multi-crystalline silicon	20 to 22 % [105]
From 100% UMG silicon feedstock n-type Czochralski-grown silicon solar cell	> 21 % [10]
n-PERT_RJ	22 to 23 % [106]
Hetero Junction (HJ)	> 24 % [107]

2.2.3   Factors Affecting the Solar Cell Efficiency

One of the main reasons for reduced solar PV cell efficiency, lies in the sun's physical conversion energy. The fundamental principle of the solar PV industry is a study by Queisser and Shockley developed in 1961. The maximum efficiency of 33.7 % is possible based on a theory by which a PV cell can achieve from a light source to obtain electricity. This theory is called the Shockley-Queisser limit [14]. This is related with the process of photon absorption to generate an electron (e⁻) and then pass it to the conduction

band [18]. There is no specific technology or manufacturing process development which can change the limitation fact. This Shockley-Queisser limit is computed as energy conversion efficiency of a solar cell with the maximum theoretical boundary. Few environmental and material factors affecting solar cell efficiency are listed below:

1. Snow, ice, dust and humidity
2. Insulation resistance
3. Temperature
4. Solar cell type (crystalline, amorphous, thin-film & perovskite) and
5. Design configuration

By observing the I-V characteristics of P on N and N on P solar cells as shown in Figure 2.2 a) and b) and also with lithium doped solar cells, the surface effects in solar cells can be analysed. Lithium doped solar cells performance with respect to variation in temperature indicates that lithium (Li) in the region of n-type "P on N" silicon solar cells interact by 1 MeV electrons (e⁻) or 16.8 MeV protons [108] exposure with induced radiation damage. At low radiation rates and room temperature, the PV cell power output does not decreases and at high radiation rates and temperature, the output from cell decreases even then it retrieves after irradiation degradation, i.e. the Lithium doped PV cells acts as self-healing summarized by Wysocki [108]. Proton-induced humiliation of the cell characteristics can be summarised before, after and during proton exposure. Anomalous damage, including significant losses of P_{max}, and partially recoverable losses of V_{oc} can be identified within different regions of the PV cells with the penetration of proton into depths by correlation [109].

Tallent *et al* in the year 2013 [110] tested silicon solar cell performance with Archimedes array of mirrors which are capable of concentrating the sun's energy. The I-V characteristics are obtained at 40 ^{0}C temperature and at different illumination levels. Concentrating the sun's energy increased the output but with raise in the temperature, the cell's efficiency is decreased and it increases heat on solar cell's surface damaging the cell. In practical terms, the energy conversion efficiency can be affected by one of the major factors by temperature as discussed earlier in section 2.2. The temperature effect could be decreased by using cooling methods, which in turn improves the efficiency of solar cell.

2.3   Efficiency Improvement of Solar Cells

The efficiency of PV cell decreases due to temperature elevation. The temperature degradation rate varies within 0.25 % to 0.5 % per ^{0}C, based on the type of material used for PV cell. Specifically, in case of concentrated PV (CPV) cells, which utilize focused sunlight and provides large output power with low-cost PV equipment. It is also evident that operating at high temperatures significantly reduces the life time of the CPV systems. The effect of temperature on PV cells can be reduced by adapting cooling techniques and there are two types of cooling techniques used which are forced and natural cooling. The forced cooling systems are further subdivided into active cooling, passive cooling, thermo-electric cooling and nano-fluid cooling. The natural cooling system includes floating PV (FPV) systems which use natural water as a cooling liquid. The subsections 2.3.1 and 2.3.2 discuss the respective techniques and their advantages in detail.

The temperature effect can be decreased with the below technical methods:

1. Forced cooling systems
2. Natural cooling systems

2.3.1   Forced cooling systems

The forced cooling system uses additional equipment like pipes, motor drives etc., to force the cooling liquid to flow in the front side, backside and on both of the sides of PV panels and the coolant used may be air, water, metal oxides, organic or inorganic liquids. The different types of forced cooling mechanisms are discussed in [111]–[114], [115]. A 5 % increase in output power is obtained by using cooling techniques in [116]. Nevertheless, 87 % of irradiated energy will convert into heat and the waste heat is harnessed into useful thermal energy in recent developments. In general, hybrid elements which mobilize both thermal and electrical power of solar are known as PV- thermal units (PV/T unit). These PV/T units generally have lower specific efficiency but higher overall efficiency when collated with solar collectors and stand-alone PV [117]. Early in PV exploitation cooling techniques for heat applications are proposed [118] with the commonly used forced cooling techniques like passive cooling and active cooling and this classification is relied on whether power is consumed during the cooling process or not.

2.3.1.1 Active cooling method

Active cooling methods consume power continuously to force the coolant (air or water) through the panel sides. The primary power consumption unit is either a pump or fan which is used for circulating the fluid. In [119], the active cooling technique is adopted and the coolant is forced to flow into both front and backside. The flow rate of water is 0.0625 kg/s which is the maximum value that can be pumped using a pump. A water jet is used there for forced cooling which further increased the effect of cooling on solar panels. The disadvantage in this method is that the power consumed by pump will be more than that of the power being generated from the PV panels.

2.3.1.2 Passive cooling method

Passive cooling method utilizes the conduction/convection techniques to eliminate heat naturally. The passive methods of cooling are categorized into three main types as conductive cooling, water cooling, and air cooling. The conductive cooling is similar to air cooling but a significant difference in the heat transfer mechanism from solar cells is conductive. Phase Change Material (PCM) cooling is a selective type of passive conductive cooling. The PCM in the strict sense can't be observed as cooling, it helps in maintaining a less steady temperature. PCM cooling can be considered as a passive cooling technique because in this method no additional power is needed, and the heat dissipation is conductive in nature.

Smith *et al.* The global potential of PCM observed in [120]. Han *et al.*[121] proposed immersing PV cell in different types of cooling fluids. The three different immersion liquids are isolation liquid, organic liquids, and deionized water. The irradiance considered is 10, 20, and 30 suns, where one sun is equal to 1000 W/m^2. The efficiency is 15 % under one sun but under 10, 20 and 30 suns are quite higher than single sun but thermal effects observed are again increased. In practical more than one sun is not possible to act on surface of solar panel.

The heat pipe cooling is a combination of PCM in conjunction with the convection mechanism of cooling and it is one of the types of passive cooling. This type of cooling uses an additional setting of pipes. Cooling medium on one side expands and evaporates (or rises, depending on the type) at one side taking up the heat. The cooling medium

residing over other side releases and condensates heat to surroundings. The cooling material via capillary tubes travels back as liquid and it evaporates, completing one cycle. Some of the references listed in Table 2.2 used heat pipe cooling technique.

2.3.1.3   Nano fluids cooling method

Nano fluids are the combination of solid nano-particles such as Al_2O_3, CuO etc., and cooling fluid. The particle's weight is between 0.10 to 2.00 % and experiences Brownian motion throughout the cooling material. The important advantages of nano-fluids are reasonably higher heat capacity and their excellent thermal conductivity [122]. A 5 % increase in efficiency is obtained after utilizing nano-fluids as cooling mechanism in solar thermal collectors.

2.3.1.4   Thermoelectric cooling method

The thermoelectric cooling depends on the Peltier effect, and can be observed at a junction where electrification occurs when heat flows in a particular direction [123] which results in cooling effect on one side, while on the other side it produces heat. The heating or cooling strength depends on the variation in temperature as well as the voltage or current intensity. The thermoelectric cooling requires more electricity.

A review on different cooling methods is presented by Kalaiselvan *et al.*[25]. They have also compared the active and passive cooling methods on various parameters and presented in their article. Saadodeh *et al.*[20] in their work used water as the cooling liquid and obtained increased efficiency. Through experimental results, the loss of heat between the water and PV panel's upper surface by convection causes an increase in efficiency of about 15 % is achieved as output at maximum irradiation conditions. Table 2.2 provides details about various types of forced cooling mechanisms that are used to improve efficiency of solar panels from the selected literature.

Active cooling techniques produce more accessible thermal energy and power, but the power produced itself is sufficient to drive the cooling equipment used to cool the PV cell. Whereas, When CPV cells are used, this type of cooling method can comfortably be availed because of the able usage of less cooling fluid and less fluid-to-cell mass ratio. Thus, very little power is needed to maintain the CPV system. The main disadvantage of

nano fluid cooling is the overall change in flow regime, and pumping process i.e., at different speeds and geometries, natural turbulent flow occurs, when compared with regular fluids. Water is an economic liquid and has higher thermal capacity hence we can ensure that the passive water cooling is more efficient compared to the other cooling methods.

Table 2.2 List of Some references used forced cooling methods

Cooling method	Type of Si solar cell	Area (m²)	Coolant used and mechanism	Temperature decrease (⁰C)	Efficiency improvement (%)	Author & reference
Active	polycrystalline solar PV module	0.924	Water & Aluminium casing on the backside to act as a flow channel	12	8.9	Farhana *et al.* [124]
Active	Mono-crystalline solar PV module	0.152	Water Backside cooling via two aluminum pipes	10 (peak temperature 60 °C)	0.8	Du *et al.*[125]
Active	Mono-crystalline solar PV module	1.24	Water Backside cooling via closed casing	10	2.8	Bahaidarah *et al.*[126]
Active	PV module	374	Water Both front and back side	15 to 26	Back side-14.8, front side-19.1, Both sides-20.4	Rahimi *et al.* [127]
Passive	Mono-crystalline PV module	-	Thermosyphon effect is used with PCM	-	19	El-Seesy *et al.*[128]
Passive	Mono-crystalline PV module	0.36	Water At the rear side of the module cotton wick structures wrapped spirally	-	1.4	Chandrasekar *et al.* [129]
Passive	Mono-crystalline PV module	0.150	Water Heat pipes are constructed	13	6	Nowee *et al.*[130]
Nano fluid-cooling	Crystalline and thin film PV modules	-	Metal oxides & Brownian motion of nano-particles	10-30	6-12 (minimum 5 %)	A. N. Al-Shamani *et al.*[122]

Even though forced cooling systems improve efficiency it has certain disadvantages like, requirement of a separate setup to take out heat from the solar cells, the construction and maintenance of such setup is expensive and the cost of maintaining the system outweighs the advantages of the electrical output improvement. Hence another way of improving efficiency by cooling is by natural cooling which includes the use of solar panels on water surfaces. It can be in two ways either floating PV (FPV) panels and immersed/submerged PV panels. The major disadvantages of forced cooling systems are overcome by the FPV system and FPV systems are tested and studied in different

environments [22], [24], [29], [131]–[137] and water types. Environment conditions like high/ low tide, wind speed, summer, winter and rainy seasons involve variation of irradiation and temperature falling on solar panels. Water types like ocean water, lake water, distilled water which have the variation in salinity, turbidity, algae formation is considered because of the variation in irradiation and temperature transmission into the water bodies.

2.3.2   Floating Solar Photovoltaic Panels

FPV systems install PV modules on water bodies, in general on human-constructed water bodies like irrigation, storage, retention lakes or reservoirs and ponds, and the capacity of plant varies from 4 kW to 20 MW [31]. By placing PV modules over water bodies, on one hand, power output from the PV module increases by 5.9 % due to the backwater cooling of modules [28] while on the other side, water conservation increases as the evaporation of water reduces up to 70 % from water bodies [138]. The first FPV system was installed in California, in 2007, USA and the other FPV systems existing in different regions of the world are mostly established after 2014. Worldwide, the installed capacity of FPV is almost 94 MW, and the plants installed in Japan contribute the most in that. The construction of FPV system with the different basic components
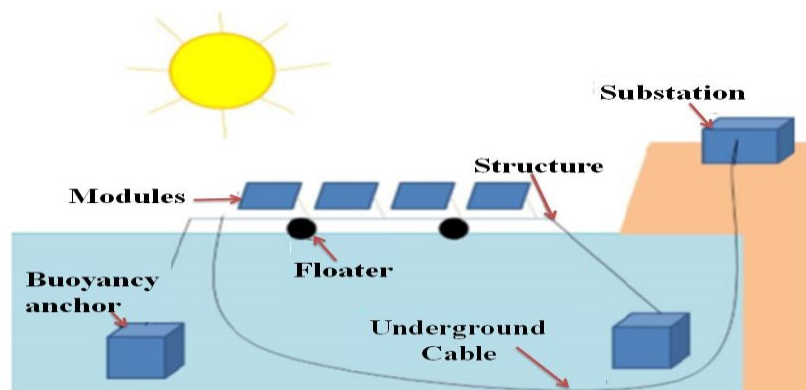
Figure 2.4 FPV system model with basic components

2.3.2.1   *Construction of FPV System*

The basic components/parts of an FPV system as shown in Figure 2.4, are mooring system, floating system, PV panel and the connecting cables. These components can also be used for all different types of floating systems. The floating system comprises of a mixer of floater and structure and the PV panel is placed above it. Mooring system is a

construction, to which a vessel may be attached by means of anchor or cables. It prevents the installed PV modules from floating away or turning. The PV system has the power conditioning devices and solar modules which converts into electrical energy from solar energy. In general, crystalline PV cells are utilized in FPVs, but in PV modules fabrication research is needed that will adapt to the water bodies or reservoir atmosphere. Underground cables are required to transmit the generated electrical energy from the FPV's to land. Later the power can be stored in batteries or can be fed to the grid [139].

2.3.2.2 *Classification and advantages of FPV System*

FPV systems are classified into different types based on the module tracking system and the floating system used and the classification is shown in Figure 2.5.
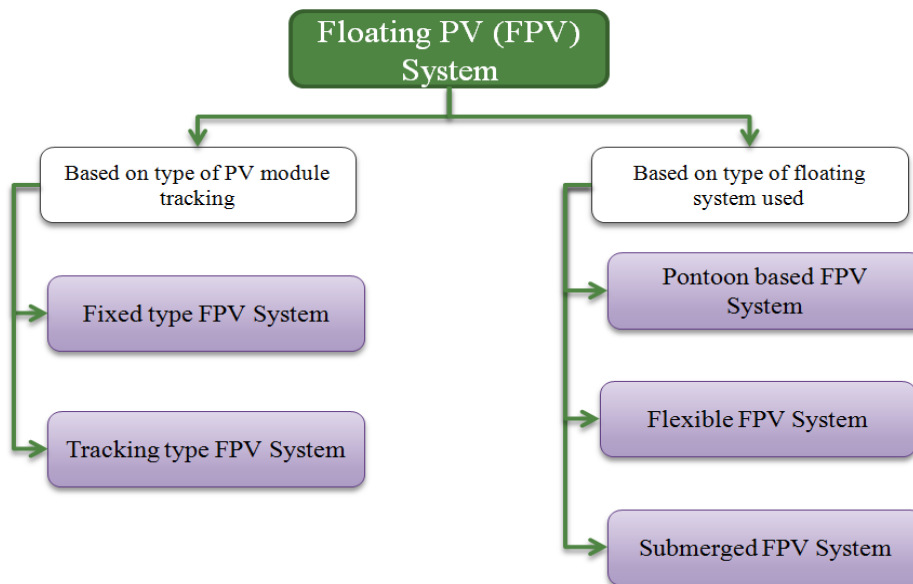
Figure 2.5 Classification of FPV System

In a **fixed type FPV** system, at a certain angle, PV modules are fixed. Fixed system has a normal design but to avoid turning away of PV module, the mooring should be constructed precisely. The main advantage with fixed FPV systems is that the PV system weight used can be less, which ease in selecting a less mechanical strength flotation structure [140]. In **tracking type FPV**, to track the altitude of the sun and azimuth angle, a tracking system is installed. Choi *et al*. [140] have proposed an algorithm for 100 kW floating plant and by using both passive and active tracking systems, the azimuth angle tracking is attained. Fiber Reinforced plastic polymer membrane used as a round rotary

material and it detected to be more stable and durable than aluminium and steel [141]. 25 % efficiency increment is achieved after utilizing vertical axis system tracking stated by Cazzaniga *et al*. [142]. In general tracking type floating systems have power output 60-70 % greater than a fixed plant [143].

Based on the type of floating, FPVs are classified as pontoon, flexible and submerged PV systems. A **pontoon** has good buoyancy enough to float on itself with high load and is referred as floating device. Most of the FPV systems that are preinstalled are pontoon based. Pontoons are manufactured by rotational moulding and are usually made from polyethylene which has medium density. The main drawback of pontoons is that they cannot withstand drastic environmental conditions and they also create a limitation on the size of the plant.

Flexible FPV is a thin-film concept stated to have more reliability, with the significant system performance. The performance of a flexible FPV system is compared against a ground-mounted PV system by Trapani *et al*. [144]. They reported increase in electrical power an average of 5% due to the effect of cooling the water. Flexible FPVs can simply distort with the wave motion and the infrastructure requirement is also less. The radiation will fall with several angles of incident on the surface of solar cells and to maintain the close contact of PV array with the water surface the surface tension is used [144]. If the depth of water on the surface of PV is increases it is called as SSPV.

Submerged Solar PV System (SSPV):

In PV system which is submerged, solar panels are immersed in the shallow water. Solar panels are more vulnerable to thermal degradation at more than the critical temperature value. For efficiency improvement, one of the options is temperature reduction. At various water flow rates and different depths in an underwater environment, the performance can be achieved better with the irradiation presence in depth of water which is also called a submerged PV system. The performance of PV solar panels in submerged systems is affected due to the change of the radiation spectrum and by the decrease in utilizing temperature of PV modules. The factors that affect the performance of submerged panels depend on solar cell technology, environmental conditions, and the depth of water.

Tina *et al.*[30] explored the submerged PV panels energy advantages by studying its thermal and optical behaviour at a depth of 1 cm, 5 cm, 10 cm, and 15 cm water. From submerged PV panels there is a sizable increment in the power output due to two main reasons: absence of thermal drift and reduction of light reflection. Lanzafame *et al.* [33] examined electrical as well as thermal ways of a mono-crystalline module which is submerged by changing the water depth from 1 cm to 15 cm. 10 to 20 % increase in efficiency is obtained from a depth of 8 to 10 cm water. They analysed a best depth of water that exist till which the module efficiency rises. Scienza Industria Technologia (SCINTEC) designed solar cell which will work under 0 to 2 mm of water as shown in Figure 2.6 and is also known as submergible PV concept [145].
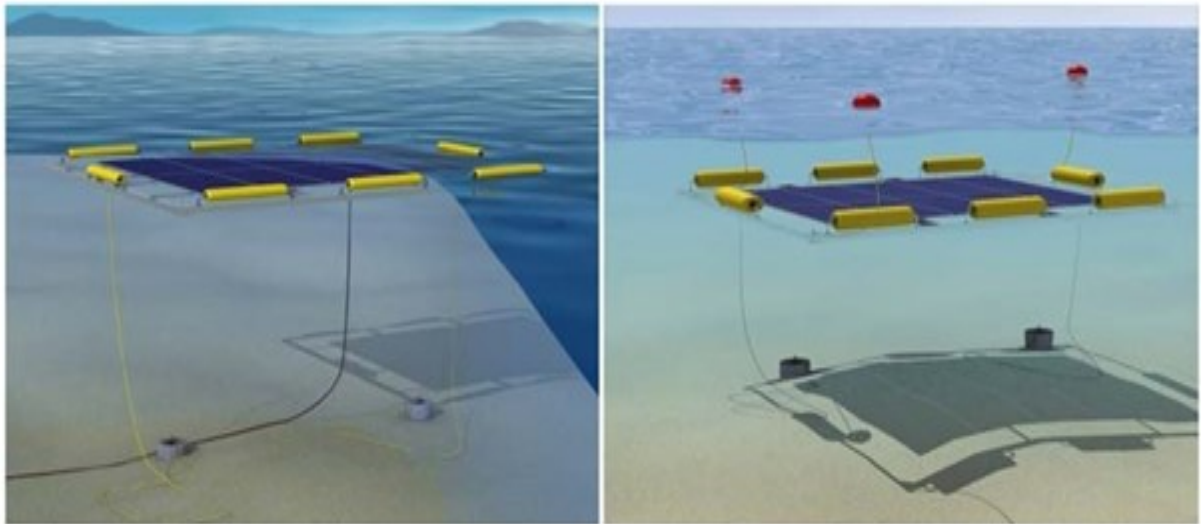
Figure 2.6 SCINTEC SSPV concept [145]

2.3.3   Advantages of FPV System

There are several advantages of the FPV system and a few are listed here. As the FPV system does not require any foundation work it can be easily deployed and maintained. Placement of PV modules over the aquatic surface and in water body reduces the evaporation of water, algae growth on water bodies and also conserves land space. Dust accumulation and its impact on the PV panels will be reduced which will improve the efficiency and another major reason for increase in efficiency of PV systems is because of the cooling effect of water present in the water bodies. But as discussed in sections 3.1 and 3.2 the liquid used for cooling the PV panels needs to satisfy the following requirements such as good heat conduction, non-toxic, good chemical stability, economical and easily

available. Also, the absorption of sunlight by the liquid should match the spectral response of solar cells. Considering all these factors water is the most suitable liquid as it has a high thermal capacity and ensures passive cooling which improves the efficiency of PV panels.

Above specified data indicates about solar panel improved performance under different water environmental conditions. With various designs and structural materials specified above improves the performance of PV system. The issues encountered in an offshore environment, and design complexity, prevents implementation of the large-scale FPV system. Even though, the natural evaporative cooling and reflection of light from the water can uphold the temperatures lesser than land-based PV panel and therefore increases efficiency. The FPV system contributes shading over the water surface and decreases evaporation. FPV system provides shading over the water surface and reduces evaporation. The reduced photosynthesis and algae growth lead to better water quality. Generally, areas with more potential of solar energy lean to be arid and dusty, therefore compared to ground-mounted system, FPV systems can work in a less dust ambience. It conserves precious area for tourism, mining, agricultural, and other land-impulsive actions and turns non-profits generating and unexploited surface of water into profit-oriented PV power plants.

2.4   Hydro-optical Characteristics of Water and its Suitability for Solar Cells

Natural waters, both saline and fresh, are of diffused and contains impure matter. The solutes and particles are both highly variable and optically significant in concentration and type. The hydro-optical properties of waters show more spatial and temporal variations and resemble those of pure water. The water large-scale optical properties are divided into two unique classes mutually: one is inherent and the other is apparent [146]–[149].

Inherent optical properties (IOP's) rely solely on the medium, and are not dependent on the field of "ambient light" inside the medium. The main IOPs are the volume scattering function and the absorption coefficient. Other IOPs contain the beam attenuation coefficient, the single-scattering albedo, and the index of refraction. Apparent optical properties (AOPs) depend both on the "geometric (directional) structure" and on the medium of the "ambient light field", and that shows ample stability and regular characteristics to be useful descriptors of water body. General AOPs used are various diffuse attenuation coefficients, the average cosines, and the irradiance reflectance.

Radiative transfer theory came up with the connection between the AOPs and the IOP's. The water body physical territory –the incident radiance from the sky, waves on its surface, the character of its bottom –via the boundary conditions enters the theory to have solution for the equations arising within the theory. The IOPs specify the need of radiative transfer theory through the optical properties of natural waters.

The inherent optical properties (IOP) include:

    a. Index of refraction

    b. Volume scattering function

    c. Scattering phase function

    d. Absorption coefficient

    e. Beam attenuation coefficient

    f. Single-scattering albedo

    g. Scattering coefficient

        i. Forward scattering coefficient

        ii. Backward scattering coefficient

The Apparent optical properties (AOP) include:

    a. Distribution function

    b. Remote sensing reflectance

    c. Average cosine of light field of

        i. Downwelling light dimensionless

        ii. Upwelling light dimensionless

    d. Irradiance reflectance

    e. Diffuse attenuation (vertical) coefficients of

        i. Downward irradiance

        ii. Upward irradiance

        iii. Downward scalar irradiance

        iv. Upward scalar irradiance

        v. Total scalar irradiance

        vi. Photosynthetically Available Radiation (PAR)

The seawater created by Ions resulting from the dissolved salts, a better electricity conductor than pure water. The seawater conductivity is more than one million times when compared with pure water. The absorption at wavelengths cannot be affected by ions.

However, the conductor behaviour of sea water gives it a higher absorption than pure water at very long wavelengths. The electromagnetic (EM) radiation wavelength is in the order of thousands of Kilo meters (KM) and the sea water have an equitable absorption at visible wavelengths to the low values.

2.4.1 Solar Irradiation Inside Ocean Water at Different Depths

If we take the planet as a whole, we will be able to notice that all water bodies are not a uniform blue and preferably vary in shade based on the depth of water. The deeper waters are darker blue and lighter blue at shallower waters. In presence of natural light without any artificial source of light, is we take a picture, everything takes on a bluish hue, further if we go down and reach 30 meters, 100 meters, 200 meters and more water depths, everything appears blue. When light passes through the atmosphere it primarily absorbs instead of scattering. Water is like atmosphere, it is made out of a finite size molecule: smaller than the visible light wavelengths. Rather than a straight forward wavelength dependence, the water absorbs ultraviolet light, infrared light, and red visible light. When go down to a moderate depth, the Sun's warmth won't be experienced, things will start to turn blue, and will be protected from UV radiation as the red light is taken away. Headed little down, the orange then the yellows, violets and greens start to disappear. As go to depths down of multiple kilometres, the blue light finally disappears as well. That's why the deepest ocean appears a dark blue: as all the wavelengths other than blue get absorbed.

In water, among all the wavelengths of light, the deepest blue is unique and has the more probability of getting re-emitted and reflected. The reflectivity or global average albedo of our planet is 0.30, which means the incident light reflected back into the space is 30 %. But if the earth considered is totally a deep-water ocean, the albedo would be just 0.11 as the ocean absorbs more sunlight [150]. About 2 % of the incident solar energy at the air-water interface is reflected to atmosphere, the remaining is transmitted. The solar energy reflected fraction at the interface is more in the area of the solar spectrum short-wavelength part. The deletion of scattering centres due to dust particles and colloid materials makes seawater similar in its properties of light transmission in the pure water. In seawater, the dissolved salts of 3.5 % by weight make no contribution for the process of solar energy absorption, but they enhance the seawater scattering coefficient by a significant amount. Solar energy inside water depth does not show trend of an exponential decrease with depth.

The solar radiation, at depth more than 3 meters in water, beam behaves as a mono-energetic radiation beam. The 3 m of water depth acts as a filter and separates the lower energy part of the spectrum. At lower energy part, the extinction coefficient is high. A considerable fraction of absorption is noticed by Jamal *et al.*[151] in the first one cm of water and is about 27 %, of the energy transmitted by solar, and in the first 3 m, about 70 % and predicted absorption at a depth of 100 m is about 0.25 % of the energy is transmitted. Solar spectrum transmitted in pure water exhibits different interesting characteristics. At first centimetre, above 1300 nm wavelength photons are absorbed by the water and fully detached from the spectrum. The spectral distribution becomes limited at a depth more than 2 m, i.e., to the visible region only.

The solar energy beam steadily loses its heterogeneity with depth of water. In the solar spectrum IR region, selective absorption grabs place because of the active vibration modes of the water molecules inside the water. In the spectral range of 300 to 2500 nm, ionization cannot take place in pure water as the energy of photons are lesser than 12.6 eV which is the initial potential ionization of water. The seawater transparency is less than pure water delinquent to the particulate substances scattering at which it acts as soothe agents. The seawater will have optical properties which are similar as pure water, by removing the scattering centres explained by Mauddi *et al. in* [94].

2.5   Recent Usage of SSPV concept

Remote marine sensing systems like telemetry tags or underwater autonomous vehicles, are limited in deployment duration and collection of data because of the finite energy available from the battery placed onboard. With limited power available, maintaining a high data resolution, and migrating to large distances over deep-routed deployments is difficult and such systems often yield non-ideal data sets. The application of solar PV panels on such marine systems and harvesting energy could improve the tag longevity and/or collected data fidelity.

Hahn *et al* [36] presented a model assessment which evaluates the output energy of a migrating or stationary solar cell below or above the surface of ocean water. The assumptions and theory beyond the model are explained in detail which includes review concepts established for the purpose of variable consistency and consolidation.

Jenkins *et al.* [63] demonstrated that maximum utilized power is procured at a water depth of 9.1 m utilizing high-band gap InGaP solar cells. These solar cells absorb the "blue" segment of the spectrum and light persisting is transmitted. The light absorption done by the N-contact of the solar cell is having decreased band gap. At the greatest depth of 9.1 m, the output power obtained was 7 W/m^2 of solar cells which will be sufficient for sensor systems used in modern electronics.

Sheeba *et al.* [23] conducted experiments at Center for Energy and Environmental Science and Technology (CEESAT), a India-UK- Renewable Energy Corporation project at the National Institute of Technology-Trichy, India, in both continuous and batch mode. Most of the investigations aimed at assessing the efficiency deviation of an amorphous-silicon PV panel by changing the depth of water in the range of 2 to 20 cm in submersed condition. The efficiency deviation with various water flow rates of 20, 30, and 40 ml/s is also considered for the optimal depth.

Walters in 2015 presented the pattern design of a novel organic PV device tailored for UW operation. The organic PV cell is multi-junction design with same spectral response of two absorber layers. The UW environment analysis is also presented highlighting the advantage of OPV cells. An OPV enabled efficient conversion of the narrow UW spectrum resulting in high voltage output.

Mol'kov *et al.* [35] determined the inherent hydro-optical performance of water utilizing the vision means in UW environment. The analytical methods of the solar UW path, framed by single and multiple scattered light, and direct light are suggested. The optical depths at which the water-scattered light the contribution is predominant are estimated using numerical simulation. Algorithms for attenuation coefficients and rejuvenating the water scattering from the underwater sculpture of solar path are also suggested.

Tina *et al.* [37] designed the feasibility to utilize PV modules under a layer of water. They considered PV cell under different conditions: submerged, under a translucent box that carries water, and covered by a water layer. In common, all the above test conditions have the benefits of water as a filter for solar radiation spectrum and to decrease the heating of the PV cells. Highly depending on the PV cell technology, the effect of the radiation spectrum varies on the PV cells.

Rosa-Clot *et al.*[27] to cool the mono-crystalline module used a technique to cool in the submerged water conditions. The temperature at 30 °C, yielded an increase in efficiency of 20 %, but irradiation intensity decreases with water depth. The relative efficiency is increased by 11 % at a depth of 4 cm.

Abdulgafar *et al.*[21] compared 0.12 Watts and 15 cm^2 polycrystalline solar cells efficiencies drenched in deionised depths of water. At the lowest depth of 1 cm, the overall power gained is high. However, at a depth of 6 cm, the greatest efficiency of 22 % was achieved.

2.6   Summary and Conclusion

From the literature survey, it has been observed that by decreasing the temperature on the surface of PV cells, efficiency of the cells can be improved tremendously. The temperature of PV panel can be decreased by using two cooling techniques: forced cooling and natural cooling. Forced cooling systems require additional electrical equipment to force the cooling liquid which consumes more power than the generated power and natural cooling technique has different construction for installation of PV panels. It is also observed that while comparing the literature based on forced and natural cooling techniques, the natural cooling techniques were mostly preferred with the PV systems. This is mainly due to less cost factor involved and the effective operation of PV cells under natural cooling techniques.

The natural cooling system involves FPV systems and among the FPV systems, the SSPV systems are mostly considered. The factors affecting the PV cell efficiency are majorly eliminated in case of SSPV systems. Because of the two types of optical properties of water, the inherent and apparent optical properties, there is difference in the presence of irradiation at different water depths. The spectrum has different wavelengths and the distribution of wavelengths inside water also varies with the presence of particulate matter and type of water (normal, ocean, lake, organic etc.,).

At different depths, the optical properties of solar cells vary with the environmental conditions but are suitable for SSPV systems to operate and produce electricity. SSPV save valuable land for tourism, mining, agricultural, and other land-impulse actions and turns non-profit generating and unexploited surface of water into profit-oriented PV power

plants. The hydro-optical characteristics of water proves the irradiation presence inside the water and the physical properties of water makes decrease in temperature by increasing the efficiency of submerged PV cells. On the whole, mentioned above advantages will allow SSPV system, suitable for an efficient energy generation which is the need of the hour.

CHAPTER 3

SUBMERGED SOLAR PHOTOVOLTAIC (SSPV) MODELING

3.1   Introduction

To solve the overwhelming energy crisis, the world is steadily shifting its power generation and usage to renewable energy sources (RES) [152], [153]. Among the available RES, solar power generation has proven to be the leader by primarily employing PV cells to convert solar energy into electrical energy. However, the huge available solar energy potential remains still untapped due to the lack of efficient design of PV cells and lack of better efficiency in solar cells due to heat losses.

The PV effect, found while experimenting on an electrolytic cell in 1839, captured solar energy by a semiconductor device and in 1894, Fritts created the first PV cell with an efficiency of 1 % [154]. Later on due to improvements in PV technologies [155], like optical shifting frequency, CPV system [156] and multi-junction PV cells [157], the efficiency of PV cells improved to 22 % to 23 % [106]. Even with this benchmarked improved efficiency, the Solar PV technologies [158], [159] are expensive, both in terms of maintenance and acquisition [160]. There are also mono-junction Si-PV cells that have reported a maximum efficiency of 23 % [161] and used widely. However, Mono-junction PV cells are limited theoretically to 19.4 % [162]conversion efficiency, while multi-junction III-V material PV cells reached efficiency up to 18.8 % [163], [164] under 1-sun condition experimentally.

The III-V PV cell material junction includes: GaAs, InP, InGaAs, and similar compounds with a direct band gap. These PV cells cost is high so its applications include terrestrial flat plate-modules and space [165]. Because of this, the Si, Ge and III-V multi-junction PV cells are receiving increased demand in the PV community. The PV cells can work both in hot and cold regions with the direct and diffuse radiation availability. The increase in temperature is the major reason for the drastic decrease in efficiency which varies from place to place. In Himalayas, the annual average Global Horizontal Insolation (GHI) is around 4.5 kWh/m^2/day [166], which is more than the Standard Test Conditions (STC) of PV cell. Also, the temperatures like -18 ^{0}C and +15 ^{0}C are possible in cold regions and southern regions of India respectively. The lowest recorded temperature in India was -45^{0}C in Kashmir at coordinates 33.2778 ^{0} N, 75.3412 ^{0} E, and the highest temperature was

51 ^{0}C in Phalodi at coordinates 27.1312 ^{0}N, 72.3589 ^{0}E, Rajasthan [100]. For increasing the efficiency to certain level, different types of cooling technologies can be implemented with the variety of cooling liquids available [167].

Another reason for the lower efficiency in PV cell is the fact that only a fraction of solar energy can be absorbed by a typical solar cell which gets converted into electricity and the rest remains untapped as thermal loss [168], [169]. The thermal loss varies with the difference in temperatures, optical characteristics of material used, photon generation and recombination by the solar cell and environmental conditions. These issues can be investigated and later incorporated during manufacturing if a practical solar cell is modeled in a 3-dimensional (3-D) perspective with a coupled optical and thermal module [170].

The prediction of PV performance at different temperatures is required by decreasing the experimental cost. V.N. Vapnik [171] has predicted the performance using the popular tool of Artificial Intelligence (AI) technique, the Support Vector Machine (SVM). From SVM, the Support Vector Regression (SVR) tool is extended and is intended for the load forecasting [172]. SVR uses four kernels namely: Polynomial, Linear, sigmoid and Radial Basis Function (RBF) kernels. It is developed for the global horizontal radiation estimation by P. Bhola and S. Bhardwaj [173]. The Root Mean Square Error (RMSE) is considered as the performance metric for estimation using the data from the National Institute of Solar Energy (NISE) for predicting the radiation. The SVR model's findings were evaluated and found to be superior to other cutting-edge models such as the Artificial Neural Networks, and Hidden Markov Model. According to the result analysis [173], temperature is the most critical performance indicator, followed by relative humidity, air pressure, and wind speed. In [174], [175] also, the SVR and KRR is observed as a best regression technique for power prediction compared to other techniques.

Tina et.al [64], presented a review about the applications of Machine Learning (ML) techniques in different fields of PV. ML-based models are mostly proposed for the field of PV production forecasting. Berny Carrera and Kwanho Kim [65], presented linear regression (LR) and Polynomial Regression (PR) with different ANN techniques for 36Hrs prediction of PV power production with weather forecast and observations. A review based on Deep Learning (DL) techniques to forecast different cell technologies and utilization of them for the prediction of PV power is available in [66]–[68] and solar irradiance in [69], [70]. The Mean Square Error (MSE), Mean Absolute Error (MAE), RMSE, and Mean Absolute Percentage Error (MAPE) are considered as metrics and measured to find

accuracy. As per the references cited above, the data points for the LR, PR, KRR and SVR are medium for the power prediction and are effectively implemented.

In order to study the physics of PV cell/panel, Multiphysics modeling of PV cell/panel is needed where all the PV parameters variations can be observed. In such case the modeled PV cell has to perform similar to the commercially available cell, which can be utilized further for different material coatings and environmental conditions. Similarly, the analysis of PV performance at different intervals of temperatures with standard irradiation take more time through modeling and can be predicted with the AI based ML prediction techniques in less time.

Objectives of research and key contributions:

The four main objectives of this research include Mathematical/ Multiphysics modeling of PV cell/panel using different materials under different environmental conditions, implementation of SSPV in mathematical/ Multiphysics modeling and using ML techniques for predicting the PV cell/panel performance. In this work,

1) The mathematical modelling of PV cell/ Panel in MATLAB environment via non-ideal conditions like temperature variations, irradiation variation, equivalent circuit at single and double diode conditions via the consideration of series and parallel resistances.

2) A Mono-crystalline Si PV is modeled both in cell level and panel level with 3-D geometry via coupled semiconductor, optical, and thermal Multiphysics modules by using Finite Volume Discretization Method (FVDM).

3) The I-V and P-V characteristics of the modeled PV cell and panel are validated with the commercially available mono-crystalline Si cell/panel, both with the data sheet and experimental data.

4) The temperature distribution, recombination of Shockley-Read-Hall (SRH) and Joule heating via absorption of sunlight at constant irradiation levels are analyzed for the modeled PV cell. The Joule heating distribution analysis is also performed for the PV cell/panel modeled using Ge, GaAs and InP and efficiency is estimated.

5) The parameters of PV -like V_{oc}, $I_{sc,}$ and P_{max}, efficiency and FF are obtained at different temperatures and tabulated.

6) In this chapter, the LR, PR, SVR and KRR algorithms are implemented and trained with the obtained mono-crystalline Si simulation data at temperatures 0 ^{0}C, 51 ^{0}C,

-45 ^{0}C and the values are predicted for 25 ^{0}C. The predicted data is compared with the datasheet/modeling data at 25 ^{0}C temperature and best model is selected. With the addition of 25 ^{0}C temperature data in training, the performance of PV cell is evaluated at the15 ^{0}C and -18 ^{0}C [176], the maximum and minimum temperatures of Indian Himalayan region with Si, Ge, GaAs, and InP materials.

7) Implementation of SSPV both in mathematical and Multiphysics modelling with the variation of water depth, materials, temperatures and PV cell material parameters with the performance measurement having I-V and P-V characteristics.

8) The suitable material with higher efficiency, good RMSE, MAE, MAPE and coefficient of determination (R^2-Score) is predicted using the best ML algorithm at different temperature conditions.

3.2   Mathematical Modeling of PV Cell/Panel Using MATLAB/SIMULINK

The mathematical modeling of PV cell/ panel is based on the electrical equivalent circuit of PV and are divided in to ideal and practical equivalent circuits where the series and parallel resistances of the PV are taken as zero for ideal which is practically not possible. So here, the equivalent electrical diode circuit is used to derive mathematical modeling of PV solar cell as shown in Figure 3.1 with the consideration of series and parallel resistances. PV cell STC values are given as temperature 25 ^{0}C, irradiance 1000 W/m² and air mass 1.5. Current developed from the PV cell to the load is represented as I and the equations (3.1) to (3.10) are specified for the load current calculation and to find the maximum power obtained from the PV with efficiency.
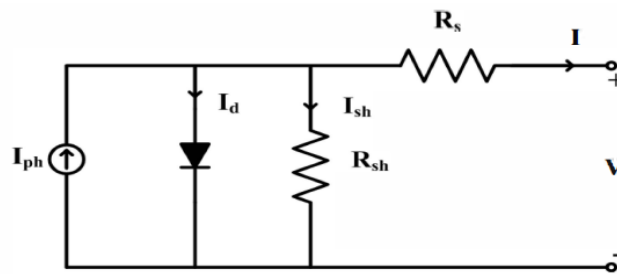
Figure 3.1 Electrical equivalent circuit of PV cell[3]

➤ [3]C. S. Durganjali and R. Sudha, "PV Cell Performance with Varying Temperature Levels," *2019 Glob. Conf. Adv. Technol. GCAT 2019*, pp. 1–5, 2019, doi:10.1109/GCAT47503.2019.8978302

From Figure 3.1, the load current (I) is given as equation (3.1),

$$I = \{(I_{ph} * N_p) - I_d - I_{sh}\} \qquad\qquad \textbf{3.1}$$

Where

Photon current I_{ph} is given by equation 3.2,

$$I_{ph} = [I_s + K_i(T_{op} - T_{ref})] * \left(\frac{\lambda}{1000}\right) \qquad\qquad \textbf{3.2}$$

Saturation current I_s

$$I_s = I_{rs} * (T_{op}/T_{ref})^3 * e^{\left[\left(q*E_{go}*\left[\left(\frac{1}{T_{op}}\right)-\left(\frac{1}{T_{ref}}\right)\right]\right)(n*K)\right]} \qquad\qquad \textbf{3.3}$$

Reverse saturation current

$$I_{rs} = I_s / \{e^{[(q*V_{oc})/(n*K*N_s*T_{op})]} - 1\} \qquad\qquad \textbf{3.4}$$

Diode current

$$I_d = I_s * N_p \{e^{[(V_{oc}+I*R_s)q/(n*K*T*N_s)]} - 1\} \qquad\qquad \textbf{3.5}$$

Shunt current

$$I_{sh} = (V + I * R_s)/R_{sh} \qquad\qquad \textbf{3.6}$$

Thermal voltage

$$V_t = (K * T_{op})/q \qquad\qquad \textbf{3.7}$$

The conversion efficiency (η) is given as,

$$\eta = (V_m * I_m / I * S)\ 100\% \qquad\qquad \textbf{3.8}$$

The fill factor of a solar panel is given by,

$$FillFactor\ (ff) = V_m * I_m / V_{oc} * I_{sc} \qquad\qquad \textbf{3.9}$$

Maximum power obtained from the panel is,

$$P_m = V_m * I_m = V_{oc} * I_{sc} * ff \qquad\qquad \textbf{3.10}$$

At STC values of 223mW PV cell and 20W PV panel has specifications as shown in Table 3.1.

Table 3.1 Parameter specifications of solar PV cell

Parameter	22.3mW PV cell	10 PV cells	20W PV panel
Maximum power (P_{max})	22.3 mW	223 mW	20.0 W
Open circuit voltage (V_{oc})	0.63 V	6.3 V	22.0 V
Short circuit current (I_{sc})	5 mA	50 mA	1.30 A
Voltage maximum power (V_{mp})	0.5 V	5 V	18.0 V
Current at maximum power (I_{mp})	4.46 mA	44.6 mA	1.12 A
Cell temperature	25 ^{0}C	25 ^{0}C	25 ^{0}C
Irradiation	1000 W/m^2	1000 W/m^2	1000 W/m^2

3.2.1 MATLAB/SIMULINK Model for The Electrical Equivalent Circuit

The equation (3.1) to (3.7), of PV cell are represented as shown in Figure 3.2 to Figure 3.8 respectively modeled in MATLAB/SIMULINK.
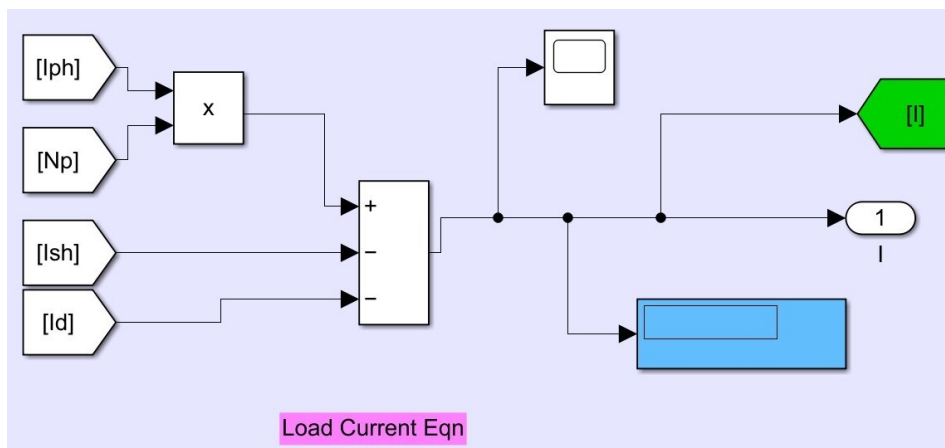
Figure 3.2 Load current
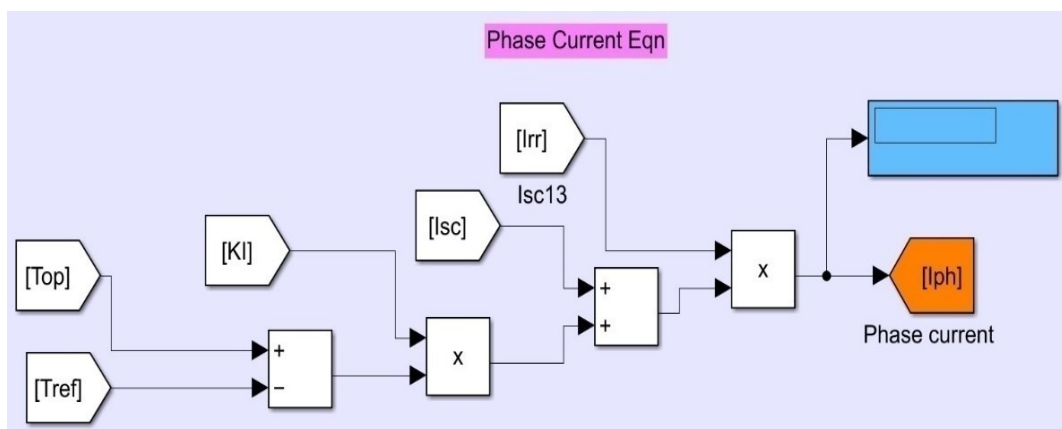
Figure 3.3 Phase current
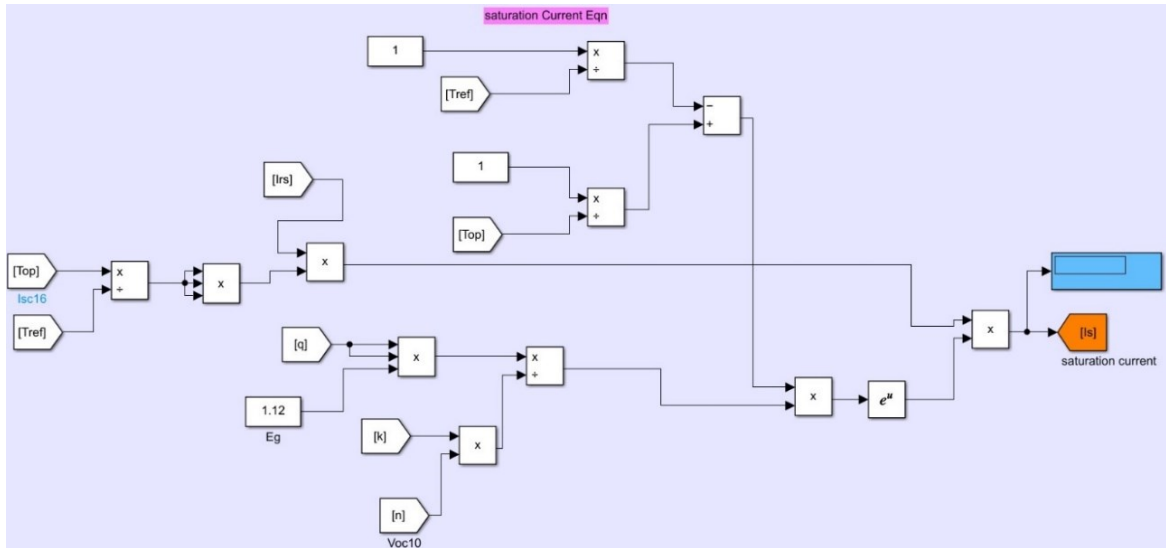
Figure 3.4 Saturation current
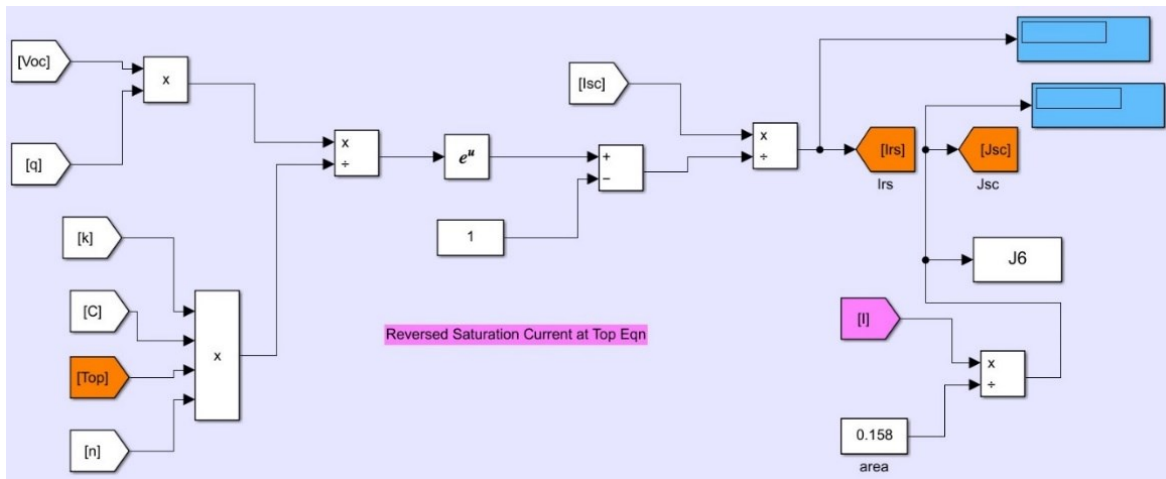
Figure 3.5 Reverse saturation current
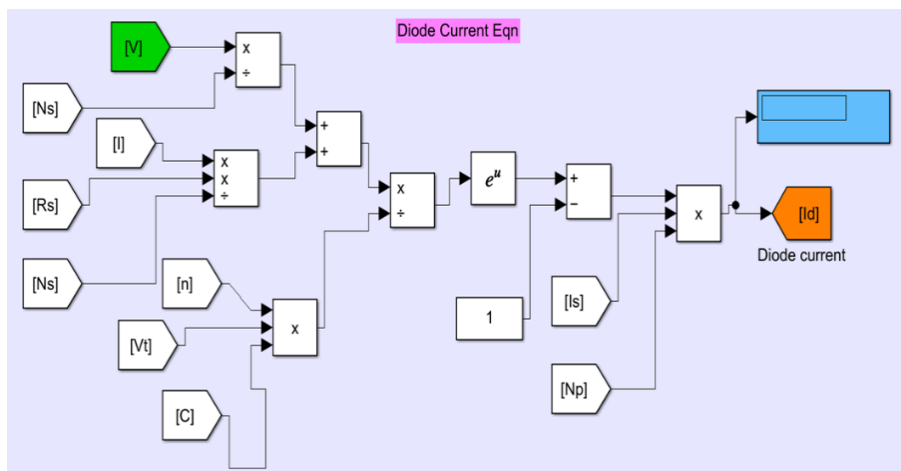
Figure 3.6 Diode current
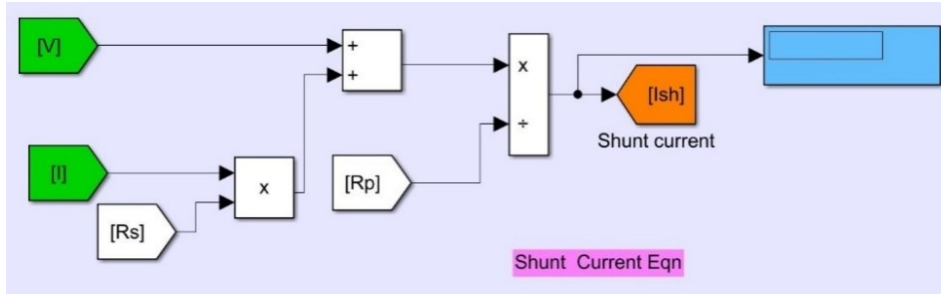
Figure 3.7 Shunt current
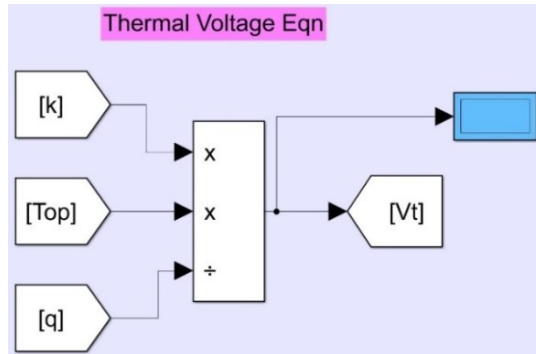
Figure 3.8 Thermal voltage

The combined model for all the models from Figure 3.2 to 3.8 is represented as shown in Figure 3.9 from which, the total load current, FF, conversion efficiency can be calculated with variation of temperature and irradiance at a time.
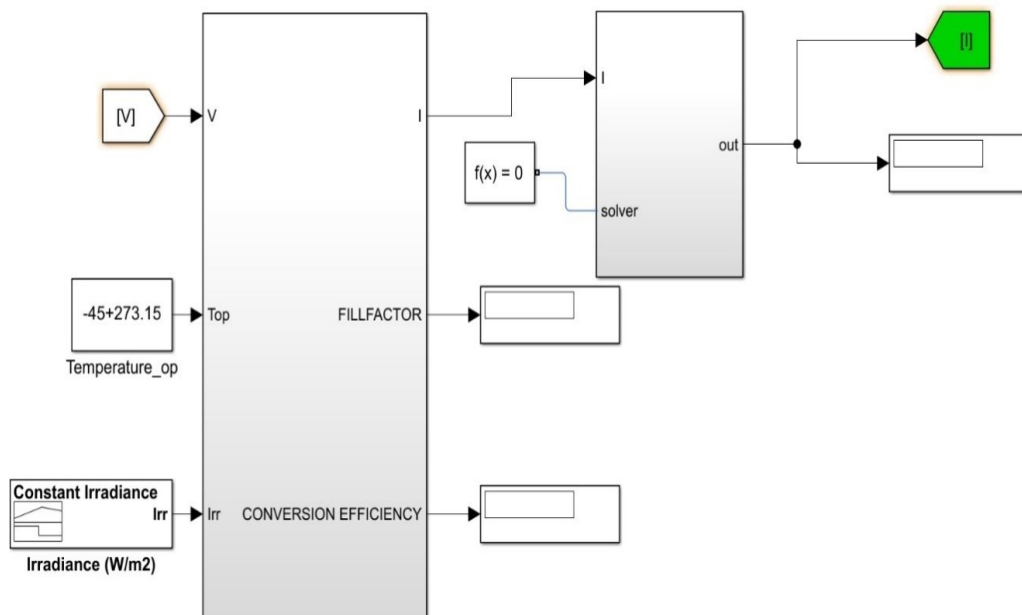
Figure 3.9 PV cell/panel mathematical modeling via MATLAB/SIMULINK

3.3 Multiphysics Modeling of PV Cell/Panel Using COMSOL

The flow diagram shown in Figure 3.10 details the steps involved in the proposed work. First a PV cell is modeled in the multi physics environment in line with the commercially available mono-crystalline Si cell and validated. After its performance parameters validation, many such cells are connected in series and parallel to obtain the model of the PV panel. PV cell and panel are also modeled using different other materials such as Ge, GaAs and InP and their performance parameters are obtained at four different temperature conditions.

The obtained data is used for training and testing of the developed ML algorithms for predicting PV parameters. The following subsections describe in detail about the steps involved in the modeling of the PV cell, panel and prediction of performance of panel parameters using four different ML algorithms.

Step.1: PV Cell Designing
- Geometry and Physics selection
- Material selction
- Meshing
- Joule heating Distribution
- PV cell characteristics

Step.2: PV Panel Designing
- Geometry (Series and parallel connection of PV cell designed in Step.1)
- Material parameter selection
- Experimental Setup

Step.3: Prediction using ML techniques
- Choosing suitable ML algorithms
- Finding best ML algorithm

Figure 3.10 Evolution of the work flow

3.3.1 PV Cell Modeling

Modeling of PV cell involves cell geometry selection, material selection, and meshing with physics selection and is discussed in the following subsection. The PV model implementation flow diagram is represented in Figure 3.11 with the explanation of each section as sub topics below.

3.3.1.1 Solar Cell Geometry and Physics Selection

3.3.1.1.1 Geometry Selection

As shown in Figure 3.12 (a) and (b), an existing or practical mono-crystalline Si PV cell has been designed in 3-D scheme. The cell dimensions were considered to be 20 mm × 6.16 mm × 2 mm matching with the single PV cell in the datasheet that is used for validation [177]. The different layers of modeled PV cell are shown in Figure 3.13 and include: Aluminium (Al) frame, anti-reflection coating (tempered glass), Ethylene Vinyl Acetate (EVA) on top and bottom of solar cell with p-layer and n-layer to form junction and back contact.
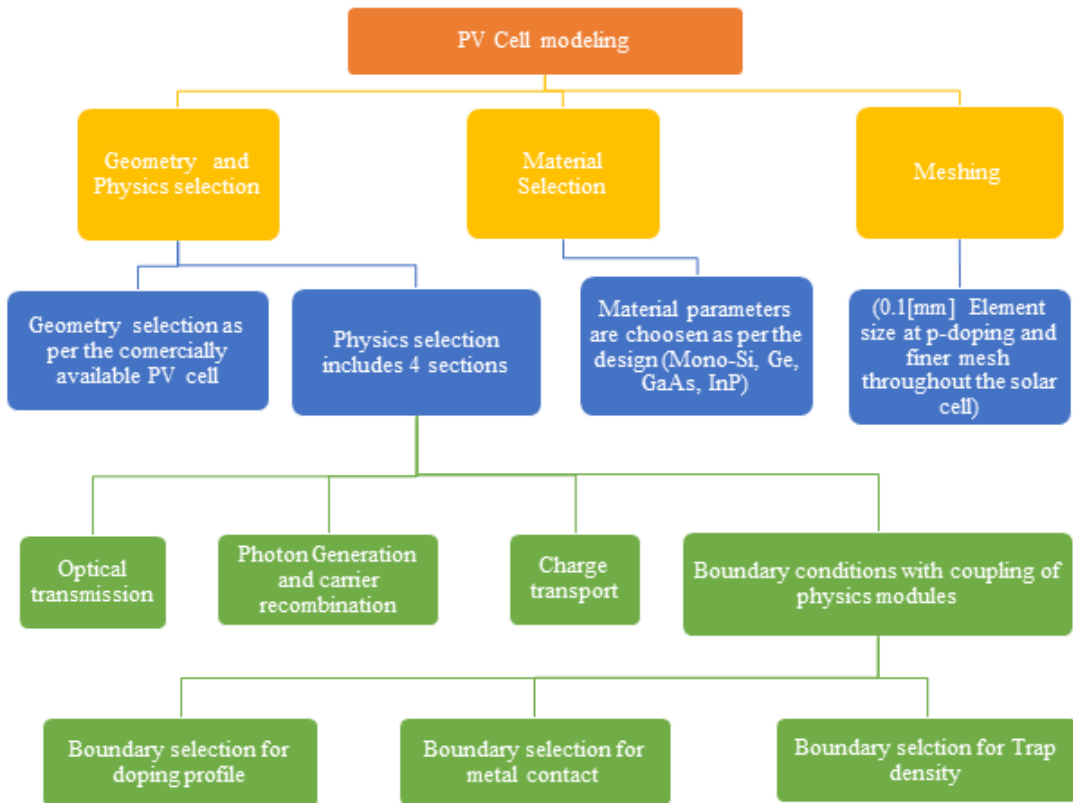
Figure 3.11 Processes involved in Multiphysics modeling of PV cell

While modeling the mono-crystalline Si PV cell using FVDM at STC conditions used are irradiation of 1 Sun = 1000W/m^2, air mass 1.5, and temperature25^{0}C (298.15K). The thermal conduction coefficient values also used as the parameters and the cells were initially considered to be at room temperature (T_{room} = 298.15 K) and later the temperature is varied for different testing conditions.

(a)   (b)
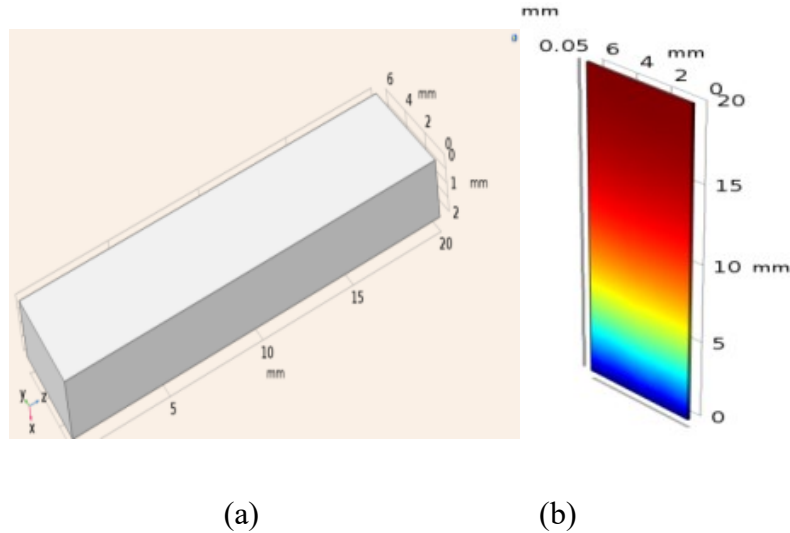
Figure 3.12 a) Geometry of solar cell b) Penetration of energy in mono-crystalline Si cell layer
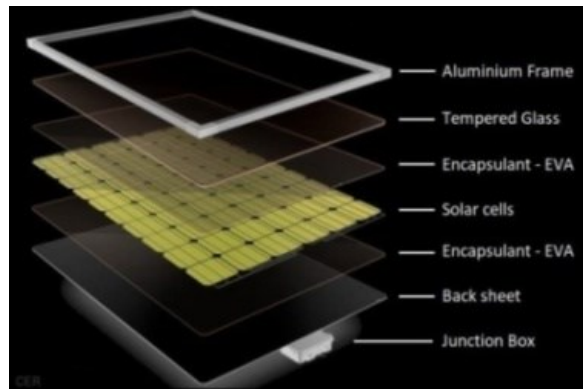
Figure 3.13 Layers of modeled PV cell

3.3.1.1.2 Physics Selection

In the process of modeling, the physics selection involves the combination of semiconductor, optical and thermal modules to resemble the commercial PV cell. These module selections include optical transmission, photon generation and recombination, charge transport physics selection within the modeled PV cell. After coupling the modules, the boundary conditions are decided considering the optical profile of cell. The electric potential formation with the hole-electron pair thermalization is possible during electron – hole pair formation. The thermalization causes chemical energy which gets converted into electrical energy with the flow of electrons from external circuit connected at two ends and is called as the PV current. The optical behavior of PV cell varies with different materials and their energy bandgap.

a) Optical transmission:

The optical absorption, spontaneous emission and stimulation of the mono-crystalline Si cell can be modeled using the optical transition feature. The electromagnetic wave can produce absorption or stimulated emission between two quantum states when a transition takes place in the presence of electric field oscillation. In the valence band, when an electron absorbs photon and transmits to conduction band, it results in coherent light absorption. The non-linearity and the carrier energy distribution at a given temperature can be assumed using Maxwell-Boltzmann carrier statistics for non-degenerated semiconductors. On the other hand, the Fermi-Dirac statistics can be used for degenerated semiconductors at lower temperatures. In the model, for carrier statistics and solution variables, the in-built model properties are utilized.

Carrier Statistics:

- When both the electron and hole Fermi levels are within the band gap and away from edges of band then Maxwell-Boltzmann statistics can be applied.
- When some of the quasi-Fermi levels are near to the edges of band or inside the band gap, the Fermi-Dirac statistics play a major role to simulate degenerated semi-conductors.

In this work to model the PV cell, the frequency domain Maxwell equations which are given in (3.11) and (3.12) are considered.

$$\nabla \times \overrightarrow{H_{opt}} = j2\pi\varepsilon_r\varepsilon_0 \, \overrightarrow{E_{opt}} \qquad\qquad \textbf{3.11}$$

$$\nabla \times \overrightarrow{E_{opt}} = -j2\pi v\mu_0 \overrightarrow{H_{opt}} \qquad\qquad \textbf{3.12}$$

where, $\overrightarrow{H_{opt}}$ is the magnetic field vector, $\overrightarrow{E_{opt}}$ is the electric field vector, v is frequency, ε_r is relative permittivity and ε_0 is permittivity of free space

b) Photon generation and carrier recombination:

For electric field generation in frequency domain, the Helmholtz equation is used. These equations are part of Maxwell-Boltzmann equations. The module output is the photon-generation rate across thickness of the device for the absolute spectrum at each frequency v and position (x,y,z) and is given in equation (3.13) [178], [179].

$$G(v,x,y,z) = \frac{Q}{hv} = \frac{\pi \varepsilon_r \varepsilon_0}{h} E_{opt}^2 \qquad \textbf{3.13}$$

Integration of frequency dependent G over the AM 1.5G solar spectrum is given by (3.14)

$$G_{tot}(x,y,z) = \int_{AM\ 1.5G}^{G} G(v,x,y,z)S(v)dv \qquad \textbf{3.14}$$

Where $S(v)$ is spectral density of the AM 1.5G solar spectrum, h is plank's constant, Q is charge density and G is irradiation distribution with spectrum wavelength.

C) Charge transport:

The charge transport in the semiconductor material depends on the Poisson's equation with drift and diffusion equation into consideration. At steady state, the Poisson's equation is written as continuity equation as derived in the equations (3.15) to (3.19).

The drift and diffusion equations are:

$$J_n = -en_f \mu_n \nabla V + eD_n \nabla n_f \qquad \textbf{3.15}$$

$$J_p = -ep_f \mu_p \nabla V + eD_p \nabla p_f \qquad \textbf{3.16}$$

The Poisson's equation is considered as,

$$\nabla^2 V = \frac{q}{\varepsilon_0 \varepsilon_r}\left(n_f + n_t - p_f - p_t\right) \qquad \textbf{3.17}$$

and at the steady state current continuity equations for electron and holes are given by equations 3.18 to 3.19.

$$\frac{dn}{dt} = \frac{1}{q}\nabla J_n + k_d X - R_n = 0 \text{ (Steady state)} \qquad \textbf{3.18}$$

$$\frac{dp}{dt} = \frac{1}{q}\nabla J_p + k_d X - R_p = 0 \text{ (Steady state)} \qquad \textbf{3.19}$$

where, J_n and J_p are current densities of electrons and holes, $\mu_{n(p)}$ is mobility of electrons (holes), $n_f(p_f)$ is free electron (hole) concentration, $n_t(p_t)$ is electron (hole) trapped concentration, $R_n(R_p)$ is recombination rate of electron (hole) and D_n (D_p) = Electron

(hole) impact ionization. The charge transport in the cell require insulation at boundary conditions of the cell with its metal contact representation.

d) Boundary conditions with coupling of modules:

By interfacing semiconductor module, appropriate boundary conditions are included for the PV model material as a feature. Separate boundary conditions have to be included if insulating regions are added by charge conversion feature. The boundary conditions are selected for three different profiles, such as:

- Doping profile
- Metal Contacts
- Trap density

3.3.1.2   Material Selection

The Modeled PV has layers of Al frame, Glass, EVA and solar PV cell with back contact. The material properties of the different layers are listed in Table 3.2.

Table 3.2 Properties of materials used for different layers of PV cell model [12], [98], [180]

Parameter	Aluminium (Al)	Glass	EVA	Silver
Density [kg/m^3]	2700	2200	935	10500
Thermal conductivity [W/(m×K)]	210	1.1	0.34	429
Heat capacity at constant pressure [J/(kg×K)]	900	480	480	235
Electrical conductivity [S/m]	3.5×10^7	10^{-14}	-	6.16×10^7
Relative permittivity	10	4.2	-	11.7
Refractive index	-	1.5	1.5	-
Emissivity	-	-	-	0.01

The limiting parameters of crystalline Si PV cell [162] are temperature, Shockley - Queisser limit, anti-reflection coating/cover glass effects and internal resistance variations.

3.3.1.3 Meshing

After the complete geometrical design is done, meshing is performed and then the model is analysed. Various types of analysis can be performed using the Multiphysics software, which include:

- Linear and non-linear analysis
- Stationary and transient analysis and
- Eigen frequency response analysis

In this work, linear analysis is considered to obtain better characteristics of the solar cell [181].

The coupled model by FVDM can be solved numerically with the different element size of mesh for total cell structure. The structured mesh is shown in Figure 3.14 Two types of meshing can be done, where one is physics-controlled meshing and the other is user-controlled meshing. In this work physics-controlled meshing has been adopted. The minimum and maximum size of element for total sequence of meshing was set to 0.1mm and 0.5 mm respectively, which makes cell into a finer mesh and easy to analyze each and every element of the solar cell. At curvature factor of 0.5, the maximum growth rate of element is set to 1.13, to make curved boundary into swept mesh. With the use of swept mesh, the size of the model and computational complexity is reduced for every component in the overall structure.
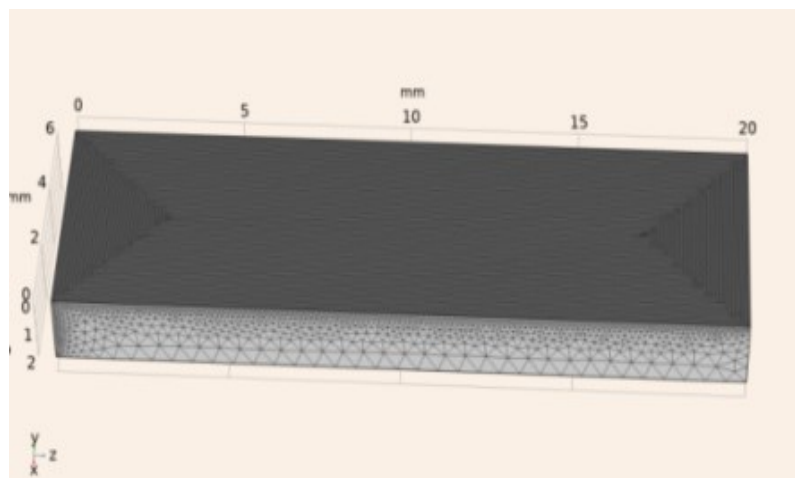
Figure 3.14 Meshing of PV cell model

49

3.3.1.4   Joule heating distribution

Typically, thermal distribution in the cell is based on heat transfer through convection, radiation, and conduction. The thermal dissipation occurs when two objects with different temperatures kept in the same environment undergo electric current passage, which is called joule heating. To calculate the PV cell temperature profile and heat dispersion, in Multiphysics, heat transfer in solids module is preferably utilized. As shown in Table 3.2, several parameters like heat capacity, heat transfer coefficient, and thermal conductivity of each layer are chosen. The heat transmits from higher temperature region to lower following thermodynamic laws.

Every material generates its own heat and it increases with the increase in temperature on the top of the PV cell. Hence to observe the joule heat in the PV cell, heat transfer module is considered in the design of mono-crystalline Si cell. Heat conduction takes place when electron carries heat in metals and semi-conductors. In other materials, heat conduction occurs through lattice vibration which is also called molecular motion. The temperature gradient is always proportional to heat flux. To control the temperature profile, internal heat generation has to be maintained in limits and at steady state the internal generation of heat is calculated using partial differential equation as given in (3.20).

$$-s\nabla^2 T + Q = \rho_p C_p \frac{dT}{dt} \qquad\qquad \textbf{3.20}$$

where, s is the semi-conductor material thermal conductivity [W/(m*K)], ρ_p is the density, C_p is specific heat of material [J/(kg*K)], and Q is the generation of heat rate which controls the absorption of light on surface.

The different sources of thermal generation like joule heat, thermalization, Peltier heat, bulk and surface recombination with their roles have been presented by Shang and Li, 2017 [182], for solar cell analysis. Out of 1000 W/m^2 of the incident light, 122 W/m^2 get converted to Joule heat, 157 W/m^{2}goesfor thermalization, 15 W/m^2 is utilized for heat generation and the remaining as Peltier heat at interfaces of metals and loss of reflection [182]. The generation of heat for Joule effects (H$_{Joule}$) and SRH (H$_{SRH}$) is given by (3.21) and (3.22).

Joule heat, $H_{Joule} = J \times E$ $\qquad\qquad$ **3.21**

$$\text{SRH heat,} H_{SRH} = \left(E_g + 3kT\right) \times \left(U_{SRH} + U_{Aug}\right) \qquad \textbf{3.22}$$

here, U_{Aug} is Auger recombination rate, U_{SRH} is Shokley-Read-Hall recombination rate, E_g is band gap of semi-conductor material and J is the Conducting current density in the cell.

The Joule heating is one of the most common examples of Multiphysics coupling where a conductive material with the flow of electrical current leads to heat losses, which in turn leads to a rise in the temperature. The thermal conductivity and Joule heating distribution were analyzed in results section for different temperatures. The different temperatures include: the maximum and minimum temperatures occurred in India (51 ^{0}C, -45 ^{0}C), ambient temperature (25 ^{0}C), 0 ^{0}C and temperatures -18 ^{0}C and +15 ^{0}C in cold regions and southern regions of India respectively.

3.3.1.5 *Characteristics of PV cell*
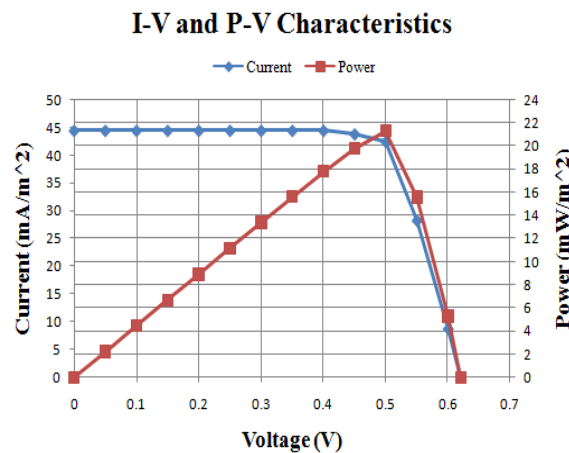
Figure 3.15 P-V and I-V characteristics of simulated solar cell

From Figure 3.15, the I-V and P-V characteristics of the modeled Mono-crystalline Si PV cell can be observed. With the consideration of different material properties and thermal co-efficient as specified in Table 3.3, the values of the different parameters obtained from modeled solar cell are I_{sc}= 45.69 mA, V_{oc}= 0.62 V, maximum current (I_{max}) 39.39 mA, maximum voltage (V_{max}) 0.50 V, and the P_{max} =19.77 mW. The efficiency of the modeled PV cell is approximately 19.69 % with a FF of 0.69. The cells can be connected in series and parallel to make a panel depending on the voltage and current requirements.

3.3.2 PV Panel modeling

3.3.2.1 PV panel geometry

The PV panel is obtained by connecting PV cells in series and parallel. The PV panel modeled in this work is similar to the IXOLAR™ SLMD121H10L and it is an IXYS product line of solar module made of mono-crystalline Si, high efficiency solar cell [177]. The panel dimensions are 42.0 × 35.0 × 2.0 mm in 3-Dimensions top view and is shown in Figure 3.16 and the 3-D image is as shown in Appendix: A – Fig.A1. The physics, meshing and layer properties of PV panel are considered as discussed in Section 4.3 of modeling of PV cell.
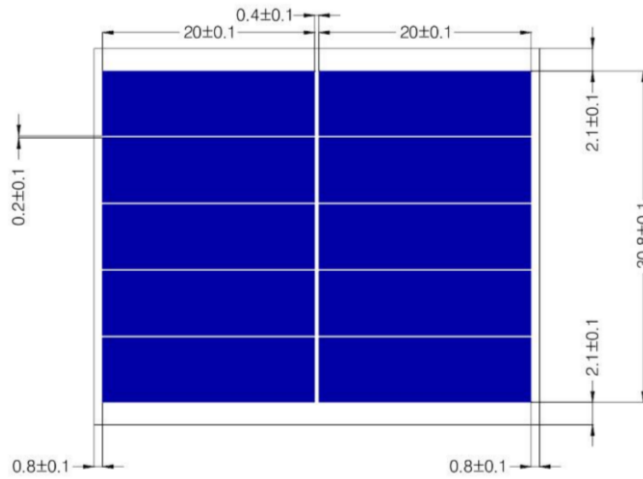
Figure 3.16 3-D top view of PV solar panel

3.3.2.2 PV panel material selection

The solar cell in this work is modeled using materials like mono-crystalline Si, Ge, GaAs, and InP. The impurity doping profile for the PV panel is N-type as donor and P-type as acceptor. The junction depth of the panel is $5\mu m$ and the generation rate of the panel is considered as 11×10^{20} ($[1/(cm^3 \times s)] \times exp^{(-x/1[\mu m])}$) at different temperatures like 0 ^{0}C, 25 ^{0}C, 51 ^{0}C, and -45 ^{0}C as specified in section 3.1. General element mesh size is considered as 0.1mm at p-doping and finer mesh throughout the solar panel. The material for the solar cell can be included from the library or physically including material properties like absorption and scattering. The design parameters and properties of the different materials used for modeling are listed in Table 3.3.

Table 3.3 Material properties of PV cell considered for modeling

Parameter	Mono-crystalline Si [180], [183]	Ge [14]	GaAs [12], [17]	InP [163], [184], [185]
Relative permittivity	11.7	16.2	12.9	12.5
Electron lifetime, SRH	10[μs]	10[ms]	50[ns]	2[ns]
Hole lifetime, SRH	10[μs]	10[ms]	30[ns]	3[μs]
Electron mobility (cm^2/(V×s))	1450	3900	8500	5400
Hole mobility (cm^2/(V×s))	500	1900	400	200
Band gap (eV)	1.12	0.67	1.424	1.344

The efficiency of the materials is different because of their material properties and limit variations as specified in Appendix: A - Fig.A2. The GaAs has high external quantum efficiency in the visible spectrum compared to both Si and InP. Due to less joule heat production and high temperature resistance, GaAs material is mostly used for space applications irrespective of its cost. Detailed discussion of parameters of materials along with performance characteristics is presented in Section 4.4.

The characteristics of PV solar panel is obtained for all the materials and are tabulated, plotted and presented in the results section. The efficiency of PV panels at different temperatures like 0 ^{0}C, 51 ^{0}C, -45 ^{0}C, 15 ^{0}C, 25 ^{0}C and -18 ^{0}C are obtained for mono-crystalline Si and at temperatures: 0 ^{0}C, 51 ^{0}C, -45 ^{0}C, and 25 ^{0}C for other materials (Ge, GaAs, and InP) to select the suitable material at variable temperature conditions. These obtained results are used as training data for predicting the performance at 15 ^{0}C, and -18 ^{0}C as specified in section 3.1.

3.3.2.3 *Experimental set up*

In the experimental setup, for creating the STC, solar simulator is used and the irradiation is measured using a LUX meter. The solar simulator is shown in Figure 3.17 (a) and experimental setup is as shown in Figure 3.17 (b) and (c).

Figure 3.17 a) Solar simulator providing STC b) Experimental setup of mono-crystalline solar cell under solar simulator c) Experimental setup of mono-crystalline Si cell under sun at 12 PM with >1000 W/m^2

The characteristics of the data sheet and experimental result are considered for validating the modeled PV cell.

3.3.3 ML algorithms implementation

In this chapter, the I-V and P-V characteristics of the PV cell modeled using four different materials is predicted using four different ML algorithms at both positive and negative temperature levels. The ML algorithms used are: LR, PR, SVR and KRR using Scikit-Learn software package and Python programming language. Firstly, mono-crystalline Si is tested and from the results, the optimum parameters are selected for prediction of performance of other materials with ML algorithms. This is because Si is mostly available and used PV material.

The PV cell/panel materials voltage, current and power data acquired from modeling in section 3.2.1 and 3.2.2 are utilized as train data and predicted the data for (15^0C and -18^0C) after testing the data at 25^0C. The flow chart detailing the steps involved in the prediction of performance parameters using ML algorithms is shown in Figure 3.18. The obtained datasets from sections 3.2.1 and 3.2.2 are segregated into input and output features. The input features are temperature (T) and voltage (V) and the output features are current (I) and power (P).
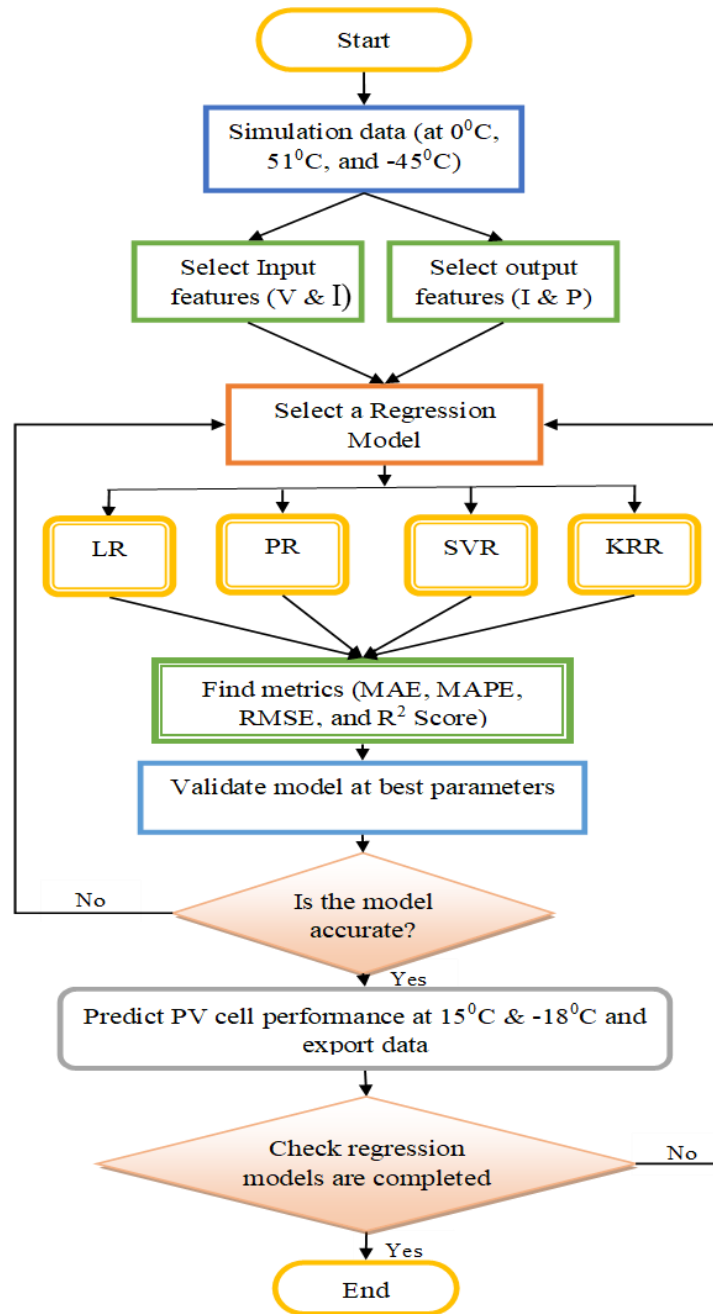
Figure 3.18 Flow chart depicting the process of prediction of PV cell/model performance parameters using ML Algorithms

3.3.3.1   Linear Regression (LR)

The most commonly used ML algorithm is LR. Training data is used to find the relation between the input and output features. The algorithm generally tries to find the line of best fit by using the training data. The model tries to find a generalized line which can be used to predict outputs for outside data. The form of LR is straight line, which can be represented as in (3.23).

$$a = mb + C \qquad\qquad\qquad \textbf{3.23}$$

Where, m is the slope, C is the intercept of a, b is the independent variable, and a is the dependent variable. The most crucial point is to figure out how the LR model finds the line of best fit. Generally, LR algorithm tries its best to fit a line on the training data, reducing the error between the actual and predicted values. They use a method called the "least squares" method. In terms of machine learning, equation (3.23) is represented with weights as in (3.24)

$$a = w_0 + w_1 b \qquad\qquad\qquad \textbf{3.24}$$

here w_0 and w_1 are weights, b is the input, and a is the output.

LR tries to get the best possible values of the weights, namely w_0 and w_1, which helps to get the line of best fit for the input features "b" to map to the output features "a". In LR, there is a cost function which helps in finding how good the model has performed. For LR, cost function is nothing but RMSE from which correlation factor (R^2_Score) can be determined.

3.3.3.2 Polynomial Regression (PR)

PR helps to find the relation between the simulation data and features by trying to find the best curve fit. Before training the model, first transform the input data into polynomial features, which then can be trained. The degree of a polynomial is a parameter which does not have a fixed value, and the value keeps changing based on application and the data which is provided for training. The general equation of polynomial regression is given in (25).

$$b = w_0 + w_1 a + w_2 x^2 \dots \dots \dots.. \qquad\qquad \textbf{3.25}$$

where w_0, w_1, w_2 ...are the weights of polynomial, a is the input and b is the output.

Finding the optimal parameter is the most challenging task in polynomial regression. If the degree of polynomial is high, the data may tend to get over / under fitted. In general, the best degree of the polynomial for the provided data is the one which gives the lowest RMSE value and the highest R^2_score for the test data.

3.3.3.3 Support Vector Regression (SVR)

The prediction of discrete values is possible through SVR which is a supervised learning algorithm. It is a popular prediction technique in regression which tries to model a hyperplane in a higher dimensional space which best fits the training data provided accurately [186], [187]. The best fit line has the hyperplane which has the maximum points that lies inside and outside of the margin and is represented with threshold epsilon (ε). SVR uses kernels (ϕ) to map data points from lower dimension to a higher dimension and constructs hyperplane. Four steps involved in SVR before utilizing it for prediction are:

1. Data visualization
2. Extraction of features
3. Model fitting

Once the model is fit, then the ML technique is ready to predict the values and further study. SVR has advantages like: decision model easy updating, quick implementation, excellent capability of generalization with improved prediction accuracy and robustness to outliers. SVR is not suitable for large data sets and also its performance decreases if the number of training data samples is less than the number of features for each data point.

The mathematical formulation for SVR can be expressed as an optimization problem shown in (3.26), (3.27). Given a set of training data points (x_1, y_1), (x_2, y_2), …..,(x_n, y_n), then the function $f(x_i)$ best fits the data and minimizes the residual sum of squares (3.28).

The optimization problem can be written as follows:

$$Min \left[\frac{1}{2}\|w\|^2 + C * \sum_{i=1}^{n}|y_i - f(x_i)|^2\right] \qquad \textbf{3.26}$$

Constraints:

$$y_i - f(x_i) >= \varepsilon, and \, y_i - f(x_i) >= -\varepsilon \qquad \textbf{3.27}$$

Where, w is the weight vector, C is a regularization parameter that controls the trade-off between fitting the data and allowing for noise, ε is the insensitive loss function that allows for some error or tolerance in the prediction.

$$f(x_i) = \sum(\alpha_i * y_i * k(x, x_i)) + b_0 \qquad\qquad \textbf{3.28}$$

where, $k(x, x_i)$ is a kernel function that transforms the input data into a higher dimensional space to allow for non-linear modeling and b_0 is the bias.

SVR allows the freedom to determine how much inaccuracy in the model is acceptable and will define an approximate hyper plane that best fits the data. It specifies the epsilon-tube in the training loss function where no penalty is associated with points predicted within an epsilon (ε) distance of the actual value. Gamma (γ) refers to the kernel coefficient for Radial Basis Function (RBF), polynomial and sigmoid functions. To develop SVR, the data is scaled between 0 and 1 and is used for training and testing where the hyper parameters are initialized randomly. The random initialization takes more time so the grid search Cross-Validation (CV) is implemented and the hyper parameters for both I-V and P-V are fitted with k-fold cross validation.

In SVR prediction, grid search CV is utilized and tries out various models using all possible combinations of hyper parameters. In order to evaluate these models, the library uses a technique called k-fold CV and divides the data into k parts, each part acts as a testing and the training data. The final accuracy of the model is the accuracy over all these k testing sets, and is a popular method to test the strength of a model. The hyper parameters are alpha (α) and gamma (γ) which varies depending on the type of kernel used and data sets for feature extraction [186]–[189]. An additional hyper parameter, regularization (C), is also preferred for tuning. The tolerance value for points outside of ϵ increases with increase in C. The equation collapses into the simplified (infeasible sometimes) one and the tolerance approaches to "0" with the "0" reaching point of C. The flow chart for SVR is as shown in Appendix: A - Fig.A3.

3.3.3.4   *Kernel Ridge Regression (KRR)*

KRR is a regression technique used for prediction and is capable of modeling non-linear and linear affiliation between the input and output variables which are also called

predictor variables and predicted variables respectively. KRR performs ridge regression on the data in a higher space induced by the kernel. Here, hyper parameters refer to the gamma used for RBF and polynomial kernel functions, and alpha used for the regularization strength. The simulated data is split into training and testing where 20 % is used as testing data and 80 % is used for training data.

The mathematical formulation for KRR can be expressed as an optimization problem in (3.29). Given a set of training data points $(x_1, y_1), (x_2, y_2), \ldots,(x_n, y_n)$, then the function f(x) best fits the data and minimizes the residual sum of squares given in (3.30).

The optimization problem can be written as follows:

$$Min\left[\frac{1}{2}\|f(x) - y\|^2 + \frac{\lambda}{2} * \|f(x)\|^2\right] \qquad \textbf{3.29}$$

Subject to constraints:

$$f(x) = \sum(\alpha_i * y_i * k(x, x_i)) + b_0 \qquad \textbf{3.30}$$

Where, λ is a regularization parameter that controls the trade-off between fitting the data and allowing for noise, $\|f(x) - y\|^2$ is the MSE between the predicted values and the actual values, $\|f(x)\|^2$ is the L_2 regularization term that penalizes the complexity of the model, $k(x, x_i)$ is a kernel function that transforms the input data into a higher dimensional space to allow for non-linear modeling, α_i are the weights of the model and b_0 is the bias.

Table 3.4 Comparison between KRR and SVR

S.No.	KRR	SVR
1	12-norm regularization	12-norm regularization
2	Uses squared error loss	Sigma-intensive loss
3	Faster for medium size data set	Faster for large size data set
4	Non-sparse	Sparse for sigma >0
5	Built in support for multi variant regression	Supports for multivariate Regression

Similar to SVR, in KRR also grid search CV is utilized through K-fold CV to find the best hyper parameters and to predict current and power output from PV cell. Comparison

between KRR and SVR is given in Table 3.4, and the kernels used for both KRR and SVR are explained below.

Kernels used in general in both KVR and SVR are Linear, RBF, polynomial and sigmoid kernel [188], [189]. In this work, the most utilized RBF and polynomial kernels are preferred for studying the non-linearity PV cell characteristics in both SVR and KRR algorithms.

All ML algorithms discussed have two sections in common: Data import and training, and prediction implementation till plotting the data. The flow of data import and training is shown in Appendix: A - Fig.A4. Similarly, Appendix: A - Fig.A5 shows the result flow of prediction implementation.

The performance metrics used to find the best fitted model for the PV characteristics performance prediction are co-efficient of determination (R^2_score or correlation factor), MAE, RMSE, and MAPE. The equations of the performance metrics are expressed in (3.21) to (3.24). If $\widehat{x_k}$ is the kth sample predicted value, and x_k is the subsequent true value, then the MAE, RMSE, and MAPE estimated over N samples are defined as in (3.31), (3.32) and (3.33).

$$MAE = \frac{1}{N_{samples}} \sum_{k=0}^{N_{samples}-1} |x_k - \widehat{x_k}| \qquad \textbf{3.31}$$

$$RMSE = \sqrt{\frac{\sum_{k=0}^{N_{samples}-1}(x_k - \widehat{x_k})^2}{N_{samples}}} \qquad \textbf{3.32}$$

$$MAPE = \frac{100}{N_{samples}} \sum_{k=0}^{N_{samples}-1} \frac{|x_k - \widehat{x_k}|}{max(\in, |x_k|)} \qquad \textbf{3.33}$$

In (3.33), $\in$ is selected as an arbitrary small positive number to avoid errors when x is zero. The correlation factor is expressed in (3.34)

$$R^2\_score = 1 - \frac{\sum_{k=1}^{N}(x_k - \widehat{x_k})^2}{\sum_{k=1}^{N}(x_k - \bar{x})^2} \qquad \textbf{3.34}$$

where, $\bar{x} = \frac{1}{N}\sum_{k=1}^{N} x_k$ and $\sum_{k=1}^{N}(x_k - \widehat{x_k})^2 = \sum_{k=1}^{N} \in_k^2$

All the metrics discussed are used further for analyzing the performance of the four ML algorithms.

3.4 SSPV Panel Modeling Mathematical/Multi-physics

The SSPV modeling is also developed in mathematical and Multiphysics modeling, where the performance characteristics of the PV panel are obtained. The validation of the models is done with the experimental data parameters characteristics.

3.4.1 Mathematical modeling of SSPV panel

Consider a semiconductor device which work as solar cell by converting photon (light) energy into electrical energy. The potential difference of pn-junction is the result of the electrochemical equilibrium of the electrons in the n and p- regions i.e., φ^n-φ^p. With the distribution of charge density (ρ_Q) the distribution of potential difference is explained below.

The density of the space charge in the n-region is

$$\rho_Q^n(x) = e\left(n_D^+ - n_e(x)\right) = en_D^+\left(1 - exp\left\{\frac{e[\varphi(x)-\varphi^n]}{KT}\right\}\right) \qquad \textbf{3.35}$$

Similarly, for p-region is also considered.

To compensate positive and negative space charge in the n and p-regions with depths ω_n & ω_p the density is,

$$\rho_Q^n = en_D^+ \approx en_D \qquad for \ -\omega_n < x \le 0 \text{and}$$

$$\rho_Q^p = -en_A^- \approx -en_A \qquad for \ 0 \le x < \omega_p$$

The sum of charges $Q_n + Q_p = 0$. Where $Q_n = en_D\omega_n$ in n-region, $Q_p = -en_A\omega_p$ in p-region. From sum of charges depth is expressed as,

$$\omega_p = \frac{n_D}{n_A}\omega_n \qquad \textbf{3.36}$$

The thickness of space charge layer is,

$$\omega = \omega_n + \omega_p = \left(1 + \frac{n_D}{n_A}\right)\omega_n \qquad \textbf{3.37}$$

For the boundary conditions E(-ω_n) = 0 for the electric field and φ(-ω_n) = φ^n for the electrical potential in the region $-\omega_n < x \le 0$ of the n-region yields

$$\varphi_n(x) = -\frac{en_D}{2\varepsilon\varepsilon_0}(x + \omega_n)^2 + \varphi^n \qquad \textbf{3.38}$$

and for the boundary conditions $E(w_p) = 0$ and $\varphi(\omega_p) = \varphi^p$ in the range $0 \le x < \omega_p$ of the p-region yields

$$\varphi_p(x) = -\frac{en_A}{2\varepsilon\varepsilon_0}(x - \omega_p)^2 + \varphi^p \qquad \textbf{3.39}$$

Considering equal charge distribution, from $\varphi_n(0) = \varphi_p(0)$ even at x=0, then,

$$\varphi^n - \varphi^p = \frac{e}{2\varepsilon\varepsilon_0}\left(n_D\omega_n^2 + n_A\omega_p^2\right) \qquad \textbf{3.40}$$

From Equations (3.36) and (3.37), total thickness of the space charge layer is given as,

$$\omega = \sqrt{\frac{2\varepsilon\varepsilon_0}{e}\frac{n_A + n_D}{n_A n_D}(\varphi^n - \varphi^p)} \qquad \textbf{3.41}$$

The band gap energy of a metal is deriving by the thickness of the space charge layer and the acceptor and donor concentrations $(n_D \& n_A)$. The charge current rate with the rate of recombination and generation G_h also the concentration of electron and holes (η_e, η_h) is,

$$j_Q = -e \int_{L_h}^{L_e} \left\{ G_h^0 \left[1 - exp\left(\frac{\eta_e + \eta_h}{KT}\right) \right] + \Delta G_h \right\} dx \qquad \textbf{3.42}$$

From Equation (3.42) the short circuit current at V=0 is given by equation (3.43),

$$j_{sc} = -e \int_0^\infty a(h\omega, L_e) dj_\gamma(h\omega, 0) \qquad \textbf{3.43}$$

From Eq (3.44), charge current

$$j_Q = j_s \left[exp\left(\frac{eV_{oc}}{KT}\right) - 1 \right] + j_{sc} \qquad \textbf{3.44}$$

The open circuit voltage from Equation (3.45),

$$V_{oc} = \frac{KT}{e} ln\left(1 - \frac{j_{sc}}{j_s}\right) \qquad \textbf{3.45}$$

Where j_s is the saturation current of solar cell as represented in equation (3.46),

$$j_s = en_i^2 \left(\frac{D_e}{n_A L_e} + \frac{D_h}{n_D L_h}\right) \qquad \textbf{3.46}$$

The solar cell junction depth can be found from Eq (3.41) in order to calculate the band gap energy of a material (like silicon (Si), GaInP, CGS, CdTe, etc.,) utilized. The characteristics of solar cells like V_{oc} and J_{sc} are plotted from Eqs (3.43), (3.44), (3.45) and (3.46). The solar PV cell in under water conditions from radiation transmitted inside the water layer is developed with Snell's law [27]. The reflection and refraction of the radiation is explained by Fresnel's law and Snell's law respectively. The angle of reflection is equal to the angle of incidence. The proportion of the light which is reflected is described by Fresnel's law. The Snell's law is $\frac{\sin \alpha}{\sin \beta} = \eta$ where α is the angle of incident light, β is the angle of transmitted light and η is the refractive index of water (approx. 1.33) [27], [30], [32]. The transmitted and attenuation of transmitted light inside the water is explained by absorbed, scattered and attenuation constants.

Attenuation with depth: Light intensity decreases with depth because of absorption and scatter. The attenuation of light may be described by:

$$I_Z = I_0 e^{-kz} \qquad \textbf{3.47}$$

Where,

I_Z = light intensity at depth Z, I_0 = light intensity at the surface, and k = the extinction coefficient of the water.

(a) Effect of water on light transmission.

Water scatters light proportional to the inverse 4th power of the wavelength. That is, scatter light $\propto 1/\lambda^4$ where λ is the wavelength.

(b) Effect of particles and dissolved coloured materials.

$$I_z = I_o e^{-(k_w + k_p + k_d)z} \qquad \textbf{3.48}$$

Where, k_w= extinction due to scatter and absorption due to water, k_p= extinction due to scatter and absorption due to particles, and k_d= extinction due to scatter and absorption due to dissolved color. Total extinction is due to the sum of the three.

From Equations (3.47 and 3.48) the transmitted radiation to the surface of different solar cell is calculated. This value is substituted to calculate Equations (3.42), (3.43), (3.44), (3.45), and (3.46) through which the performance of the solar cell underwater is calculated. Similarly, by considering the water turbulence effect the performance measurement of the solar cell is obtained.

3.4.2 Multiphysics modeling of SSPV panel

The PV panel designed in section 3.3.2 is considered for the submerging into water at different depths in a tank to make SSPV panel. The geometry of the are $42.0 \times 35.0 \times 2.0$ mm in 3-Dimensions top view and is shown in Figure 3.16 and the dimensions of the tank are $10.0 \times 10.0 \times 100$ cm as shown in Figure 3.19.
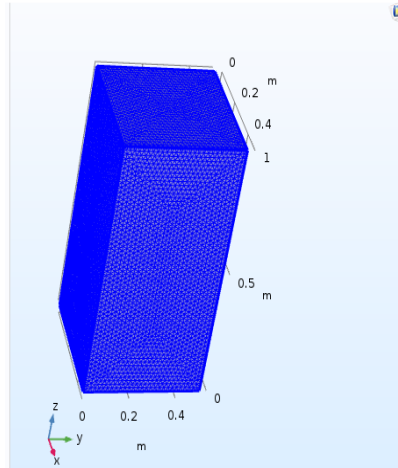
Figure 3.19 Dimensions of the tank

Now combining the Figure 3.16 and Figure 3.19 together, the SSPV is created and is as shown in Figure 3.20 a) and the top view is provided in Figure 3.20.b).

a)   b)
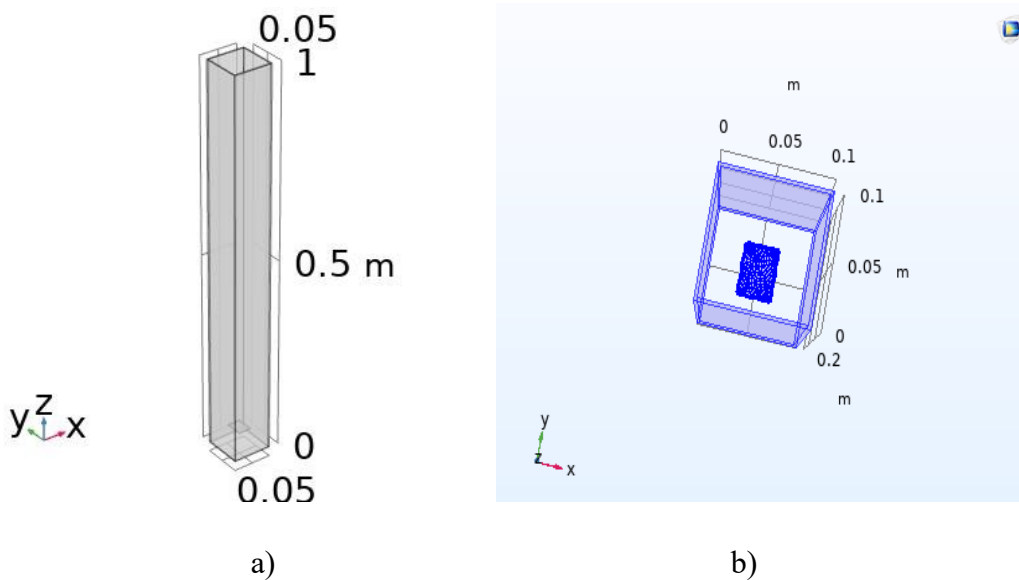
Figure 3.20 a) SSPV design geometry b) top view of SSPV at cross section of 10 cm

The tank is filled with water and at top of the tank, the flow of air at 25 m/s is considered to create turbulence on the surface of the water which in turn creates the change

in irradiation with respect to the depth of the water as shown in Figure 3.21. The height of the tank is considered as 1 meter and at each 2 cm variation, the solar panel is moved to find the I-V and P-V characteristics of the panel at each interval. The meshing of the tank is considered at 0.1 mm to incorporate finer mesh and the meshing for the panel is similar to the Figure 3.14 for each solar cell.
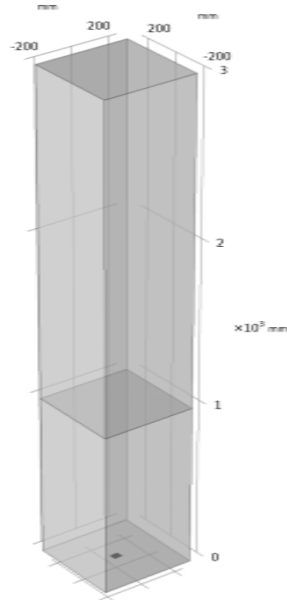
Figure 3.21 SSPV with air as medium on top of the tank

The different layers like Al frame, Glass, EVA and solar PV cell with back contact of the PV cell properties are considered as specified in Table 3.2. The material properties of the solar cell are changed to Si, Ge, GaAs and InP as specified in Table 3.3 so that the performance characteristics of all the materials are calculated at 2 cm each till 20 cm and then directly measured at 1 m depth to eliminate computational delay because of the finer mesh created for FVDM. The physics included in the modeling CFD additionally to incorporate, flow of water and air. The other modules are similar to the modules used in the PV cell designing specified in section 3.3.

3.5   Results and Discussion

The results presented in this chapter include PV cell/Panel performance characteristics with mathematical modeling by changing irradiation and temperature. Also, using different materials at different temperatures, joule heating of materials developed,

ML techniques implementation and finding best material with efficiency calculations. The SSPV performance with different materials at different depths is estimated and the best ML is applied to find the performance characteristics with different materials and depths.

The flow of result section is developed in four steps and is as follows:

1. PV characteristics at different temperature and irradiations
2. PV cell modeling characteristics
3. PV characteristics for different materials
4. PV characteristics for different temperatures
5. ML based prediction of PV characteristics
6. SSPV performance characteristics and validation
7. ML based prediction of SSPV characteristics

3.5.1 PV characteristics at different temperatures and irradiations

At STC values, a 20W PV solar panel has specifications as shown in Table 3.1. The zero-circuit voltage is observed when the circuit is shorted i.e., there is no resistance across the diode and the current at short circuit condition becomes maximum. So, in this mathematical modeling, there is a presence of very less shunt and series resistance. Depending on the voltage-temperature at P-N junction causes a negative co-efficient of temperature in open circuit voltage and positive co-efficient of temperature in output current, this generates larger photon current.
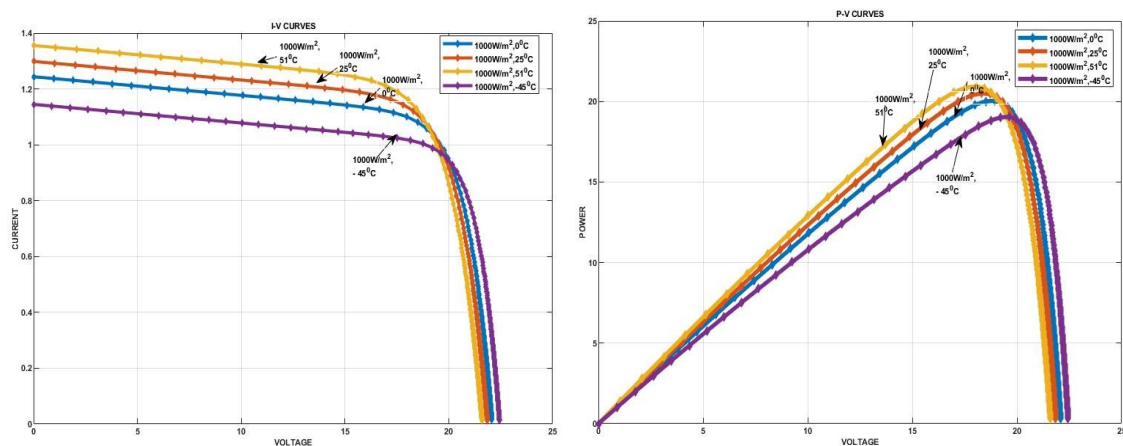
Figure 3.22 a) I-V curves at 1000 W/m^2 and different temperature levels b) P-V curves at 1000 W/m^2 and different temperature levels
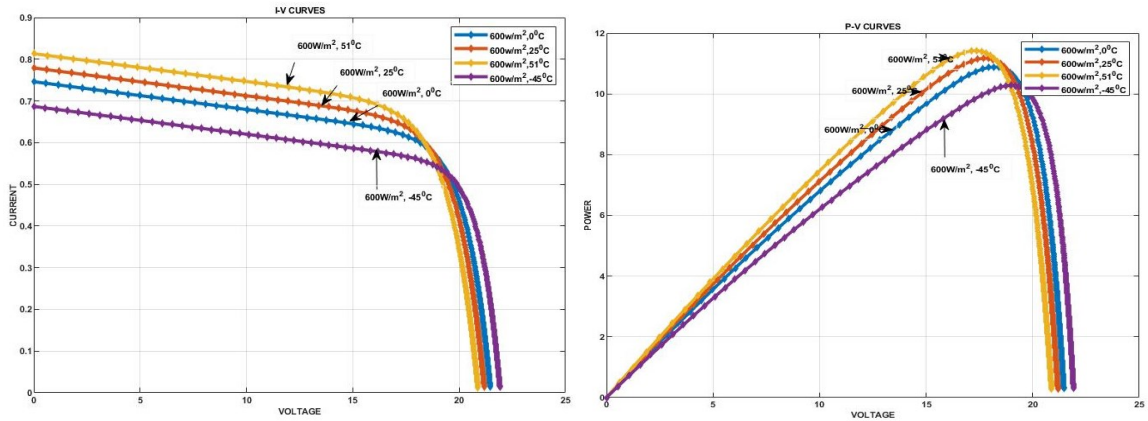
Figure 3.23 a) I-V curves at 600 W/m² and different temperature levels b) P-V curves at 600 W/m² and different temperature levels
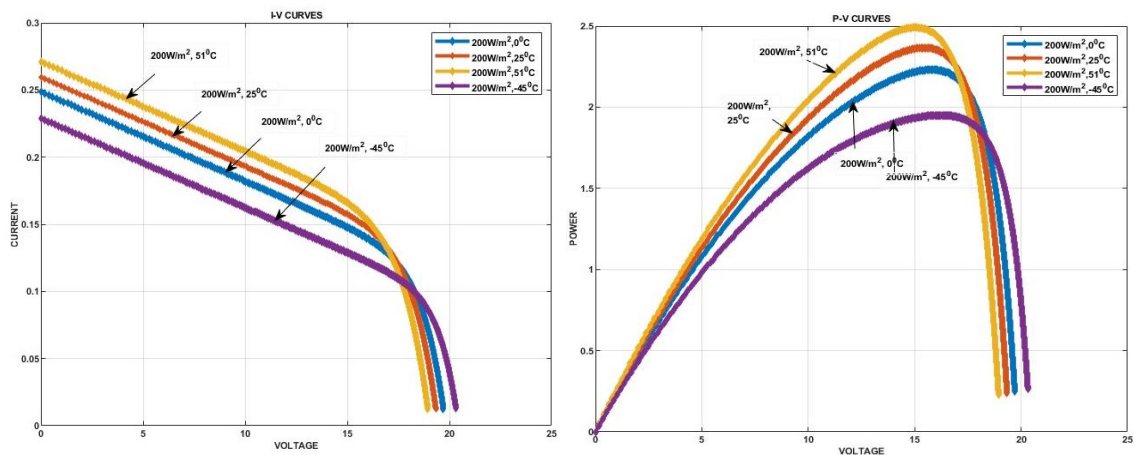
Figure 3.24 a) I-V curves at 200 W/m² and different temperature levels b) P-V curves at 200 W/m² and different temperature levels

The authentic MATLAB/SIMULINK software is preferred for modeling and simulation. The 20W panel is designed with the mathematical equations for obtaining the characteristics of a solar panel. The solar PV cell is designed in MATLAB/SIMULINK with mathematical equations as above specified in section 3.2. The I-V and P-V characteristics of PV cell are taken at different levels of temperatures like -45 ^{0}C, 0 ^{0}C, 25 ^{0}C, 51 ^{0}C and also at different irradiations like 1000 W/m², 600 W/m², 200 W/m² by using MATLAB simulation. These electrical characteristics are exhibited below as shown from Figure 3. 22 to Figure 3.24.

The Figure 3.22 (a) shows the I-V characteristics and Figure 3.22 (b)shows the P-V characteristics of PV panel at irradiation1000 W/m² and at distinctive temperatures like -45 ^{0}C, 0 ^{0}C,25 ^{0}C, 51 ^{0}C. Figure 3.23 (a) and (b) gives the I-V and P-V characteristics of

a panel at distinctive temperatures and at irradiation of 600 W/m². Similarly Figure 3.24 (a) & (b) shows the I-V and P-V characteristics of a panel at irradiation200 W/m² and at different temperatures. From simulation outputs, it is realized that the increase in temperature levels makes the voltage output (V_{oc}) decrease and the output current (I_{sc}) increase. The increase in temperature coefficient is positive for current and negative for voltage.

3.5.2 PV Cell Modeling Characteristics

3.5.2.1 *Electron - hole concentration of mono- crystalline Si*

The log of electron and hole concentration throughout the volume is shown in Figure 3.25 a) and Figure 3.10 b) respectively.

a)   b)
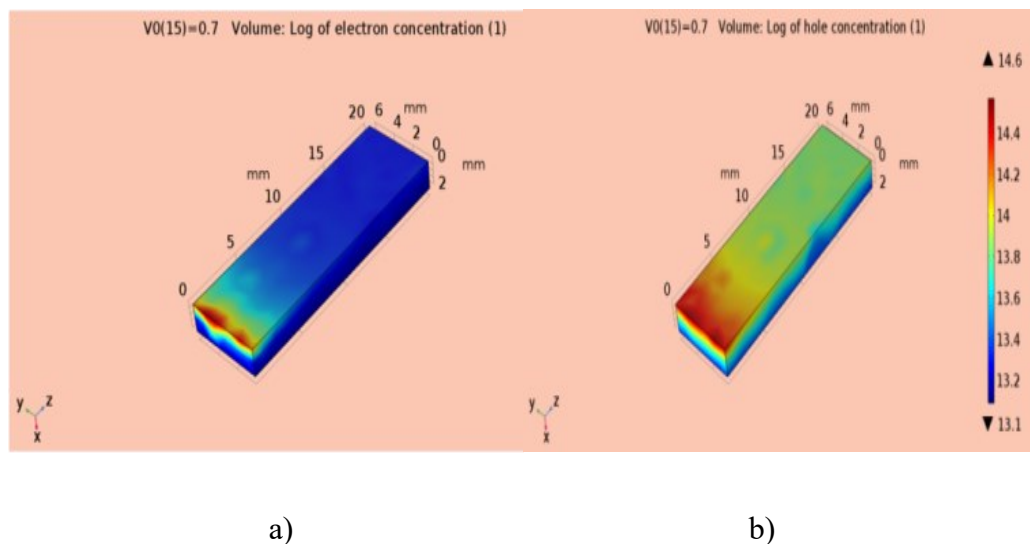
Figure 3.25 a) Electron concentration throughout the PV cell b) Hole concentration throughout the PV cell

The electron accumulation at the junction barrier for electron-hole pair formation is shown in Figure 3.25. (a) with more than the cut off voltage of Si, while Figure 3.25. (b) shows the hole concentration and transportation with the irradiation reflection, refraction and absorption within the mono-crystalline Si PV cell. The electron - hole concentration of Mono-crystalline Si cell is plotted in Figure 3.26 showing the depth of PV cell model on x-axis and log of electron – hole concentration on y-axis. The electron distribution throughout the PV cell is constant within all the layers of design and the hole concentration is decreasing with the increase in depth of irradiation penetration.
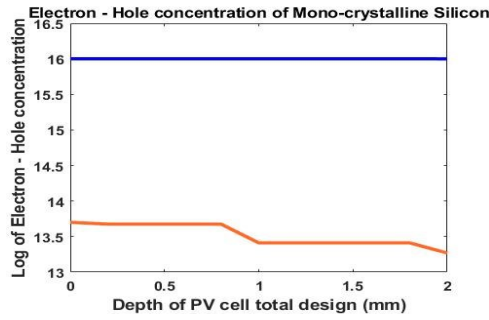
Figure 3.26 Electron-hole concentration through the depth of mono-crystalline Si

3.5.2.2 *Joule heating of mono-crystalline Si*

The series as well as shunt resistance of the PV panel causes this parasitic effect as discussed in section 3.2.3. The joule heat generation throughout the 2 mm depth of PV cell is plotted and presented in Figure 3.27.
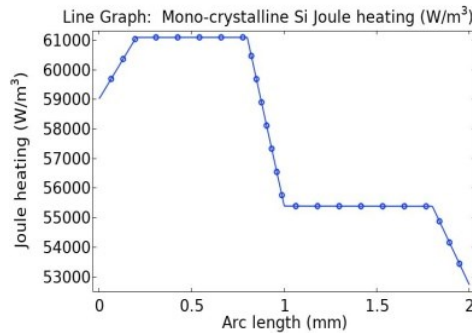
Figure 3.27 Joule heat distribution of mono-crystalline Si

From the graph it can be observed that the top layer of the design, the joule heat increases towards the top layer and then decreases throughout the P-N junction, because of the Si layer. Again, at back contact and EVA layer, the heat is decreased when compared to the top layer of the P-N junction. From Figure 3.27, the joule heat generated for mono-crystalline Si is 61kW/m^3.

3.5.2.3 *Validation and calibration of simulated PV cell with experimental data*

The modeled PV cell is compared with the PV cell/slice of practical SLMD121H10L, Mono-crystalline Si solar cell module having dimensions of 6.16 mm×20 mm×2 mm (Figure 3.12. (a) and (b)) using semiconductor, optical and thermal modules. The characteristics of the designed model, datasheet and experimental Si PV cell are plotted

and shown in Figure 3.28. (a) and (b). With the consideration of Si material properties and thermal co-efficient values specified in Table 3.1 and 3.2, the performance characteristics of modeled PV cell are plotted using FVDM and by considering input power as 100 W.

a)   b)
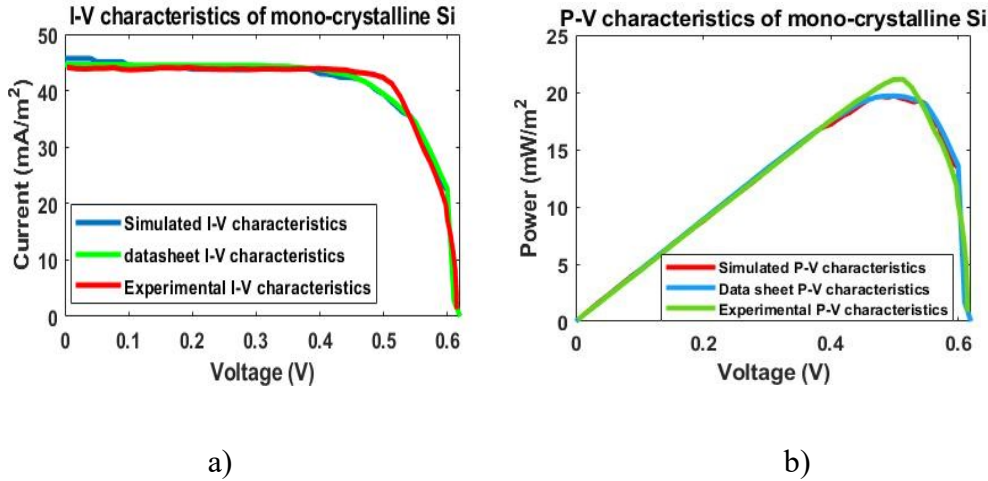
Figure 3.28 a) I-V characteristics of simulation, data sheet and experimental data of mono-crystalline Si b) P-V characteristics of simulation, data sheet and experimental data of mono-crystalline Si[4]

Table 3.5 Mono-crystalline Si parameters (obtained from Figure 3.13. a) and b))

PV cell	V_{oc} (V)	I_{sc} (mA)	V_{max} (V)	I_{max} (mA)	P_{max} (mW)	FF	P_{in} (W)	Efficiency (%)
Mono-crystalline Silicon (Simulated design)	0.62	45.69	0.50	39.39	19.69	0.69	100	19.69
Mono-crystalline Silicon (commercial Si data sheet)	0.62	44.57	0.50	39.39	19.69	0.69	100	19.69
Mono-crystalline Silicon (Experimental setup)	0.61	44.12	0.51	40.22	20.15	0.71	100	20.01

Table 3.5 shows the parameters of the simulated PV cell, commercially available PV cell and the parameters obtained from the experimental setup. The parameter values of the simulated cells are the same as the data sheet of practical solar cell and experimental

---

[4]C. S. Durganjali, G. Avinash, K. Megha, R. N. Ponnalagu, S. Goel, and S. Radhika, "Prediction of PV cell parameters at different temperatures via ML algorithms and comparative performance analysis in Multiphysics environment," *Energy Convers. Manag.*, vol. 282, p. 116881, 2023, doi: https://doi.org/10.1016/j.enconman.2023.116881.

data (performance characteristics shown Figure 3.28 (a) and (b)). The maximum efficiency value of the commercially available solar cell obtained from data sheet is 19.69 % and the maximum efficiency of modeled solar cell is 19.69 % (Figure 3.13. (a) and (b)).

It can be observed that the difference between the efficiency of the practical and simulated solar cell is small (only 0.00005 %) showing the workability of the model. The efficiency of the PV cell obtained from the experimental setup is slightly higher (0.005 %) when compared to both modeled and data sheet. This may be due to the direct irradiation of 1000 W/m^2 without diffusion for experimental work through solar simulator.

3.5.3 PV Cell Characteristics for Different Materials

3.5.3.1 Characteristics of modeled PV Cell

The validated PV cell which is designed of Mono-crystalline Si material and extended to panel with material change from Si to Ge, GaAs and InP with the different properties of the material listed in Table 3.2.

a)   b)
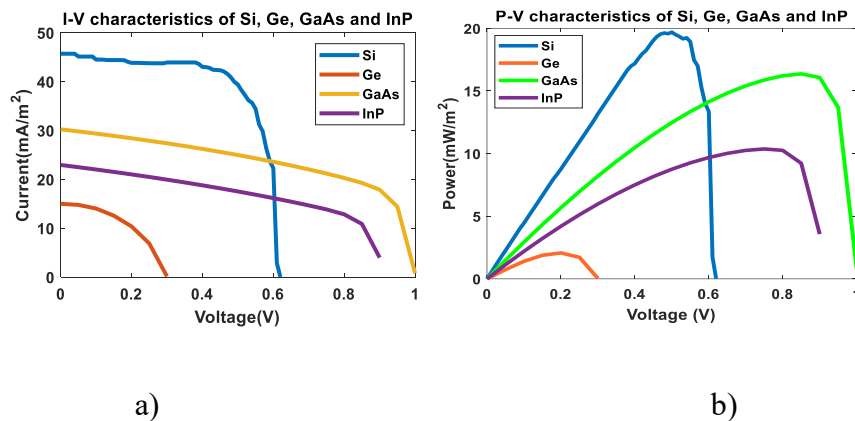
Figure 3.29 (a) I-V characteristics of PV cell modeled using Si, Ge, GaAs and InP b) P-V characteristics of PV cell modeled using Si, Ge, GaAs, and InP

Figure 3.29 (a) and (b) shows the I-V and P-V characteristics of PV cell modeled using four different materials such as Si, Ge, GaAs and InP. The plots are obtained at STC. From Figure 3.29 (a) and (b), it can be observed that, mono-crystalline Si gives maximum current and power but the efficiency of GaAs is high at STC when compared to other materials because of the high V_{oc}. The PV cell parameters including efficiency and FF for the PV cell modeled using four different materials are listed in Table 3.6.

Table 3.6 PV cell efficiency of the materials with the parameter findings at STC

Parameter	Mono-Crystalline Si	Ge	GaAs	InP
P_{max} (mW)	19.69	2.07	20.04	10.37
V_{max} (V)	0.50	0.20	0.90	0.75
I_{max} (mA)	39.39	10.36	22.82	13.83
V_{oc} (V)	0.62	0.30	1.00	0.92
I_{sc} (mA)	45.68	14.98	30.22	22.93
FF	0.69	0.46	0.68	0.492
Efficiency (%)	**19.69**	**2.07**	**20.03**	**10.38**

3.5.3.2 *Characteristics of modeled PV panel*

By connecting 10 of the modeled PV cells in series, model of the PV panel is obtained, and its performance characteristics obtained are shown in Figure 3.30 a) and b).

a)   b)
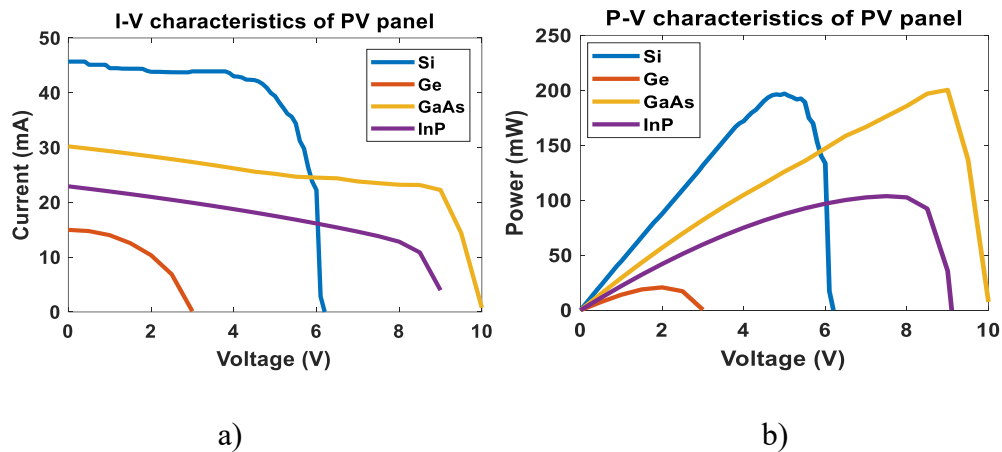
Figure 3.30 (a) I-V characteristics of PV panel modeled using Si, Ge, GaAs, and InP b) P-V characteristics of PV panel modeled using of Si, Ge, GaAs, and InP

From the Figure 3.30 (a) and (b), it can be observed that, mono-crystalline Si generates maximum current and power but the efficiency of GaAs panel is 3.6 % more than Si and it is because of the high V_{oc}. The PV panel parameters with all these materials are listed in Table 3.6 with efficiency calculation. As the panel is modeled by connecting 10 PV cells in series the voltage **V_{oc} (V)** is 10 times the V_{oc} obtained from the single PV cell and the current **I_{max} (mA)** is same both in cell and panel level but the representation will vary from mA/m² in cell level to mA in panel level as shown in Figure 3.14 (a) and Figure 3.15 (c).

Table 3.7 PV panel efficiency of the materials with the parameter findings at STC

Parameter	Mono-Crystalline Si	Ge	GaAs	InP
P_{max} (mW)	196.97	20.72	210.54	103.07
V_{max} (V)	5.00	2.00	9.00	7.50
I_{max} (mA)	39.39	10.36	25.86	13.83
V_{oc} (V)	6.20	3.00	10.00	9.20
I_{sc} (mA)	45.59	14.98	30.22	22.93
FF	0.69	0.46	0.77	0.49
Efficiency (%)	**19.69**	**2.07**	**23.27**	**10.38**

3.5.3.3 *Joule heating distribution*

The series and shunt resistance of the PV panel causes this parasitic effect as discussed in section 3.1.4. Every material generates its own heat and it increases with the increase in temperature on the top of the PV. To observe the joule heat in the PV panelrepeatedly, heat transfer module is considered in the design model of mono-crystalline Si cell and the same is done in case of Ge, GaAs and InP. The joule heat distribution throughout the 2 mm depth of panel is plotted and is shown in Figure 3.31 for all the four different materials at 25 ^{0}C. The individual material joule heat distribution is presented in Appendix: A - Fig.A6 a), b), and c) with a consideration of cutline in the geometry across the axis of depth.

Table 3.8 Joule heat of different materials

Material	Joule Heat generation (kW/m^3)
Si	61
Ge	234
GaAs	5.05
InP	3.95

If a cutline is drawn in 3D-axis, the joule heat across the cell is as shown in Appendix A - Fig. A7. (a) for all the materials. The InP shows less joule heat generation and Ge provides higher joule heat generation which is possible at 25 ^{0}C and the values are tabulated in Table 3.7. The Si and GaAs shows moderate production of joule heat.

From this, it can be noted that at higher temperatures, InP can be utilised with less heat loss of PV cell. The 3-D images of joule heat generation are shown in Appendix: A - Fig.A7 (b).
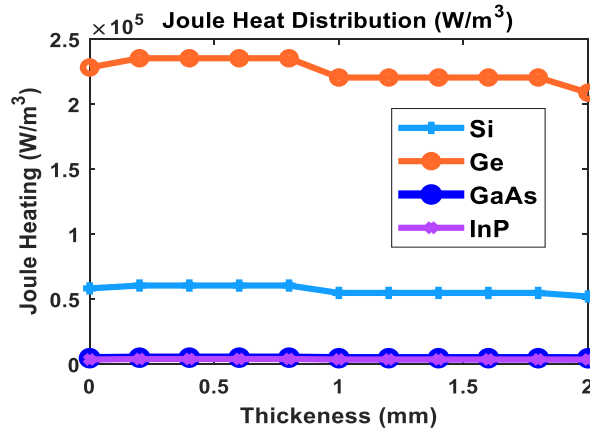
Figure 3.31 Joule heat generation in Si, Ge, GaAs and InP at 25 ^{0}C

3.5.4 PV panel characteristics at different temperatures

Initially the temperature is considered as 25 ^{0}C and is then changed to 0 ^{0}C, 51 ^{0}C and -45 ^{0}C to obtain the performance at extreme temperature conditions. Temperatures 51 ^{0}C and -45 ^{0}C are the maximum and minimum temperatures occurred in India at different seasons and days.

For better understanding of the characteristics at different temperatures, Figure 3.32 (a) and (b) are presented which shows the I-V and P-V characteristics of mono-crystalline Si PV cell at 25 ^{0}C, 0 ^{0}C, 51 ^{0}C and -45 ^{0}C. Similarly, for other materials, the I-V characteristics and P-V characteristics are drawn and are shown in Figure 3.32 (c) to (h). The efficiency and other parameters of the PV cell modeled using the four different materials are measured and tabulated in Table 3.9.

From Figure 3.32, it is observed that, as the temperature decreases, the performance of the solar cell increases with increase in V_{oc} and decrease in I_{sc}. For every ^{0}C temperature, the PV cell will have 0.05 % increase in $V_{oc.}$ The efficiency variation is possible by varying the temperature on the PV. The efficiency and other parameters of the PV panel modeled using the four different materials are measured and tabulated in Table 3.10.

Table 3.9 PV cell material parameters at different temperatures (25 ^{0}C, 0 ^{0}C, 51 ^{0}C, and -45 ^{0}C)

Material	Parameter	-45 ^{0}C	0 ^{0}C	25 ^{0}C	51 ^{0}C
Si		0.68	0.65	0.62	0.61
Ge		0.37	0.35	0.30	0.22
GaAs	V_{oc} (V)	**1.06**	**1.04**	**1.00**	**0.96**
InP		1.00	0.95	0.92	0.85
Si		**44.19**	**44.94**	**45.59**	**46.43**
Ge		14.77	14.94	14.98	14.75
GaAs	I_{sc} (mA)	41.76	30.21	30.22	24.44
InP		23.05	22.97	22.93	22.85
Si		20.26	19.97	19.69	19.01
Ge		3.12	2.36	2.07	1.51
GaAs	P_{max} (mW)	**24.65**	**22.52**	**20.03**	**19.24**
InP		10.63	10.46	10.37	10.08
Si		20.256	19.972	19.686	19.02
Ge		3.126	2.362	2.072	1.51
GaAs	Efficiency (%)	**24.66**	**22.51**	**20.03**	**19.22**
InP		10.64	10.47	10.38	10.09

While the temperature decreases, the efficiency of PV cell/panel increases irrespective the type of material. But when compared to Si, the GaAs is giving better efficiency which is approximately 4 % more at the cell level and 7% more at the panel level. Ge gives less efficiency compared to other 3 materials. Mostly, GaAs and Si gives good efficiency to use in most of the applications.

Through modeling, the time taken for the computation is high for each temperature values hence it is better to use ML algorithms for prediction of PV performance at different temperatures and materials. The major change is in V_{oc} which is 10 times for panel compared to PV cell because of series connection of 10 cells. So further for prediction, the cell level data is considered by decreasing the computation time and to predict the performance at 15 ^{0}C and -18 ^{0}C. To find best ML algorithm for parameters prediction 25 ^{0}C is used for validation.

a)   b)

c)   d)

e)   f)

g)   h)
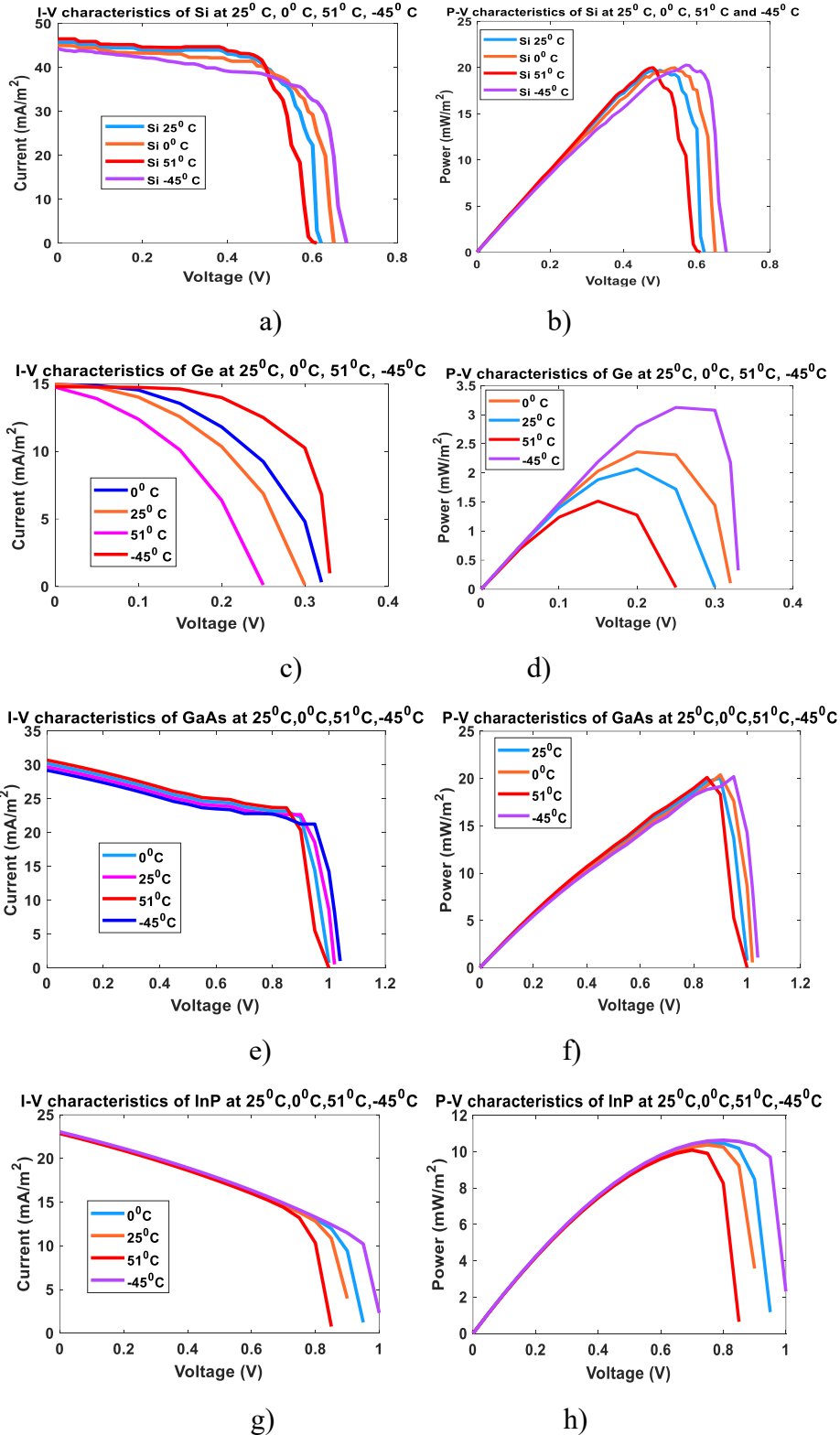
Figure 3.32 (a), (c), (e) and g) I-V characteristics of mono-crystalline Si, Ge, GaAs and InP at different temperatures (25 ^{0}C, 0 ^{0}C, 51 ^{0}C and -45 ^{0}C) at cell level (b), (d), (f) and (h) P-V characteristics of mono-crystalline Si, Ge, GaAs and InP at different temperature

Table 3.10 PV panel material parameters at different temperatures (25 ^{0}C, 0 ^{0}C, 51 ^{0}C, and -45 ^{0}C)

Material	Parameter	-45 ^{0}C	0 ^{0}C	25 ^{0}C	51 ^{0}C
Si		6.80	6.50	6.20	6.10
Ge		3.70	3.50	3.00	2.20
GaAs	V_{oc} (V)	**10.60**	**10.40**	**10.00**	**9.55**
InP		10.00	9.52	9.20	8.50
Si		**44.19**	**44.94**	**45.59**	**46.43**
Ge		14.77	14.95	14.98	14.75
GaAs	I_{sc} (mA)	41.77	30.22	30.22	24.44
InP		23.05	22.97	22.93	22.85
Si		20.26	19.97	19.69	19.02
Ge		3.12	2.36	2.07	1.52
GaAs	P_{max} (mW)	**28.57**	**26.18**	**21.28**	**18.94**
InP		10.63	10.46	10.37	10.09
Si		20.26	19.97	19.69	19.02
Ge		3.13	2.36	2.07	1.52
GaAs	Efficiency (%)	**28.57**	**26.15**	**21.27**	**18.92**
InP		10.64	10.47	10.38	10.09

3.5.5 ML based prediction of solar PV characteristics

While using ML algorithms for predicting the performance of PV cell/panel, the values obtained from the simulation are considered as input data at all different temperatures. The data is subsequently divided into training and testing (80 % and 20 %) and the data for 15 ^{0}C and -18 ^{0}C are predicted. The mono-crystalline Si, I-V and P-V characteristic values at 0 ^{0}C, 51 ^{0}C and -45 ^{0}C are considered as training data and the 25 ^{0}C is considered for testing as the data sheet (I-V & P-V) values are available for that.

After testing, with the metrics, hyper parameters are found and then the best hyper parameters with respective ML technique are used for prediction of I-V characteristics and P-V characteristics at temperatures 15 ^{0}C and -18 ^{0}C and are compared with the Si simulated data. The Appendix: A, Fig. A8 flow diagram is used for ML techniques procedure for Si step by step and the same is implemented with best hyper parameters to Ge, GaAs, and InP for prediction of 15 ^{0}C and -18 ^{0}C.

3.5.5.1 *Prediction algorithms for mono-crystalline Si at different temperatures*

3.5.5.1.1 Linear Regression (LR)

LR is used to find the coefficients of the data line and are determined by the train data, and it trains upon it to give the best line. The data obtained has been divided into 80 % for training and 20 % for testing. Within the training data, the metrics obtained for I-V curve are RMSE: 0.151 and R^2_SCORE: 0.617. Now, the 25 ^{0}C data is predicted for characteristics of I-V, P-V and compared with the simulation and data sheet data of I-V and P-V at 25 ^{0}C are as shown in Figure 3.33 (a) and (b) respectively. The graphs for 15 ^{0}C and -18 ^{0}C are presented in Appendix: A, Fig.A9 and A10.

3.5.5.1.2 Polynomial Regression (PR)

PR is used to locate the optimal degree of the polynomial from the first 10 degrees, the data is trained, and obtained the RMSE for each degree. The graphs representing the RMSE and R^2-score are shown in Appendix: A - Fig.A11 (a), (c), (b) and (d) for I-V data and P-V data at an interval of 1 to 7 as degree of freedom. It can be observed that lesser the RMSE value and higher R^2-score then that polynomial degree gives better result. In the proposed work the degree 4 is giving lesser RMSE = 0.05 and higher R^2-score = 0.93 for I-V and RMSE = 0.07 and higher R^2-score = 0.95 for P-V.

The degree 4 is considered as hyper parameter for the PR further and predicted the values of I and Pat 25 ^{0}C, 15 ^{0}C and -18 ^{0}C. For 25 ^{0}C, the values of simulated data and data sheet data both are available to validate the PR prediction results and are shown in Figure 3.33 (c) and (d) as I-V and P-V characteristics. Similarly, for 15 ^{0}C and -18 ^{0}C, Fig. A12 in Appendix: A, shows the I-V and P-V characteristics prediction through PR at 15 ^{0}C and -18^{0}C. The PR predictions values are almost similar to the simulated data and the efficiency of mono-crystalline Si at 25 ^{0}C.

3.5.5.1.3 Support Vector Regression (SVR)

The best fit hyper parameters for I-V characteristics are C = 1000, ϵ = 0.01 and γ (for RBF kernel) = 1 and for P-V characteristics C = 1000, ϵ = 0.1 and γ (for RBF kernel) = 1. With the best parameters, the characteristics are drawn for 25 ^{0}C, the values of simulated data and data sheet both are available to validate the SVR prediction results and

are shown in Figure 3.33 (e) and (f) as I-V and P-V characteristics. Similarly, 15 ^{0}C and -18 ^{0}C are as shown in Appendix: A - Fig.A13. (a) to (d).

a)   b)

c)   d)

e)   f)

g)   h)
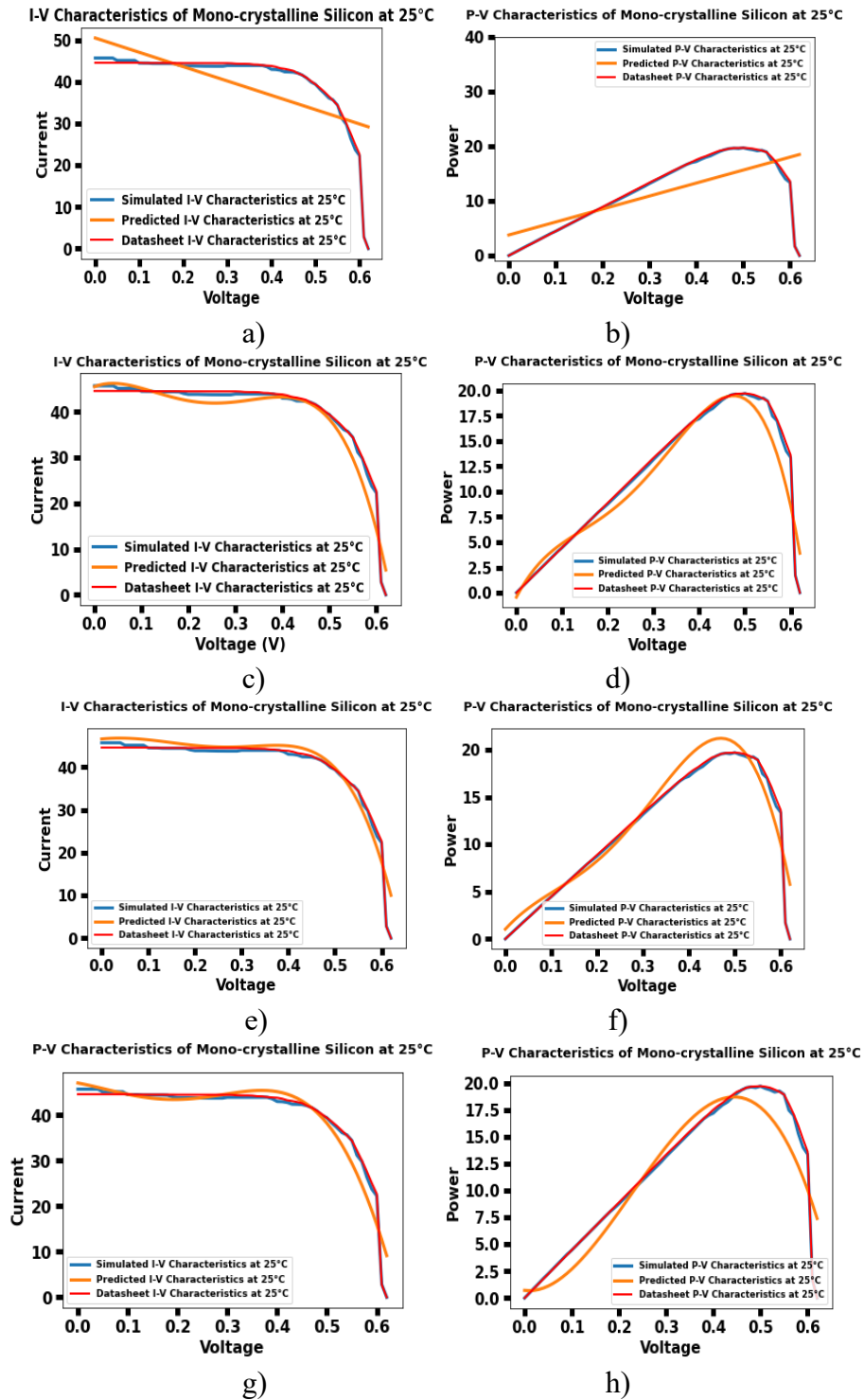
Figure 3.33 (a), (c), (e) and (g) I-V characteristics (b), (d), (f) and (h) P-V

characteristics of mono-crystalline Si at 25 ^{0}C with Simulated, predicted and data

sheet data by LR, PR, SVR and KRR algorithms respectively

Table 3.11 Mono-crystalline Si performance prediction at different temperatures with different ML algorithms

ML	Parameter	25 ^{0}C	15 ^{0}C	-18 ^{0}C
PR	Efficiency	19.32	20.11	20.92
SVR		19.99	19.77	20.75
KRR	(%)	19.23	19.43	19.75
PR		0.62	0.63	0.66
SVR	V_{oc}	0.62	0.63	0.66
KRR		0.62	0.63	0.66
PR		46.22	45.79	44.96
SVR	I_{sc}	46.58	44.56	45.82
KRR		47.04	46.14	44.95
PR		19.46	20.32	21.12
SVR	P_{max}	19.55	21.09	22.51
KRR		18.70	19.24	19.98
PR		0.47	0.48	0.52
SVR	V_{max}	0.47	0.49	0.52
KRR		0.44	0.45	0.48
PR		41.12	41.90	40.22
SVR	I_{max}	42.53	40.35	39.38
KRR		43.69	43.18	41.14
PR		0.67	0.69	0.71
SVR	FF	0.69	0.70	0.68
KRR		0.66	0.67	0.67

3.5.5.1.4 Kernel Ridge Regression (KRR)

To find best fit hyper parameters, grid-search CV is utilized and the best hyper parameters for I-V characteristics are alpha (α) = 0.001 and gamma (γ) =1.0, using RBF kernel and similarly for P-V, alpha (α) = 0.1 and gamma (γ) = 100.0, using polynomial kernel. The best hyper parameters are used as best fit for the simulated data and the characteristics of I-V and P-V are plotted at 25 ^{0}C as shown in Fig 3.33 (g) and (h). Similarly, 15 ^{0}C and -18 ^{0}C and are represented in Appendix: A - Fig. A14 (a) to (d).

From Figure 3.33, the parameters of mono-crystalline Si by PR, SVR, and KRR prediction algorithms are plotted and obtained PV parameters are tabulated in Table 3.11 with efficiency calculations. The LR prediction is a straight line (linear) so unable to calculate parameters of Si. Figure 3.34 a), and b) depicts the bar charts for I-V and P-V prediction metrics using the four ML algorithms respectively, where the less RMSE, MAE, and MAPE have the higher chance of predicting the fine values with higher R^2-score.

a)   b)
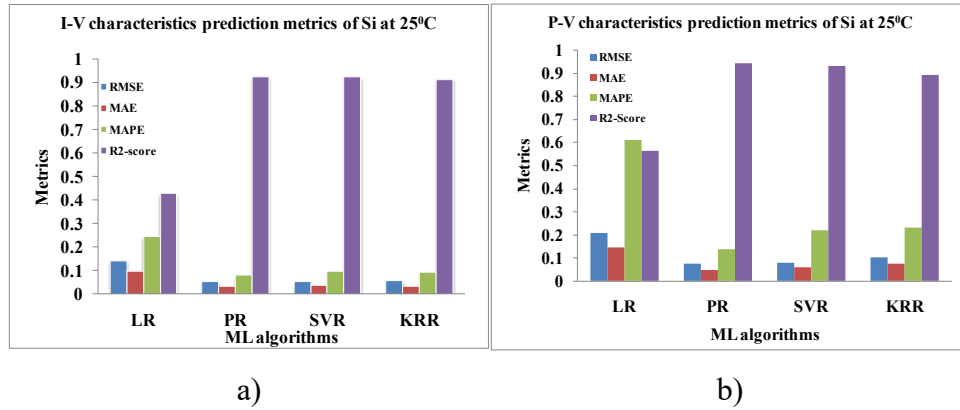
Figure 3.34 a) Metrics for I-V characteristics prediction at 25 ^{0}C b) Metrics for P-V characteristics prediction at 25 ^{0}C

The RMSE, MAE, MAPE and R^2- score metrics obtained from the four ML techniques at 25 ^{0}C, 15 ^{0}C and -18 ^{0}C are listed in Table 3.12. It can be observed that except LR model, the other PR, SVR, KRR techniques results in better performance.

3.5.5.2 *Prediction algorithms for different materials at different temperatures*

Now, the ML algorithms are implemented for Ge, GaAs and InP too in the sections below. The 25 ^{0}C data are predicted and the metrics for Ge, GaAs and InP are listed in Table 3.13 and the performance of Ge, GaAs and InP at 15 ^{0}C and -18 ^{0}C are also predicted and listed in the same. The I-V and P-V prediction and simulated data for Ge with LR, PR, SVR and KRR are represented in Appendix: A- Fig. A15 (a) to (h). The MAE, MAPE, RMSE and R^2-score metrics are measured at 25 ^{0}C and tabulated in Appendix: A – Table A1. The I-V and P-V of GaAs with LR, PR, SVR, and KRR ML techniques are shown in Appendix: A - Fig. A16 (a) to (h), and the corresponding MAE, MAPE, RMSE and R^2-score metrics are measured at 25 ^{0}C and tabulated in Appendix: A – Table A2. I-V and P-V of InP with LR, PR, SVR and KRR ML techniques are shown in Appendix: A - Fig. A17 (a) to (h). Also, from the prediction, the MAE, MAPE, RMSE and R^2-score metrics are

measured at 25 ^{0}C and tabulated in Appendix: A – Table A3. The bar charts for Ge, GaAs and InP are shown in Fig 3.35 (a), (b) and (c) for I-V characteristics and (d), (e) and (f) for P-V characteristics of Ge, GaAs and InP.
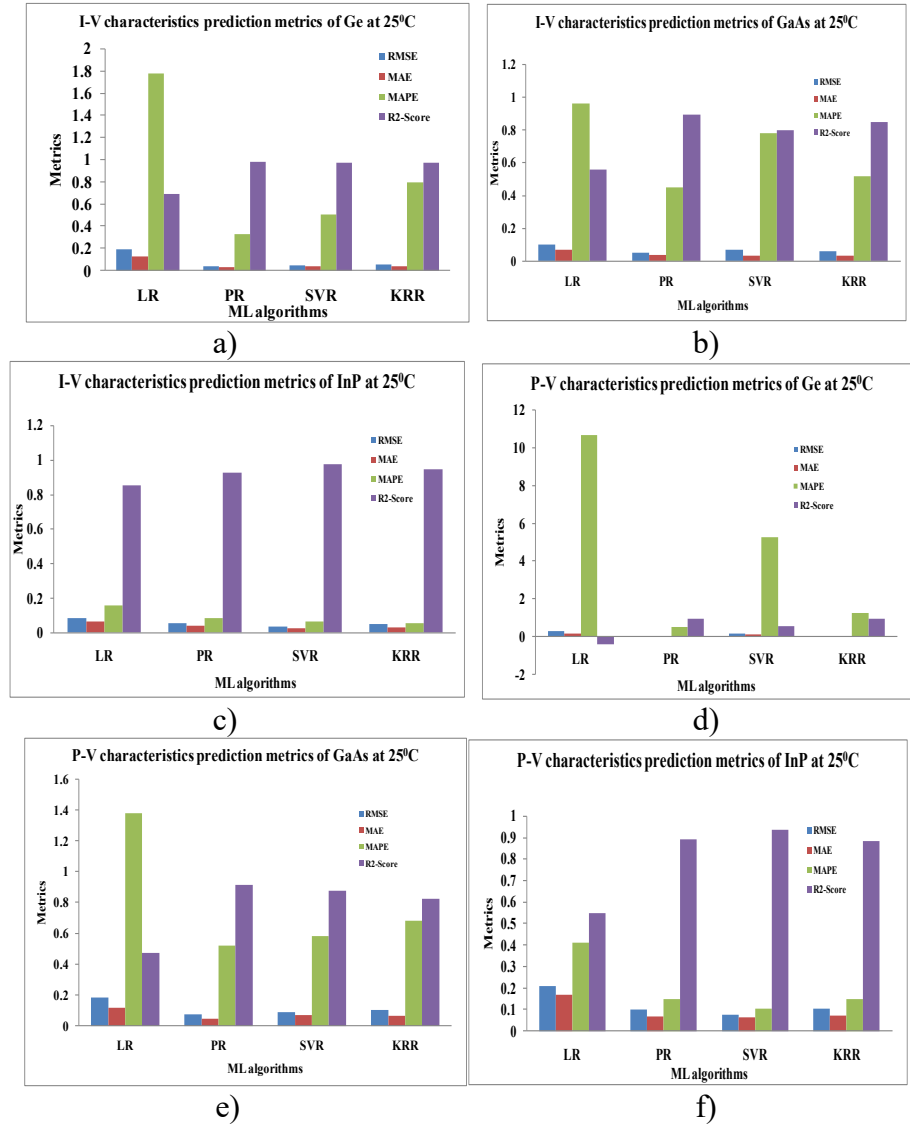
Figure 3.35 (a) and (d) Metrics of Ge (b) and (e) Metrics of GaAs (c) and (f) Metrics of InP for I-V and P-V performance characteristics respectively at 25 ^{0}C

From Figure 3.35, it can be seen that KRR algorithm is giving better performance at less time with best R^2-score which represents the best ML algorithm for PV parameter and efficiency prediction. Due to non-linearity, the PR gives good result at degree 4 but as the data increases, the degree of freedom for PR varies which will affect the prediction parameters with data limit. LR is not at all a fit for the PV parameter prediction. SVR is less efficient when compared to KRR with its best hyper parameters.

Table 3.12 List of metrics for ML techniques of mono-crystalline Si at 25 ^{0}C 15 ^{0}C, and -18 ^{0}C

Metric	Temperature	LR		PR		SVR		KRR	
		IV	PV	IV	PV	IV	PV	IV	PV
RMSE	25 ^{0}C	0.142	0.208	0.051	0.073	0.052	0.080	0.055	0.102
MAE		0.098	0.147	0.034	0.048	0.036	0.057	0.034	0.075
MAPE		0.245	0.612	0.082	0.138	0.098	0.219	0.093	0.231
R^2-Score		0.429	0.564	0.927	0.947	0.924	0.935	0.915	0.895
RMSE	15 ^{0}C	0.131	0.195	0.039	0.060	0.046	0.081	0.046	0.091
MAE		0.092	0.138	0.026	0.040	0.020	0.067	0.029	0.068
MAPE		4.540	5.106	1.267	1.425	2.123	1.596	1.582	2.165
R^2-Score		0.459	0.606	0.952	0.963	0.932	0.932	0.933	0.914
RMSE	-18 ^{0}C	0.115	0.182	0.045	0.069	0.060	0.105	0.049	0.098
MAE		0.079	0.122	0.033	0.049	0.041	0.082	0.029	0.076
MAPE		30.868	34.163	10.836	11.649	18.136	15.181	15.018	15.421
R^2-Score		0.511	0.656	0.924	0.950	0.864	0.885	0.910	0.901

Table 3.13 Parameter listing of Ge, GaAs, InP at 25 ^{0}C, 15 ^{0}C, and -18 ^{0}C with PR, SVR, and KRR

Parameter	ML	Ge			GaAs			InP		
		25 ^{0}C	15 ^{0}C	-18 ^{0}C	25 ^{0}C	15 ^{0}C	-18 ^{0}C	25 ^{0}C	15 ^{0}C	-18 ^{0}C
PR	Efficiency (%)	1.93	2.28	2.56	20.52	21.23	24.97	10.37	10.71	10.99
SVR		1.86	2.01	2.46	17.36	19.70	24.56	10.32	10.46	10.87
KRR		**1.86**	**2.17**	**2.68**	**17.16**	**18.92**	**22.74**	**10.04**	**10.16**	**10.35**
PR	V$_{oc}$	0.30	0.30	0.30	1.00	1.00	1.00	0.90	0.90	0.90
SVR		0.30	0.30	0.30	1.00	1.00	1.00	0.90	0.90	0.90
KRR		0.30	0.30	0.30	1.00	1.00	1.00	0.90	0.90	0.90
PR	I$_{sc}$	14.95	15.05	14.92	31.46	32.72	39.61	22.93	22.73	22.77
SVR		14.93	15.05	15.13	30.29	31.54	40.07	23.25	22.86	22.85
KRR		14.99	15.05	14.67	30.78	35.12	41.17	23.42	23.47	23.58
PR	P$_{max}$	1.91	2.32	2.56	19.09	20.70	25.68	10.37	10.86	11.12
SVR		1.60	2.21	2.74	19.48	21.30	26.89	11.18	11.16	11.85
KRR		1.91	2.18	2.69	17.17	19.38	22.87	9.88	10.29	10.54
PR	V$_{max}$	0.20	0.20	0.25	0.80	0.80	0.80	0.75	0.70	0.75
SVR		0.20	0.15	0.20	0.75	0.80	0.85	0.65	0.70	0.75
KRR		0.20	0.20	0.25	0.75	0.75	0.75	0.60	0.65	0.65
PR	I$_{max}$	9.65	11.41	10.26	23.55	25.47	31.22	13.83	15.29	14.66
SVR		9.31	13.39	12.30	23.15	24.63	28.89	15.87	14.94	14.49
KRR		9.31	10.87	10.72	22.87	25.23	30.32	16.74	15.62	15.93
PR	FF	0.43	0.51	0.57	0.59	0.62	0.63	0.50	0.52	0.54
SVR		0.42	0.45	0.54	0.57	0.63	0.61	0.49	0.51	0.53
KRR		0.41	0.48	0.61	0.56	0.54	0.55	0.48	0.48	0.49

3.5.6 SSPV performance characteristics and validation

From section 3.5.4, it is observed that, GaAs and Si are performing better at different temperature conditions with an efficiency of 20-25%. The same materials are

implemented in SSPV design to find the performance characteristics at different depths of water. The Si and GaAs are considered as shown in Figure 3.21, and the performance characteristics are as shown below. The I-V and P-V characteristics of Si at 0 cm to 20 cm at 2 cm interval obtained and at 1m depth is also obtained and plotted as shown in Figure 3.36 a) and b). Similarly, the GaAs material is considered in the Figure 3.21 and the I-V and P-V characteristics are plotted as shown in Figure 3.37 a) and b).

a)   b)
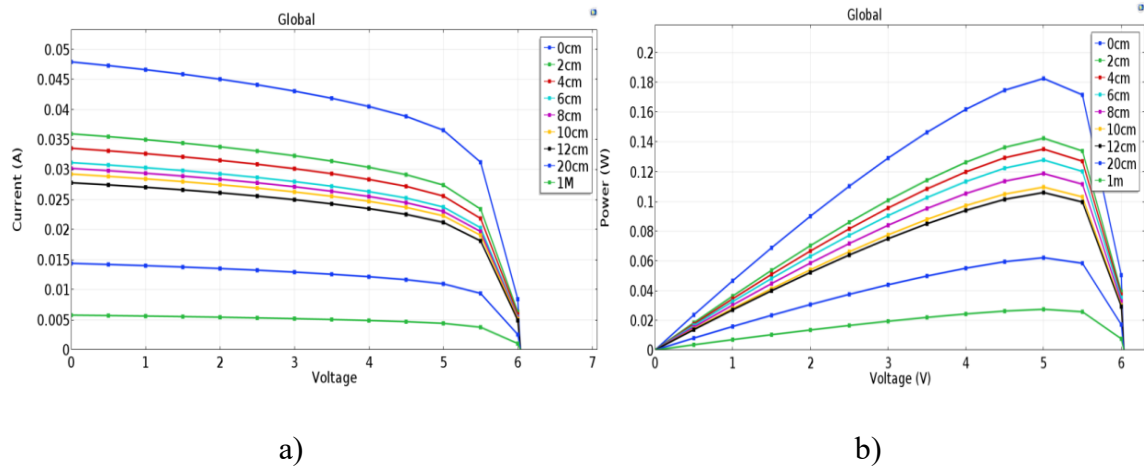
Figure 3.36 a) I-V characteristics of Si at different depths of water level b) P-V characteristics of Si at different depths of water level

a)   b)
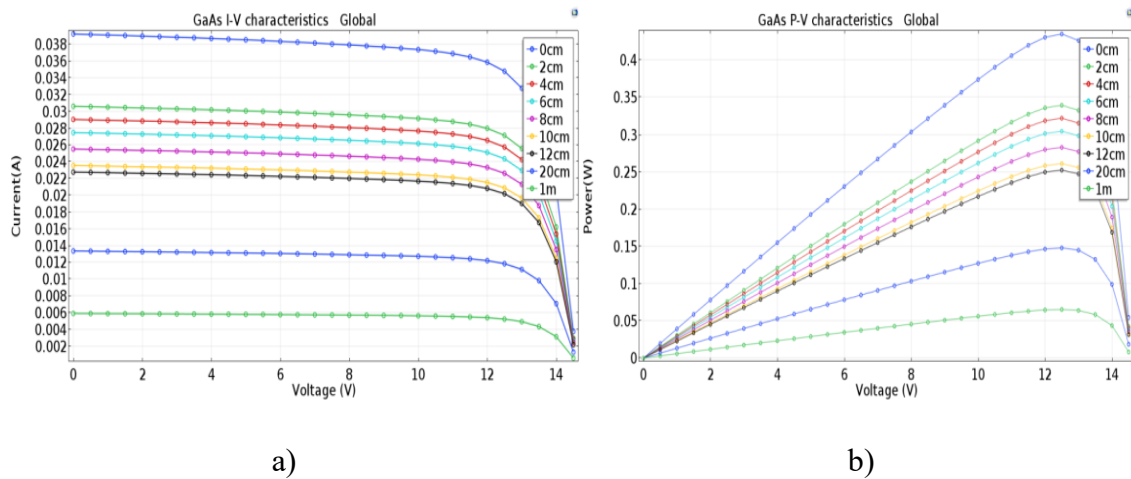
Figure 3.37 a) I-V characteristics of GaAs at different depths of water level b) P-V characteristics of GaAs at different depths of water level

It is observed that, as the depth increases, the performance of PV panel decreases with the decrease in V_{oc} and I_{sc} which in turn decreases the P_{max} causing decrease in efficiency but it exhibits presence of irradiation at 1m depth also. The energy obtained is less at 1m depth when compared to 0 cm depth which is floating on water surface.

Further to compare the Si performance of SSPV panel with FPV panel, the depth of the water level varied with 0.1 cm variation till 0.5 cm as specified in reference [37] with a water layer. The performance of PV panel increases at a depth of 0.5 cm and the performance characteristics are as shown in Figure 3.38 a) and b) at an interval of 0.1 cm.

a)
b)
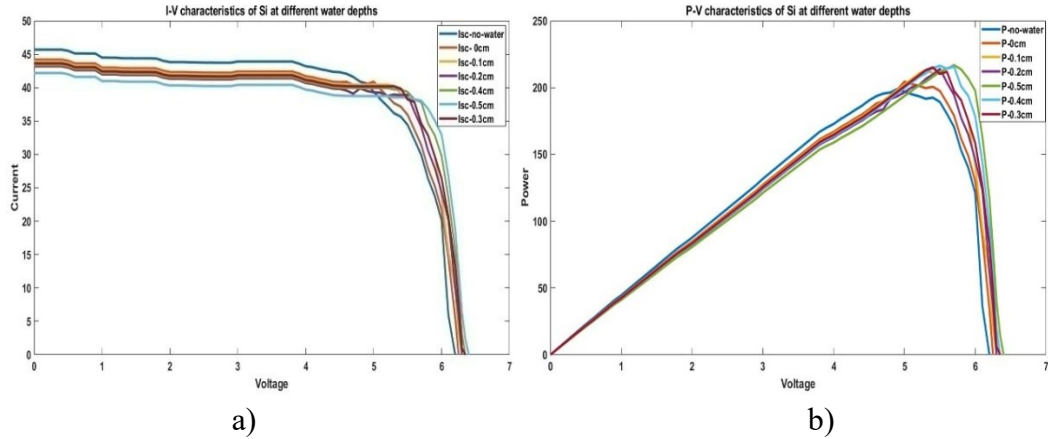
Figure 3.38 a) I-V characteristics of Si at different water depths at an interval of 0.1 cm b) P-V characteristics of Si at different water depths at an interval of 0.1 cm
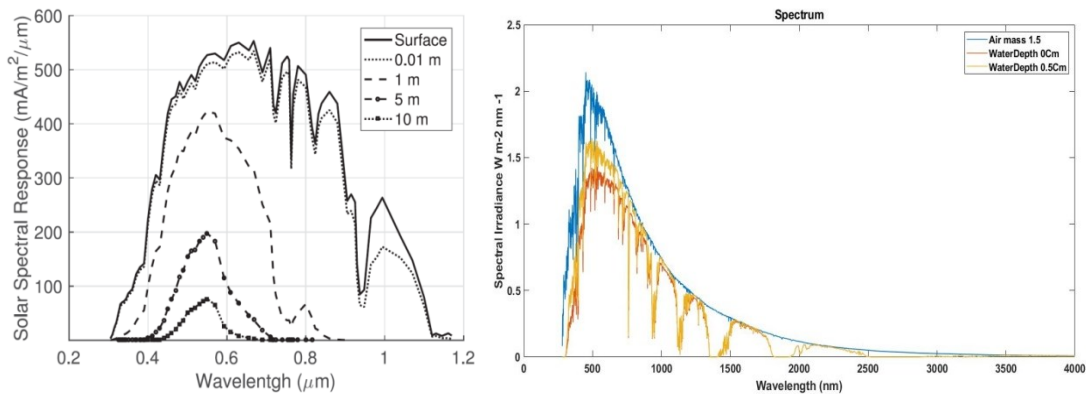
Figure 3.39 a) solar spectrum response of IXYS Si solar cell at different water depths b) Solar spectrum response of the Si solar cell at different water depths via Multiphysics modeling [36]

3.5.7 ML based performance characteristics prediction

From section 3.5.5, it is observed that, KRR and SVR are the best ML algorithms used for prediction of I-V and P-V characteristics at all metrices findings. Now, in SSPV also, the prediction of performance characteristics validation is done at 0.3 cm by considering the performance at 0cm, 0.1 cm, 0.2 cm, 0.4 cm and 0.5 cm as training data. The ML algorithm SVR gave 89 % prediction and the KRR gave around 92 % of prediction efficiency via training. While validating at 0.3 cm, the metrices of the ML algorithms are obtained and listed in Table 3.14.

Table 3.14 Parameter metrics for Si with SVR and KRR algorithms at 0.3 cm of water depth

Metrics	SVR		KRR	
	IV	PV	IV	PV
RMSE	0.0609	0.082	0.072	0.1133
MAE	0.0303	0.072	0.043	0.083
MAPE	0.2486	0.355	0.289	0.486
R² Score	0.915	0.927	0.895	0.862

The parameters of SVR to predict current is fixed at C = 1000, ϵ = 0.01 and γ (for RBF kernel) = 1. The parameters of SVR to predict power is fixed at C = 1000, ϵ = 0.1 and γ (for RBF kernel) = 1. The best hyperparameters to predict currents through a solar panel using voltage and depth using KRR is alpha = 0.01 and gamma =1.0, using RBF kernel. The best hyperparameters to predict powers using through a solar panel using voltage and depth using KRR is alpha = 0.001 and gamma = 100.0, using polynomial kernel. One thing to note is that during the calculation of MAPE, the least datapoint has been omitted, as when it is scaled down (using Min Max Scaler), it results in a 0. Any 0 datapoint in the calculation of MAPE leads to an arbitrarily large value.

a)   b)
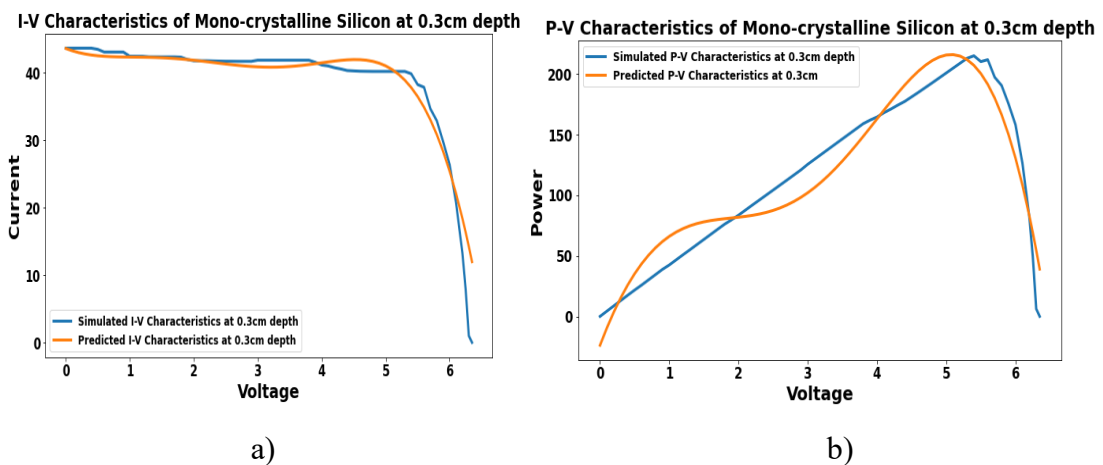
Figure 3.40 a) I-V characteristics b) P-V characteristics of the SVR prediction at 0.3 cm depth
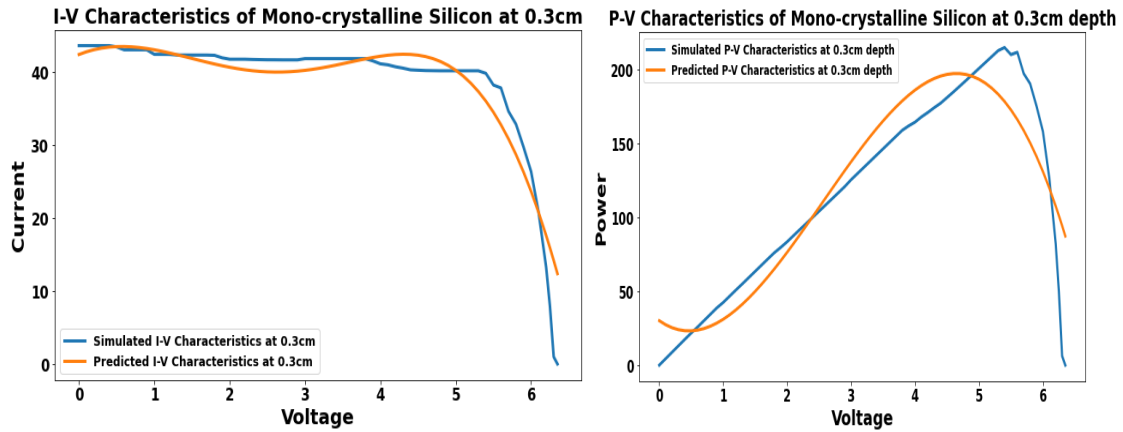
Figure 3.41 a) I-V characteristics b) P-V characteristics of the KRR prediction at 0.3 cm depth

The Figure 3.40 a) and b) shows the I-V and P-V characteristics of the SVR prediction at 0.3 cm depth, and the Figure 3.41 a) and b) shows the I-V and P-V characteristics of the KRR prediction at 0.3cm depth. The SVR gave best prediction of power at different water depths when compared to KRR, and KRR gave best prediction performance of current at different water depths when compared to SVR from the SSPV output performance characteristics.

3.6   Conclusion

The PV cell/panel is designed mathematically and obtained the characteristics at different irradiations and temperatures, where the PV cell/panel is having higher V_{oc} and lesser I_{sc} creating higher P_{max} with the decrease in temperature (0, 25, 51 and -45 ^{0}C) and irradiation (1000, 600, 200 W/m^2). The mono-crystalline Si PV cell/panel is modeled as shown in Figure 3.12 / Figure 3.16 in an experimentally validated Multiphysics environment, and the I-V and P-V performance characteristics are plotted as shown in Figure 3.28 (a) and (b). The efficiency of the simulated PV cell is 19.69 % which is almost equal to the efficiency of the commercially available mono-crystalline Si (19.69 %) experimental and data sheet data as tabulated in Table 3.4. The PV cell is also modeled using Ge, GaAs, and InP materials, as discussed in section 3.2.2, at 25 ^{0}C at both cell/panel level and at the cell level, the GaAs have 20.53 % efficiency while the mono-crystalline Si has 19.69 % efficiency.

The cell level model is extended to the panel level with material and temperature variations where GaAs have achieved 23.27 % (3 % increase) efficiency while Si has 19.69 % efficiency, the same as a cell. The materials efficiency at STC is as follows: GaAs > mono-crystalline Si > InP > Ge and the GaAs exhibit 28.57 % at -45 ^{0}C. The efficiency of the PV cell/panel is estimated based on the thermal losses, bandgap, and thickness of the model. It is observed that the Joule heat distribution is more in Ge, and the order of Joule heat distribution is Ge (**234 KW/m³**) > Si (**61 KW/m³**) > GaAs (**5.05 KW/m³**)> InP (**3.95 KW/m³**) representing less joule heat in InP throughout due to the thickness of PV.

The prediction is done to predict the values of current and power to obtain I-V and P-V characteristics of PV cells with all the other parameters and also to obtain efficiency. The LR, PR, SVR, and KRR algorithms are chosen for the prediction due to data points availability from low to medium and the popularity of algorithms for the characteristics. LR provides less accuracy because of the non-linearity in the characteristics, which is almost less than 80 % of the R^2-score. Similarly, PR and KRR resulted in > 85 % R^2-score. The degree 4 is the best hyper parameter of PR, the best fit hyper parameters for I-V characteristics are C = 1000, ϵ = 0.01 and γ (for RBF kernel) = 1 and for P-V characteristics C = 1000, ϵ = 0.10 and γ (for RBF kernel) =1 in SVR prediction. Similarly, for KRR, the best hyper parameters for I-V characteristics are alpha (α) = 0.001 and gamma (γ) = 1.0, using RBF kernel, and similarly for P-V, alpha (α) = 0.1 and gamma (γ) = 100.0, using a polynomial kernel.

The GaAs efficiency is 20.52 % at 25 ^{0}C, 21.23 % at 15 ^{0}C, and 24.97 % at -18 ^{0}C, and the mono-crystalline Si has 19.32 % efficiency at 25 ^{0}C, 20.11 % at 15 ^{0}C, and 20.92 % at -18 ^{0}C both using PR and KRR ML algorithms. From this, it can be observed that GaAs provides higher efficiency at all levels of temperatures through modeling and prediction. In materials point of view, GaAs is capable of providing higher efficiency (28.57 % at -45 ^{0}C) under different environmental conditions. With temperature variations, GaAs and Si materials are capable of higher efficiency with the decrease in temperature from +51 ^{0}C to -45 ^{0}C via modeling. With ML techniques, the PR is capable of predicting the data with less data provision by eliminating over/under fit of data, but the degree of polynomial is not fixed, and KRR is capable of predicting (92.23 %) the data at different intervals of temperatures for different materials with higher data input for training and testing.

Implementing SSPV with Si and GaAs materials is done both mathematical and Multiphysics modeling and the performance characteristics are obtained as shown in section 3.5.6. The KRR and SVR ML algorithms are implemented for SSPV till 0.5 cm and validated at 0.3 cm of water depth which gave better efficiency. The GaAs is giving better efficiency compared to Si at different depths of water and KRR is giving more efficiency at both current and power prediction when compared to SVR.

CHAPTER 4

EFFICIENT ENERGY STORAGE SYSTEM (EESS) WITH FAST CHARGING OF LI-ION BATTERY (LIB) AND SLOW DISCHARGING OF SUPER CAPACITOR (SC)

4.1 Introduction

The captured energy from the RER like PV or SSPV must be stored efficiently to meet the energy demand. The demand for energy varies from day to day, from season to time. Moreover, between day and night there is a major difference in the peak to valley [71]. Therefore, the generated power needs to be stored and vacant energy is provided during peak loads by peak shaving and load leveling [72]. Utilities are shifted to utilize RER to meet the rapidly increasing load demand. However, due to intermittent nature of these RER, the grid may experience instability and power quality issues [73] like harmonic distortion, phase unbalance and voltage drop. This significant increases in demand for RER, as well as the intermittent nature of renewable energy resources, have promoted and necessitated the development of electrical energy storage systems [74], [75]. The energy storage systems like batteries and SC can effectively store renewable energy generated [76], [77] to deliver the energy to load demand during peak leveling. The most commonly used energy storage technologies are lithium-ion (Li-ion) and lead-acid battery storage systems.

Compared to lead-acid battery technology, LIBs have the advantages of high energy and power density, less maintenance requirements, and more cycles number [190]–[192]. LIBs require higher charging time because of their variable power and energy densities. There are several battery alternatives available, one of which is the SC. The SCs are large capacitance special capacitors that combine the properties of batteries and capacitors into a single device. SC has significantly evolved in recent years and has demonstrated the potential to provide advances in energy storage systems [193], [194]. The charging time of a SC is much shorter than that of a conventional battery or capacitor, and it can discharge like a regular battery. These are lightweight and environmentally friendly in comparison.

The LIB and SC are widely used in applications of small electronic devices to Electric Vehicles (EV). The performance and capability of energy storage elements changes depending upon the different applications. When using a storage element in EV

applications, durability, long life, fast charging and slow discharging are preferred [195], [196] . LIBs are good choice for the energy storage solution for EV due to the parameters like high energy ($\approx$705 Wh/L) and power density ($\approx$10,000 W/L), longer cycle life, low self-discharge, fast charging, high capacity and efficiency when compared to lead acid battery [197]–[200]. Among all the above factors against the widespread adoption of EVs, the long charging time is relatively one of the most difficult parameters for consumers. Achieving fast charge of LIB [201], [202] has been deemed as one of the most important directions for the progression of EVs in the field of battery technology. The electrical model [203], lumped thermal model [204], and electro-chemical models [205] of LIB are designed and characteristics of LIB are provided in different conditions.

The available fast charging strategies, which determine how the current density is varied during the charging process, are an important category of such solutions. An off-board fast charging is cable to recharge a battery completely in less than 1 hour [206] through fast charger with charging at different levels. The rapid power refueling is extensively approved, though the fast-charging high-power load is a challenge to grid. The distribution transformer losses, harmonic distortion, and increasing demand voltage deviations caused by fast charging are analyzed in [207]–[210]. The power electronics technologies such as harmonic elimination, active correction of power factor, and the problems of the load non-linearity can be decreased to quench the grid [211]. However, the modification of power electronic charging topology does not have any effect on the fast charging with the increase in active power demand.

While performing power-flow analysis, voltage sag and swell occurs even when a 2 MW charging load with 0.99 power factor fed into the grid [212]. This sag and swell exist because of a large number of fast chargers that are installed at the grid. The impact on voltage and frequency stability by fast charging causes limitations in the capacity of grid while connecting it to fast charger. To eliminate this impact without interrupting the fast chargers, load compensation is done by an energy storage system such as flywheel as presented by Mauri et.al, in 2020 [209]and Dragicevic in 2014 [213]. However, application of this flywheel-storage system in practice is limited due to its low energy density. This limitation of flywheel system is overcome by the introduction of hybrid energy storage systems [214]. These hybrid energy storage systems having battery and SCs, performance was limited due the allocation of variable power to load.

Wang et al. in 2015 [215] modified this system to effectively allocate power between two units of hybrid storage system by the fuzzy logic control strategy. However, the output characteristics of the energy storage system and fast charging technology are not considered. In order to overcome the variable power distribution, voltage and frequency instability, fast charging of LIB with SC is the need of the hour. On the other hand, due to its initial high-cost necessity of RER, there is an argument on the extensive and efficient utilization of LIBs and SCs. So, the techno-economic analysis and characteristics of LIB and SC are investigated for finding economically feasible fast charging technology [88]– [91]. Hence, in this chapter, FCLIB is designed with the best identified characteristics such as life cycles, charge/discharge time, internal resistance and power/energy densities of both LIB and SC forming as an EESS. In the current research, six different power electronic circuit topologies for fast charging are designed with the inter connection of both LIB and SCs. Among these six, the best topology of extreme fast FCLIB is identified and analyzed with optimum CoE estimation for 80 % as well as 100 % of SOC.

4.2 Basics of Energy Storage System (ESS)

A battery is a grouping of cells with the management energy system. Even a tiny battery is capable of managing the energy as per the utility system. Depending on the tolerance levels, the capability of every battery varies. Batteries are made up of two electrodes (positive & negative) with an electrolyte as separator between and converts chemical energy into electrical energy. Depending on the conversion capability, batteries are divided into two types. They are,

1) **Primary batteries** (not rechargeable): Converts chemical energy into electrical energy only. Once the energy of the battery completes, the battery cannot be utilized again because of non-conversion probability from electrical energy to chemical energy.

2) **Secondary batteries** (rechargeable): Converts chemical energy into electrical energy and vice versa. These batteries can be utilized again and again depending on the life cycle. After completion of life cycles, these batteries give degraded performance.

Before the introduction of Lithium batteries, Lead acid batteries are mostly preferred with rechargeable capability because of the material availability. After EV implementation, LIBs are coming into usage with varied range of storage applications mainly because of its high specific energy, excessive power density and flat discharge

profile compared to lead acid battery. The energy restored into the LIB by forcing electric current into the battery, called as recharging of battery.

4.3 Design of LIB

The design of LIB includes three sections namely, mathematical, Multiphysics and temperature modeling.

4.3.1 Mathematical Modeling of LIB

A precise battery model is the first step in the development to build and parameterize an equivalent circuit that reflects the battery behavior. The modeled LIB is combination of cells and used to find the different charging and discharging conditions of LIB. Figure 4.1. shows, the mathematical design of LIB having input parameters as nominal voltage, rated capacity in Ah, initial state of charge and response time of the battery. By giving the input parameters, the modeled LIB determines its cutoff voltage, maximum capacity and nominal discharge current.
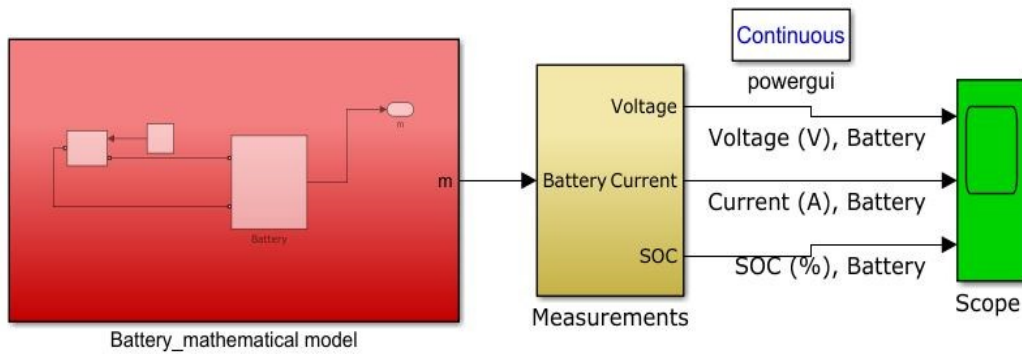
Figure 4.1 Mathematical design of LIB

For designing Figure 4.1, the mathematical analysis [216] is followed from equation (4.1) to equation (4.10) by the equivalent circuit as shown in Figure 4.2.
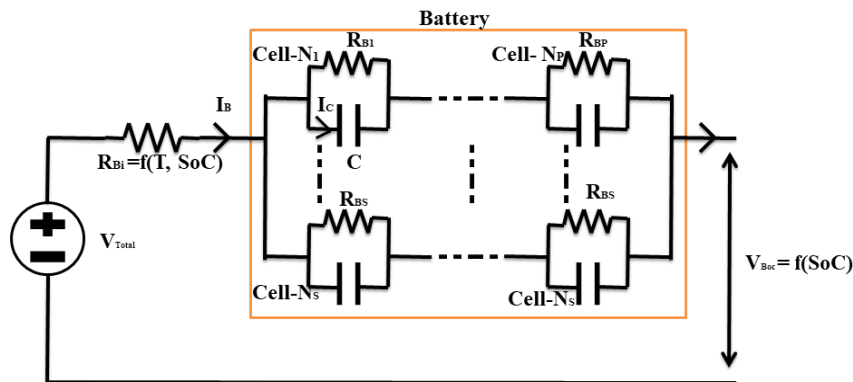
Figure 4.2 Equivalent circuit of battery

The open circuit voltage of battery (V_{Boc}) is given by,

$$V_{Boc} = f(SoC) \qquad\qquad \textbf{4.1}$$

where, *f(SoC)* is a function of state of charge and the internal resistance of battery (R_{Bi}) is represented as,

$$R_{Bi} = f(T, SoC) \qquad\qquad \textbf{4.2}$$

where, T represents temperature of battery. The total calculated voltage (V_{Total}) of battery is given below in eqn (4.3),

$$V_{Total} = V_{Boc} + I_B R_{Bi} \qquad\qquad \textbf{4.3}$$

where, R_{Bi} is the internal battery resistance and I_B is the battery current, which is represented as,

$$I_B = \frac{I_C}{N_p} \qquad\qquad \textbf{4.4}$$

Here, I_c is current through the capacitor and N_p is the number of cells in parallel. The combined battery voltage output (V_{Bout}) is given by,

$$V_{Bout} = \begin{cases} N_s V_{Total}, & unfiltered \\ \frac{V_{Bout}}{\tau s + 1}, & filtered \end{cases} \qquad\qquad \textbf{4.5}$$

Where, N_s is number of cells in series and C_B is capacity of battery, and τ is the transfer function variable

Battery State of Charge (SoC) is calculated using equation (4.6)

$$SoC = \frac{1}{C_B} \int_0^t I_B \, dt \qquad\qquad \textbf{4.6}$$

In equation (4.6), C_B is capacity of battery.

Energy of battery, $E_B = \int_0^t P_B \, dt$ \qquad\qquad **4.7**

Battery power, $P_B = V_{Bout} I_B$ \qquad\qquad **4.8**

Total power loss in battery, $P_{Bl} = -N_p N_s I_B^2 R_{Bi}$ \qquad\qquad **4.9**

The entire power stored, $P_{Bs} = P_B + P_{Bl}$ \qquad\qquad **4.10**

4.3.2 Multiphysics Modeling of LIB

A battery has three essential components- the positive electrode, negative electrode and an electrolyte. In addition to that, there is a micro porous polymer separator, that prevents the short circuit of the battery, by separating the electrodes.
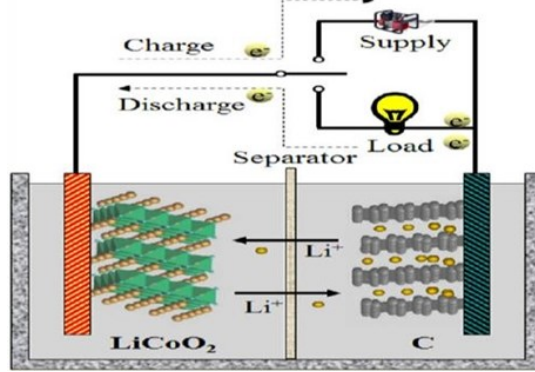
Figure 4.3 Working principle of a Li-Ion Battery (LIB)[5]

Figure 4.3 describes the cell chemistry of a battery. During charging, lithium ions move from cathode to anode internally (via the polymer electrolyte and separator), electrons move from cathode to anode externally. During discharging, lithium ions move from anode to cathode internally, whereas the electrons move in the same direction, but externally. The discussion for this section involves two parts - (a) The description of the materials for the 2D model, and (b) The description of the 3D model.

4.3.2.1 Two-Dimensional (2D) Model

A planar cross-section of the battery cell shown in Figure 4.4 was modeled. This geometry is not that of a realistic battery, it was chosen for easy representation of the electrochemistry of a battery. The porous positive electrode material was varied to obtain the cell discharge characteristic, and hence find which of the materials performs best.

The negative electrode used was Lithium metal and the electrolyte was Lithium hexafluoro Phosphate (LiPF_6) in 1:2 Ethylene Carbonate: Dimethyl Carbonate (EC: DMC) and p(VdF-HFP) solution. The positive electrodes used were $LiMn_2O_4\ Spinel$(LMO), $LiFePO_4$ (LFP), $LiCoO_2$(LCO) and $LiNi_{0.8}Co_{0.15}Al_{0.05}O_2$(NCA). Although the negative electrode Lithium, has some dimension, it has been modeled as a surface. This approximation is valid because Lithium has a high conductivity, and only the reactions at

[5]C. S. Durganjali, H. Raghavan, and S. Radhika, "Modelling and Performance Analysis of Different Types of Li-Ion Battery," in *Volume 8: Energy*, Nov. 2020, vol. 8, pp. 2–8. doi: 10.1115/IMECE2020-24404

the surface in contact with the electrolyte will matter. This approximation is not valid in the case of any other electrode.

a)   b)
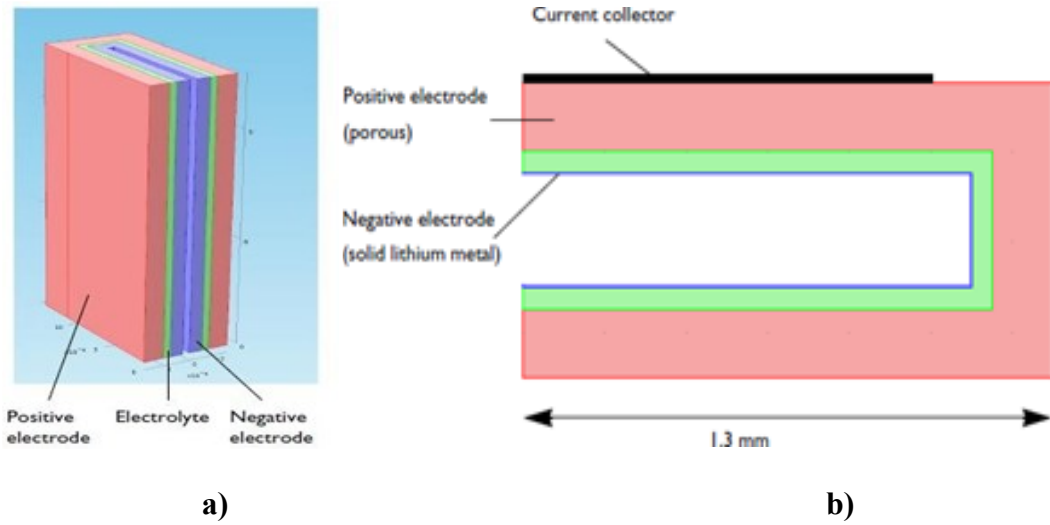
Figure 4.4 a) 3-D Li-Ion geometry b) 2D cross-sectional model geometry with the thickness of the negative lithium metal electrode neglected

The exact dimensions of each component are as shown in Figure 4.5. The study was set as "Time Dependent with Initialization" and the mesh used was a normal mesh. The parameters studied were State of Charge (SoC), Depth of Discharge (DoD) and the cell voltage. It should be noted that the SoC and DoD are complementary terms, which represent the level of charge in the cell relative to its capacity.

$$DoD = 1 - SoC \qquad \qquad \textbf{4.11}$$
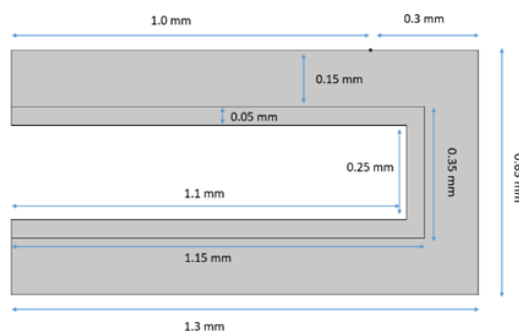
Figure 4.5 Dimensions of the cell as taken in the model

SoC can be defined in multiple ways, in this chapter it is defined as the ratio of the concentration of lithium ions, as in equation (4.11).

$$SoC = \frac{c_{s,Li}^{surf}}{c_{s,Li}^{max}} \qquad \qquad \textbf{4.12}$$

In the below sub-sections, we list the variables, constants and equations solved at the electrodes and the electrolyte. The list of variables and constants used while solving electrolyte region are listed in Table 4.1.

4.3.2.1.1 Electrolyte

The equations solved for the electrolyte phase assuming current distribution initialization are (subscript l represents the solution phase) given from equation (4.13) to (4.16)

$$\nabla. N_l = R_l \tag{4.13}$$

$$\nabla. i_l = Q_l \tag{4.14}$$

The equations solved assuming time dependent initialization are

$$\frac{\partial c_l}{\partial t} + \nabla. N_l = R_l \tag{4.15}$$

$$\nabla. i_l = Q_l \tag{4.16}$$

Where, $N_l = -D_l \nabla c_l + \frac{i_l t_+}{F}$ and the current density insolution phase i_l is given as,

$$i_l = -\sigma_l \nabla \phi_l + \frac{2\sigma_l RT}{F} \left(1 + \frac{\partial lnf}{\partial lnc_l}\right)(1 - t_+)\nabla lnc_l$$

Table 4.1 Variables and constants in equations solved at the electrolyte region

Symbol	Parameter	Value	Unit
D	Diffusion Coefficient	7.5×10^{-11}	m/s^2
t_+	Transport Number	0.363	1
$\left(\frac{\partial lnf}{\partial lnc_l}\right)$	Activity dependence	0	1
$c_{l,ref}$	Salt concentration reference value	1000	mol/m^3
ϕ	Electrolyte potential (initialized to zero throughout)	-	V
σ	Ionic conductivity	-	S/m

4.3.2.1.2 Negative Electrode (Li)

With the equilibrium potential and its temperature derivative set to zero, and the electrode kinetics defined as in the table below, the equations (4.17) and (4.18) are solved for the cathode called as negative electrode.

$$n.i_l = i_{total} \qquad\qquad \textbf{4.17}$$

$$n.N_l = -\sum_m \frac{\gamma_{Li+,m} i_{loc,m}}{F} - \frac{\gamma_{Li+} i_{dl}}{n_m F} \qquad\qquad \textbf{4.18}$$

Where $i_{total} = \sum_m i_{loc,m} + i_{dl}$,

$$i_{loc} = i_0 \left(exp\left(\frac{\alpha_a F \eta}{RT}\right) - exp\left(-\frac{\alpha_c F \eta}{RT}\right) \right), \; and \; i_0 = F(k_a)^{\alpha_c}(k_c)^{\alpha_a} \left(\frac{c_l}{c_{l,ref}}\right)^{\alpha_a}$$

The list of variables and constants used while solving negative electrode are listed in Table 4.2.

Table 4.2 Variables and constants in equations solved at negative electrode

Symbol	Parameter	Value	Unit
α_a	Anodic transfer coefficient	0.5	1
α_c	Cathodic transfer coefficient	0.5	1
k_a	Anodic rate constant	10^{-3}	m/s
k_c	Cathodic rate constant	10^{-3}	m/s
n	Number of participating electrons	1	1
γ_{Li+}	Stoichiometric coefficient	-1	1
η	Electrode potential ($\phi_{\text{solid matrix}} - \phi_{\text{solution phase}}$)	-	V
i_0	Exchange current density	-	A/m^2

4.3.2.1.3 Positive Electrode

For the positive electrode, a porous electrode setting was used with the following initializations. The subscript l denotes the electrolyte property and the subscript s denotes the electrode property. The list of variables and constants used while solving positive electrode are listed in Table 4.3.

Table 4.3 Variables and constants in equations solved at positive electrode

Symbol	Parameter	Value	Unit
α_a	Anodic transfer coefficient	0.5	1
α_c	Cathodic transfer coefficient	0.5	1
k_a	Anodic rate constant	2×10^{-11}	m/s
k_c	Cathodic rate constant	2×10^{-11}	m/s

The equations solved for electrode kinetics are the same as in section 4.3.2.1.2. In addition to that, the following equations (4.19) to (4.23) are also solved (assuming current distribution initialization):

$$\nabla . N_l = R_l \tag{4.19}$$

Where $R_l = -\sum_m \frac{\gamma_{Li+,m} i_{v,m}}{F} + R_{l,src}$ and $N_l = -D_{l,eff}\nabla c_l + \frac{i_l t_+}{F}$.

$$\nabla . i_l = i_{v,total} + Q_l \tag{4.20}$$

$$\nabla . i_s = -i_{v,total} + Q_s \tag{4.21}$$

Where $i_s = -\sigma_{s,eff}\nabla\phi_s$ and $i_l = -\sigma_{l,eff}\nabla\phi_l + \frac{2\sigma_{l,eff}RT}{F}\left(1 + \frac{\partial lnf}{\partial lnc_l}\right)(1 - t_+)\nabla lnc_l$.

Here, $D_{l,eff} = \epsilon_l^{1.5}D_l$, $\sigma_{l,eff} = \epsilon_l^{1.5}\sigma_l$ and $\sigma_{s,eff} = \epsilon_s^{1.5}\sigma_s$.

The only difference when time dependence is assumed, that Equation (4.19) becomes

$$\frac{\partial \epsilon_l c_l}{\partial t} + \nabla . N_l = R_l \tag{4.22}$$

Where R_l now is defined as

$$R_l = -\sum_m \frac{\gamma_{Li+,m} i_{v,m}}{F} - \frac{\gamma_{Li+} i_{v,dl}}{n_m F} + R_{l,src} \tag{4.23}$$

The values of the constants used for the different electrodes are listed in the Table 4.4.

Table 4.4 Values of constants used in equations- for different electrode materials

Property	LMO	LCO	LFP	NCA	LNO
Diffusion coefficient (D_s) (10^{-13} m²/s)	0.1	5	3.2	0.0015	100
Electrical conductivity (σ_s)(S/m)	3.8	0.113	91	91	100
Density (ρ) (kg/m³)	4140	4678	3600	4740	4100
SoC, max	0.995	1	0.99	0.98	1
SoC, min	0.175	0.43	0.01	0.23	0.45

4.3.2.2 *Three dimensional (3-D) model*

LIB can be analyzed with the depth analysis, using multiphysics model to study its behavior with different temperature conditions. The multiphysics model is designed by coupling the battery chemistry modeled in one dimensional (1D) as shown in Figure 4.6,

with the geometry and thermal effects modeled in 3 dimensional (3D) as shown in Figure 4.7. The 1D model was defined by taking the ideas presented in [217] into consideration.
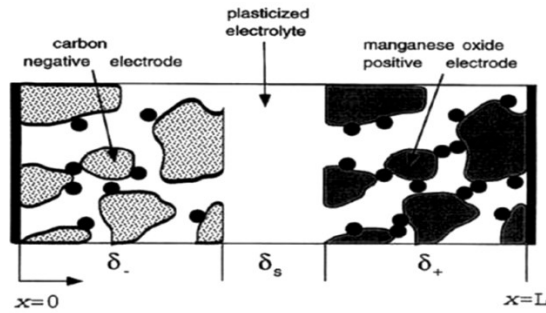
Figure 4.6 Battery chemistry with geometry parameters of LIB-1D model
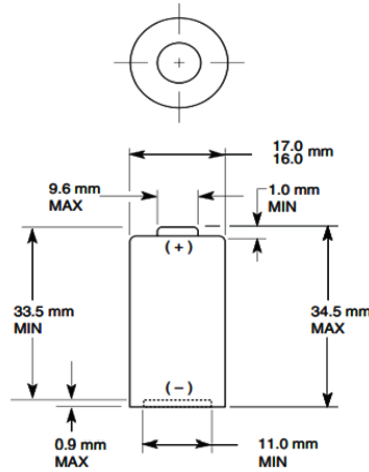
Figure 4.7 Geometry of LIB-Data sheet [218]

The length of the positive electrode (δ_+), the length of the negative electrode (δ_-) and the length of the electrolyte section (δ_s) were considered 183 μm, 100 μm, and 52 μm respectively from Figure 4.6. The parameters required to model a cell mathematically is given as 3 types:

1. Design adjustable parameters (like the electrode thickness, volume fraction, particle size, separator thickness, salt concentration and initial cell temperature),
2. Transport parameters (includes conductivity, diffusion coefficients and transport parameters)
3. Thermodynamic and Kinetic data (includes exchange current density and Open Circuit Voltage)

The maximum voltage capacity is given by open circuit voltage of the cell, and it depends heavily on the initial SoC values of the electrodes. Figure 4.8 shows the Multiphysics model of the LIB by coupling Figure 4.6 and Figure 4.7. The Li-ion cell dimensions were considered matching with the Duracell 3.2 V Lithium battery in the datasheet [218]. The positive electrode and negative electrodes are designed with Li-ion composition [219]. The electrolyte was Lithium hexafluoro Phosphate ($LiPF_6$) with 1:2 Ethylene Carbonate: Dimethyl Carbonate (EC: DMC) solution. The 3D and 1D model were coupled by the generated heat source and the average temperature. The initial cell temperature was taken as 298.15 K for the positive and negative electrode, respectively. These small batteries can be connected in series and parallel connections as shown in Figure 4.9, to make a larger capacity battery also called as battery pack.
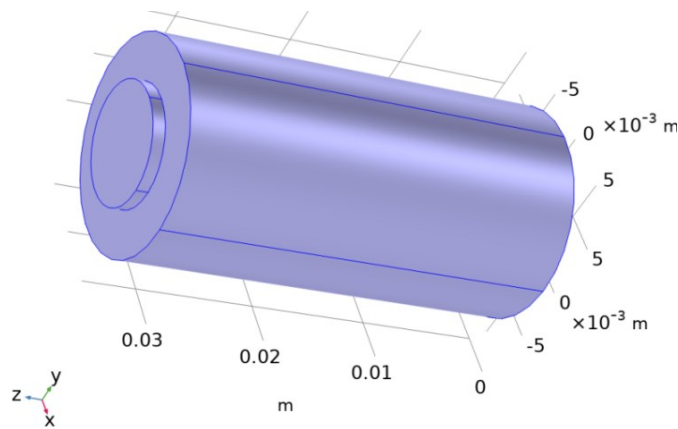
Figure 4.8 Geometry selection of LIB-3D model[6]
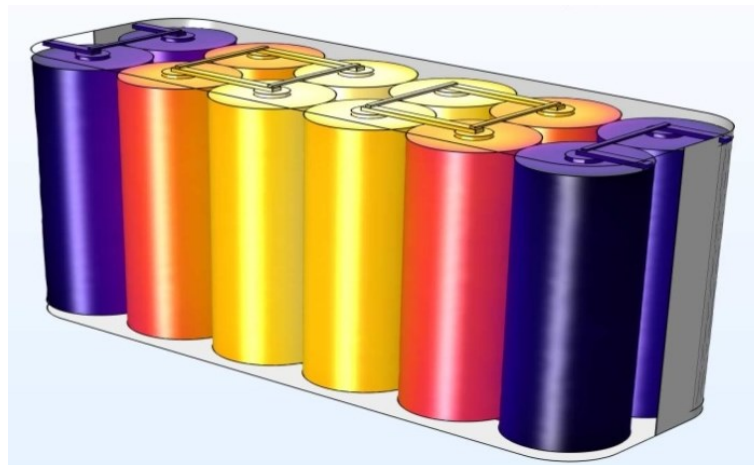
Figure 4.9 Lithium Battery pack design

[6]C. S. Durganjali, V. Chawla, H. Raghavan, and S. Radhika, "Design, development, and techno-economic analysis of extreme fast charging topologies using Super Capacitor and Li-Ion Battery combinations," *J. Energy Storage*, vol. 56, p. 106140, Dec. 2022, https://doi.org/10.1016/j.est.2022.106140.

4.3.3 Thermal Management of LIB

As the rate of discharge (C-rate) of battery increases, the heat on the battery shell increases. To maintain the stability of the battery, thermal management is required, which is designed as shown in Figure 4.10.
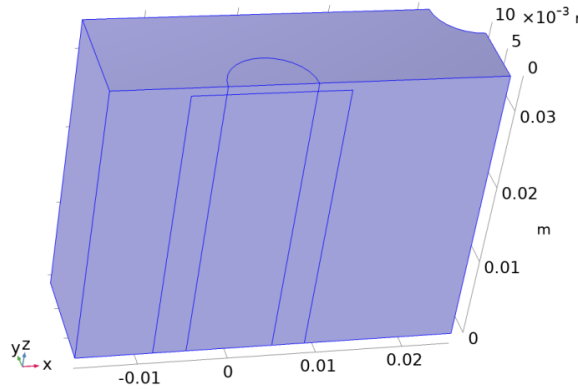
Figure 4.10 Thermal management of LIB

For a LIB having 3.3 V nominal voltage and 2.3 Ah rated capacity at 100 % SoC input parameters, the fully charged voltage becomes 3.84 V, maximum capacity as 2.3 Ah and the cut-off voltage becomes 3.475 V at 1 C-rate. The SoC characteristics with voltage and current waveform at 1 C- rate is as shown in Figure 4.11. Where the battery discharged to 77 % and battery voltage decreased from 3.84 V to 3.52 V in 1000 seconds. The discharge is at 1 C-rate so the maximum 2 A current is drawn constantly.
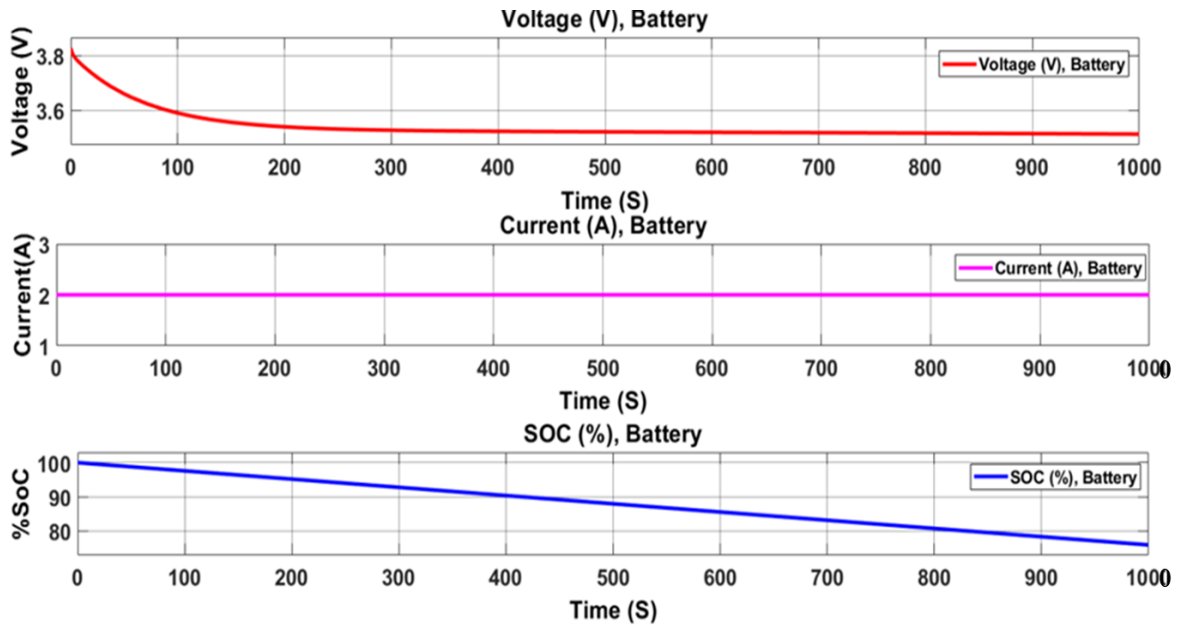
Figure 4.11 Discharge characteristics of LIB at 1C rate

The two main disadvantages of using just a battery for energy storage are

a. Low power densities – Batteries have excellent energy densities and are excellent for storing energy. However, due to their low power density, enough power cannot be provided to the load during peak hours and hence the model does not work properly.

b. Low charging rate – Batteries require much time to get completely charged and hence using them is not feasible where time is a constraint.

To overcome these issues and limitations [220], LIBs along with SCs can be used. A SC can store million times more charge than an ordinary capacitor. Being a capacitor, it provides a high energy density compared to the LIBs. This energy can be provided quickly to the load in case of peak power demand with the SCs full charge capacity in few seconds.

4.4   Design of SC

A SC like a capacitor is used to store extremely large amounts of electrical charge. It differs from an ordinary capacitor in two important ways:

a. Double-layer capacitance (is electrostatic in origin) and

b. Pseudo capacitance (electrochemical)

It can be inferred that SC combine the working of normal capacitors with that of an ordinary battery. They exhibit high power density and low energy density. SCs usage is ideal when a quick charge is required, whereas batteries are used to provide long-term energy. The combination of the two technologies into a hybrid will ideally satisfy both purposes and reduce battery stress, for a longer service life. Rapid charging for regenerative braking and high current for acceleration are ideal for hybrid vehicle applications. Broad temperature range and longer shelf life offer an advantage over the battery.

4.4.1   Mathematical Modeling of SC

The SC is modeled with mathematical equations as shown below from equation (4.24) to equation (4.28) from equivalent circuit model as shown in Figure 4.12.
The equations are as follows,
The total electric charge of SC (Q_{ScT}) is given by equation (4.24),

$$Q_{ScT} = \int_0^t i_{Sc} \, dt \qquad\qquad\qquad \textbf{4.24}$$
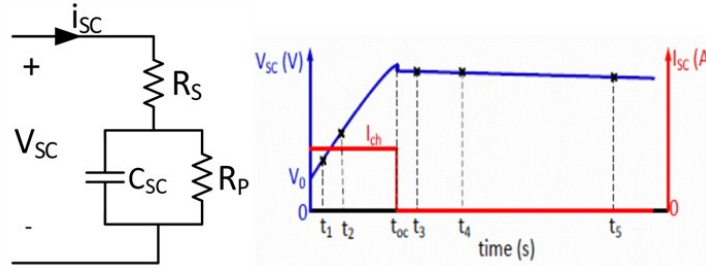
Figure 4.12 SC equivalent circuit with self-discharge characteristics

When self-discharge of SC ($i_{self\_discharge}$) is considered as given in equation (4.25),

$$Q_{ScT} = \int_0^t i_{self\_discharge} \, dt \qquad\qquad 4.25$$

where,

$$i_{self\_discharge} = \begin{cases} \dfrac{C_T \alpha_1}{1 + sR_{Sc}C_T}, & time\ before\ opencircuit \\[2mm] \dfrac{C_T \alpha_2}{1 + sR_{Sc}C_T}, & time\ during\ opencircuit \\[2mm] \dfrac{C_T \alpha_3}{1 + sR_{Sc}C_T}, & time\ after\ opencircuit \end{cases} \qquad 4.26$$

now the total SC voltage (V_{ScT}) is given as,

$$V_{ScT} = \frac{N_s Q_{ScT} d}{N_p N_e \varepsilon \varepsilon_0 A_i} + \frac{2N_e N_s GT}{F_C} \sinh^{-1}\left(\frac{Q_{ScT}}{N_p N_e^2 A_i \sqrt{8GT\varepsilon\varepsilon_0 C}}\right) - R_{int} i_{Sc} \qquad 4.27$$

where,

A_i is Interfacial area between electrodes and electrolyte (m^2), F_C is Faraday constant, C is Molar concentration (mol/m^3) equal to $C = 1/(8N_A r^3)$, r is molecular radius (m), N_A is Avogadro constant, i_{Sc} SC current (A), R_{int} is total internal resistance (ohms), N_e is number of electrode layers, d is the molecular radius, Q_{ScT} is the total SC charge, T is operating temperature (K), ε is permittivity of material, ε_0 is permittivity of free space, G is ideal gas constant, C_T is total capacitance (F), N_p is number of parallel supercapacitors and N_s is number of supercapacitors in series.

SCs are placed between batteries and capacitors in the taxonomy of electronic components [193]. A single SC stores a lot more energy than a capacitor of a conventional design, with a solid dielectric. Other advantages of SCs are instantaneous turn on, take significantly less time to charge and require reasonably simple charging circuits. When they can store enough energy required for the application of the system, they prove to be an

attractive choice for designing energy storage systems. However, LIBs have more storage capacity compared to SCs. The SC is mathematically modeled from above equation (4.24) to (4.28) and is as shown in Figure 4.13.
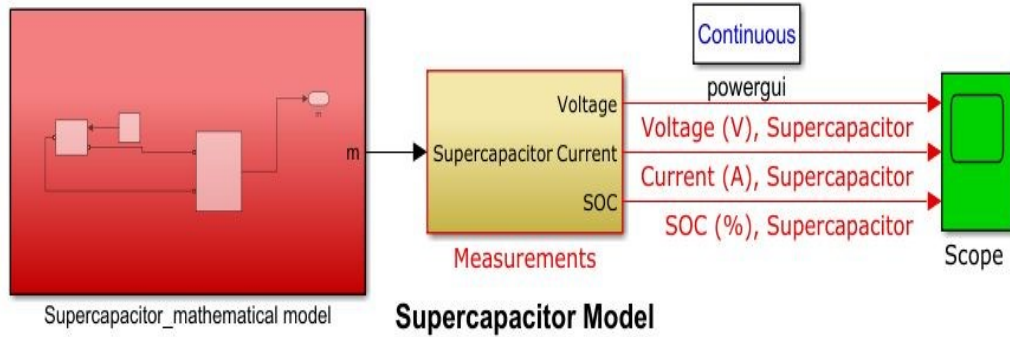
Figure 4.13 Mathematical design of SC

The state of charge of SC is given by,

$$SoC = \frac{Q_{initial} - \int_0^t i(t)dt}{Q_{ScT}} \times 100 \qquad\qquad 4.28$$

where, $Q_{initial}$ is the initial charge of SC.

4.4.2   Charge/ Discharge Characteristics of SC

The charge and discharge characteristics of SC are as shown in Figure 4.14 and Figure 4.15. Where the SC charges and discharges very fastly. The charge characteristics of the supercapacitor happens fastly to the current increment. In Figure 4.14, it can be observed that at high ampere rating (500A), the supercapacitor is charged very fastly and at less ampere rating (10A), the charge time for a supercapacitor is more than 550 seconds. From the charge characteristics, higher current rating makes fast charging of supercapacitor.
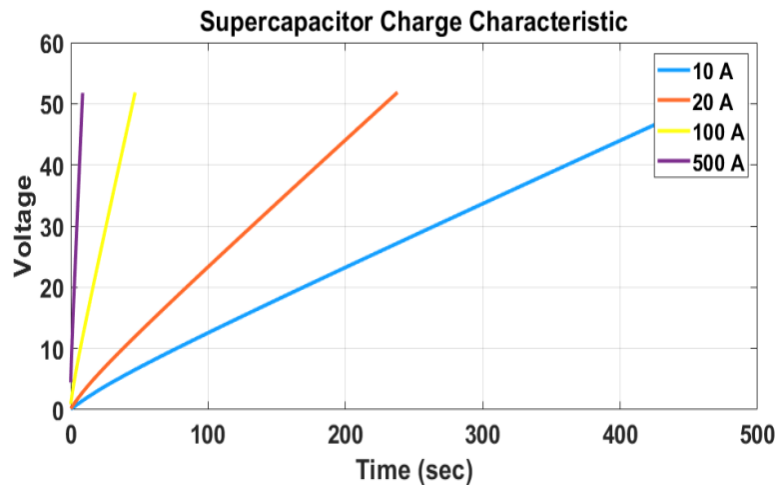
Figure 4.14 Charge characteristics of supercapacitor
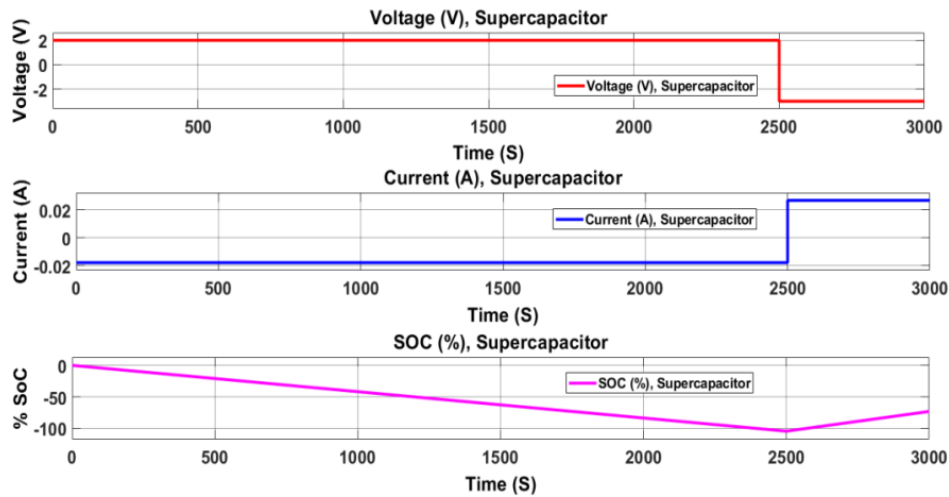
Figure 4.15 Super capacitor self-discharge characteristics (Voltage, Current and % SoC)

SC has faster charging and faster discharging capability. Where faster charging is considered as an advantage and faster discharging is considered as disadvantage of SC. The self-discharge is due to internal resistance of the SC. If the internal resistance of the SC increases, the self-discharge will be faster which is a disadvantage during non-working condition. The SC used for design is 11 V and its internal DC resistance is 8.9×10^{-3} ohm. The time for total self-discharge of SC is 2500 Seconds (41.67 minutes) as shown in Figure 4.12. At the time of full self-discharge, the voltage of the battery also reaches zero volts. During self-discharge, the SC current is constant and at full self-discharge, the current moves from -0.02 A suddenly and reaches to zero currents.

4.5 Comparison of Commercially Available Li-Ion Capacitor (LIC) with LIB, SC and FCLIB

The LIC is the combination of graphite pre-doped Li ion and activated carbon (AC) electrode with electrolyte as $LiPF_6$ [221], [222]. LIC works with anion and cation consuming reaction, which is unlike with FCLIB having rocking chair reaction. However, high voltage and efficient performance is possible at high temperature condition which is also possible in FCLIB. In general, at the negative graphite electrode, instead of high energy density achievement, an electrolyte decomposition occurs due to high working voltage, but a FCLIB has high energy density compared to LIC, LIB and SC. This electrolyte decomposition in LIC leads to high impedance interface eventually creating deterioration in the performance of power over longer cycles.

If a LIC with large capacity is considered, the Li+ pre-doping takes longer duration and require more research to protect Li+ decomposition during working condition. However, the LIC system has poor performance at low temperatures due to metal decomposition and at high voltage/current regenerative breaking which is eventually overcome by FCLIB system with fast charging capability. When coming to the cost, the LIC costs approximately $0.9/piece but the fast charge for LIC is not commercially available, and is still in research [223] which will increase its cost. This intern makes FCLIB with fast charging topology is more advantageous than LIC which is commercially available at both low and high temperature conditions with effective cost.

4.5.1 FCLIB Parameter Selection

There are various methodologies to charge both LIB and SC individually. Constant current/constant voltage (CC/CV) is the more commonly used and the preferred method [200]. In the CCCV algorithm, a constant current is given to charge the LIB/SC until its voltage moves up to a specified maximum voltage. When the LIB/SC reaches a target voltage, constant voltage loop becomes active, and the current is decreased. This process halts when the current comes down to a specified low current.

A LIB takes minutes - hours to charge depending on the rating of LIB and type of charging topology utilized. LIBs are at risk of being overcharged so full charge monitoring is required. A SC takes a few seconds - minutes to charge. The magnitude of the charging current greatly affected by the charger utilized. Almost the entire charging process is completed in a few seconds, with just the topping charge taking additional time. There is an inrush current which should be accounted for, taking the necessary precautions to restrict the same. SCs, unlike LIBs are not at risk of being overcharged and hence there is no requirement for full charge monitoring.

The time taken for SC to discharge till 50 % is around a month whereas LIBs take about 5 % per month. However, when it comes to the life cycle of a SC, it can undergo an infinite number of cycles of charging and discharging. Unlike LIBs, there is minimal depreciation in SCs with an exception of when they have an applied voltage greater than the allowed voltage. Under normal conditions, a SC fades from 100 % to 80 % capacity in 10 years. Applying higher voltages rather than the specified voltages, shortens the life and duration of discharge. When a SC is used to run an appliance, its voltage at terminals goes down. Converters are used to maintain a constant output voltage for the appliance for a sizable drop at terminals of the SC, for instance from 100 % to 50 % of the rated values.

A LIB maintains a steady voltage in most of its applications with little change. However, the terminal voltage of the SC decreases on a linear scale, reducing the usable power spectrum. As discussed above, an elective DC-DC converter assists to improve the energy at low voltage band, but this will be expensive and might result in energy losses as well. The self-discharge of a SC compared to an electrostatic capacitor and a battery is somewhere in between the two; due to the presence of the organic electrolyte. The characteristics of LIB, SC, and Lithium-Ion Capacitor (LIC) which are commercially available with FCLIB parameter selection is tabulated in Table 4.5. In later section, the comparison of LIC with FCLIB is given in terms of performance and cost.

Table 4.5 FCLIB parameter selection from LIB, SC and LIC

LIB characteristics	SC characteristics	LIC [221], [222]	FCLIB parameter selection
Charge-in minutes to hour	Charge- in seconds to minutes	Charge in minutes	Charge -in less minutes
Number of cycles <10,000	Number of cycles >50,000	Number of cycles decreases with increase in voltage	Increase in cycles
High energy density compared to SC	Low energy density compared to LIB	Instead of high energy density, electrolyte decomposition occurs	High energy density
Slow discharge	Fast discharge	Nominal discharge	Slow discharge
High storage capacity	Low storage capacity compared to LIB	High storage capacity	High storage capacity
Need additional storage system for fast charging	Need DC-DC converter for fast charging circuit	Need extra fast charging circuit	Efficient storage with fast charging
Resistor and Capacitor are connected in parallel circuit and series connection of different number of RCs is considered for equivalent model as shown in Fig.3.	Resistor and Capacitor are connected in series circuit and parallel connection of different number of RCs is considered for equivalent model as shown in Fig.10	graphite pre-doped Li ion and activated carbon (AC) electrode with electrolyte as $LiPF_6$ are used for LIC designing	Parallel connection of LIB and SC can consider for design development
Low internal resistance	High internal resistance	Nominal internal resistance which fails at negative temperatures totally	Variable resistance for fast charging

All these characteristics of LIB and SC lead to failures in the energy storage system when used alone. So, the combination of LIB and SC is preferred, with the useful characteristics of LIB like slow discharge at less power energy densities and the SC with fast charging capability to decrease the charging time of LIB.

4.6 Different Topologies for Fast Charging of LIB with Slow Discharging of SC

In this chapter, fast charging of LIB with direct SC is considered. The use of direct SC for FC should have higher energy density compared to the LIB [224]–[226]. The internal resistance of the SC should be minimum in order to deliver the energy to LIB. Here in this section, the parallel connection of SC with LIB having different energy densities and internal resistances are considered. The FCLIB is designed from the parameters selected from Table. 4.5 is as shown in Figure 4.16.

The SC and LIB are interconnected to form a renewable energy storage system. If, SC with less energy density and LIB with higher energy density considered, the SC will not be capable of charging the LIB. The 0 % SoC of LIB and 100 % SoC of SC is considered initially. So, both SC and LIB at equal energy storage or SC with high energy and lesser LIB energy can be used for FCLIB efficiently. The internal resistance of SC is a major parameter, which makes a difference in charging the LIB slowly or quickly [38], [40], [48].
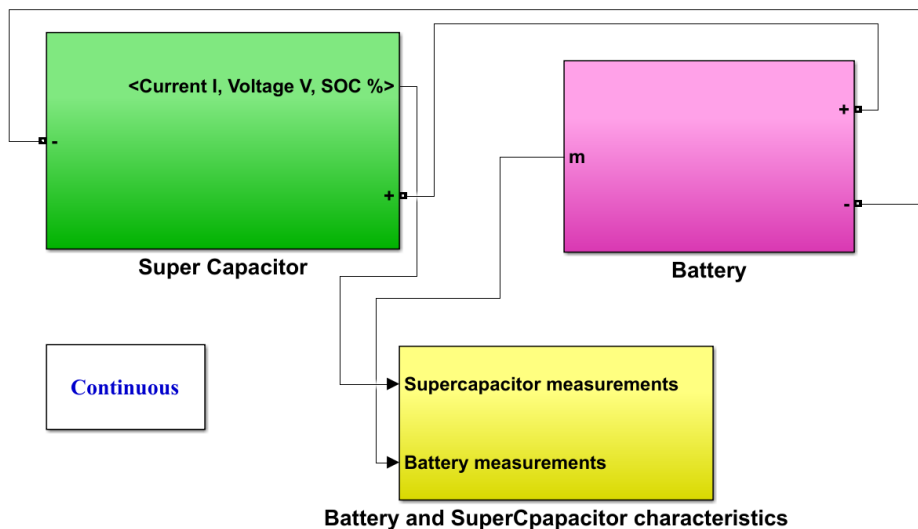
Figure 4.16 FCLIB design with parallel connection of LIB and SC

Six different topologies are explored for LIB charging with different SC internal resistances and energy densities. The six topologies are performed as shown in Figure 4.17.
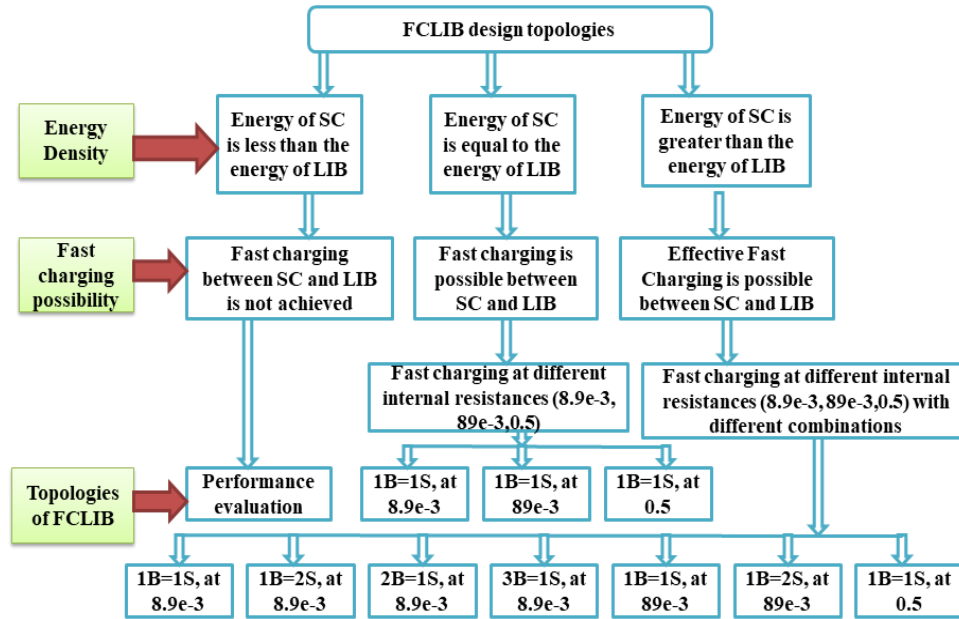
Figure 4.17 Flow chart of FCLIB with all combinations

Topologies in the list include:

1. The energy of SC is less than the energy of battery (1B parallel to 1S): This topology is designed with one LIB and one SC in parallel at SC less energy density compared to LIB as shown in Figure 4.16. Due to less energy state, LIB charging will be very slow by SC, so this topology is not specified for fast charging.

2. The energy of both the SC and the LIB is equal, (1B parallel to 1S, internal resistance at 8.9×10^{-3}, 89×10^{-3}, 0.5): One LIB in parallel to one SC is connected in parallel at different internal resistance and charge/discharge characteristics are analyzed for both storage systems similar to Figure 4.16. In this, the energy density of LIB and SC are equal, and SC is at 100%SoC and LIB is at 0% SoC. LIB starts charging from 0% to 100% and SC discharges from 100% to different levels depending on the internal resistance.

3. The energy of a SC is greater than the energy of a LIB (1S parallel to 1B, internal resistance at 8.9×10^{-3}, 89×10^{-3}, 0.5): In this topology, SC is at higher energy density compared to single LIB and the design is similar to Figure 4.16. Here, depending on the internal resistance, the fast charging of LIB can be achieved at different times. Less internal resistance takes more time to charge, compared to higher internal resistance. Similarly, higher internal resistance causes sudden peak voltages at starting and then stabilizes after some time.

4. Parallel connection of a higher energy SC to two LIBs (2B1S internal resistance at 8.9×10^{-3}): Two LIBs are connected in parallel to one SC at higher energy density of SC compared to single LIB as shown in Figure 4.18. The charging will be faster and leakage currents also decreases due to two LIBs acting as load for single SC. This topology takes more time to charge compared to topology 3.
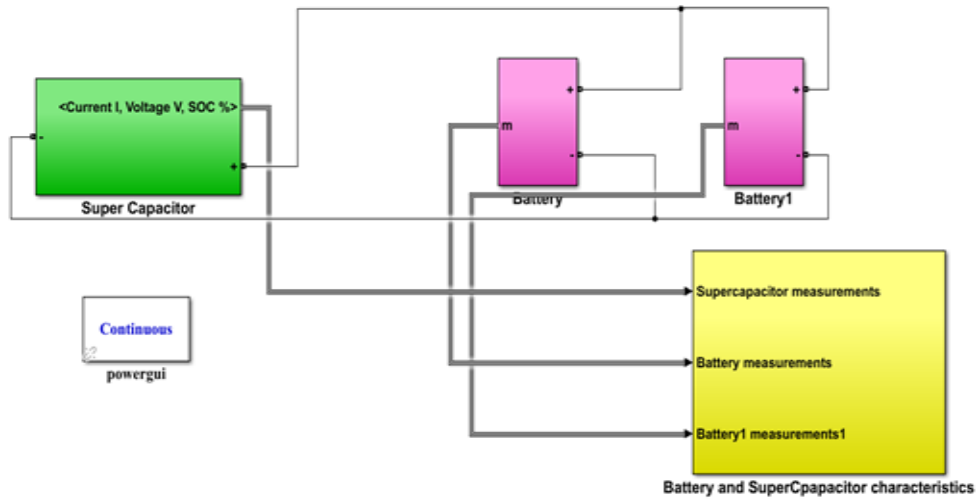
Figure 4.18 Model of 2B1S with internal resistance at 8.9×10^{-3}

5. Parallel connection of a higher energy SC to three LIBs (3B1S, internal resistance at 89×10^{-3}): In this topology, three LIBs are connected in parallel to one SC at 89×10^{-3} as internal resistance as shown in Figure 4.19. This internal resistance is considered as best internal resistance from topology 3. At this topology, the LIB and SC peak current and voltages decreases but time taken to charge three batteries is very high due to load sharing among them by SC.
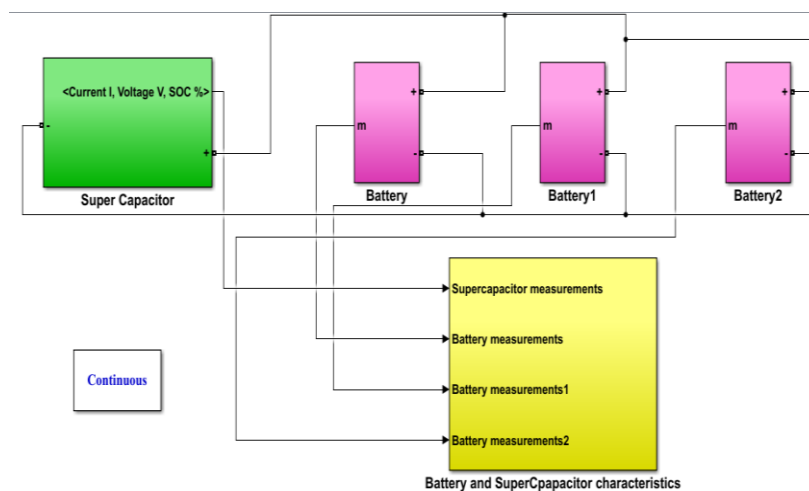
Figure 4.19 Model of 3B1S with internal resistance at 89×10^{-3}

6. Parallel connection of two SCs to a one battery (2S1B, internal resistance at 8.9*10^{-3}, 89*10^{-3}): This topology has two SC in parallel to one LIB at two levels of internal resistance as in Figure 4.20. The charge/discharge characteristics are analyzed for both SC and LIB.
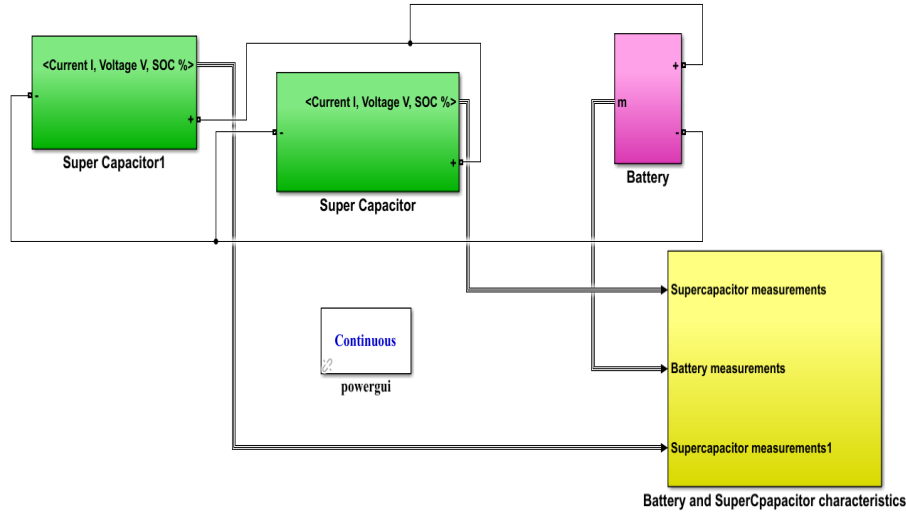
Figure 4.20 Model of 1B2S with internal resistance at 8.9*10^{-3} and 89×10^{-3}

4.7 Results and Discussion

4.7.1 2D Model with Material Variation

From the 2D model design the plots obtained for different positive electrodes in combination with lithium metal cathode $LiPF_6$ in $1:2$ $EC:DMC$ $(VdF-HFP)$ electrolyte, are attached in below Figures. The positive electrodes studied are $LiMn_2O_4$ $Spinel$ (LMO), $LiFePO_4$ (LFP), $LiCoO_2$ (LCO), $LiNi_{0.8}Co_{0.15}Al_{0.05}O_2$ (NCA) and $LiNiO_2$ (LNO). Here output SoC of porous electrode and electric potential at current collector surface for the LMO, LCO, LFP, NCA and LNO are presented in Figures 4.5 to 4.14. A comparison table for all the materials simulated is represented in Table 4.6.

a) $LiMn_2O_4Spinel$ (LMO)

Figure 4.21 a) and b) represents the electric potential and average SoC of Li-ion battery with positive electrode as LMO, negative electrode as Lithium, and electrolyte as $LiPF_6$. By joining the points of inverse slope of average SoC gives the plot of average DoD of porous electrode. From Figure 4.21 a), it can be observed that, the electrical potential of LMO is at 4.02 V at initial state and then decreased gradually to 3.7 V at 1-C rate and the average SoC increases linearly with time as shown in Figure 4.21 b).
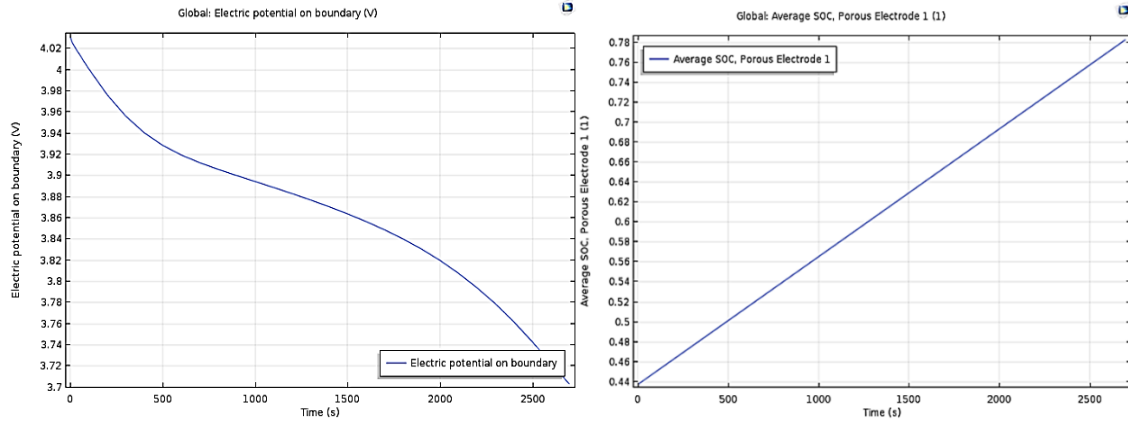
Figure 4.21 a) Cell Voltage Vs Time- LMO/Li b) Average Soc Variation with Time For LMO/Li

b) $LiCoO_2$ **(LCO)**

Now considering the positive electrode as LCO, Lithium metal as cathode and electrolyte as $LiPF_6$ the output plots are obtained and are shown in Figure 4.22 a) and b). The Figure 4.22 a) represents the electric potential at boundary of LCO and Figure 4.22 b) represents the average SoC of porous electrode.
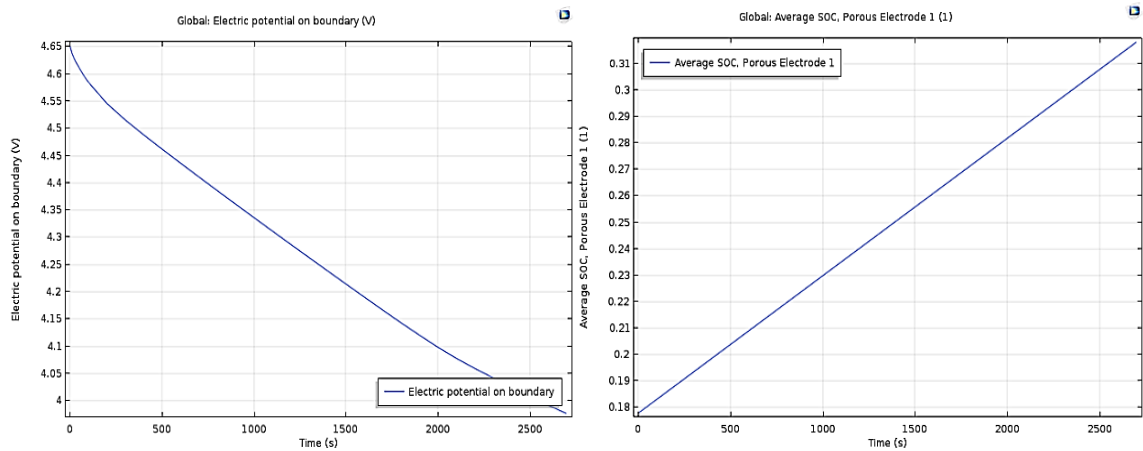
Figure 4.22 a) Cell Voltage Vs Time- LCO/Li b) Average Soc Variation with Time For LCO/Li

From Figure 4.22 a), it can be observed that, the electrical potential of LCO is at 4.65 V at initial state and then decreased gradually to 3.95 V at 1-C rate and the average SoC increases linearly with time as shown in Figure 4.22 b).

c) $LiFePO_4$ **(LFP)**

Now considering the positive electrode as LCO, Lithium metal as cathode and electrolyte as $LiPF_6$ the output plots are obtained and are shown in Figure 4.23 a) and b). The Figure 4.23 a) represents the electric potential at boundary of LNO and Figure 4.23

113

b) represents the average SoC of porous electrode. From Figure 4.22 a), it can be observed that, the electrical potential of LFP is at 3.37 V at initial state and then decreased gradually to 3.29 V at 1-C rate and the average SoC increases linearly with time as shown in Figure 4.23 b).
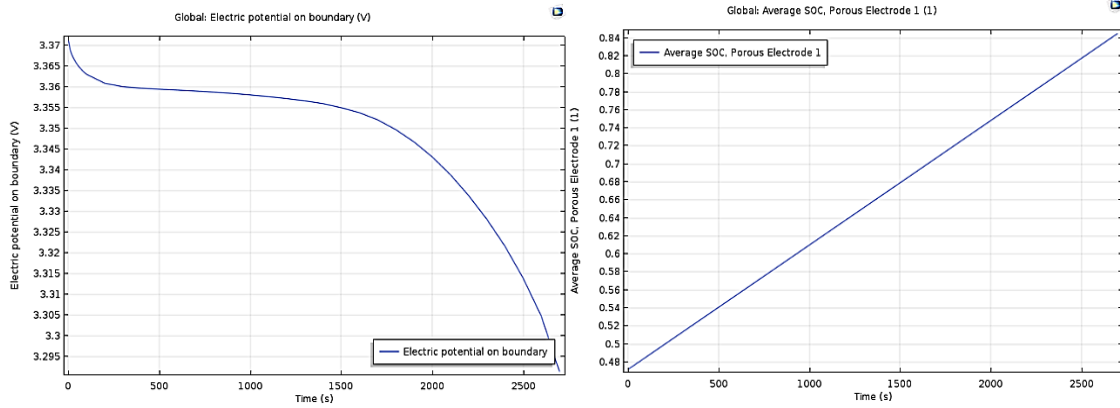
Figure 4.23 a) Cell Voltage Vs Time- LFP/Li b) Average Soc Variation with Time For LFP/Li

d) $LiNi_{0.8}Co_{0.15}Al_{0.05}O_2$ (NCA)

Now considering the positive electrode as NCA, Lithium metal as cathode and electrolyte as $LiPF_6$ the output plots are obtained and are shown in Figure 4.24 a) and b). The Figure 4.24 a) represents the electric potential at boundary of NCA and Figure 4.24 b) represents the average SoC of porous electrode.
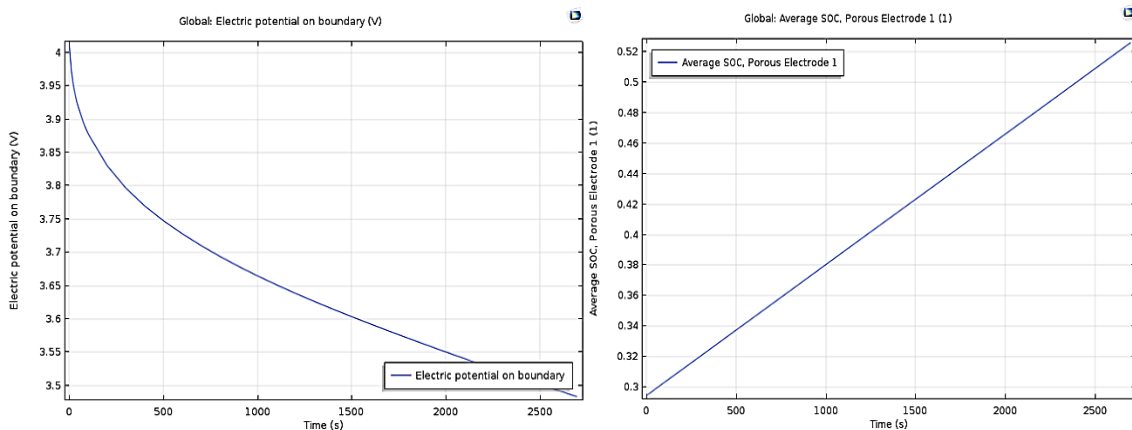
Figure 4.24 a) Cell Voltage Vs Time- NCA/Li b) Average Soc Variation with Time For NCA/Li

From Figure 4.24 a), it can be observed that, the electrical potential of NCA is at 4.02 V at initial state and then decreased gradually to 3.5 V at 1-C rate and the average SoC increases linearly with time as shown in Figure 4.24 b).

e) $LiNiO_2$ (LNO)

Now considering the positive electrode as LCO, Lithium metal as cathode and electrolyte as $LiPF_6$ the output plots are obtained and are shown in Figure 4.25 a) and b). The Figure 4.25 a) represents the electric potential at boundary of LNO and Figure 4.25 b) represents the average SoC of porous electrode.
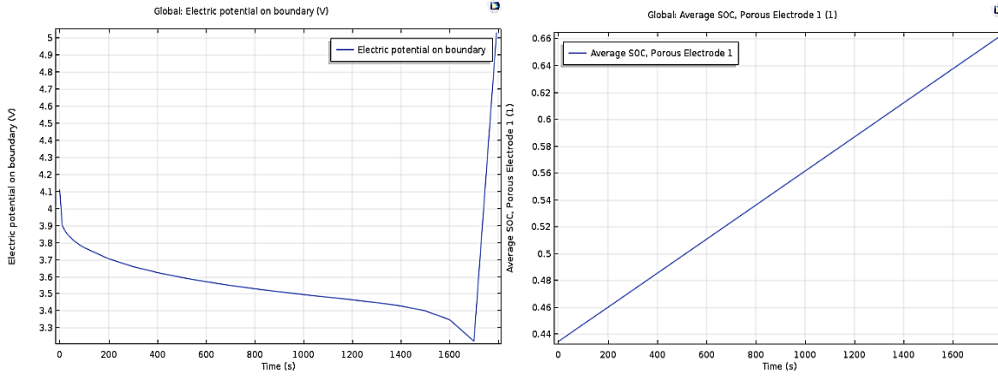
Figure 4.25 a) Cell Voltage Vs Time- LNO/Li b) Average Soc Variation with Time For LNO/Li

From Figure 4.25 a), it can be observed that, the electrical potential of LNO is at 4.1 V at initial state and then decreased gradually to 3.3 V and then suddenly rises to 5V because of the internal resistance variations at 1-C rate and the average SoC increases linearly with time as shown in Figure 4.25 b).

Table 4.6 Comparison of Different Positive Electrode Materials

Electrode Material	Maximum Battery Voltage (V)	Slope of SoC graph ($\times 10^{-5}$)	Inverse of Slope of SoC graph
LMO	4.0313	13.00	7692
LCO	4.6520	5.22	19157
LFP	3.3714	13.62	7342
NCA	4.0109	8.60	11628
LNO	4.1149	12.89	7752

Table 4.6 summarizes the data extracted from the graphs. We see that the value of the maximum cell voltage is between 3-4 V, in keeping with studies that validate this for lithium-ion batteries. The general trend for the cell voltage versus time curve was a decrease to 0 V within 2700 seconds. For the last case alone (LNO), a singularity error was encountered, hence the deviation from the general gradual decrease. This may be because of the choice of the average current density at the current collector boundary which was set at 1 A/m^2 for all the cases.

4.7.2   3D Model Output Characteristics

The 3D model as shown in Figure 4.8 is prepared with the geometry selection from Figure 4.6 and Figure 4.7 and considers the thermal effects due to adjacent batteries (Figure 4.10) in a hypothetical battery pack (Figure 4.9). The Figure 4.11 represents the discharge characteristics of LIB at only 1C-rate. By considering the thermal management with air as a medium the battery potential is increased to 3.67 V at 0.1C-rate. Similarly, at different C-rate the electric potential will vary. These variations in electric potential with different C-rates (0.1C, 1C, 2C, 4C) are as shown in Figure 4.26. As the C-rate of battery increases, the potential discharge of the battery is faster. Compared to the 0.1 C-rate, the initial electrical potential is less in 1C, 2C, 4C rates. At 0.1 C-rate, the discharge time is more than one hour and at 4C-rate, the discharge time is less than one hour which is less compared to 0.1C-rate. The x-axis of the Figure 4.26 is represented with $(t[s]/1[h]) * i\_app\_p$ (C/m^2) which is Ampere hours (Ah)/ m^2.
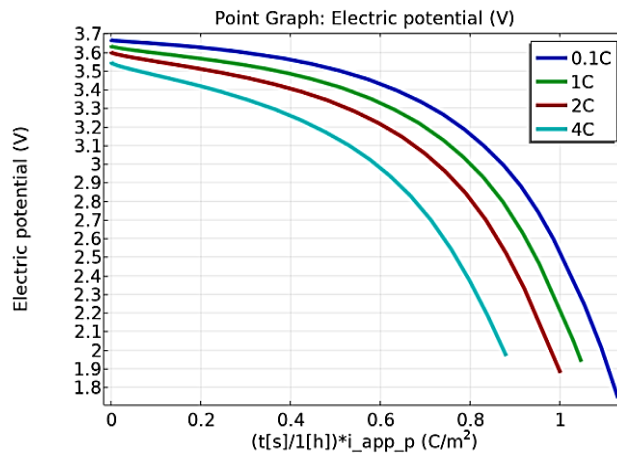
Figure 4.26 Discharge curves of LIB at different C-rates (0.1C, 1C, 2C, 4C)
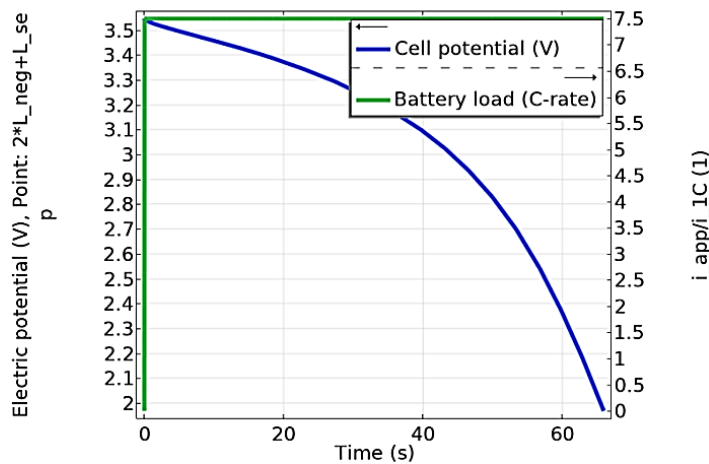
Figure 4.27 LIB discharge and battery load at 1C-rate

Figure 4.27. shows the discharge rate for a single load cycle and the battery load distribution throughout the cell potential at 1 C-rate. From Figure 4.28 it is observed that, after 1 hr, the LIB is discharged almost 44.44 % at 1 C-rate. The cell potential decreased from 3.6 V to 2 V with the battery load (1C-rate).

4.7.3 Validation of Battery Design with Discharge Curves

a)   b)
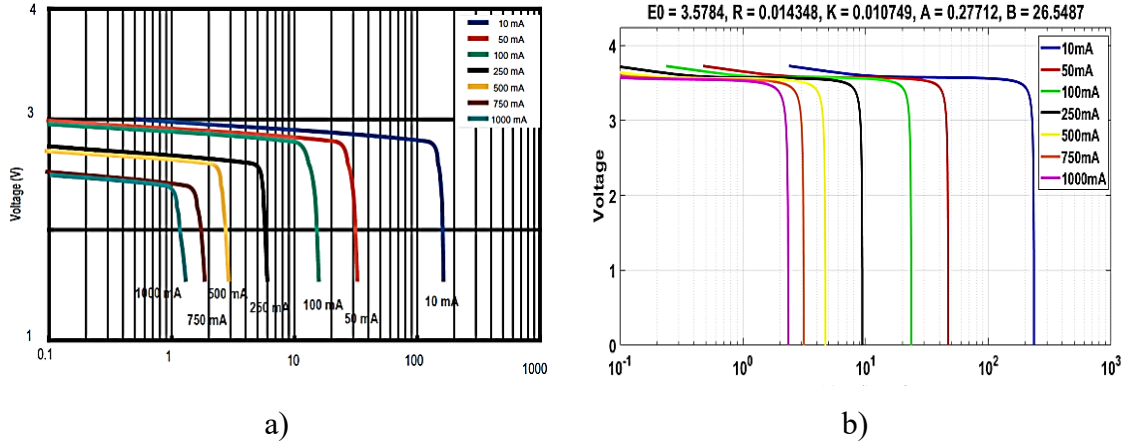
Figure 4.28 a) Battery datasheet Discharge curves b) Modeled battery discharge curves at discharge current 10 mA, 50 mA,100 mA, 250 mA, 500 mA, 750 mA, 1000 mA respectively

Figure 4.28 a) shows the discharge voltage curves at discharge currents of 10 mA, 50 mA, 100 mA, 250 mA, 500 mA, 750 mA, 1000 mA respectively in a log scale. Similarly, the designed battery discharge curves are plotted as shown in Figure 4.28.b).

The temperature is considered as -55 ^{0}C and +55 ^{0}C in order to match Indian climate conditions at Himalayas [176] and Rajasthan [227] which are the coldest and hottest states. The increase in current makes the battery to discharge faster. From Figure 4.28. a) and b), the 10 mA load is having full voltage discharge more than 10^2 in log scale and 1000 mA is having full discharge below 10 in log scale representation. The initial voltage is suddenly dropped because of high initial load in both data sheet and simulation. The discharge curves of the battery for datasheet and the modeling are slightly deviated because of the series of factors such as discharge current density, electrolyte concentration and temperature, depth of discharge, internal resistance and temperature variations.

4.7.4 The Temperature Effects

The temperature on surroundings of battery was considered at normal room temperature, which is 298.15 [K] (25 ^{0}C). The steam line velocity on battery is shown in Figure 4.29 at standard temperature.
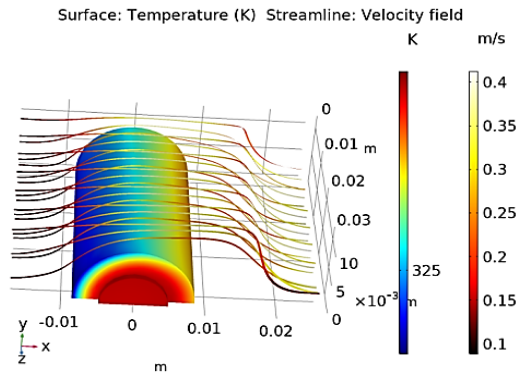
Figure 4.29 Streamline velocity field at temperature 298.15 K (25 ^{0}C)

Similarly, if both low and higher temperature ranges considered, the fast discharge characteristics of battery will be observed at different C-rates rather than 1C-rate. The discharge characteristics of LIB at +55 ^{0}C, and -55 ^{0}C are shown in Figure 4.30 a), b), c), and d) at different C-rates (0.1C, 1C, 2C and 4C) with respect to (w.r.to) capacity (C/m^2) and time (min). At 25 ^{0}C, the discharge capacity is normal and now abnormal behaviors are observed. The capacity in modeling is taken as (t[s]/1[h]) * i_app_p and the units are Ah/m^2 and is also represented as C/m^2.
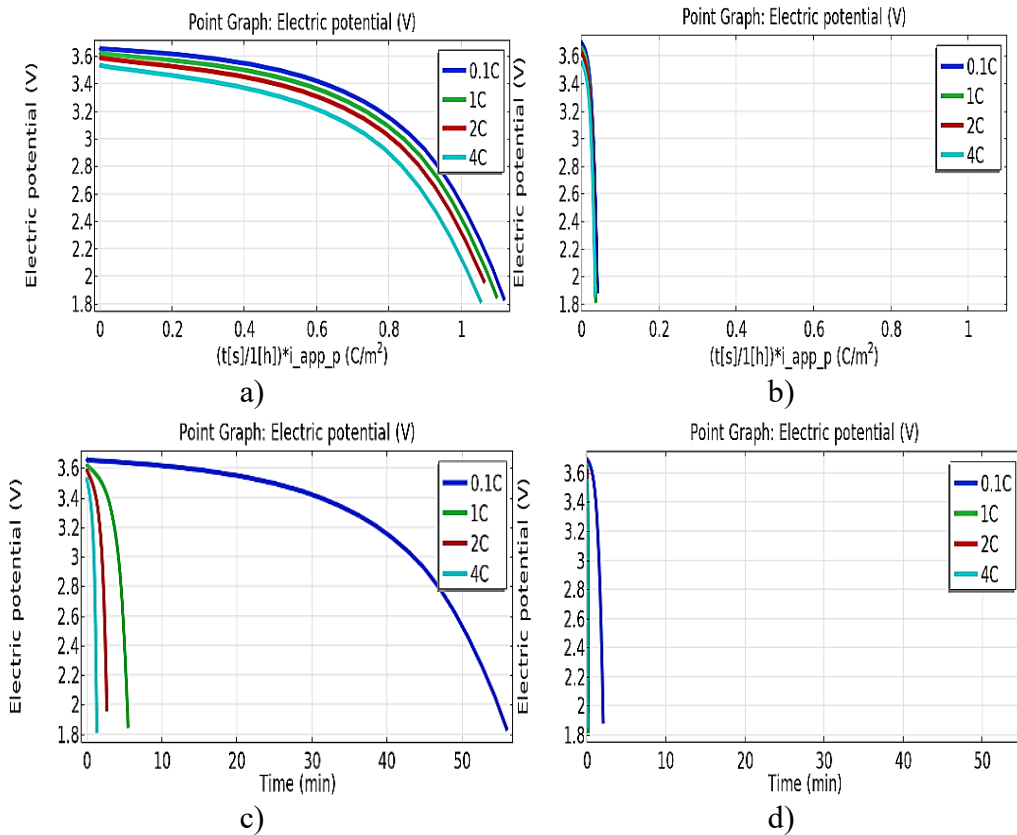
Figure 4.30 a) Discharge characteristics of LIB at +55 ^{0}C w.r.to capacity (C/m^2) b) Discharge characteristics of LIB at -55 ^{0}C w.r.to capacity (C/m^2) c) Discharge characteristics of LIB at +55 ^{0}C w.r.to time (min) d) Discharge characteristics of LIB at -55 ^{0}C w.r.to time (min) [(C-rate_0.1C, 1C, 2C & 4C)]

From Figure 4.30.a, the LIB capacity is approximately 1.1 C/m^2 at +55 ^0C, and from Figure 4.22 b), the LIB capacity is approximately 0.04 C/m^2 at almost all C-rates. The LIB exhibits almost 96.36 % of the drop-in capacity (Which is almost nil capacity) from +55 ^0C to -55 ^0C temperature change. Similarly, Figure 4.22 c) and d) show the time taken for discharge of capacity in minutes (min) where at +55 ^0C, and 0.1 C, the time taken for discharge is 56 min, and at -55 ^0C, and 0.1 C, the time taken for discharge is 2.06 min. The time taken for discharge at all C-rates and at +55 ^0C and -55 ^0C are listed in Table 4.7.

Table 4.7 Discharge time with respect to C-rate at +55 ^0C and -55 ^0C

C-rate	Discharge Time (min)	
	At + 55 ^0C	At - 55 ^0C
0.1C	56	2.06
1C	5.5	0.18
2C	2.7	0.09
4C	1.3	0.04 (approximately zero)

From Table 4.7, at -55 ^0C, the internal resistance of the LIB is increased and exhibits a 96.36 % drop in capacity (0.04 C/m^2) when compared to the LIB at + 55 ^0C (1.1 C/m^2). The discharge time of the LIB at - 55 ^0C is 0.04 min (2.4 seconds) because of the nil capacity, and at +55 ^0C, the battery discharge time is 1.3 min (78 seconds), and this variation is represented as shown in Figure 4.31 at 4 C-rate.
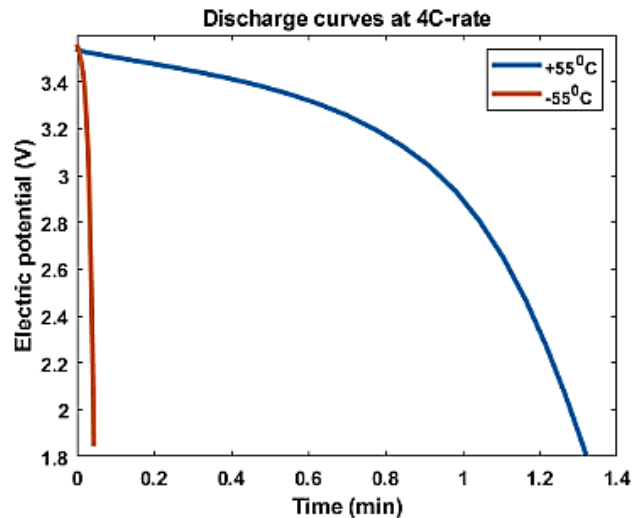
Figure 4.31 Discharge characteristics of LIB at + 55 ^0C, and - 55 ^0C w.r.to time (min) at 4 C rate

At negative temperatures, the LIB electrolyte performance degrades with fewer chemical reactions, which causes faster discharge even at a 0.1 C rate. As the LIB load (C-rate) increases, the draw of currents from LIB also increases. Also, the negative temperatures cause an increase in internal resistance, which decreases the discharge time of LIB with a capacity decrease.

4.7.5 FCLIB Topologies with SoC of LIB and SC

The summarization of the topologies is consolidated in Table 4.8. The parameters of both SC and LIB are given in Table 4.5. Those parameters are utilized during the topologies design and SoC of LIB and SC are measured at each stage and tabulated with all percentage levels. From Table 4.8, all the topologies are observed with different charging time of LIB. When we consider time, 1B 2S topology with 8.9×10^{-3} internal resistance gives very less time which is 3.38 minutes only, but it has high peak currents which cause heating and failure of battery.

If peak current, voltage and time are considered as effective parameters of LIB, 1B1S topology with high energy SC than LIB and 89×10^{-3} internal resistance gives fast charge of LIB within 13.67 minutes (820 seconds). 1B1S with 89×10^{-3} internal resistance and 18V SC gives 100 % SOC of LIB with minor effects in 13.67 minutes and 80 % in 6.7 minutes only. In this topology, the SC discharged till 40 % from 100 %. The discharge of SC is constant after 40 % at 8.3 minutes and till 100 % of LIB charging. All the topologies are summarized in Table. 3 with charge/discharge time of LIB/SC, peak voltage, peak current, with different % of SoC at different internal resistances of SC. At high 0.5 internal resistance of SC, both LIB and SC gives abnormal response of voltage and current response with charge characteristics of SC and discharge characteristics of LIB after some time as represented in Table 4.8.

From Figure 4.32, time taken for two SCs in parallel to one LIB is 3.38 minutes which is very much lesser, but the voltage and current at starting charging reaches to double the rated voltage and 110 A current. Remaining topologies are also having similar issues, but good performance is achieved at higher energy SC compared to LIB with 1B1S topology at 89×10^{-3} internal resistance, considering as best topology.

120

Table 4.8 Summarization of all the topologies used

Rating	LIB-3.9 V, 2.2 Ah, 0 % initial SoC — SC- 11 V, 500 F, 100 % initial SoC							LIB-3.9 V, 2.2 Ah, 0 % initial SoC — SC- 18 V, 500 F, 100 % initial SoC						
Internal DC resistance of SC (ohm)	8.9e^{-3}	89e^{-3}			0.5			8.9e^{-3}				89e^{-3}		0.5
Topology used	1B 1S	1B 1S			1B 1S			1B 1S	2B 1S	3B 1S	1B 2S	1B 1S	1B 2S	1B 1S
LIB SOC (%)	35	50	80	100	50	80	100	79.5	41	26.2	100	100	100	100
Time (minutes)	3.67	9.42	24.67	36.67	8.3	11.3	13.67	7.67	6.33	5.33	3.38	13.67	3.8	9.67
LIB Peak voltage(V)	4.8	4.5			8.2 (Double the rated Voltage)			6	5.5	4.6	7.8	5.4	8.1	8.2 (Double the rated Voltage)
LIB Peak current (A)	55	33			32			110	70	40	110	70	84	21
Saturated Voltage	3.9	4.2			8.2 (Double the rated Voltage)			4	3.9	3.9	4.2	4.8	8.1	8.2 (Double the rated Voltage)
SC decreased SOC (%)	100 to 0	100 to 50			> 100% SC failure			100 to 0	100 to 23	100 to 0	100 to 5	100 to 40	100 to 53	>100
Time for DOD in minutes	33.3	8.3 to 41.7			>3.33			33.3	6.3	33.3	41.7	8.3 to 41.7	7.5 to 41.7	9.7
SC peak current (A)	55	33			32			110	140	120	55	70	42	21
SC peak voltage (V)	11	11			> 25			18	18	18	18	18	18	>18
Sudden Voltage drop (V)	9	9			9				18 to 6	18 to 15	18 to 16	18 to 11.5	18 to 14	Increase in voltage

The charging rates of all the topologies are given in the Figure 4.32.
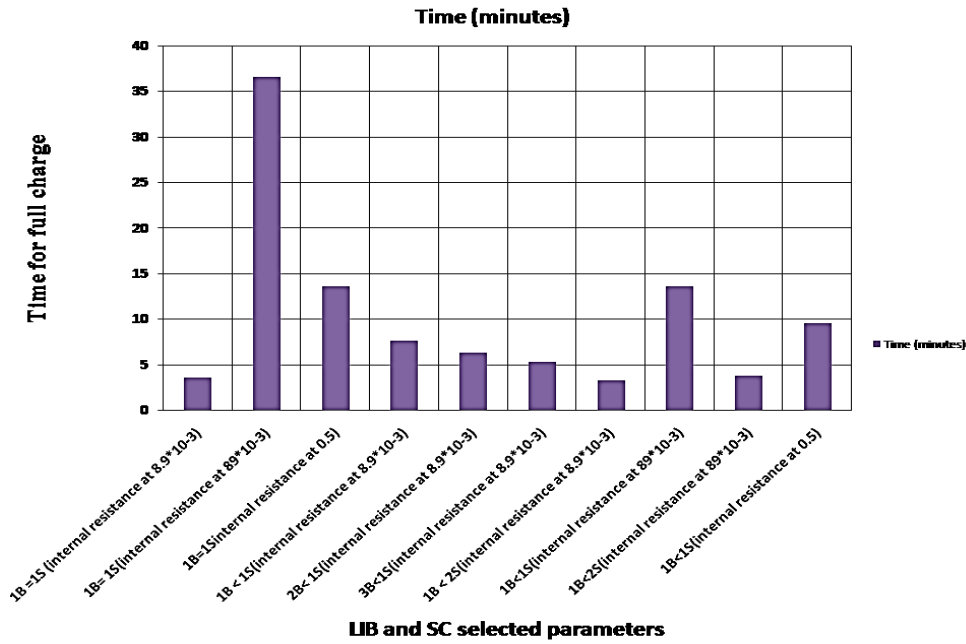
Figure 4.32 Topologies with the respective time to full charge

4.8　Conclusion and Recommendations

A simplified mathematical equivalent model was used in this work to examine and evaluate the effect and severity of charge/discharge rate of lithium-ion battery (LIB) and Super Capacitor (SC). The SoC, current, terminal voltage, and lifetime properties of LIBs were determined with the identical input parameters. Furthermore, it has been shown that the response of discharge characteristics for LIBs results in an extended lifespan for useable capacity extraction. As a result, it might be observed as an indicator that LIBs with higher energy capacity would be used in renewable generation-based stationary applications.

Accordingly, the system with FCLIB having SC, results in equal cost with better performance with fast charging capability of LIB. When using architecture of two SCs with a greater energy level and charging one battery, the battery fast charging to 100 % SoC takes 203 seconds (3.38 minutes) but reaches very high voltages and currents. When the internal DC resistance of the SC is 0.5 ohm, the SC exhibits aberrant behavior when operating from 100% to more than 100 % SoC. Furthermore, the battery exceeds its rated voltage, resulting in battery damage. When the internal DC resistance of the SC is reduced (89e-3) and at SC high energy levels, the battery charges fast, 13.67 minutes with one battery and one super capacitor (1B1S) topology and 80 % is achieved at 6.7 minutes. The initial current and voltages are higher, causing damage to the LIB and SC as temperatures rise.

CHAPTER 5

TECHNO-ECONOMIC ANALYSIS OF INTEGRATED SSPV WITH EESS AND DESIGN OF WIND ENERGY CONVERSION SYSTEM

5.1 Introduction

The increasing demand for renewable energy sources has led to the development of off-shore micro-grid systems that integrate SSPV as discussed in Chapter 2 and chapter 3 and EESS as discussed in Chapter 4 to provide reliable and sustainable energy supply in remote areas. The modeling of these systems is crucial to optimize their design, operation, and maintenance, and ensure their economic and environmental feasibility. HOMER-Pro is a powerful software tool widely used for modeling and analyzing off-grid and grid-connected renewable energy systems, including off-shore micro-grids. This chapter presents a detailed study on the modeling of off-shore micro-grid systems using HOMER-Pro, with a focus on the integration of SSPV and EESS components.

Wind Energy Conversion Systems (WECS) have gained widespread attention in recent years due to their potential to generate electricity from renewable sources. WECS harness the kinetic energy of wind to generate electricity and have been adopted around the world as a means of reducing greenhouse gas emissions and meeting the increasing demand for electricity. A significant amount of research has been conducted on WECS, covering various aspects of their design, performance, and optimization. For instance, in [228]–[230] investigated the effects of wind shear and turbulence on the power output of a WECS, demonstrating the need for accurate models to predict the system's performance. In [80], the potential of integrating a WECS with a compressed air energy storage system evaluated, demonstrating improved system performance and energy management with the integration of energy storage.

Moreover, the literature survey reveals that the optimization of WECS has been the focus of extensive research efforts. The optimization studies have explored various aspects such as control strategies, blade design, and turbine placement. For example, in [231] proposed a hybrid control strategy for a WECS with permanent magnet synchronous generator (PMSG) that combines model predictive control and adaptive fuzzy logic control,

demonstrating improved system performance and energy management giving more scope to DFIG based WECS.

In addition, the integration of WECS with other renewable energy sources such as PV systems and energy storage systems has been identified as a key solution to the intermittency challenge of these renewable sources. Several studies have explored the benefits and challenges of this integration, including the impact on system performance, economic feasibility, and energy management strategies.

This chapter highlights the importance of accurate modeling parameters and system configuration in achieving optimal performance and cost-effectiveness. The research also discusses the challenges and opportunities associated with micro-grid systems, and the potential for future research and development in this area. The design of WECS with DFIG is also presented with the mathematical simulation in this chapter. Overall, this chapter aims to provide valuable insights into the design and modeling of off-shore micro-grid systems using HOMER-Pro, and contribute to the sustainable development of renewable energy technologies and the simulation of WECS with the DFIG.

5.2 Microgrid Modeling and Parameterization

The real time data from SCADA center, TSSPDCL Hyderabad considered as micro-grid system is chosen to explore the techno-economic analysis of LIB and SCs. The PV array, grid, and FCLIB system are the three energy sources under consideration in the micro-grid system. A load with a rating of 4–5 kVA is attached to the system and is powered mostly by the PV and FCLIB [232].

5.3 SSPV System (SSPVS)

The solar array erected at the industries is made up of two distinct arrays, each of which is made up of 14 modules connected in analogous with two arrays to make 10kW peak of total capacity. But at the facility, 56 modules with a 10-kW peak of total capacity were installed which is 4 times of industry erection. The SSPV array is placed with an azimuth angle of 0 degrees and at an inclination angle of 16 degrees. This solar plant's electricity production is affected by meteorological and geographical variables [233]. The power output of a SSPV array (P_{PV}) is computed as follows:

$$P_{PV} = G_{PV} f_{PV} \left(\frac{I_T}{I_{T,STC}} \right) \left[1 + \alpha_P \left(T_C - T_{C,STC} \right) \right] \qquad 5.1$$

where, G_{PV} is the rated capacity of PV in kW, I_T is the incident solar radiation on the SSPV array in kW/m^2, f_{PV} is derating factor of the SSPV array, T_C is cell temperature in ^{0}C, $I_{T,STC}$ is the incident radiation which is considered as 1 kW/m^2 at STC, $T_{C,STC}$ is the temperature of PV cell under STC (at 25 ^{0}C), and α_P is the power temperature coefficient (%/^{0}C).

HOMER-Pro software was used to model the grid-connected SSPV system under consideration. The system included a 10 kWp solar array, a 5 kW grid-connected converter, 83 Ah lead-acid battery storage, and a 167 Ah FCLIB [197], [234], load having a 4–5 kVA rating. The Grid connected SSPV system (GCSSPVS) with respective components is shown in Figure 5.1.
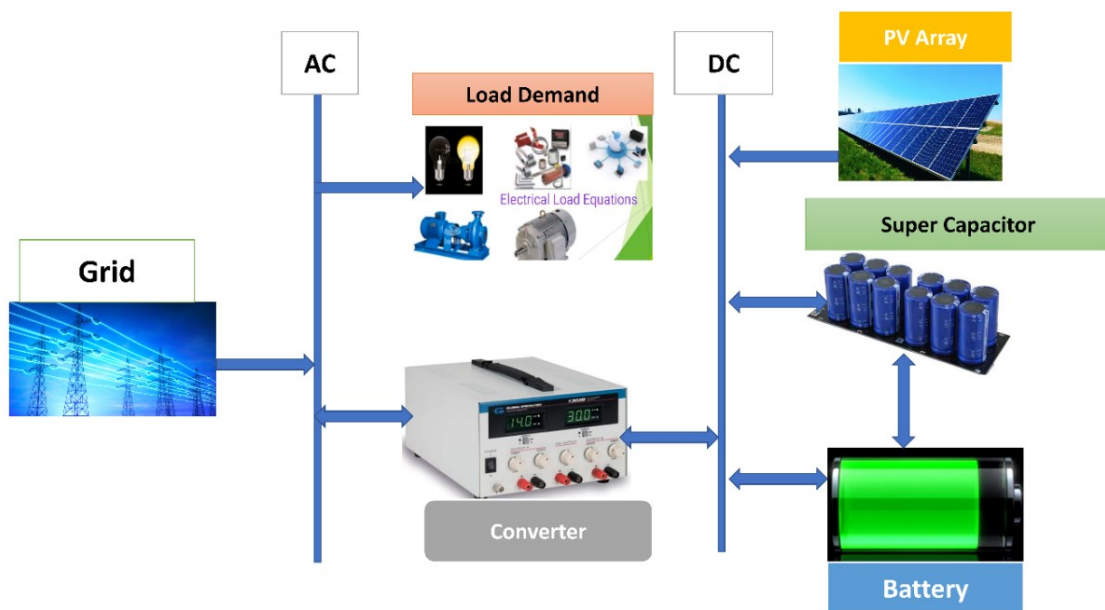
Figure 5.1 Schematic diagram of the SSPVS with FCLIB

5.4 Data on Load Profiles and Solar Resources

The load profile of the area under consideration is based on the utilization of a neighboring commercial load demand on the Telangana State Southern Power Distribution Company Limited (TSSPDCL) for a month. According to the data obtained in real-time, the commercial demand of load has a peak demand of 4.97 kW and with a maximum energy usage of 16 kWh/day at the area. When there is a power shortfall from PV and FCLIB, the load is powered mainly by the PV array and moderately by the grid. The load average profile is depicted in Figure 5.2 [232] based on load profile data average in a day collected at the TSSPDCL Hyderabad location.
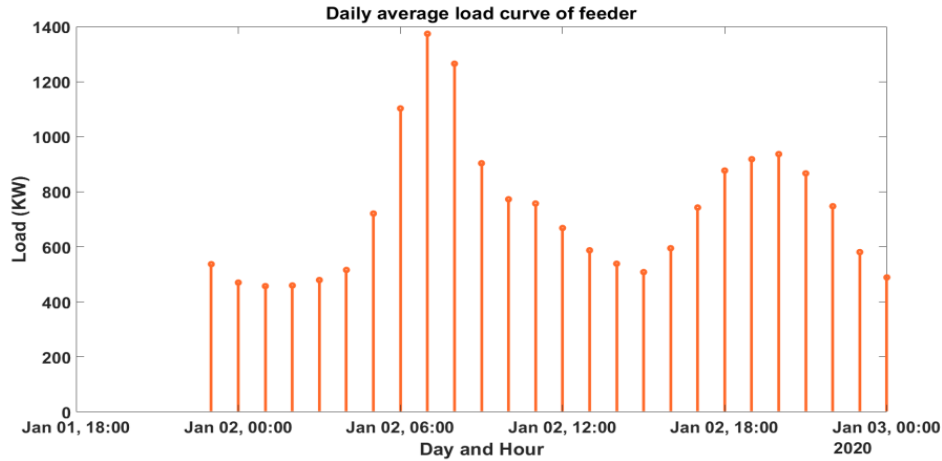
Figure 5.2 Daily load curve (Jan 2nd)

The sun radiation statistics were obtained from the site's plant data logger as well as NASA [235]. Based on the plant data and analysis, a typical yearly solar radiation of 5.8 kWh/m^2/day is obtained with 0.6 index of clearness, as shown in Figure 5.3. The measure of the lucidity of the atmosphere is clearness index, represented as the proportion of solar energy that is passed through the atmosphere and strikes the Earth's surface [232].
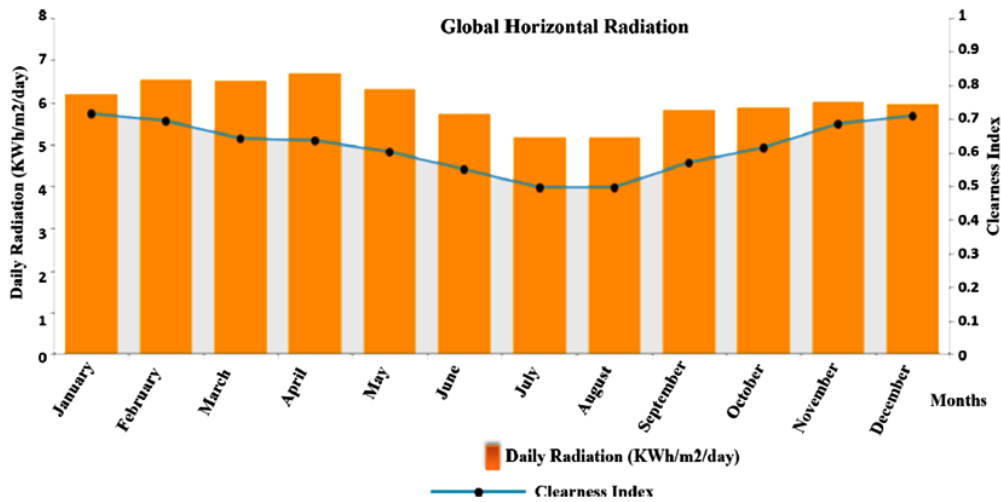
Figure 5.3 Global horizontal radiation with clearance Index [236]

5.5 Modeling of EESS

Excess electricity generated from the micro-grid is collected in energy storage devices and used when the PV plant runs out of energy to power the load demand. The FCLIBs stored energy is provided by [237].

$$B_{FCLIB} = B_{FCLIB.0} + \int_0^t V_{FCLIB} I_{FCLIB} dt \qquad\qquad 5.2$$

where $B_{FCLIB.0}$ signifies the starting FCLIB charge and V_{FCLIB} and I_{FCLIB} signify the FCLIB's voltage and current, respectively.

The number of series-connected FCLIB cells (N_{bat}) necessary to achieve the specified voltage [237].

$$N_{FCLIB} = \frac{V_{bus}}{V_{FCLIB}} \qquad\qquad 5.3$$

V_{bus} is the micro-grid system's bus voltage, while V_{FCLIB} is the rated voltage of a single FCLIB. Furthermore, the maximum power charge/discharge of a single FCLIB is specified as follows:

$$P_{FCLIB}^{max} = \frac{N_{FCLIB} V_{FCLIB} I_{FCLIB}^{max}}{1000} \qquad\qquad 5.4$$

where, I_{FCLIB}^{max} represents the utmost current charging of the LIB in amperes [238]. The technical parameters of the LIB and SC used in this study are given in Table.1.

Table 5.1 LIB and SC cost and respective parameters used for modeling in HOMER-Pro [239]–[241]

Parameters	LIB (LMO [218])	SC ([242], [243])
Nominal cell Voltage (V)	3.9	11/18
Number of strings	4	2
Cycle number at repeated maximum DOD	3000 [236]	10^6
Initial SoC %	0	100
Round Trip Efficiency	90	98
substitution cost ($/KWh)	429.68	435
Cost ($/KWh)	482.3	480/ 510
Capacitance	-	500F

5.6   Grid system

The SSPV system under consideration uses a grid system to improve supply system dependability. As a result, the load is meant to get electricity whenever it is required, even if it is usually active during the day. The electricity availability on an average during the day is about 12 hours. In the simulation for the instance under consideration, the grid electricity rates are assumed to be $0.087/kWh.

5.7   Parameters for System Economics

The CoE and total PNC (Present Net Cost) of batteries and micro-grid system were used to determine their economic feasibility.

5.7.1   PNC Estimation

Initial, replacement, operating, and maintenance costs combined the value of PNC is calculated by subtracting the costs of fuel from the income. The overall PNC is determined as follows:

$$PNC = \frac{C_A}{CRF(i,n)} \qquad\qquad \textbf{5.5}$$

where, CRF(i, n) represents the Capital Recovery Factor, i and n represent the real annual interest rate and the number of years, respectively [237]. The capital recovery factor is also defined as:

$$CRF(i,n) = \frac{i(1+i)^n}{(1+i)^n - 1} \qquad\qquad \textbf{5.6}$$

where, $i = \frac{i_{nom} - f}{1+f}$, The yearly inflation rate is represented as f and the nominal interest rate is given as i_{nom}.

5.7.2   CoE Estimation

The CoE is one of the primary parameters used to assess the economic efficacy of an energy system. The CoE is calculated by dividing the yearly cost of all system components by the amount produced energy [244]. The CoE is issued by

$$CoE = \frac{C_A}{E_S} \qquad\qquad \textbf{5.7}$$

The annual energy provided is denoted by E_S, while the total annual cost is denoted by C_A [237]. The total yearly cost is the sum of the costs for substitution, capital and operation and maintenance (O & M).

5.8   Design of WECS

The WECS consists turbine, gearbox, and generator. Depending on the wind speed, the turbine rotated and converts the wind speed into mechanical rotation which drives the rotor of the generator. The generators used in WECS are of Permanent Magnet Synchronous Generator (PMSG), and DFIG. For offshore applications, the DFIG is mostly

preferred due to harsh environmental conditions and variable high wind speeds [51], [52], [78]. The DFIG system is considered in two conditions one is healthy and other is unhealthy condition. Where the unhealthy condition is of the DFIG is considered with BRB fault and no stator fault with loading of the WECS at no load, half load and one fourth load.

5.8.1 Modeling of DFIG

The microgrid is designed as shown in Figure 5.4 using MATLAB/ SIMULINK [245]–[249]. The turbine is connected to the DFIG system, where the wind speed is considered as 25 m/s as per the SSPVS design.
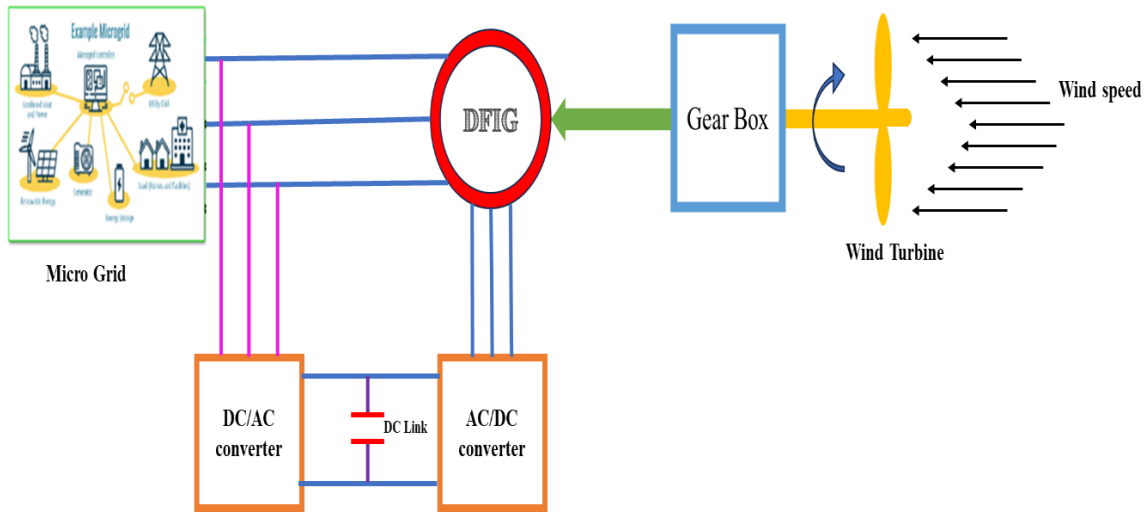
Figure 5.4 Microgrid system

The microgrid system considered inside Figure 5.4 is the combination of Figure 5.1 of SSPVS, EESS and microgrid with WECS. As specified in the above modeling references, the mathematical equations for the DFIG rotor are developed as shown in below Figure 5.5 to 5.8.

Mathematical model of the induction motor in phase coordinate system a, b, c is given for both stator and rotor as equations (5.8) and (5.9).

Stator:

$$U_a^s = r_a^s i_a^s + \frac{d}{dt}\psi_a^s, U_b^s = r_b^s i_b^s + \frac{d}{dt}\psi_b^s, U_c^s = r_c^s i_c^s + \frac{d}{dt}\psi_c^s \qquad \textbf{5.8}$$

Rotor:

$$0 = r_b^r i_b^r + \frac{d}{dt}\psi_b^r, 0 = r_b^r i_b^r + \frac{d}{dt}\psi_b^r, 0 = r_c^r i_c^r + \frac{d}{dt}\psi_c^r \qquad \textbf{5.9}$$

The controlled voltage source with back transformation creating rotor side converter of DFIG input turbine system is shown in the Figure 5.5. Where Figure 5.6

represents the park transformation of DFIG by which, the voltage and current of stator and rotor side currents are measured. Figure 5.7 represents the active and reactive power generated from DFIG.
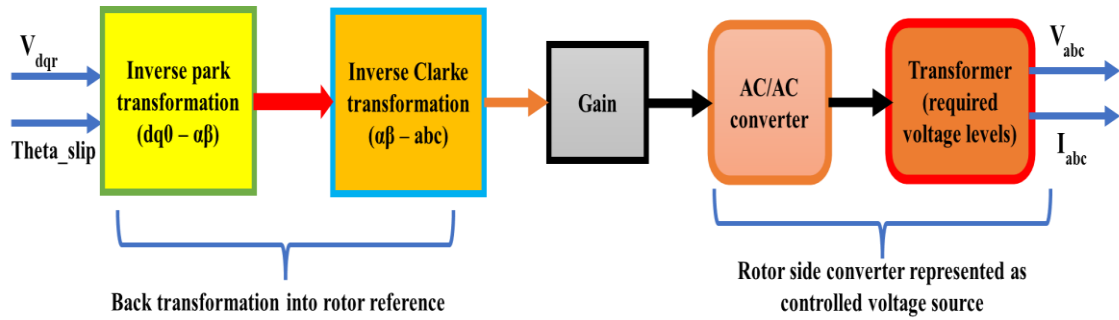
Figure 5.5 Turbine input for the DFIG system as controlled voltage source at 25 m/s wind speed
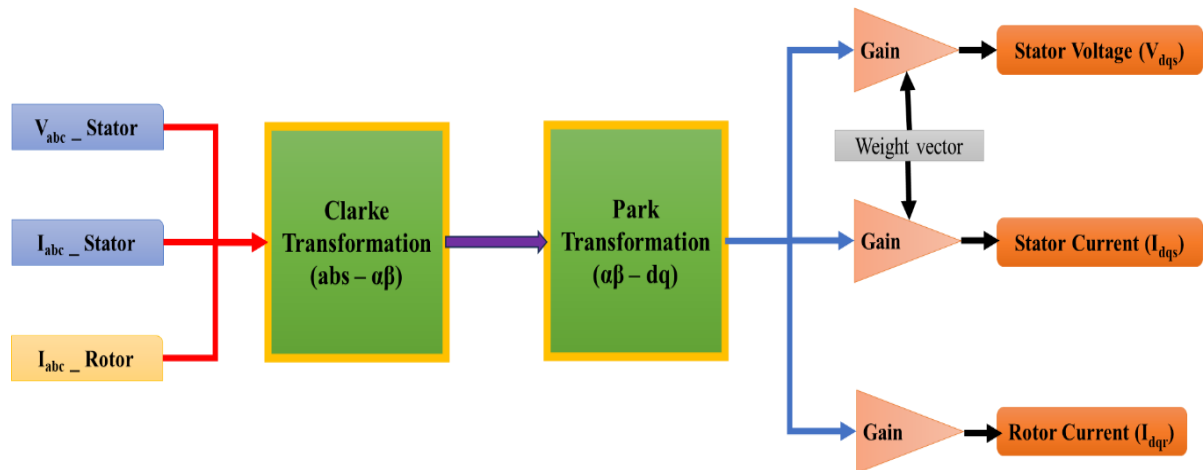
Figure 5.6 DFIG parks transformation for measurement of voltage and current
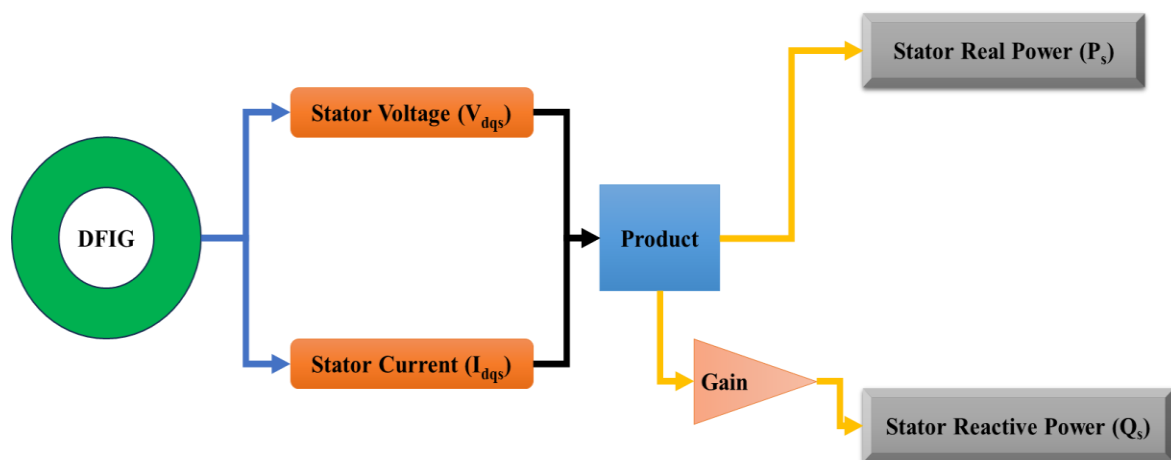
Figure 5.7 Active and Reactive power generated from DFIG

The Figure 6.5 is the current controller for the rotor currents generated. The abc - dq frame reference is considered for the three-phase rotor current. The Table 6.1 represents the rated parameters of the DFIG and the same is used in the experimental setup as shown in Figure 6.12.
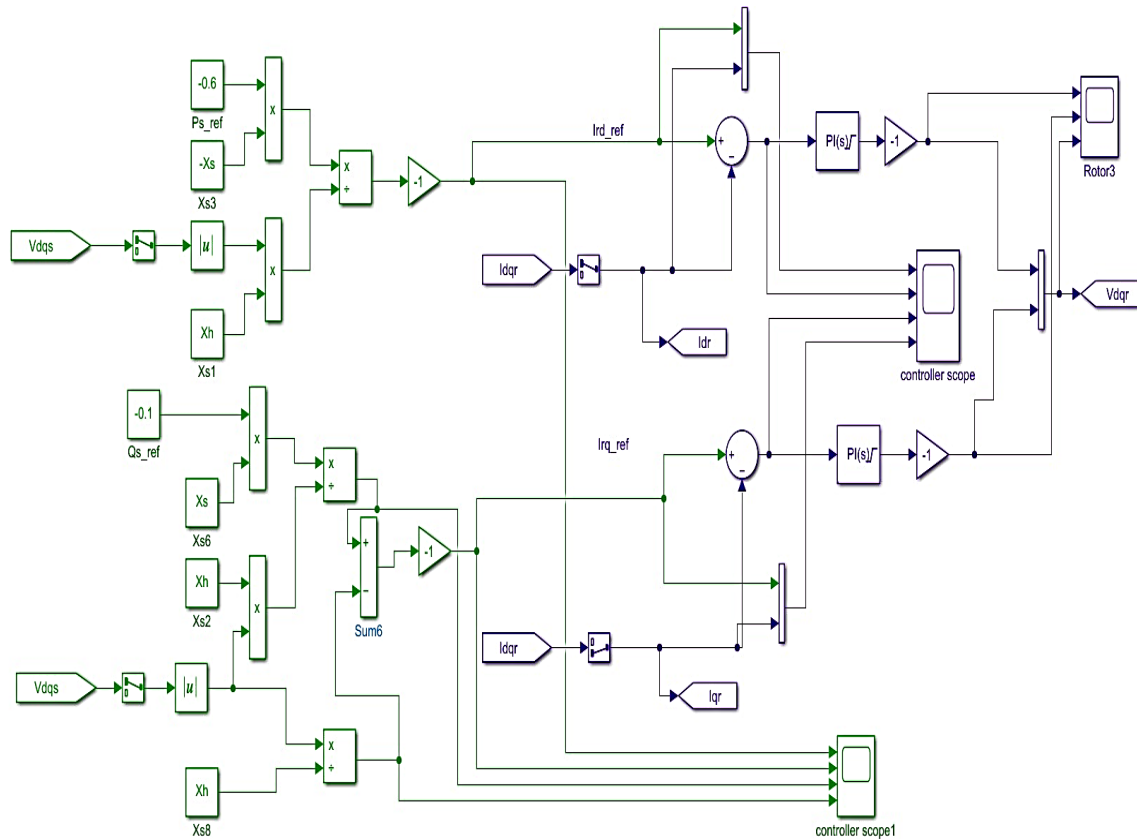
Figure 5.8 DFIG Three-phase rotor current controller

5.9   Results and Discussion

The influence of a discharge-charge profile on LIB capacity deprivation behavior at different current rate levels was studied in this article using a MATLAB-based simple equivalent circuit model in Chapter.4. Furthermore, using HOMER-Pro software, the techno-economic analysis and performance of LIB and FCLIB integrated with grid-connected PV-based micro-grid systems were analyzed. The research was carried out utilizing actual solar energy resource, load profiles and FCLIB storage data.

Figure 5.9 depicts the power output of the grid system and load demand. The additional load demand can be met by the output of the SC and LIB's SoC with normal load usage. HOMER-Pro-presents the optimized outputs of the micro-grid system considering power load from the grid as well as power shortages from PV and FCLIB. The extreme

ideal output of the system under consideration is graded according to the total CoE and PNC.
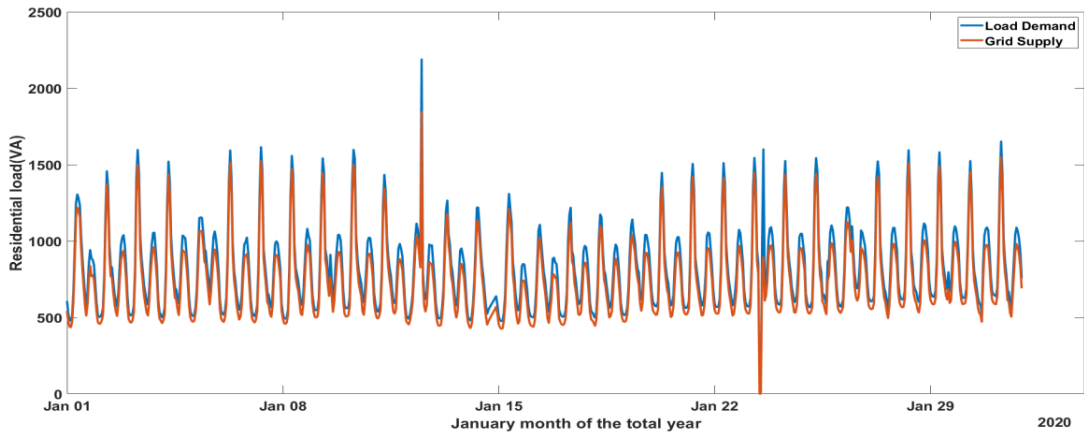
Figure 5.9 The Load demand and grid energy in KVA

The output curves of simplified electric circuit models show that LIB and SC have essentially identical charge and discharge behaviors, as shown in Figure 4.2 to 4.15. Furthermore, the duration of functional life in terms of discharge-charge cycles is determined to be different for both LIB and SC based on discharge characteristics. Furthermore, with fewer cells and lower capacity, LIB discharge characteristics are shown, resulting in longer lifespan characteristics. HOMER-Pro was also utilized to do an economic and technical examination of LIB and SC, with ampere-hour (Ah) capacity of LIBs as the input for an electric model circuit simulation. As an outcome of HOMER-pro simulation, the GCSSPVS system using a LIB, only requires 6 batteries while, the FCLIB system require 3-LIBs and 3-SC. Table 5.2 summarizes the costs of various components utilized in the SSPV system.

Table 5.2 Cost of components utilized in the SSPV system

Component	Capital ($)	O&M ($)	Substitution ($)	Salvage ($)	Fuel ($)	Total ($)
PV array (8.4KW)	816.53	0.0	0	0	9561.77	10378.3
LIB	3435.63	0.0	1068.17	105.15	0	4398.65
Converter with LIB	866.2	22.64	158.25	16.97	0	1030.12
Total system with LIB	839.13	1226.42	-122.43	0	14990.17	16933.29
Total system with LIB and SC	1655.97	2873.33	-90.58	0	15726.34	

The capital, substitution, salvages expense, and operation and maintenance (O&M) are all represented in Table.1 are the cost elements. The capital cost is the entire upfront cost of the plant, whereas the substitution, maintenance, and operation costs are expenditure incurred over the facility's operational life. Table 5.2 shows that, in the usual application scenario evaluated, the optimized simulation result shows that FCLIB operation and maintenance (O & M), substitution, and salvage costs are substantially lower than LIB and SC combination. The substitution cost of the converter with LIB and SC is determined to be economical compared to the capital cost outcome for the stipulated 15-year lifespan service, according to HOMER's optimization result. Similarly, Table 5.3 gives the performance characteristics of both LIB and SC where the charge/discharge density of SC is higher compared to LIB.

Table 5.3 The comparison of LIB and SC performance

Device storage characteristics	LIB	SC
Charging time	$1 < t < 5h$	1 - 30s
Discharging time	$T > 0.3h$	1 - 30s
Energy Density (Wh/kg)	10 – 100	1 - 10
Life time (number of cycles)	3000	10^6
Power density	< 1000	10,000
Charge/discharge Efficiency	0.7 - 0.85	0.85 - 0.98

The PNC of the LIB and SC for 10 KW PV array in the GCSSPVS is represented in Table 5.4 with CoE estimation.

Table 5.4 PNC of LIB for 10KW PV array

Parameter	LIB for 10 KW PV array	FCLIB for 10 KW PV array
Number of components	6	3LIB/3SC
Converters (KW)	5	5
Total PNC ($)	14990.8	15726.86
CoE ($)	0.33	0.35
Operating cost ($)	839.13	1656.39
Renewable Fraction (%)	90	91

5.9.1 WECS performance

The WECS is the combination of turbine system and the generator and are interconnected with the gearbox.

5.9.1.1 Turbine performance

The turbine system input is wind and the wind speeds are variable because of which, the turbine rotates at different speeds. The maximum input for the turbine is 25 m/s as specified in section 5.8 and the output from the wind turbine is as shown in Figure 5.10.
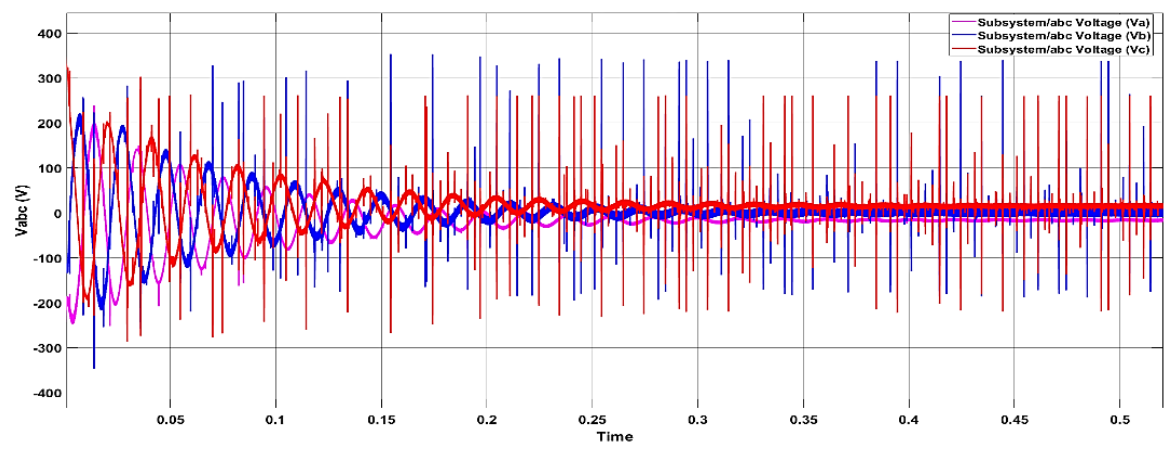
Figure 5.10 Turbine output (input for DFIG)

5.9.1.2 DFIG performance

The input for the DFIG is the output from the turbine system. So, the DFIG input is as shown in Figure 5.10. When the turbine rotates, it moves the rotor of the generator DFIG.

5.9.1.2.1 Healthy DFIG performance

The rotor generates currents and the rotor currents from the modeling are as shown in Figure 5.11.
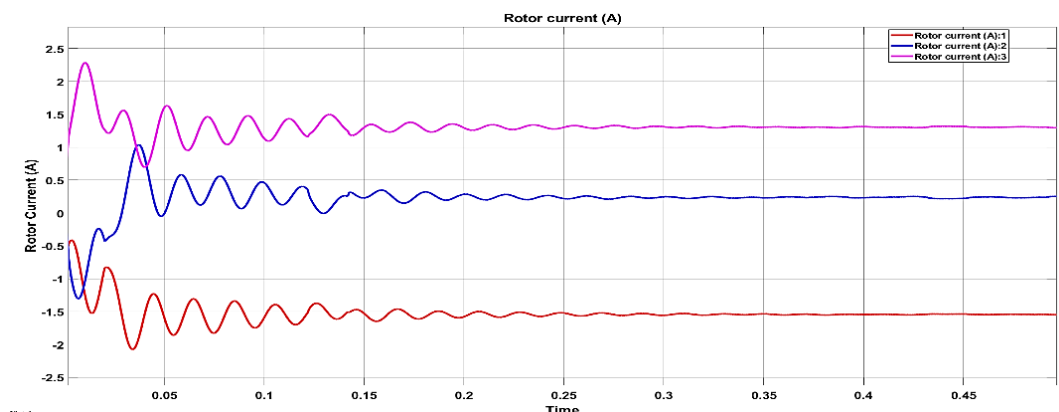
Figure 5.11 DFIG three-phase rotor currents

134

From Figure 5.11, it can be observed that, the sum of three-phase rotor currents is zero, which implies the DFIG rotor is working properly without any faults (healthy condition). Due to the flux generated by the rotor and stator windings, the flow of currents is possible in stator too. The stator currents in three-phases is as shown in Figure 5.12.
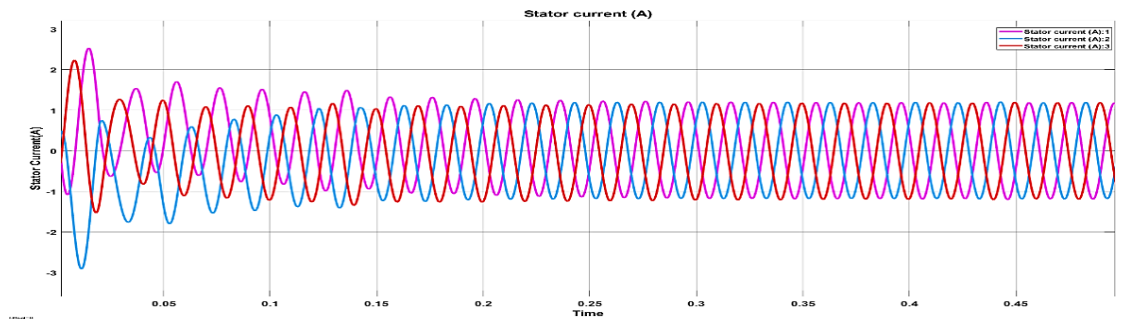
Figure 5.12 DFIG three-phase stator currents

The stator currents at starting are in damping condition, which require time to get stable by achieving the equal flux as rotor. The active and reactive power generated is as shown in Figure 5.13, where the power factor of the DFIG takes place.
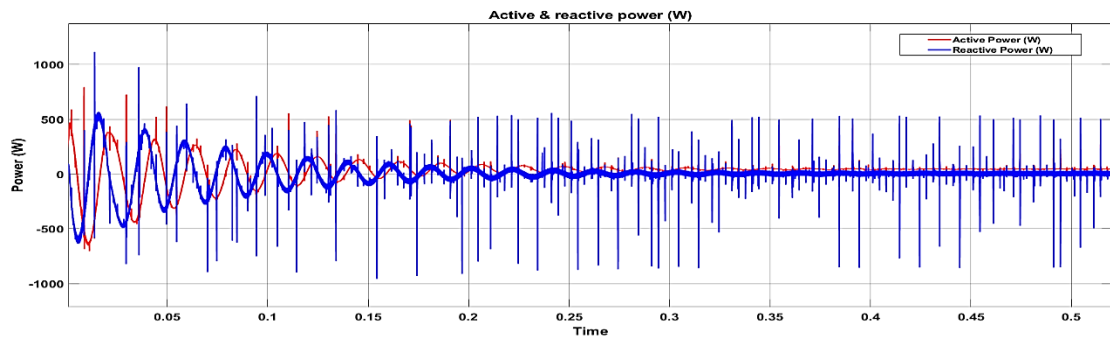
Figure 5.13 Active and reactive power generated in DFIG

The torque is generated in the DFIG due to the proportional relation of speed and the torque waveform is as shown in Figure 5.14. From this, it can be observed that, the torque is initially high and later it becomes stable.
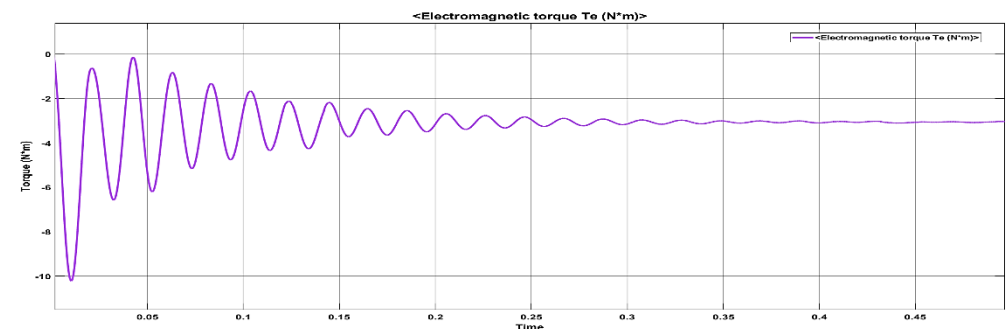
Figure 5.14 Torque generated in DFIG

5.10 Conclusion and Recommendations

In extension to the charge and discharge cycle function, the HOMER-Pro software was used to do a techno-economic study of LIB and SC with SSPVS, considering resource and actual commercial load demand profiles data provided by TSSPDCL. As a consequence, the system with a LIB had a CoE of 0.33 $/kWh, whereas the system with a LIB and SC had a CoE of 0.35 $/kWh. The PNC of the system with LIBs, on the other hand, is $14,990.8, while the PNC of the system with LIB and SC is $15,726.86.

From the investigations, FCLIB with SC topologies can be recommended depending on the time required for fast charging considering battery management system with cooling technologies. However, if fast charging is considered/not considered, the cost of the system will be same as FCLIB from Table 5.3 and 5.4 as depicted with SSPVS. So FCLIB can be considered with economic and optimal storage solution even after connecting with the SSPVS selecting best FCLIB topology.

The WECS with DFIG and the rotor current configuration is simulated using MATLAB/SIMULINK and the performance characteristics of the WECS are obtained. The stator and rotor currents are obtained with the consideration of WECS integrated with the micro-grid system. In the next chapter, the integration of SSPVS, EESS and WECS with/without the consideration of DFIG BRB fault as an offshore microgrid system is discussed with simulation and experimental setup.

Acknowledgement:

CHAPTER 6

OFFSHORE MICROGRID SYSTEM BY INTEGRATING WIND ENERGY CONVERSION SYSTEM (WECS) WITHOUT/WITH BRB FAULTS OF DFIG

6.1 Introduction

The increasing demand for energy and the need to reduce carbon emissions has led to the development of RES such as PV and wind energy. Offshore microgrid systems have the potential to integrate these renewable sources and provide a reliable and sustainable energy supply to remote areas [61]. The microgrids can perform both in standalone and grid-connected modes [62]. As discussed in Chapter 5, the off-shore microgrid system is designed with 10 kW offshore PV integrated with 5 kW grid-connected system with a converter and a 167Ah FCLIB for EESS [197], [234]. The SSPVS with respective grid and storage components is as shown in Figure 5.1 in Chapter 5. The load having a 4 to 5 KVA rating is considered with the profile of load is in Chapter 5 as shown in Figure 5.2. The integration of SSPVS and WECS in offshore microgrids can provide a reliable and consistent energy supply to areas with limited access to the grid [61].

The integration of renewable energy sources, such as wind and solar, with energy storage systems has become increasingly popular in recent years due to their potential to provide a reliable and consistent source of power [47]–[49], [54]. The intermittent nature of these renewable energy sources, particularly wind and solar, creates challenges for their effective utilization as a primary source of electricity. However, the integration of energy storage systems with these renewable energy sources presents an opportunity to address these challenges and improve the efficiency and reliability of renewable energy systems.

Among the RER, WECS and PV systems have gained significant attention due to their widespread adoption and potential to generate electricity from natural resources. The integration of PV and energy storage systems with WECS has the potential to significantly improve the reliability and efficiency of renewable energy systems [62], [82], [250]. One of the primary benefits of this integration is the ability to store excess energy generated by

137

the WECS and PV systems during periods of high availability, which can then be used to meet demand during periods of low availability. This integration enables a more consistent and reliable power output and reduces the dependence on traditional energy sources, such as fossil fuels.

Several studies have explored the benefits and challenges of integrating PV and energy storage systems with WECS. The economic feasibility of integrating PV and energy storage systems with a WECS, concludes that the integration significantly improved the system's economic performance [41], [62]. Moreover, the integration of PV and energy storage systems with WECS also offers several benefits such as reduced curtailment, enhanced energy management, and improved system reliability. The ability to manage the energy flow between the PV, WECS, and storage systems can optimize energy generation and utilization and minimize energy waste.

Offshore microgrid systems with PV and wind energy integration face various challenges. One of the primary challenges is the harsh environment, which can damage the components and affect system performance [78].The importance of reliability analysis for offshore WECS has increased with the expansion of offshore power via wind generation, as the systems operate in harsh conditions and exhibit complex behaviors that can have significant negative impacts [51], [52]. It is therefore crucial to thoroughly analyze the reliability of offshore wind turbines to ensure their safe and efficient operation. The WECS typically consists of wind turbines, generators, and a control system and exhibits more failures and are explained in [79] with fault tree analysis. Offshore, the wind blows at higher speeds and rotates the turbine blades which rotates the generator rotor via the gearbox. The Doubly-Fed Induction Generators (DFIG) at offshore WECS are mostly preferred generators due to higher wind speeds.

The DFIG exhibit faults in the stator and rotor construction, like Broken Rotor Bar (BRB), Stator Inter Turn Faults (SITF), line faults etc., [78], [80]. A thermo-gram-based fault detection method with Deep Learning (DL) recognizes eleven conditions of Induction Machine (IM) which are classified as two Stator Turn to Turn Fault (STTF), one healthy and eight SITF where different location-severity combinations are also proposed by different researchers [63], [249], [251]–[254] with DFIG implementations.

The DFIG exhibits almost 9 to 10 % of BRB fault while used as industrial machines and in the offshore environment, it is double the fault on land. The diagnosis of the incipient BRB fault in the WECS is the foremost objective to increase the reliability of the offshore micro-grid system [81], [82]. Different fault detection techniques in the experimental condition and with signature analysis are performed via Deep learning techniques using Convolution Neural Networks with IR images, voltage, and frequency variation detection [82]–[87].

The importance of reliability analysis for offshore microgrid with the detection of WECS failures is more important. In this chapter, the design of offshore microgrid with the integration of SSPVS, EESS with WECS are considered with/without BRB fault consideration (healthy, unhealthy) via mathematical modeling, and experimental setup. The different percentages of single BRB faults are considered by intentionally imposing in DFIG, and collecting of stator currents for three phases using a three-phase current sensor. The current sensor collected data is utilized and also converted into Power Spectral Density (PSD). Features are selected and five classification algorithms like Decision Trees (DT), Support Vector Machines (SVM), K-Nearest Neighbors (KNN), Logistic Regression (LOR), and Random Forests (RF) are developed for WECS fault forecasting.

6.2 Offshore microgrid system design

Offshore microgrid systems typically consist of multiple RER, storage systems, and a control system. The SSPVS and wind energy systems provide a constant and reliable source of energy, while the storage systems ensure that the energy supply is available even during the period of low generation of supply. The control system at Point of Common Coupling (PCC) manages the energy flow between components and ensures that the energy supply is stable.

6.2.1 Submerged Solar PV System (SSPVS)

The PV system typically consists of PV panels, inverters, and a control system. The PV panels generate electricity when exposed to sunlight, which is converted to usable energy by the inverters. The Power output of the PV is calculated as per equation 5.1 as specified in Chapter 5. The SSPV at 0.5 cm gives good efficiency which can also be considered as FPV system and the design is as specified in Chapter 3. The flow of air on

top of the PV system is considered as 25 m/s as wind speed on offshore as specified in section 3.4 of the Chapter 3. In experimental setup, the PV cell considered is of 20W panel as specified in Table 3.1 in chapter 3 at section 3.2.

6.2.2   Energy Efficient Storage System (EESS)

Storage systems are an essential component of offshore microgrid systems. These systems store excess energy generated by renewable energy sources during periods of high generation and deliver the stored energy during less generation. The common storage system used in offshore microgrid systems here is the combination of LIB and SC considered as FCLIB system which is named as EESS. The maximum power charge/discharge of a single FCLIB is specified in Chapter 5 in equation 5.4.

6.2.3   Wind Energy Conversion System (WECS)

Depending on the wind speed, the turbine rotated and converts the wind speed into mechanical rotation which drives the rotor of the generator as discussed in chapter 5 in section 5.8. The WECS is considered with a DFIG having a capability of 3.7 kW at a rated voltage of 400 V and the parameters of DFIG considered in practical are listed in Table 6.1.

Table 6.1 Parameters of DFIG

Parameter	Value
Rated Voltage	400V
Rated Current	7.3A
Rated power	5HP (3.7KW)
Rated Torque	22.7 N-m
Rated speed	1500 RPM
Power factor	0.82
Phase resistance	4.6 Ω
Efficiency	86.3 %

6.2.3.1   Healthy DFIG

The DFIG rotor and stator exhibits no failure and the turbine of the WECS are working without any failure. The performance parameters of the DFIG are measured and shown in results section. When the DFIG is healthy, the rotor speed matches with the stator

rated speed and the torque generated is almost stable. The experimental DFIG machine with healthy stator and rotor called as 0 % of fault and is as shown in Figure 6.1.

Figure 6.1 Three-phase healthy DFIG

6.2.3.2 Unhealthy DFIG

The unhealthy DFIG is considered with single BRB fault but the BRB fault is considered at a level of 25 %, 50 % and 75 %. The rotor current variation when the BRB fault is considered in modeling. Faults of induction motors introduce additional frequency components in the stator current signal, therefore, stator currents as input data are widely used in condition monitoring, and the frequency spectrum of the stator current is analyzed for condition monitoring purpose. The classical approach used in an industrial environment for the detection of broken rotor bars in induction motors is based on the analysis of the stator current in steady state.

Among various spectral analysis methods, Current Signature Analysis (CSA) is one of the most popular techniques for online monitoring induction generator. For a healthy DFIG, there is symmetry of winding, and only forward rotating field exist, thus, the rotor frequency (f_2) is shown in Equation (6.1) with the multiplication of rotor slip (S) and supply frequency (f_1). The deviation in supply frequency and the rotor frequency is known as a lower side band rotor frequency (f_{b_lower}) and is given as expressed in Equation (6.2). An upper sideband current constituent is prompted by the stator winding, which is due to rotor oscillation is known as upper side band rotor frequency (f_{b_upper}) as shown in Equation (6.3). From Equations (6.1) to (6.3), the broken rotor bar fault generates a resultant current constituent of frequencies in terms of rotor slip and supply frequency and is as expressed in Equation (6.4).

$$f_2 = Sf_1 \qquad\qquad\qquad \textbf{6.1}$$

$$f_{b\_lolwer} = f_1(1 - 2S) \qquad\qquad\qquad 6.2$$

$$f_{b\_upper} = f_1(1 + 2S) \qquad\qquad\qquad 6.3$$

$$f_b = f_1(1 \pm 2S) \qquad\qquad\qquad 6.4$$

Where, f_b represents broken bars frequency, f_1 is the supply frequency, and S is the rotor slip.

In experimental set up, the rotor of the DFIG is considered as shown in Figure 6.2 and the design of rotor is in such a way that single rotor bar can be removed or attached with different percentage (25 %, 50 %, 75 %) level of broken rotor bar for performance analysis. The different levels of braking are considered as shown in Figure 6.3.

Figure 6.2 Rotor of DFIG with single rotor bar (removable and attached via welding)
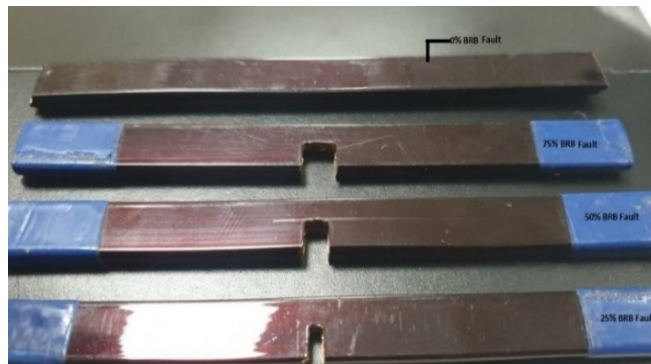
Figure 6.3 BRB with 0%, 25%, 50% and 75% of braking levels

At each iteration, the loading is considered at different no-load, half-load, and one fourth load conditions. The rotor is removed and welded with the BRB and at different load condition, the stator currents are measured with current sensor with transducer as shown in Figure 6.4.
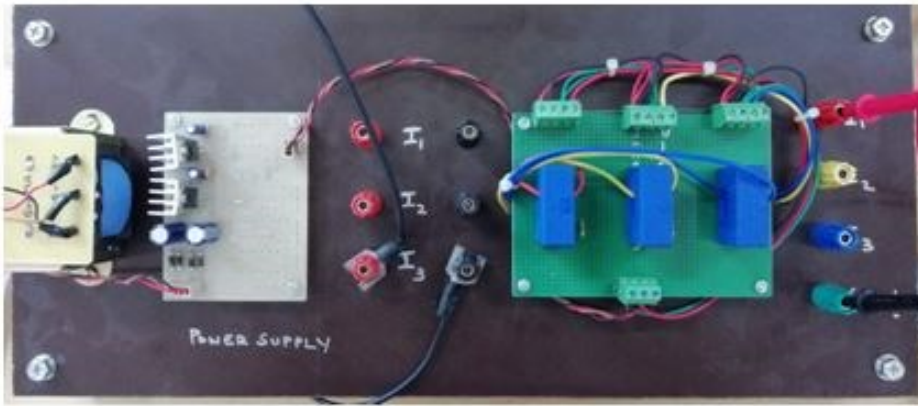
Figure 6.4 Current sensor for three-phase stator current measurement

6.2.4   Main utility grid system

The main utility grid system considered is of fossil fuels as energy sources and the output is of 5KW as specified in the Chapter 5 and the modeling in MATLAB/SIMULINK is as shown in Figure 6.5. The offshore microgrid design can be connected or disconnected from the main utility grid depending the load demand. When microgrid is connected with the utility grid, then the system is called as on grid system and if the microgrid is disconnected from the main utility grid, then the system is called as off grid system.
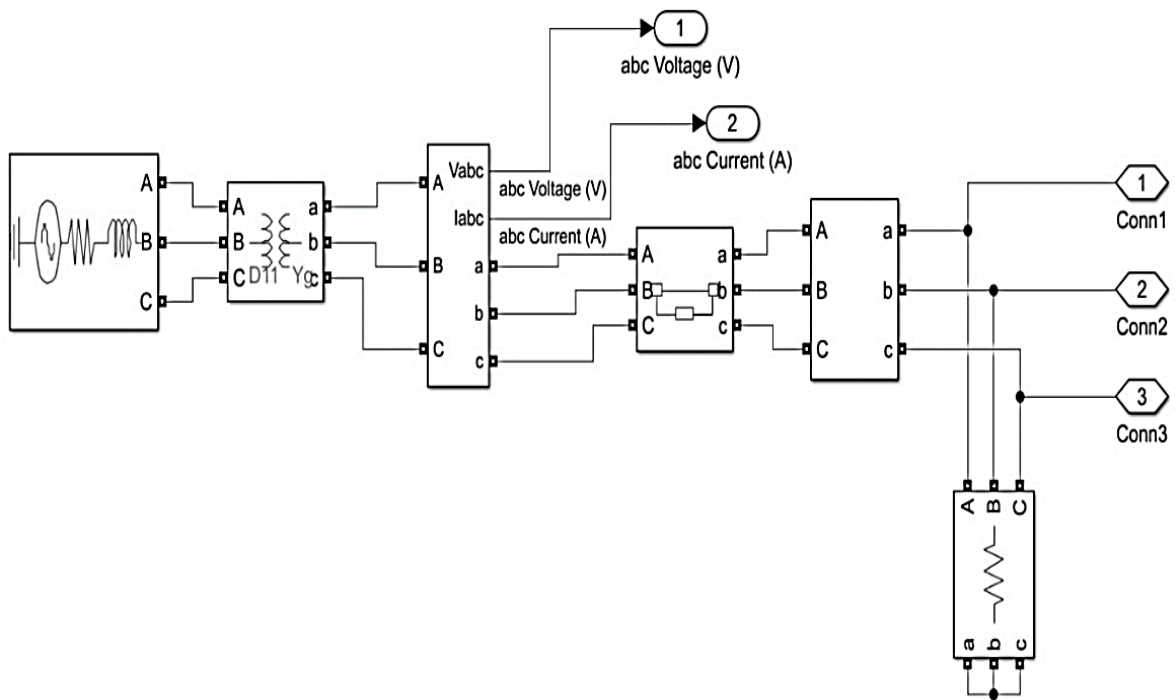
Figure 6.5 Main utility grid system model in MATLAB/SIMULINK (5KW)

6.2.5   Load demand

The load profile of the system is considered as 4-5 KVA and is variable in a day as shown in Figure 5.2 and is connected at PCC. When the load demand is less than the off-shore microgrid source output generated then the EESS stores the energy with fast charging of battery and slow discharging of SC. If the load demand is more than the generated output, then the stored energy is delivered to the load by EESS in order to provide continuous power supply. Different control systems are designed at turbine and rotor side in order to protect the grid from BRB faults.

In no-load condition, the load is zero so the current drawing is also zero. The one fourth load is considered and the current drawing will become 1.825 A and at the half load condition, the load current is 3.65A. At the above load conditions, the DFIG is considered with /without BRB fault to make healthy and unhealthy generator.

6.2.6   Offshore microgrid system in modeling and experimental setup

The full system is as shown in Figure 6.6 which is the expansion of Figure 5.4 with the combination of all RES, storage system, micro grid and load with all control systems to create offshore microgrid system.
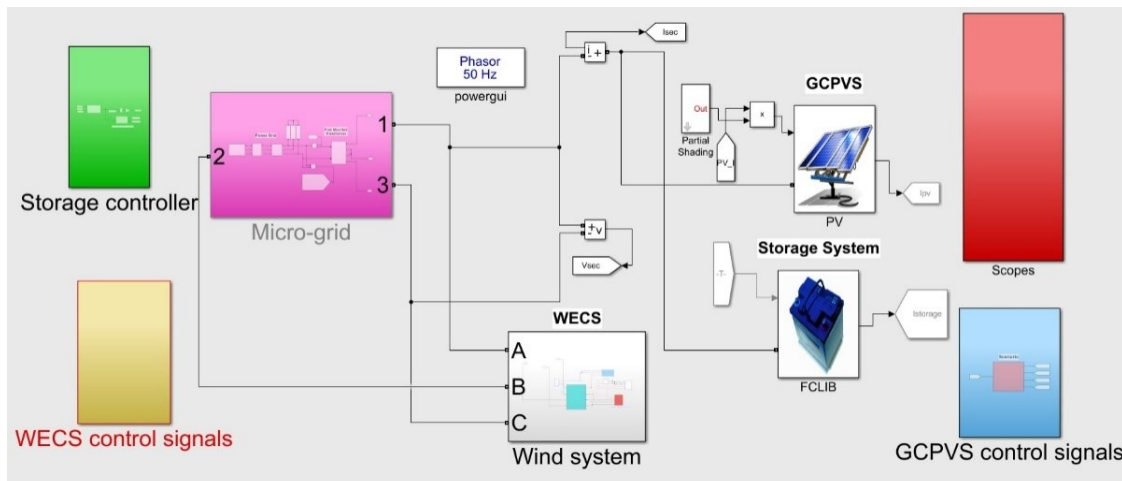
Figure 6.6 Full circuit model of the offshore microgrid system (Figure 5.4 expansion circuit)

The total offshore microgrid system work bench and schematic is considered as shown in Figure 6.12 a) and b) with the WECS with/without fault, SSPVS, and EESS.
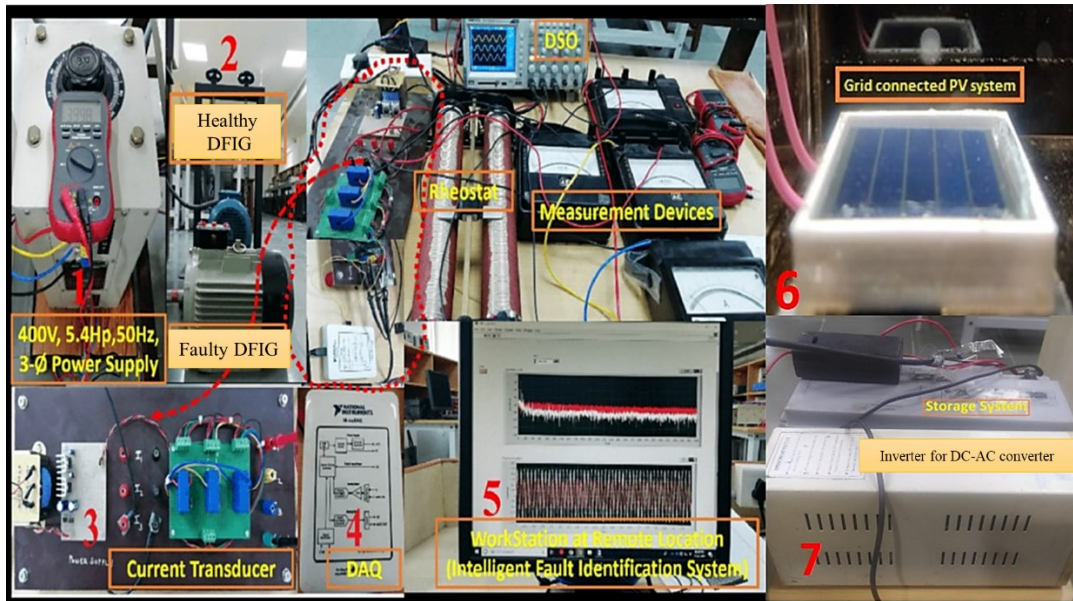
a)
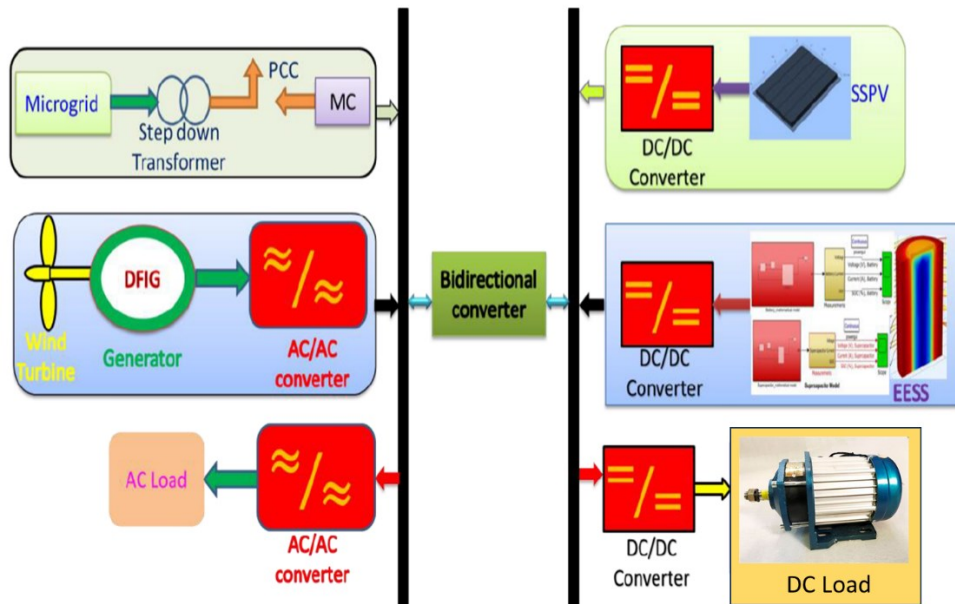
b)

Figure 6.7 a) Offshore microgrid experimental setup with DFIG stator three-phase current measurement via NI my DAQ b) Block diagram representation of the Offshore microgrid design

The NI my DAQ in Figure 6.7 a) with LabVIEW software is considered to collect the stator current data from the current sensor as shown in Figure 6.4 at both healthy and unhealthy condition of DFIG. The DFIG measured stator current variations at different levels of BRB fault and loading conditions are discussed in result section. The block diagram representation is as shown in Figure 6.7 b).

6.3   ML techniques implementation

6.3.1   Data Acquisition

The data has been obtained from the BRB fault with stator current measurement. In this study, the focus is on different Load condition of stator with different levels of BRB faults. The four cases namely: No rotor fault, 25 % rotor fault, 50 % rotor fault and 75 % rotor fault. In each case, the load is considered at no-load, one fourth load and half load conditions with 0 A, 1.825 A, and 3.65 A of current drawing respectively. All the data files have been taken from LabVIEW in .LVM file format and in each case 500 files are obtained with around 10000 data points each.

The file contains information about stator currents of three phases as I_1, I_2, I_3 and the respective Power Spectral Density (PSD) are I_1 (PSD), I_2 (PSD) and I_3 (PSD). Using python libraries, these files have been extracted into jupyter notebook. The data has been divided into train, validation, and test data. There is a total of four categories for the supervised classification and hence are labeled as classes 0, 1, 2 and 3 for no rotor fault, 25 % rotor fault, 50 % rotor fault and 75 % rotor fault respectively with all loading conditions. In each case, 50 files have been kept aside for testing purposes. The remaining data was divided into 80-20 split for training and validation.

6.3.2   Feature Selection (Extraction)

The data obtained is huge, so the models are trained using the statistical parameters from the data. The statistical features namely Mean, Median, Mode, Standard Deviation (Std), Variance (Var), Kurtosis, Skew, Max, Min, Range and Mean Absolute Deviation (Mad) are considered for training the ML algorithms. After interpretation of all the files, the statistical features are measured and all four categories are combined into a data frame. The data frame contains the statistical features for I_1, I_2 and I_3 thereby giving 34 columns and 2304 rows, and these features are the best features considered for training, testing and validation. The selected features and their definition are provided in Table 6.2

6.3.2.1   Decision Trees (DT)

DT is an important machine learning algorithm used for supervised learning and helps in classification. It follows a tree like structure and is a practical method for classification. A decision tree always starts with a root node, the node which represents the entire data, and this further gets divided into two or more sets. Splitting or dividing of data is a process of dividing any node into two or more sub nodes. A decision node is one which divides a sub node into further sub nodes. After splitting, the leaf nodes or the end nodes

are those nodes which do not have any further splitting. Initially the training data is fed into the decision tree algorithm.

The target variables are also included in the training since it is supervised learning. Then construct some decision rules from the training samples. For example, from a data set, if the value is more than 2, then the data is sent to the left half, else towards the right half. There are many ways to choose a decision. What decision trees needs to do is to find the best rule to split the node starting from the root node. For this, the algorithm starts from the root node and at each node, the algorithm calculates the information of gain. The split with the largest information gain is used to make the split and this process is repeated continuously. The process is stopped when there are no decision rules left. Overfitting is a problem which occurs in decision trees. One way to overcome this is to set a max depth for the decision tree but this comes at a cost of increasing the bias.

Table 6.2 Statistical features and definition

Statistical Feature	Definition
Mean	Sum of all elements divided by the total number of elements
Median	Middle most element in total elements
Mode	The element which occurs the maximum number of times
Std	Gives a measure of how spread the elements are from the mean
Var	Gives a measure of variability in distribution about the mean. Similar to standard deviation but difference is in the units
Kurtosis	Defines the peak of a curve. For example, if we have two curves with same standard deviation and mean, then we can differentiate between the curves using the kurtosis. More peaked the curve is, more is the kurtosis.
Skew	Gives measure of how the distribution is distributed about the central value
Max	Gives the maximum value in the list of elements
Min	Gives the minimum value in the list of elements
Range	Gives the difference between the maximum and minimum value
Mean Absolute Deviation	Sometimes there exists 2 different distributions with same mean. But some distributions may be more spread out than other distributions. To find this, there is a need to find how deviated the points are from the mean and hence mean absolute deviation can be calculated.

An important concept in decision trees is entropy. Entropy can be defined as the amount of non-uniformity present in the node of a DT. If there are two classes and both are

equal likely for example 4 classes and 2 are in category A and 2 in category B, then its entropy is high. It is given by the equation (6.5):

$$\text{Entropy} = -\sum_{i=1}^{n} p_i * log\,(p_i) \qquad\qquad 6.5$$

where, n is the total number, P_i is the probability of randomly selecting a particular example from a class i.

Now, after finding this entropy, a decision tree needs to make splits such that a term called information gain can be calculated. The information gain is defined as the difference between the entropy of the parent of a particular node and the entropy of all its children nodes. The higher the information gain, the better that variable can be used for splitting. The hyper parameters in the DT are:

➤ Max_Depth: Used to specify the maximum depth of the decision tree.

➤ Min_samples_leaf: Gives the minimum samples which are to be present in a leaf.

➤ Criterion: This is used to define how good the split is.

Figure 6.8 DT for the feature selection

The DT algorithm is considered with the statistical features selected in Table 6.2 with the stator currents variation data from the experimental setup and the 80 to 20% variation is considered for training and testing respectively. The detailed results are shown in section 6.4. The DT for the feature selection is as shown in Figure 6.8.

6.3.2.2   Random Forests (RF)

RF is a type of bagging technique. A bagging technique is a technique where a main dataset is divided into multiple samples of data and fed into multiple models which are called base models. The final prediction is taken as the majority of all the models. In RF, decision trees are used at the base models i.e. a RF has multiple decision trees and data is sampled as row sampling plus feature sampling. Now the decision trees train and give outputs accordingly. The majority of the outputs given by the decision trees is taken as the final prediction. This type of algorithm is called bootstrap aggregation.

In DT, the main problem is when the tree has a very big depth then overfitting may happen i.e. it has low bias and high variance. Overfitting is when the training accuracy is high and testing accuracy is low. To overcome this problem of overfitting, RF is used as there are multiple decision trees which split into depth, but the main advantage is for each sample of data, that corresponding DT becomes the best classifier. This helps us get a low variance and low bias for RF. The hyperparameter considered in RF is N_estimators: Number of DTs in the RF.

6.3.2.3   Logistic Regression (LoR)

LR is mainly preferred for classifications. It is used when the output variable is categorical. Here output variable refers to dependent or target variable. Example include predicting whether an email is spam or not or predicting whether a person is happy or sad. In LR, the probability of occurrence of a particular output variable is calculated. To predict the output, the independent variables are used to determine the output. There are three types of LR techniques i.e., binary, multinomial and ordinal.

  ➢ Binary logistic regression: The output can belong to only one of two categories.
  ➢ Multinomial logistic regression: The output can belong to one of three or more categories without any ordering.
  ➢ Ordinal logistic regression: The output can belong to one of three or more categories with ordering.

The question is, why not just use LR i.e. by drawing a line for all the data points and set a threshold such as values above 0.5 are category 1 and values below 0.5 are category 0. The problem is the values in the graph can occur between plus infinity and minus infinity. The main goal of LR is to determine the probability of occurrence and not the value of the variable. Since probability is estimated, the range of values varies from 0 to 1. To achieve this range, logistic function " f " is used. The LR is entirely based on the

logistic function. If the value is plus infinity, then our logistic function gives 1 and if the value is minus infinity, the logistic function gives 0. The equation of logistic function " f " is given by equation (6.7)

$$f(z) = 1/(1 + e^{-z})$$ **6.6**

Where, $z = a + b_1 x_1 + b_2 x_2 + \cdots \dots \dots + b_k x_k$, a is the bias, b is model parameters for k terms, x_1, x_2.... are data points.

The statistical software utilized will determine the coefficients b_1, b_2, … b_k and a. When X_1, X_2.... Becomes 0, then z yields the value of bias a. The hyperparameters utilized are C: defined as inverse of regularization strength, Penalty: Used to introduce L_1 or L_2 penalty into the model for train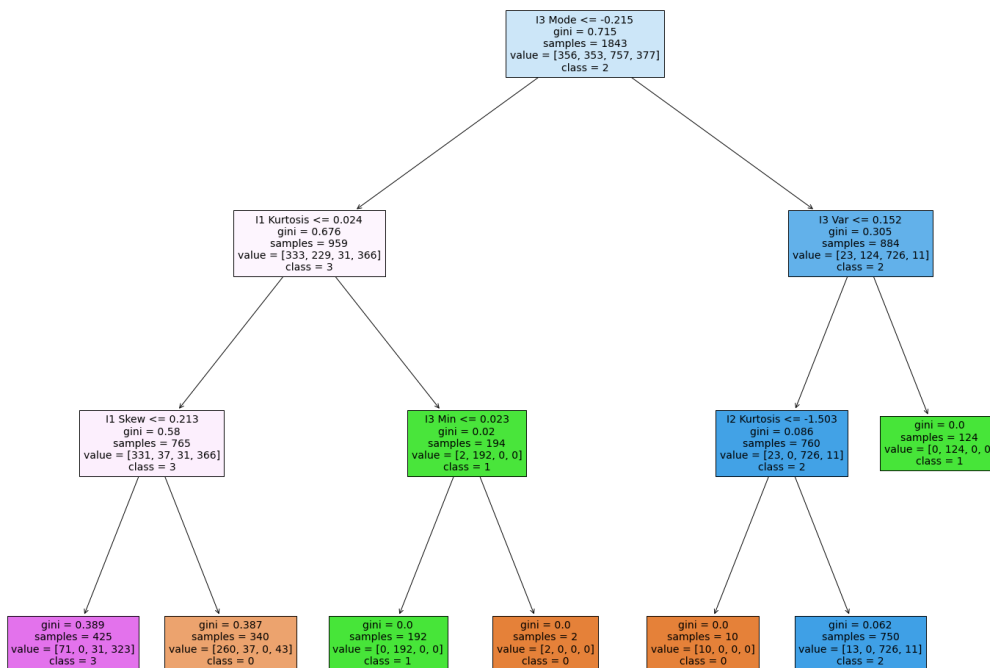ing. The LoR algorithm is considered with the statistical features selected in Table 6.2 with the stator currents variation data from the experimental setup and the 80 to 20% variation is considered for training and testing respectively. The detailed results are shown in section 6.4.

6.3.2.4 Support Vector Machines (SVM)

SVM is a powerful tool used for classification. SVM classifies a picture according to the pattern like whether a picture is a cat or a dog. SVM is also one of the best algorithms used for classification. In SVM, our target which is required to classify is represented as point in the " n " dimensional coordinate system with the features (input variables) as reference. The algorithm then does the classification by drawing a hyperplane i.e., a line in 2- dimensional or a plane in 3-dimensional space in such a way that all points of one category are on one side of the hyperplane and the other points are on the other side. There can be multiple such hyperplanes which exist. SVM tries to find the best hyperplane which divides the data. By best sense it tries to maximize the distance between the two nearest points of either category. This distance between the two points is called the margin and the points which fall exactly on the margin are called support vectors.

To determine this hyperplane, first SVM requires the training set with labels and hence it is called supervised learning algorithm. In the background, SVM tries to solve the convex optimization problem represented in equation (6.7)

$$\underset{w.b}{max} \|w\|^{-2}$$ **6.7**

Subject to the conditions $w^t x + b \geq 1$ for all $x \in C_1$ and $w^t x + b \leq -1$ for all $x \in C_2$. Where, w^t is the weight, b is the bias, x are the data points, C_1 and C_2 are the classes of classification.

In many cases the data points cannot be separated by hyperplanes like the data points form a concentric circle. In such cases, all the points are transferred to a higher dimensional space and then a hyperplane is found. This trick is called kernel trick and is widely used in SVM. For SVM, the hyperparameters tuned were C, gamma and Kernel.

➢ C: It is the penalty parameter and adds penalty to each misclassified point.

➢ Gamma: It defines the amount of curvature we need in our prediction.

➢ Kernel: Kernels are used to introduce non-linearity and transforms it in the required form.

A total of 125 fits performed on the data and obtained the best hyperparameters. Similar to the DT algorithm, in SVR algorithm also the statistical features selected in Table 6.2 are considered with the stator currents variation data from the experimental setup and the 80 to 20 % variation is considered for training and testing respectively. The detailed results are shown in section 6.4.

6.3.2.5 K Nearest Neighbors (KNN)

KNN is a very simple algorithm used for supervised classification and also for regression. In this algorithm first, the training data is plotted in the "n" dimensional space. Now during prediction of a point by taking the features as inputs, the point is plotted in the "n" dimensional space. Now the KNN algorithm tries to find the 'k' nearest neighbors of the point to estimate the class to which it belongs to. For finding the nearest neighbors, distance metrics such as Minkowski distance, Euclidean distance or Manhattan distance were used.

✓ Minkowski distance: $(\sum_{i=1}^{n} |X_i - Y_i|^p)^{1/p}$

✓ Where X and Y are data points, p is the order (an integer)

✓ Euclidean distance: In the above equation, if p=2, then it is Euclidean distance.

✓ Manhattan distance: In the above equation, if p=1, then it is Manhattan distance.

In general, for choosing K value, the following conventions may be followed.

➢ K must not be an even value for a two-class classification.

➢ K must not be a multiple of the number of classes.

For KNN, the main drawback is the time complexity. It takes a lot of time in searching for the nearest neighbors for each sample. In other words, it becomes significantly slow as the size of the data keeps increasing. To find the optimal K value, an error or an accuracy plot is used and then choose the K value which gives the lowest error rate or highest accuracy rate. The hyperparameters of the KNN are:

➢ Neighbors: Specify the number of nearest neighbors.

➢ Weights: Functions which help in predictions.

➢ Metric: Used to find the distance between the points.

6.3.3 Validation

For all the above 5 ML algorithms, the accuracy is measured. In each of the models, 80% of the data is considered as the training data and is fed for training. After training the model, 20% of data is used for testing and the extra 50 files are used for predictions to provide validation set. The prediction is done without tuning the data for hyperparameters. Then later, the data is tuned by using GridsearchCV, with the best hyperparameters calculations. The accuracy is observed with and without tuning for all the ML algorithms specified above and are listed in Table 6.3.

Table 6.3 Accuracy of the ML algorithms with/without tuning

ML algorithm	Accuracy without tuning for hyperparameters	Accuracy with tuning for the best hyperparameters
DT	83%	97%
RF	99%	100%
LR	42%	97%
SVM	42%	99%
KNN	98%	99%

From the Table 6.3, it can be observed that all ML algorithms performed exceptionally well after hyperparameters tuning and there is no overfitting.

6.4 Results and Discussion

The result section is divided as offshore microgrid system output with the addition of WECS system with healthy DFIG system in modeling and DFIG BRB fault analysis via modeling and experimental setup at different percentage of BRB fault.

6.4.1 Offshore microgrid system

The offshore micro-grid system with SSPVS, EESS, converter and micro-grid is represented as Micro-Grid System in Figure 5.4 and Figure 6.1. The voltage and current output of the offshore microgrid system is measured in per unit value and is as shown in Figure 6.9.
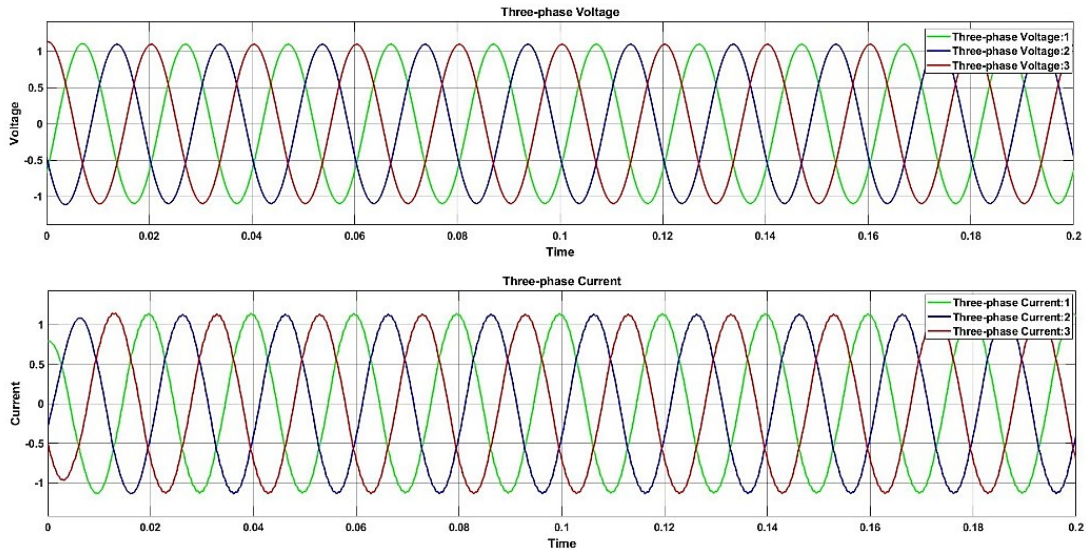
Figure 6.9 Per unit voltage and current output

In the entire offshore microgrid at PCC, the required protection with control systems are provided which will eliminate the sudden load variations, wind variations causing damage to DFIG, intermittent nature of solar. Even when the DFIG faults are considered, the grid is protected and the output voltage and current are not varied much as shown in Figure 6.9 which ensures reliability of the offshore microgrid design.

6.4.1.1.1 Unhealthy DFIG performance

The unhealthy DFIG is considered with BRB fault and different loading conditions. The measurement of stator currents in each condition are monitored experimentally, at no-load condition with stator current signature. The Figure 6.10 represents the stator currents via experimental setup at different load and BRB fault conditions.

a)

b)

c)

d)

e)

f)

g)

h)

i)

j)

k)

l)
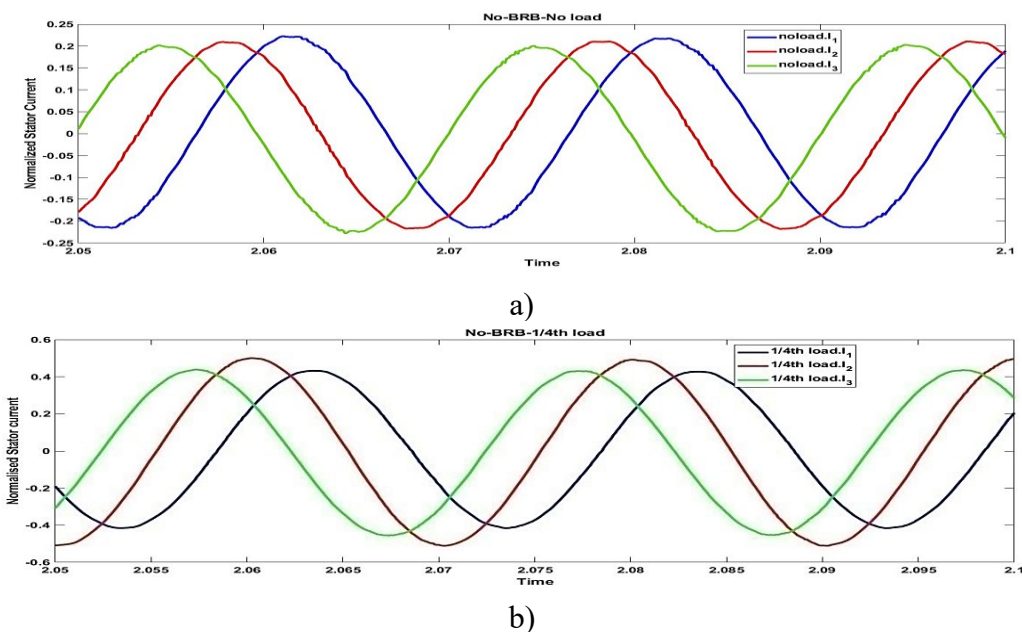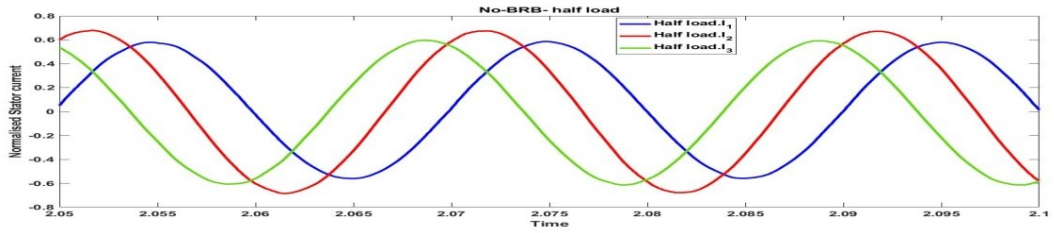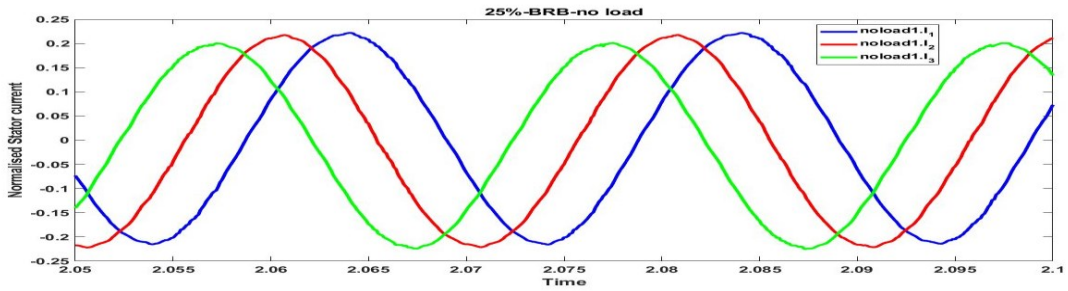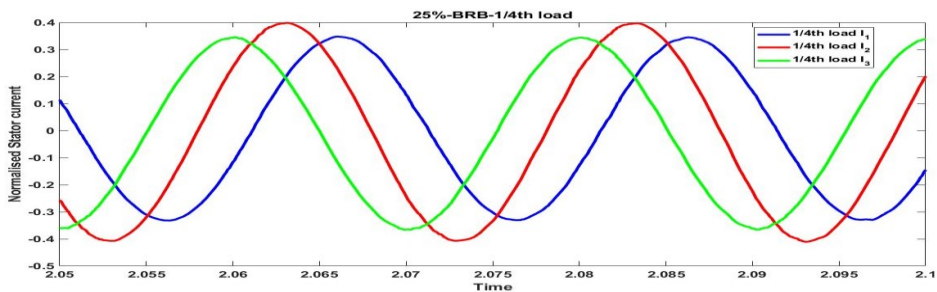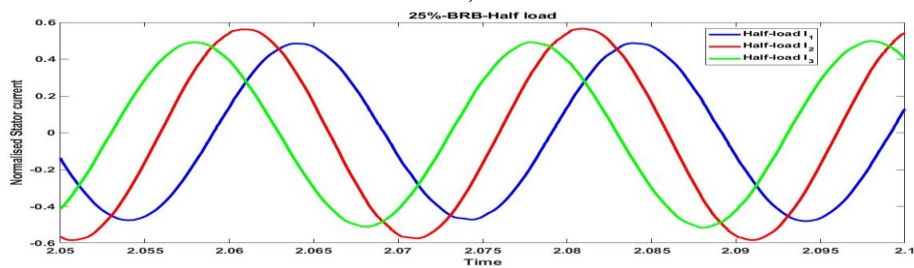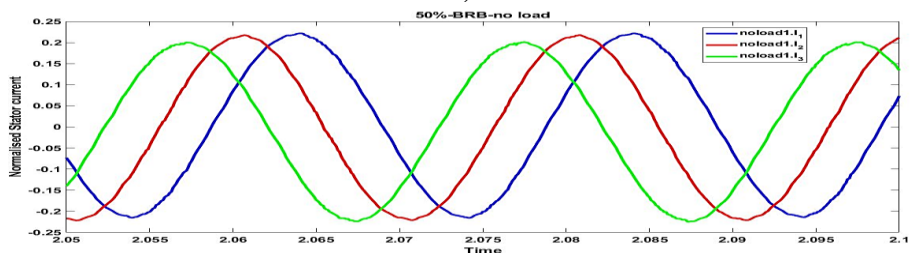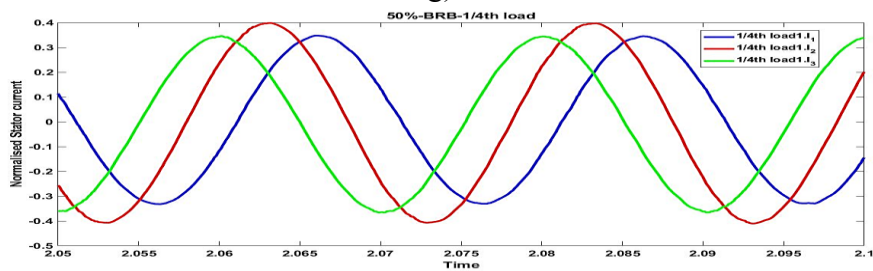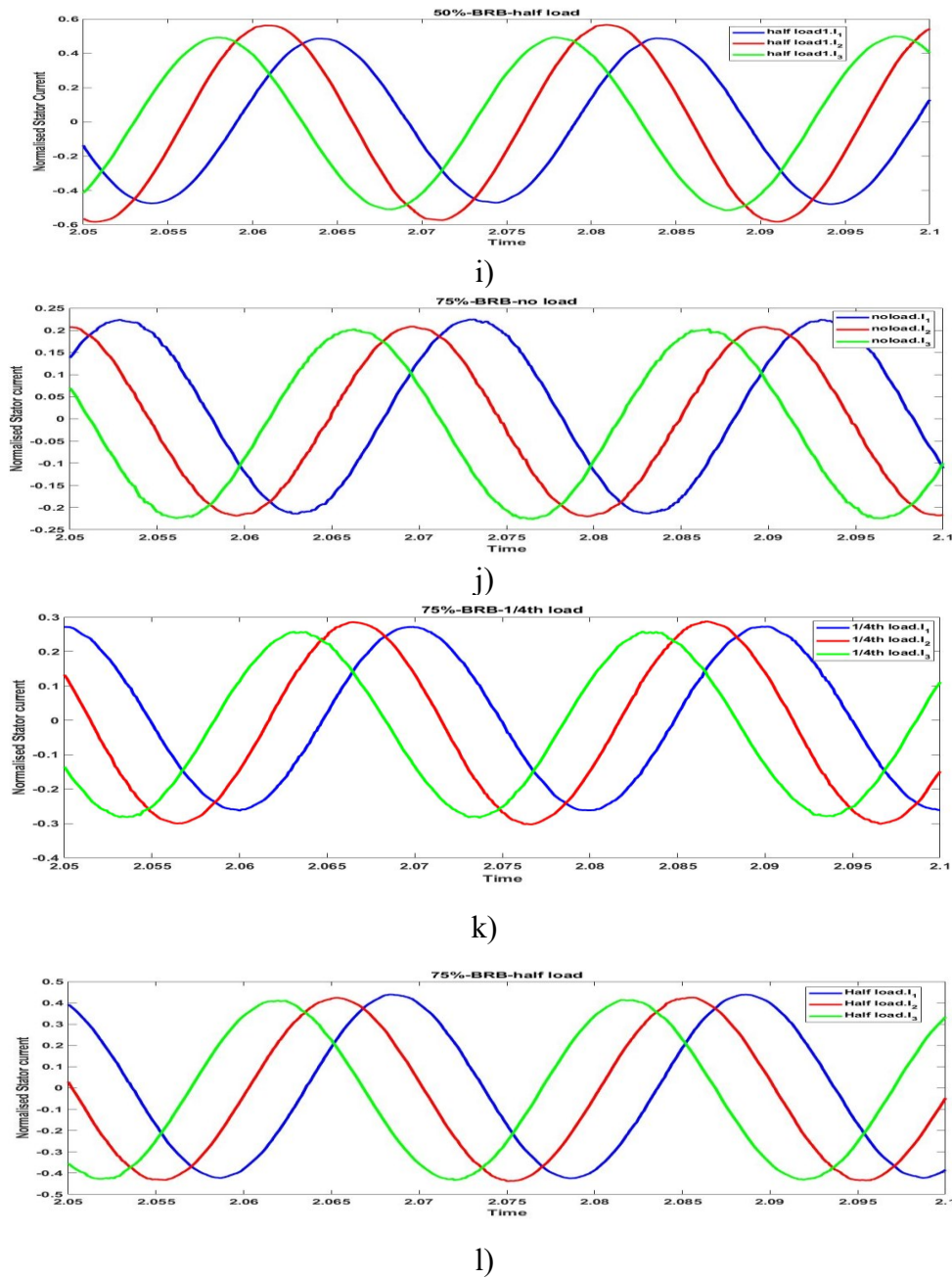
Figure 6.10 Normalized stator currents for 0 %, 25 %, 50 % and 75 % BRB faults at no load, 1/4th load and half load respectively. a) 0% BRB at no load b) 0% BRB at 1/4th load c) 0% BRB at half load d) 25% BRB at no load e) 25% BRB at 1/4th load f) 25% BRB at half load g) 50% BRB at no load h) 50% BRB at 1/4th load i) 50% BRB at half load j) 75% BRB at no load b) 75% BRB at 1/4th load c) 75% BRB at half load

From Figure 6.10, it is observed that the amplitude of the stator current varies with the percentage load and the deviation of power factor is observed with the BRB fault which

is because of the frequency variation in the system. Further to analyze more practically, the stator currents are converted into PSD values.

6.4.2 PSD waveforms at no load

The obtained stator currents are converted into the PSD values and the waveforms for the stator current with the normalized frequency are represented from Figure 6.11.
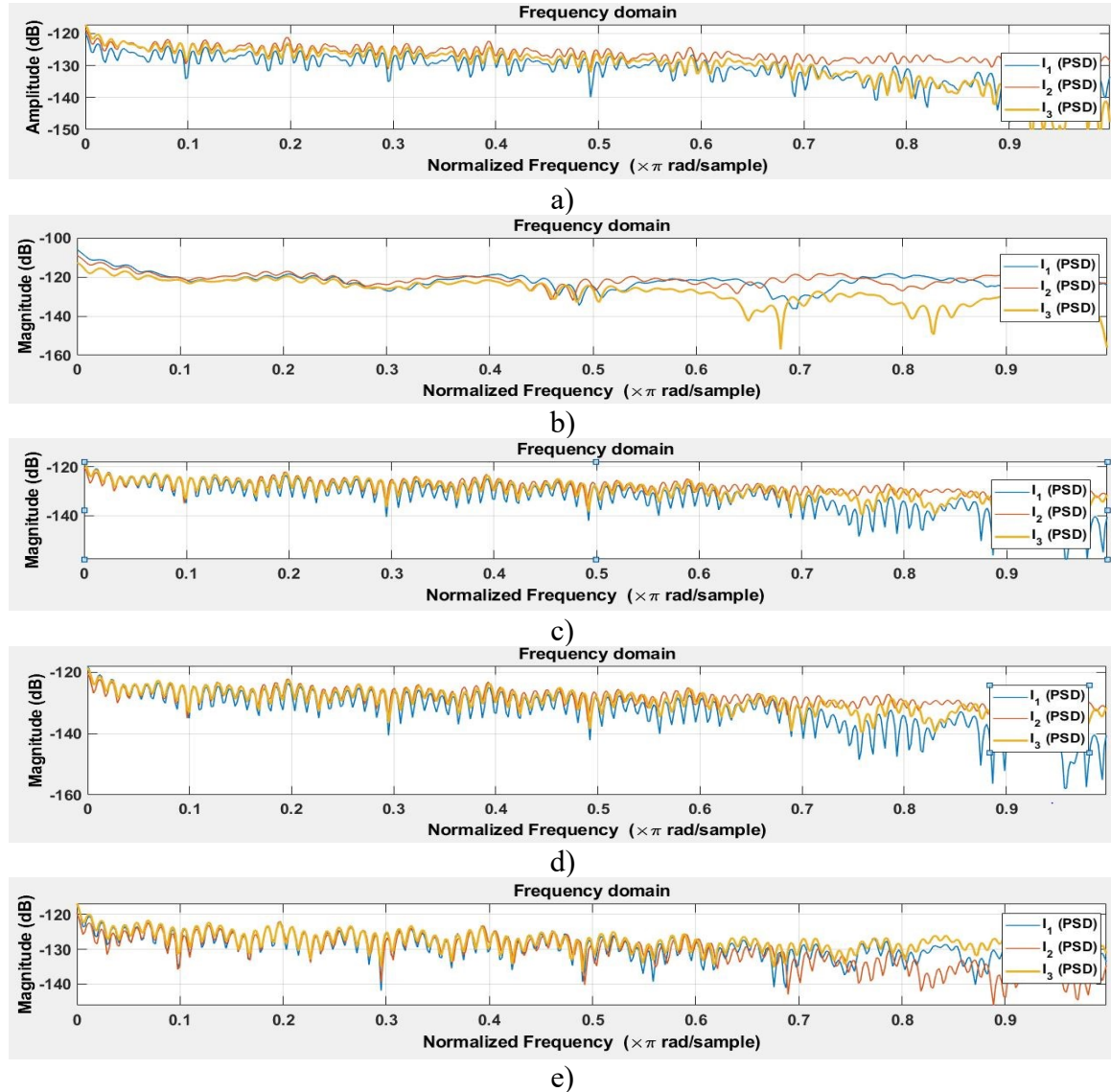
Figure 6.11 a) No BRB fault and no load condition PSD conversion b) No BRB fault and half load condition PSD conversion c) 25% BRB fault and no load condition PSD conversion d) 50% BRB fault and no load condition PSD conversion e) 75% BRB fault and no load condition PSD conversion

From Figure 6.11, it can be observed that, the stator currents magnitude becomes almost equal making the DFIG unstable. As the single BRB fault is considered in

experimental and simulation, the impact of the DFIG on offshore microgrid is less but it creates sudden drop of voltage and currents with frequency mismatch.

6.4.3   ML techniques validation

Now after performing the classification and obtaining the metrics on the training and testing sets respectively, the test data of 50 files in each condition are considered and validated the predictions on the trained models with hyperparameter tuning to see which ML algorithm performed best. The Table 6.4 shows the accuracy of the all ML techniques after hyperparameter tuning for validation.

Table 6.4 Accuracy of ML techniques during validation

ML algorithm	Accuracy after tuning
DT	80%
RF	85%
LR	92%
SVM	94%
KNN	96%

From the above results, it can be clearly seen that KNN has given the best accuracy of 96% and DT gave the least accuracy of 80% on the validation data.

6.5   Conclusion

In conclusion, the integration of PV and energy storage systems with WECS presents significant potential for improving the reliability and efficiency of renewable energy systems. Further research and development in this area helped to address the challenges associated with the integration and advance the adoption of renewable energy sources. An offshore microgrid system is designed to reduce the carbon emissions with the use of RES and to provide reliable and sustainable energy to the loads at offshore/onshore. The design of offshore microgrid with the integration of SSPVS, EESS with WECS are considered without fault consideration via mathematical modeling. The SSPVS and EESS outputs are analyzed with techno-economic analysis in Chapter 5. In this chapter, it is observed that, the WECS and the offshore microgrid are giving appropriate result, where the grid current and voltage outputs are reaching the per unit configuration. A turbine system coupled with DFIG is considered as the WECS in this case.

The turbine is considered with no-fault condition with input speeds of 25m/s. Similarly, DFIG is considered with/without single BRB fault. The different percentages of single BRB faults are considered by intentionally imposing in DFIG, and collecting of normalized stator currents for three phases using a three-phase current sensor. The current sensor collected data is utilized and also converted into Power Spectral Density (PSD) via NI my DAQ with LabVIEW software. Five classification algorithms like SVM, LR, DT, KNN, and RF are developed for DFIG fault forecasting.

The accuracy is measured for these algorithms by finding statistical features via ML techniques. For the best forecasting, GridsearchCV is utilized to obtain best fit hyperparameters for each individual algorithm. Without tuning for hyperparameters, during testing all ML algorithms gave different efficiencies and with tuning they gave almost above 95% efficiency. With best hyperparameters, the KNN is providing better validation accuracy of 96%and DT gave the least accuracy of 80%. With the implementation of KNN in the WECS, the condition monitoring of the DFIG can be done so that the prediction of the machine is exhibited with timely response of the fault condition monitoring.

CHAPTER 7

CONCLUSION

7.1   Conclusion of The Research

The Modeling and Simulation of Submerged Solar PV (SSPV) with an Efficient Energy Storage System (EESS) Integrated with wind fed Offshore Micro Grid (OMG) is implemented and explained in above chapters. From an extensive literature survey done, it has been observed that by decreasing the temperature on the surface of PV cells, efficiency of the cells can be improved tremendously. The temperature can be decreased with the use of two cooling techniques: forced cooling and natural cooling. Forced cooling systems has additional electrical equipment which consumes power more than the generated power and natural cooling technique has different construction for installation of PV panels. It is also observed that while comparing the literature based on forced and natural cooling techniques, the natural cooling techniques were mostly preferred with the PV systems. This is mainly due to the effective operation of PV cells working with natural cooling techniques as well as the cost factor when taken into account.

The natural cooling system involves FPV systems. In FPV systems, the SSPV system type is mostly considered. The factors affecting the PV cell efficiency are majorly eliminated with the SSPV systems. Even water has two types of optical properties: inherent and apparent optical properties, which shows the presence of irradiation at different water depths. The spectrum has different wavelengths and the distribution of wavelengths inside water also varies with the presence of particulate matter and type of water (normal, ocean, lake, organic etc.,). At different depths, the optical properties of solar cells vary with the environmental conditions but are suitable for SSPV systems to operate and produce electricity.

SSPV system saves valuable land for tourism, mining, agricultural, and other land-impulse actions and turns non-profit generating and unexploited surface of water into profit-oriented PV power plants. The Hydro-optical characteristics of solar cells proves the irradiation presence in water and the physical properties of water makes decrease in temperature by increasing the efficiency of submerged PV cells. On the whole, mentioned above advantages will allow submerged PV system, suitable for energy generation in the

159

present scenario and is discussed in Chapter 2 and the evolution of PV till date with different cooling techniques and efficiency improvement are also discussed.

In order to model the SSPV system, the PV cell has to be designed first and then the submerged conditions can be evaluated and is discussed in Chapter 3. The PV cell/panel is designed mathematically and obtained the characteristics at different irradiations and temperatures, where the PV cell/panel is having higher V_{oc} and lesser I_{sc} creating higher P_{max} with the decrease in temperature (0, 25, 51 and -45 ^{0}C) and irradiation (1000, 600, 200 W/m^2). The mono-crystalline Si PV cell/panel is modeled as shown in Figure 3.12 and 3.16 in an experimentally validated Multiphysics environment, and the I-V and P-V performance characteristics are plotted as shown in Figure 3.28 (a) and (b). The efficiency of the simulated PV cell is 19.69 % which is almost equal to the efficiency of the commercially available mono-crystalline Si (19.69 %) experimental and data sheet data as tabulated in Table 4. The PV cell is also modeled using Ge, GaAs, and InP materials, as discussed in section 3.2.2, at 25^{0}C at both cell/panel level and at the cell level, the GaAs have 20.53% efficiency while the mono-crystalline Si has 19.69% efficiency. The cell level model is extended to the panel level with material and temperature variations where GaAs have achieved 23.27 % (3 % increase) efficiency while Si has 19.69 % efficiency, the same as a cell. The materials efficiency at STC is as follows: GaAs > mono-crystalline Si > InP > Geand the GaAs exhibit 28.57 % at -45^{0}C. The efficiency of the PV cell/panel is estimated based on the thermal losses, bandgap, and thickness of the model. It is observed that the Joule heat distribution is more in Ge, and the order of Joule heat distribution is Ge (**234KW/m^3**)> Si (**61KW/m^3**) > GaAs (**5.05KW/m^3**)> InP (**3.95KW/m^3**) representing less joule heat in InP throughout due to the thickness of PV.

The prediction is done to predict the values of current and power to obtain I-V and P-V characteristics of PV cells with all the other parameters and also to obtain efficiency. The LR, PR, SVR, and KRR algorithms are chosen for the prediction due to data points availability from low to medium and the popularity of algorithms for the characteristics. LR provides less accuracy because of the non-linearity in the characteristics, which is almost less than 80% of the R^2-score. Similarly, PR and KRR resulted in> 85% R^2-score. The degree 4 is the best hyper parameter of PR, the best fit hyper parameters for I-V characteristics are C = 1000, ϵ = 0.01 and γ (for RBF kernel) =1and for P-V characteristics C = 1000, ϵ = 0.10 and γ (for RBF kernel) =1 in SVR prediction. Similarly, for KRR, the

best hyper parameters for I-V characteristics are alpha (α) =0.001 and gamma (γ) =1.0, using RBF kernel, and similarly for P-V, alpha (α) = 0.1 and gamma (γ) =100.0, using a polynomial kernel.

The GaAs efficiency is 20.52 % at 25^{0}C, 21.23 % at 15^{0}C, and 24.97 % at -18^{0}C, and the mono-crystalline Si has 19.32 % efficiency at 25^{0}C, 20.11 % at 15^{0}C, and 20.92 % at -18^{0}C both using PR and KRR ML algorithms. From this, it can be observed that GaAs provides higher efficiency at all levels of temperatures through modeling and prediction. In materials point of view, GaAs is capable of providing higher efficiency (28.57% at -45^{0}C) under different environmental conditions. With temperature variations, GaAs and Si materials are capable of higher efficiency with the decrease in temperature from +51^{0}Cto -45^{0}C via modeling. With ML techniques, the PR is capable of predicting the data with less data provision by eliminating over/under fit of data, but the degree of polynomial is not fixed, and KRR is capable of predicting (92.23%) the data at different intervals of temperatures for different materials with higher data input for training and testing.

Implementing SSPV with Si and GaAs materials is done both mathematical and Multiphysics modeling and the performance characteristics are obtained as shown in section 3.5.6. The KRR and SVR ML algorithms are implemented for SSPV till 0.5 cm and validated at 0.3 cm of water depth which gave better efficiency. The GaAs is giving better efficiency compared to Si at different depths of water and KRR is giving more efficiency at both current and power prediction when compared to SVR.

The energy generated from the source has to be stored efficiently in order to reduce the losses and an EESS is developed in Chapter 4. firstly, a simplified mathematical equivalent model was used in this work to examine and evaluate the effect and severity of charge/discharge rate of lithium-ion battery (LIB) and Super Capacitor (SC). The SoC, current, terminal voltage, and lifetime properties of LIBs were determined with the identical input parameters. Furthermore, it has been shown that the response of discharge characteristics for LIBs results in an extended lifespan for useable capacity extraction. As a result, it might be observed as an indicator that LIBs with higher energy capacity would be used in renewable generation-based stationary applications.

Accordingly, the system with FCLIB having SC, results in equal cost with better performance with fast charging capability of LIB. When using architecture of two SCs with

a greater energy level and charging one battery, the battery fast charging to 100 percent SoC takes 203 seconds (3.38 minutes) but reaches very high voltages and currents. When the internal DC resistance of the SC is 0.5 ohm, the SC exhibits aberrant behavior when operating from 100% to more than 100% SoC. Furthermore, the battery exceeds its rated voltage, resulting in battery damage. When the internal DC resistance of the SC is reduced (89e-3) and at SC high energy levels, the battery charges fast, 13.67minutes with one battery and one super capacitor (1B1S) topology and 80% is achieved at 6.7 minutes. The initial current and voltages are higher, causing damage to the LIB and SC as temperatures rise.

In extension to the charge and discharge cycle function, the HOMER-Pro software was used in Chapter 5, to do a techno-economic study of LIB and SC with GCSSPVS, considering resource and actual commercial load demand profiles data provided by TSSPDCL. As a consequence, the system with a LIB had a CoE of 0.33 $/kWh, whereas the system with a LIB and SC had a CoE of 0.35 $/kWh. The PNC of the system with LIBs, on the other hand, is $14,990.8, while the PNC of the system with LIB and SC is $15,726.86.

From the investigations, FCLIB with SC topologies can be recommended depending on the time required for fast charging considering battery management system with cooling technologies. However, if fast charging is considered/not considered, the cost of the system will be same as FCLIB from Table 5.3 & 5.4 as depicted with GCSSPVS. So FCLIB can be considered with economic and optimal storage solution even after connecting with the GCSSPVS selecting best FCLIB topology.

An offshore microgrid system is designed to reduce the carbon emissions with the use of RES and to provide reliable and sustainable energy to the loads at offshore/onshore. The design of offshore microgrid with the integration of GCSSPVS, EESS with WECS are considered without fault consideration via mathematical modeling. The GCSSPVS and EESS outputs are analyzed with techno-economic analysis in Chapter 5. In this chapter, it is observed that, the WECS and the offshore microgrid are giving appropriate result, where the grid current and voltage outputs are reaching the per unit configuration. The WECS is considered as mix of turbine system and DFIG. The turbine is considered with no-fault condition with input speeds of 25m/s. Similarly, DFIG is considered with/without single BRB fault. The different percentages of single BRB faults are considered by intentionally

imposing in DFIG, and collecting of normalized stator currents for three phases using a three-phase current sensor. The current sensor collected data is utilized and also converted into Power Spectral Density (PSD) via NI my DAQ with LabVIEW software. Five classification algorithms like SVM, LR, DT, KNN, and RF are developed for DFIG fault forecasting. The accuracy is measured for these algorithms by finding statistical features via ML techniques. For the best forecasting, GridsearchCV is utilized to obtain best fit hyperparameters for each individual algorithm. Without tuning for hyperparameters, during testing all ML algorithms gave different efficiencies and with tuning they gave almost above 95% efficiency. With best hyperparameters, the KNN is providing better validation accuracy of 96%and DT gave the least accuracy of 80%.

Overall, the research shows that by utilizing natural cooling techniques and SSPV systems, along with the use of high-efficiency materials such as GaAs, the efficiency of PV cells can be significantly improved, making them a viable option for sustainable energy generation. The multiphysics modeling and the mathematical design of SSPV is developed from the basic PV cell/panel model. The FCLIB is modelled with the combination of LIB and SC and working as EESS. The EESS gives the effective storage and also efficient performance resembling the fast charging capability for the RER. The WECS is modeled with the DFIG and it provides the with/without BRB fault conditions exhibiting efficient performance when integrated with the SSPV, EESS and control systems at PCC. The findings of this research can provide valuable insights for future research in field of renewable energy.

7.2 Limitations of Research

The offshore microgrid is designed with integration to the general fossil fuels microgrid system of 5KW, which can cause little carbon emissions effecting the surrounding environment. Some of the limitations are exhibited with experimental configurations of SSPV, where the prototypes of the modeling are considered and the depths are considered only till 1 m of water depth due to computation limit. The EESS is implemented only for the AC loads after integrating with the microgrid, SSPV, and WECS. The WECS design is considered only with the BRB fault in DFIG and other faults exhibited by offshore harsh environment are not considered. The Multiphysics environment takes more computational time because of the modules used in the design environment and can be eliminated with the use of High Performance Computer (HPC) or with the prediction algorithm implementations. The ML algorithms used for prediction of PV performance in

normal and submerged conditions, and feature selection used for DFIG system BRB fault analysis is limited to five algorithms each.

7.3 Future Scope

The offshore microgrid considered is of 5KVA variable load in a day. It can be modeled for the high load capacity with more generation capability from the RER. The offshore microgrid is the combination of only PV and wind combination, it can also be included with other resources like tidal and wave energy.

- ➢ The SSPV design can be further implemented for different irradiation and water conditions and also depth can be increased with high performance computing system.
- ➢ The SSPV installation in real time with the comparison of FPV can also be down with the cost, operation and maintenance analysis.
- ➢ The EESS designed can be implemented for the Electrical vehicle application by making use of SC for instantaneous energy release to provide quick start ignition.
- ➢ The EESS can also be implemented as a digital twin to measure the performance of energy charge/discharge with different application by decreasing the carbon emissions.
- ➢ The WECS designed can be further implemented with different types of faults like STTF, SITF, turbine faults etc.,
- ➢ The ML algorithms used for PV performance in normal and submerged condition prediction can also be used for combined performance evaluation of the offshore microgrid system with the relatable grid data and load data.
- ➢ The ML algorithms used for DFIG fault analysis with feature selection can also be implemented for the other faults exhibited with the offshore marine environment. Other than these ML algorithms, other algorithms can also be implemented for the prediction and fault analysis.
- ➢ Different faults during the integration of the resources can also be reduced with the use of different control techniques like impedance matching circuit, voltage and current control circuits at PCC to reduce impedance, voltage and current mismatches.

Appendix: A

Prediction of PV Cell Parameters at Different Temperatures via ML Algorithms and Comparative Performance Analysis in Multiphysics Environment

PV Panel modeling: The modelling of PV panel involves, geometry and material selection.

PV panel geometry:

| a) | b) |
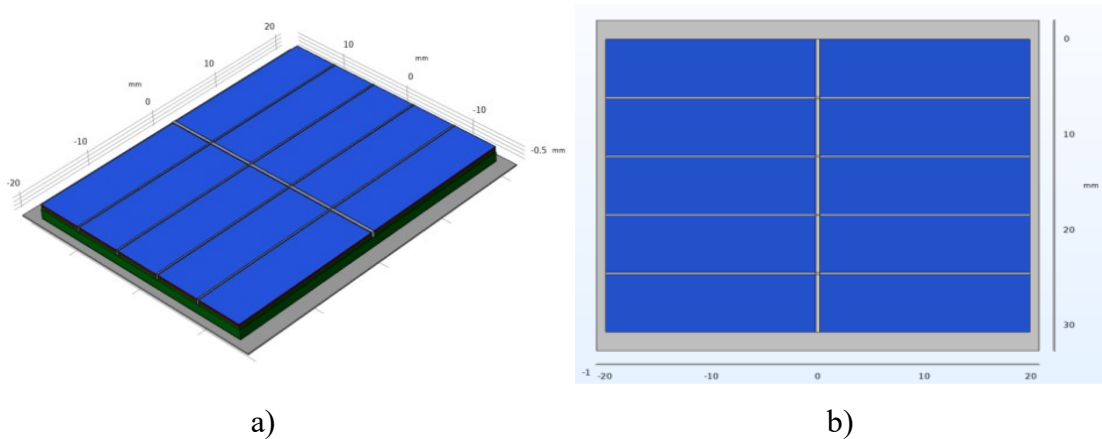
Fig. A1. a) 3-D view of PV solar panel, b) Top-view of 3-D solar panel.

The PV solar panel with all the layers is as shown in Fig. A1 a), and the top view of the panel is represented in Fig. A1 b). The panel's dimensions are $42.0 \times 35.0 \times 2.0$ mm.

PV panel material selection:
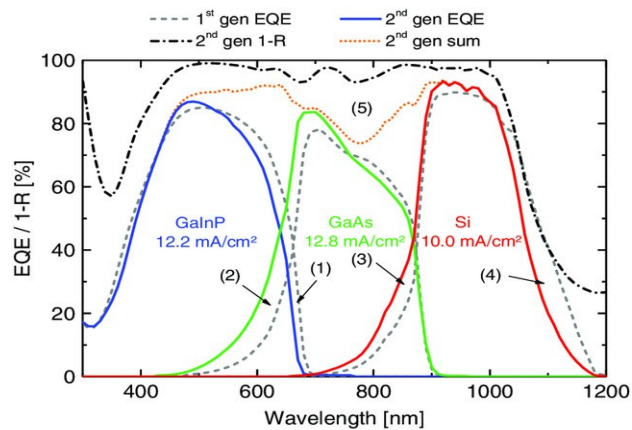
Fig. A2. EQE of Si (Red), GaAs (Green), and GaInP (Blue) for the fabrication of SPV cells [1]

The GaAs have high external quantum efficiency in the visible spectrum compared to both Si and InP, as shown in Fig. A2. Due to less joule heat production and high-temperature resistance, GaAs material is mostly used for space applications irrespective of cost.

Support Vector Regression (SVR):

The flow chart for SVR is as shown in Fig. A3 where the Grid search CV is used to find the best hyper parameters after testing with different combinations of hyper parameters.
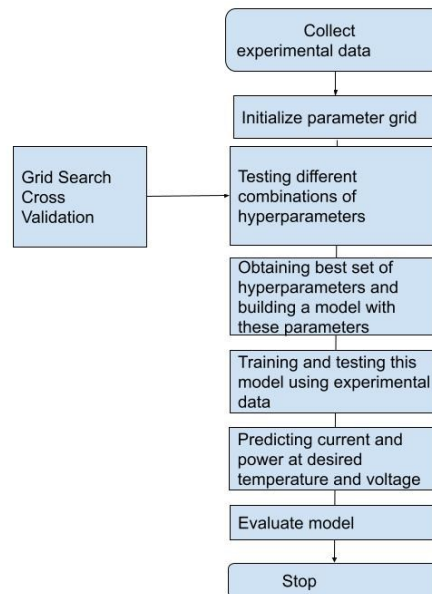
Fig. A3. Flow chart for SVR with best hyper parameters selection

All these ML techniques have two sections in common: Data import & training, and prediction method technology implementation till plotting the data. The flow of data import and training is as shown in Fig. A4. Similarly, Fig. A5 shows the flow of prediction techniques implementation.
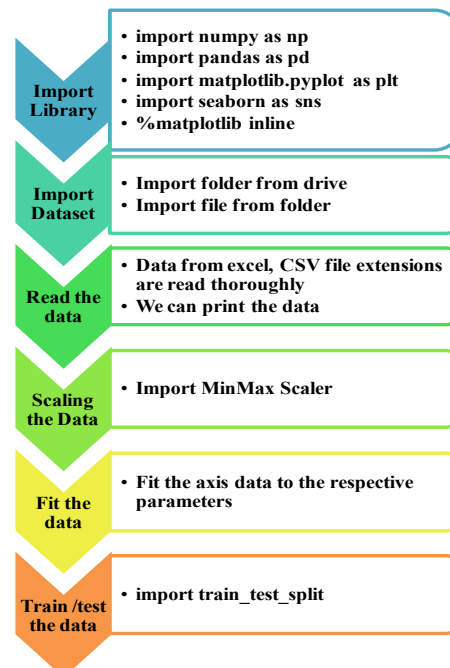
Fig. A4. Flowchart for Data import and training
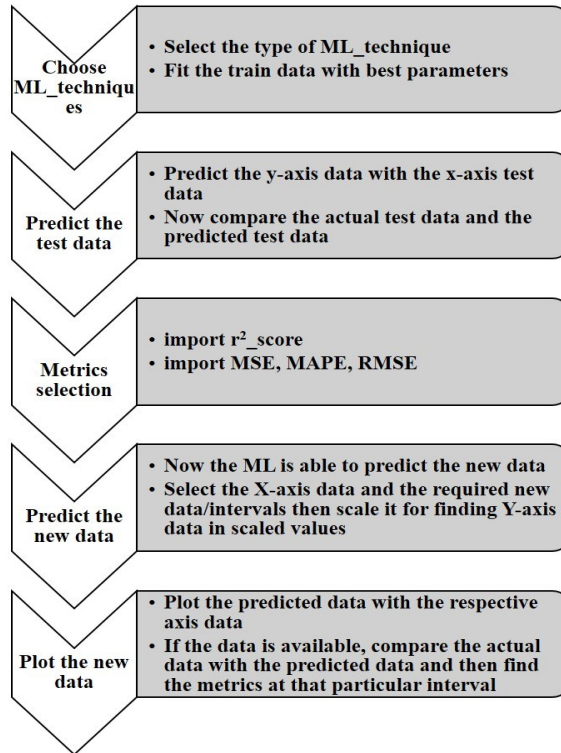
Fig. A5. Implementation of prediction techniques flow

Joule heating distribution:

a)

b)

c)
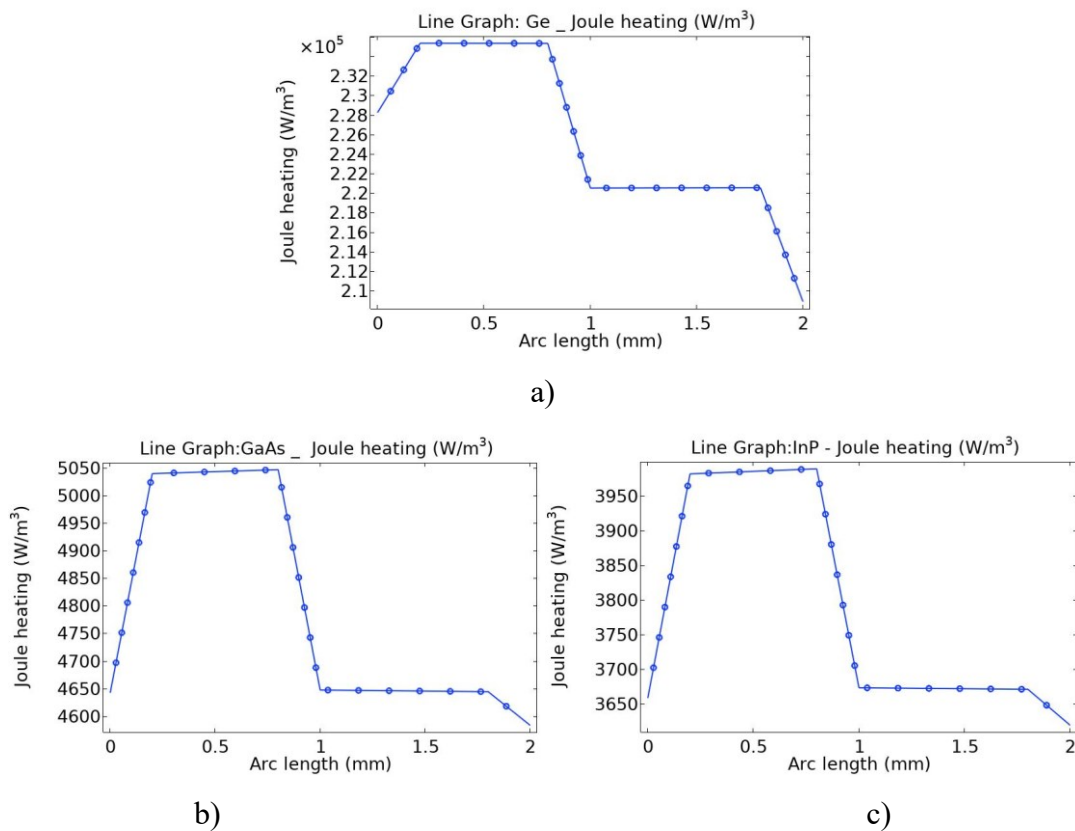
Fig. A6. (a) The joule heating of Ge, b) The joule heating of GaAs, and c) The joule heating of InP - represented at 25^0C.

The individual material joule heat distribution is presented in Fig.A6 a), b), and c) with a consideration of cutline in the geometry across the axis of depth. The heat transfer in the material varies with length of the arc considered as shown in above Fig.A6.
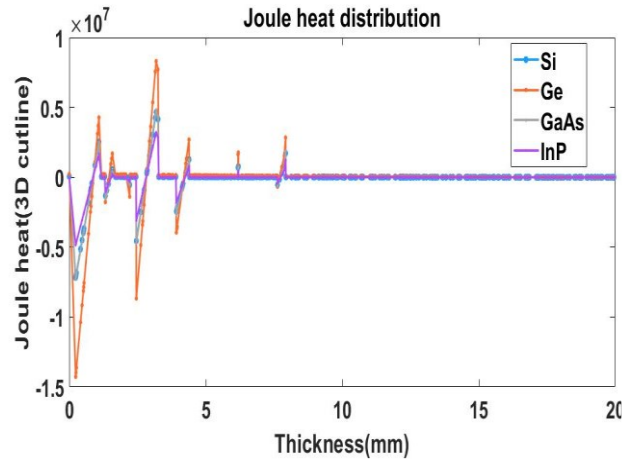
a)
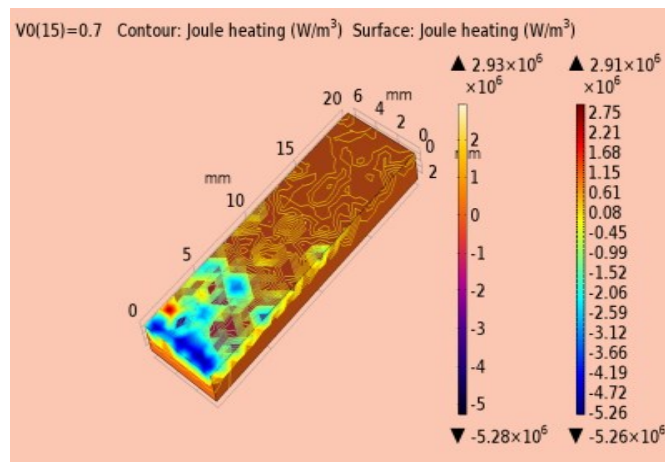
b)

Fig. A7. a) Joule Heat distribution across 3D-axis cutline on PV cell for Si, Ge, GaAs, and InP b) 3D-representation of joule heating in contour and surface of PV cell

In the modeling, a 3-D axis cutline is drawn along 20mm length and the joule heat of Si, Ge, GaAs and InPare measured and drawn as shown in Fig. A7 a). The joule heat on the surface and the contour varies along legth, width and height. The joule heat variation on contour and surface are represented as shown in Fig. A7 b).

ML based prediction of solar PV characteristics:

The flow chart for the ML techniques implementation for mono-crystalline Si at 25^0C is as shown in Fig. A8 and the best hyper parameters from 25^0C prediction are utilized further with the addition of 25^0C data to the previous training data.
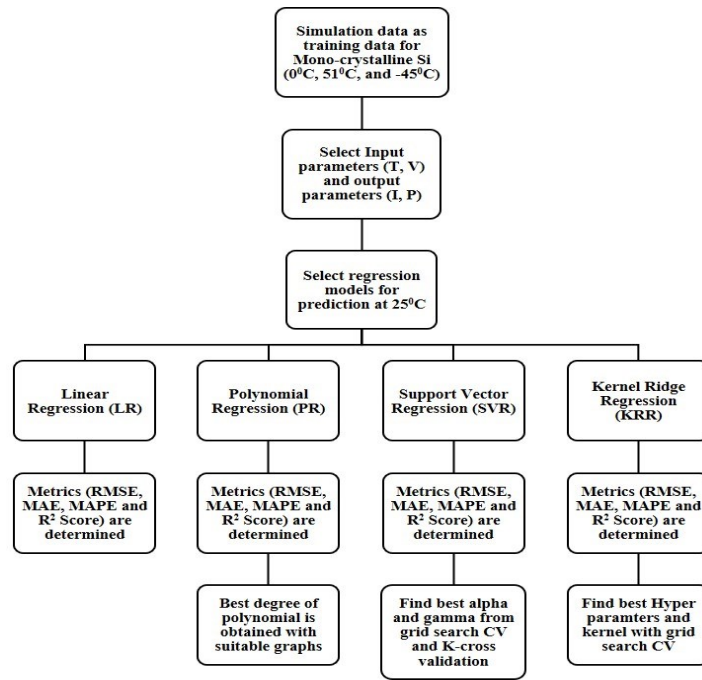
Fig. A8. Flow chart for mono-crystalline Si prediction with ML techniques

Linear Regression (LR):

a)   b)
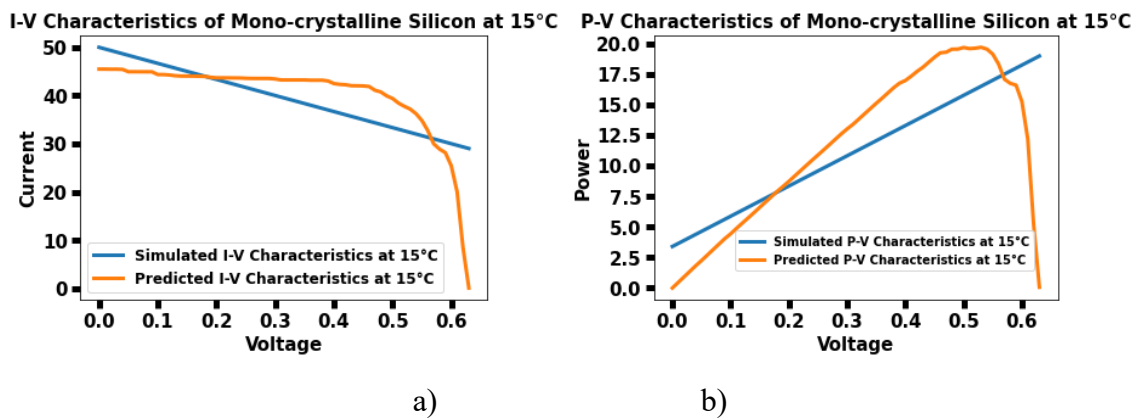
Fig. A9. a) I-V characteristics prediction at 15^0C for mono-crystalline Si b) P-V

characteristics of mono-crystalline Si at 15^0C

a)   b)
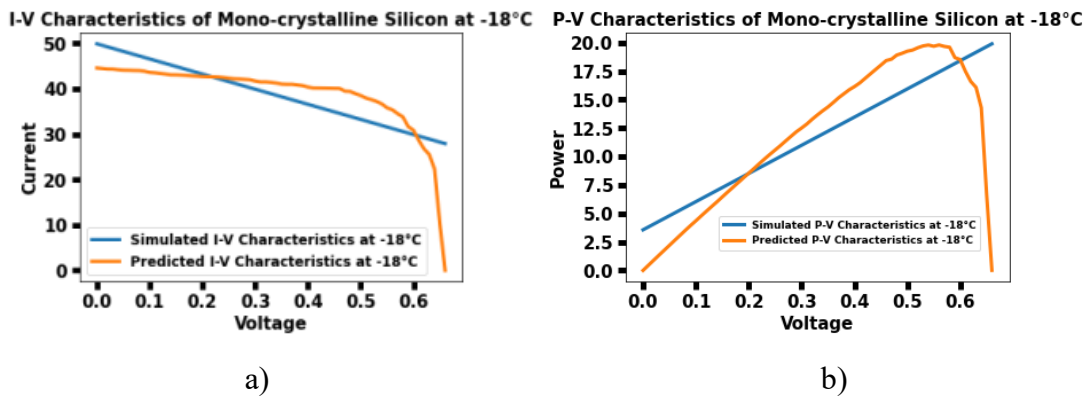
Fig. A10. a) I-V characteristics of mono-crystalline Si predictions at -18^0C b) P-V

characteristics of mono-crystalline Si predictions at -18^0C

The I-V and P-V characteristics of mono-crystalline Si are given in Fig.A9 a), b) and Fig. A10 a), b) at 15^0C and -18^0C respectively. The non-linearity in the output values makes the LR not adaptive for the PV panel performance analysis.

Polynomial Regression (PR):

a)   b)

c)   d)
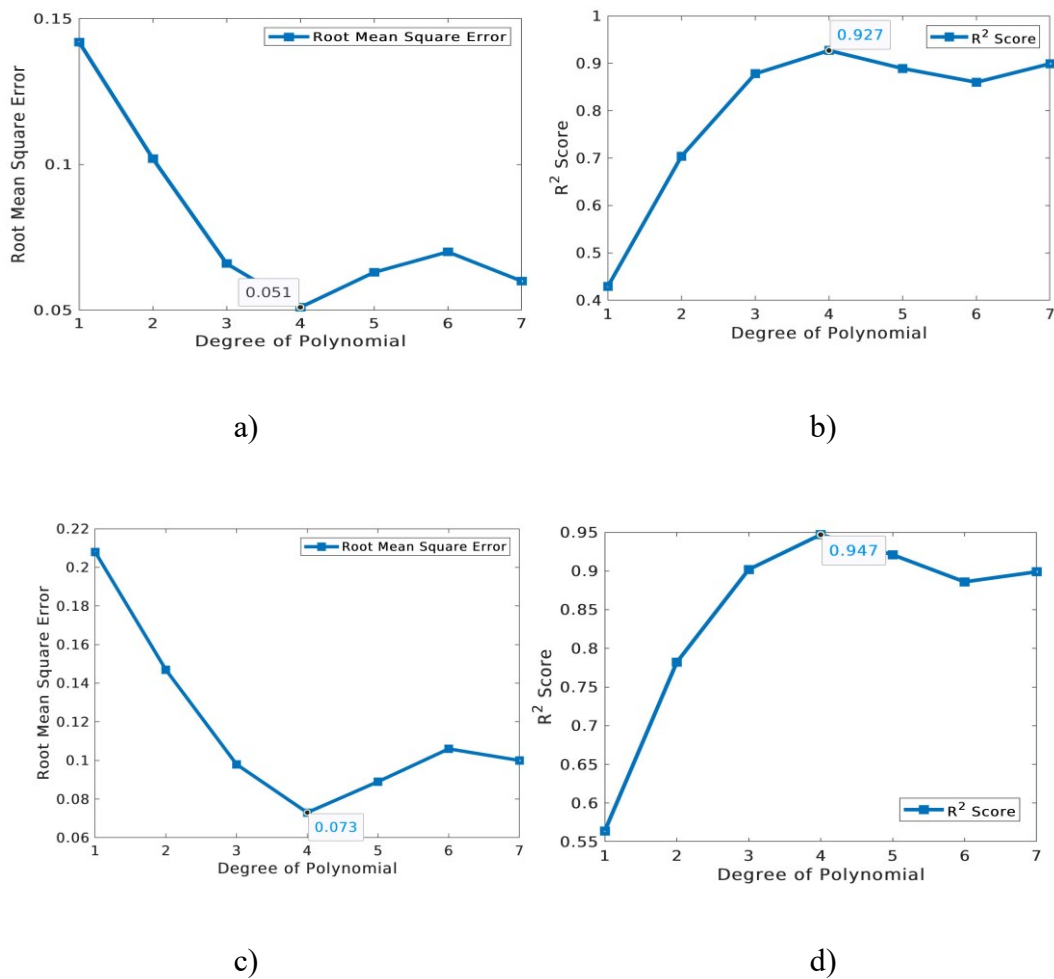
Fig. A11. a) RMSE values at different polynomial degree for I-V characteristics b) R^2-score values at different polynomial degree for I-V characteristics and c) RMSE values at different polynomial degree for P-V characteristics d) R^2-score values at different polynomial degree for P-V characteristics.

Fig. A11 (a), (c), (b) and (d) for I-V data and P-V data at an interval of 1 to 7 as degree of freedom. It can be observed that lesser the RMSE value and higher R^2-score then that polynomial degree gives better result. In the proposed work the degree 4 is giving lesser

RMSE = 0.05 and higher R^2-score = 0.93 for I-V and RMSE = 0.07 and higher R^2-score = 0.95 for P-V.

a)   b)

c)   d)
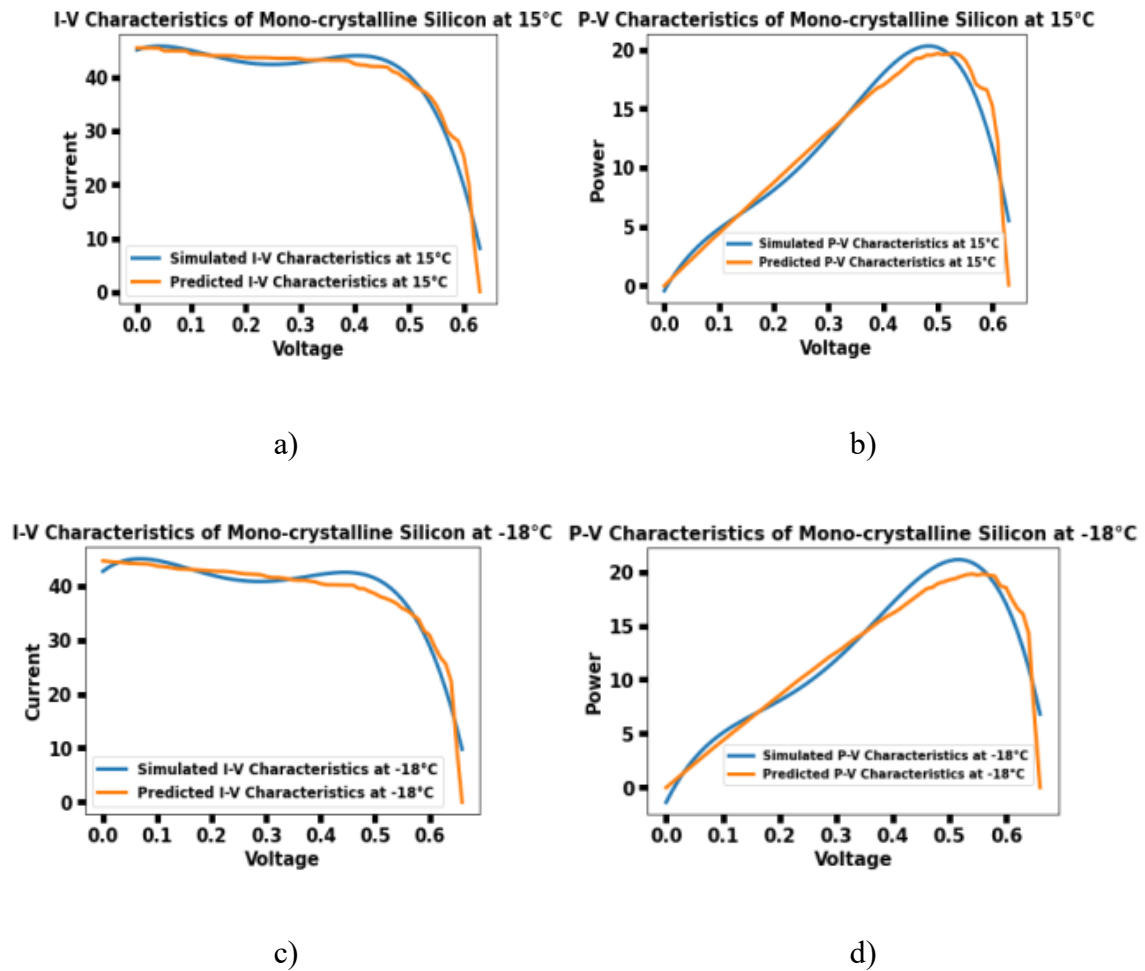
Fig. A12. a) & c) I-V characteristics of mono-crystalline Si predictions at 25^0C, 15^0C and -18^0C b) and d) P-V characteristics of mono-crystalline Si predictions at 15^0C and -18^0C respectively by PR prediction

The Fig. A12 a), c) and b), d) shows the I-V and P-V characteristics prediction through PR at 15^0C and -18^0C. The PR predictions values are almost similar to the simulated data and the efficiency of mono-crystalline Si at 15^0C and -18^0C.

Support Vector Regression (SVR):

The values of simulated data and predicted data both are available to validate the SVR prediction results and are shown in Fig. A13. a) & b) and Fig. A13. c) & d) as I-V and P-V characteristics at 15^0C and -18^0C.
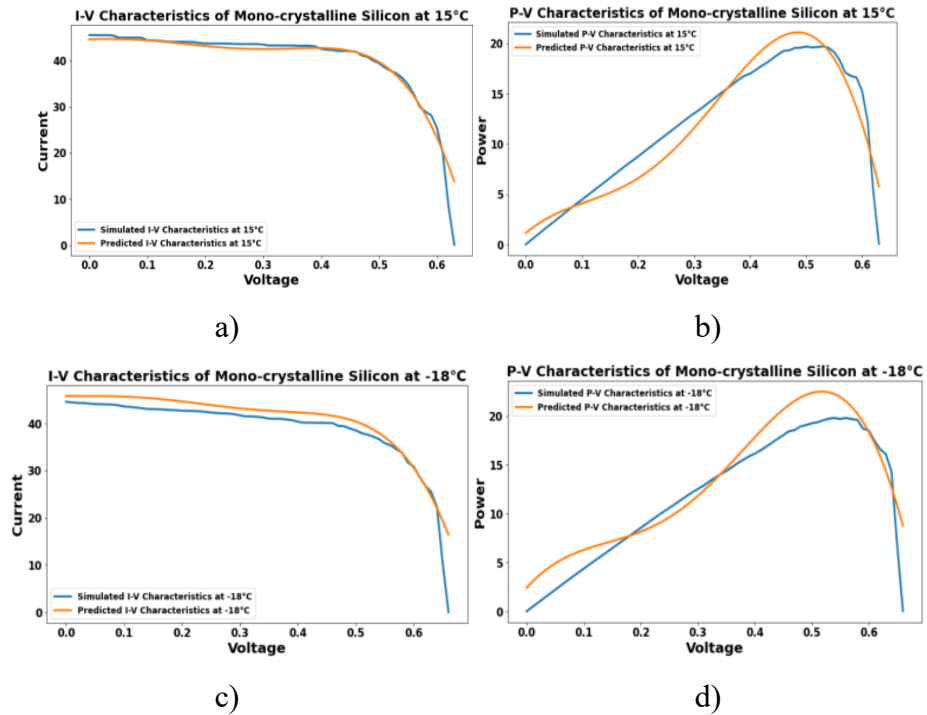
Fig. A13. a) & c) I-V characteristics b) and d) P-V characteristics of mono-crystalline Si predictions at 25^0C, 15^0C and -18^0C respectively by SVR prediction

Kernel Ridge Regression (KRR):
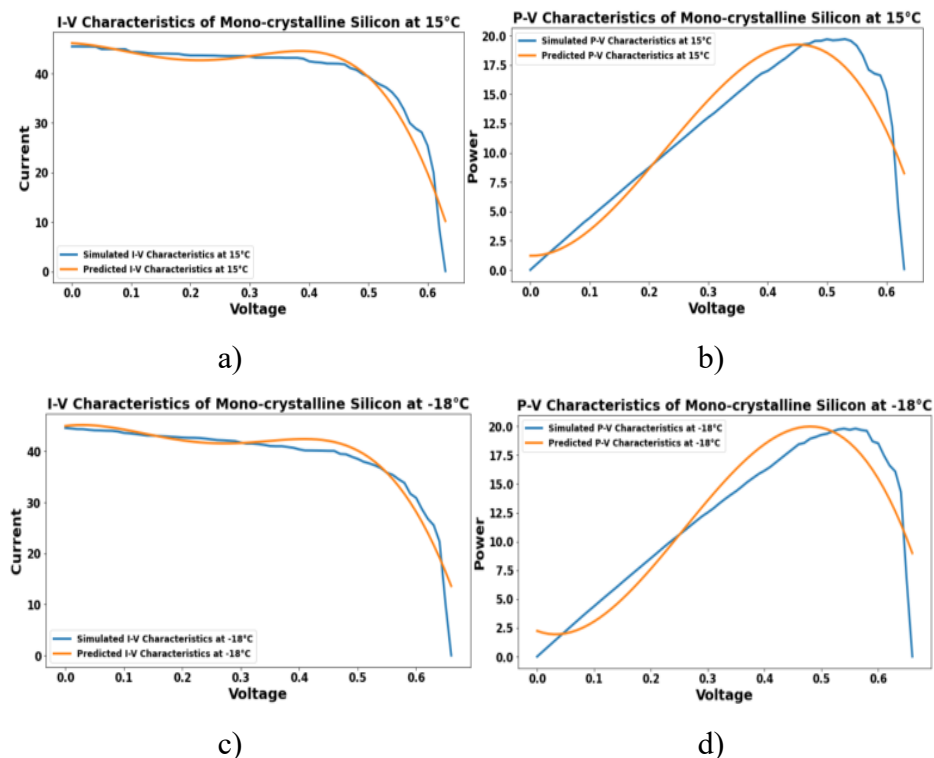
Fig. A14. a) & c) I-V characteristics of mono-crystalline Si predictions at 25^0C, 15^0C and -18^0C b) and d) P-V characteristics of mono-crystalline Si predictions at 25^0C, 15^0C and -18^0C respectively by KRR prediction

The values of simulated data and predicted data both are available to validate the PR prediction results and are shown in Fig. A14. a) & b) and Fig. A14. c) & d) as I-V and P-V characteristics at 15^0C and -18^0C.

Prediction algorithms for different materials at different temperatures:

a)

b)

c)

d)

e)

f)

g)

h)
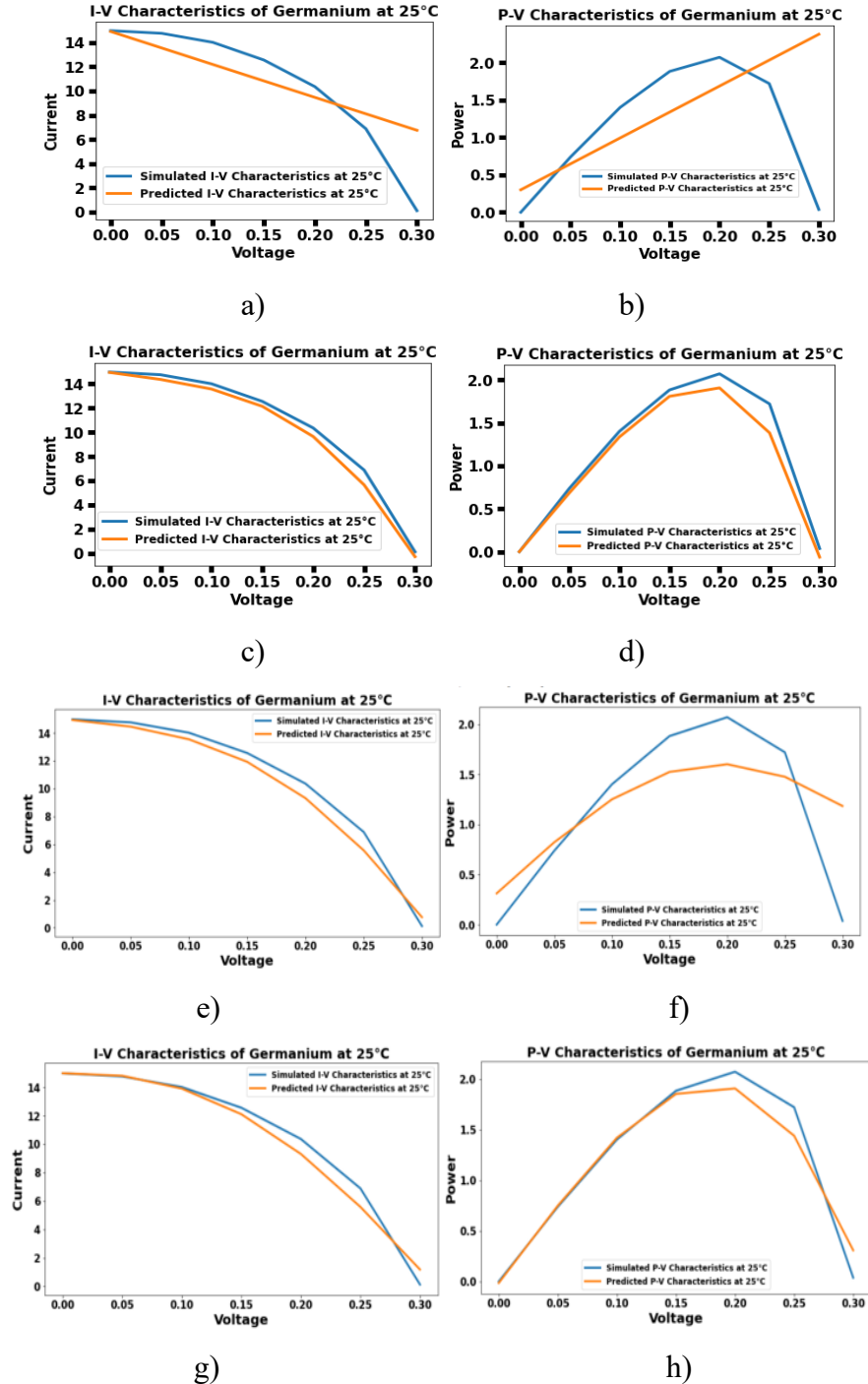
Fig. A15. a) & b) I-V and P-V characteristics of Ge with LR ML technique c) & d) I-V and P-V characteristics of Ge with PR ML technique e) & f) I-V and P-V characteristics of Ge with SVR ML technique g) & h) I-V and P-V characteristics of Ge with KRR ML technique

The I-V and P-V, prediction and simulated data for Ge with LR, PR, SVR and KRR are represented in Fig. A15 (a) to (h) where the PR and KRR are giving better prediction. The metrics for the prediction is listed in Table A1 and the 98.5% accuracy with PR and 97.6% accuracy with KRR for I-V, similarly, for P-V, 96.4% accuracy with PR and 96.1% accuracy with KRR is achieved.

Table A1.

List of metrics for ML techniques of Ge at 25^0C

Metric	Temperature	LR		PR		SVR		KRR	
		IV	PV	IV	PV	IV	PV	IV	PV
RMSE	25^0C	0.190	0.303	0.042	0.049	0.051	0.165	0.053	0.051
MAE		0.133	0.200	0.035	0.036	0.044	0.126	0.039	0.036
MAPE		4.784	10.712	0.333	0.521	0.512	5.291	0.796	1.264
R^2-Score		0.692	-0.398	0.985	0.964	0.977	0.589	0.976	0.961

Table A2.

List of metrics for ML techniques of GaAs at 25^0C

Metric	Temperature	LR		PR		SVR		KRR	
		IV	PV	IV	PV	IV	PV	IV	PV
RMSE	25^0C	0.099	0.184	0.048	0.074	0.067	0.089	0.0576	0.106
MAE		0.069	0.117	0.035	0.048	0.031	0.071	0.033	0.065
MAPE		0.962	1.381	0.451	0.523	0.784	0.584	0.517	0.686
R^2-Score		0.561	0.474	0.897	0.915	0.800	0.877	0.852	0.827
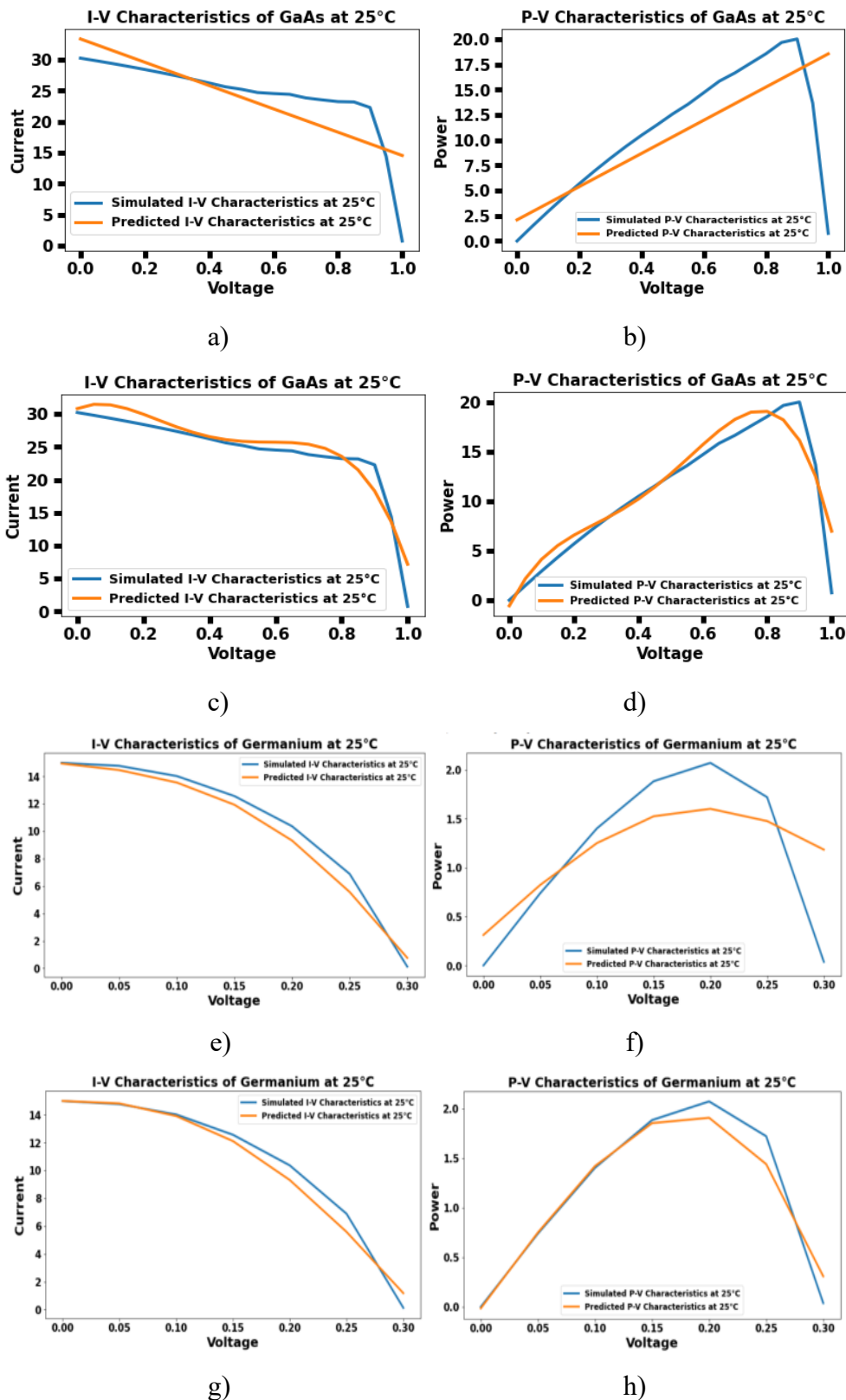
Fig. A16. a) & b) I-V and P-V characteristics of GaAs with LR ML technique c) & d) I-V
and P-V characteristics of GaAs with PR ML technique e) & f) I-V and P-V
characteristics of GaAs with SVR ML technique g) & h) I-V and P-V characteristics of
GaAs with KRR ML technique

The I-V and P-V of GaAs with LR, PR, SVR, and KRR ML techniques are shown in Fig. A16 (a) to (h), and the corresponding MAE, MAPE, RMSE and R^2-score metrics are measured at 25^0C and tabulated in Table A2. Similarly, I-V and P-V of InP with LR, PR, SVR and KRR ML techniques are shown in Fig. A17 (a) to (h). Also, from the prediction, the MAE, MAPE, RMSE and R^2-score metrics are measured at 25^0C and tabulated in Table A3.

a)

b)

c)

d)

e)

f)

g)

h)
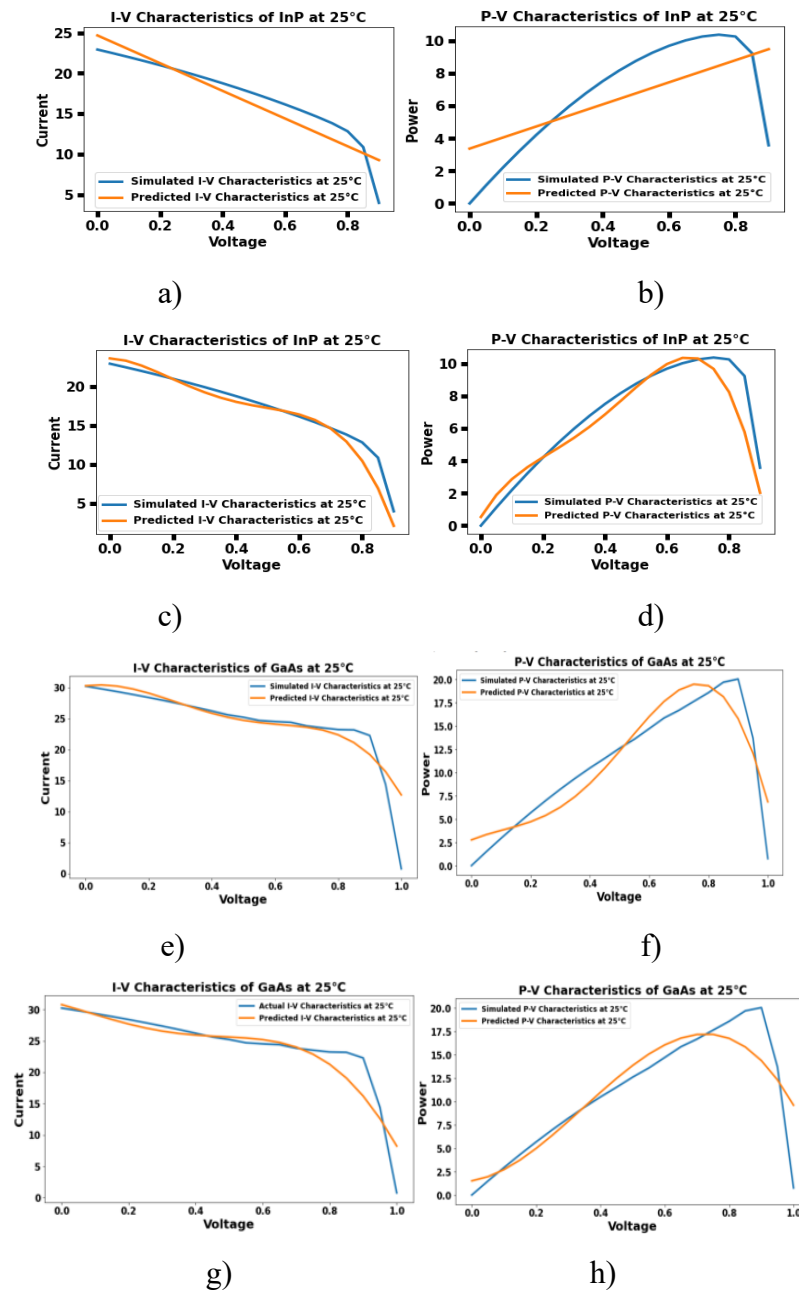
Fig. A17. a) & b) I-V and P-V characteristics of InP with LR ML technique c) & d) I-V and P-V characteristics of InP with PR ML technique e) & f) I-V and P-V characteristics of InP with SVR ML technique g) & h) I-V and P-V characteristics of InP with KRR ML technique

Table A3.

List of metrics for ML techniques of InP at 25^0C

Metric	Temperature	LR		PR		SVR		KRR	
		IV	PV	IV	PV	IV	PV	IV	PV
RMSE		0.081	0.209	0.056	0.101	0.033	0.078	0.049	0.105
MAE		0.063	0.171	0.037	0.068	0.023	0.063	0.030	0.071
MAPE	25^0C	0.158	0.411	0.084	0.149	0.063	0.106	0.055	0.148
R²-Score		0.851	0.547	0.926	0.893	0.974	0.937	0.944	0.884

BIBLIOGRAPHY

[1]   L. Essak and A. Ghosh, "Floating Photovoltaics: A Review," *Clean Technol.*, vol. 4, no. 3, pp. 752–769, 2022, doi: 10.3390/cleantechnol4030046.

[2]   A. G. Olabi and M. A. Abdelkareem, "Renewable energy and climate change," *Renew. Sustain. Energy Rev.*, vol. 158, no. November 2020, p. 112111, 2022, doi: 10.1016/j.rser.2022.112111.

[3]   International Energy Agency, "International Energy Agency (IEA) World Energy Outlook 2022," *Https://Www.Iea.Org/Reports/World-Energy-Outlook-2022/Executive-Summary*, p. 524, 2022, [Online]. Available: https://www.iea.org/reports/world-energy-outlook-2022

[4]   X. Yang, J. Pang, F. Teng, R. Gong, and C. Springer, "The environmental co-benefit and economic impact of China's low-carbon pathways: Evidence from linking bottom-up and top-down models," *Renew. Sustain. Energy Rev.*, vol. 136, no. September 2020, p. 110438, 2021, doi: 10.1016/j.rser.2020.110438.

[5]   H. Nazaripouya, Y.-W. Chung, and A. Akhil, "Energy Storage in Microgrids: Challenges, Applications and Research Need," *Int. J. Energy Smart Grid*, vol. 3, no. 2, pp. 60–70, 2019, doi: 10.23884/ijesg.2018.3.2.02.

[6]   D. Gielen, F. Boshell, D. Saygin, M. D. Bazilian, N. Wagner, and R. Gorini, "The role of renewable energy in the global energy transformation," *Energy Strateg. Rev.*, vol. 24, no. June 2018, pp. 38–50, 2019, doi: 10.1016/j.esr.2019.01.006.

[7]   E. Becquerel, "Mémoire sur les effets électriques produits sous l'influence des rayons solaires," *C. R. Hebd. Seances Acad. Sci.*, vol. 9, pp. 561–567, 1839.

[8]   K. Vijayan, S. P. Vijayachamundeeswari, K. Sivaperuman, N. Ahsan, T. Logu, and Y. Okada, "A review on advancements, challenges, and prospective of copper and non-copper based thin-film solar cells using facile spray pyrolysis technique," *Sol. Energy*, vol. 234, no. February, pp. 81–102, 2022, doi: 10.1016/j.solener.2022.01.070.

[9]   B. Rech *et al.*, "New materials and deposition techniques for highly efficient silicon thin film solar cells," *Sol. Energy Mater. Sol. Cells*, vol. 74, no. 1–4, pp. 439–447, 2002, doi: 10.1016/S0927-0248(02)00114-9.

[10]   P. Zheng *et al.*, "21.1% UMG Silicon Solar Cells," *IEEE J. Photovoltaics*, vol. 7, no. 1, pp. 58–61, 2017, doi: 10.1109/JPHOTOV.2016.2616192.

[11]   W. Wang *et al.*, "Industrial screen-printed n-type rear-junction solar cells with 20.6% efficiency," *IEEE J. Photovoltaics*, vol. 5, no. 4, pp. 1245–1249, 2015, doi: 10.1109/JPHOTOV.2015.2416919.

[12]   W. Luft, "Silicon Solar Cell Performance at High Intensities," *IEEE Trans. Aerosp. Electron. Syst.*, vol. AES-6, no. 6, pp. 797–803, 1970, doi: 10.1109/TAES.1970.310161.

[13]   H. Crystal, "Silicon solar cells for ground-level use," *Proc. Inst. Electr. Eng.*, vol. 111, no. 1, p. 173, 1964, doi: 10.1049/piee.1964.0028.

[14]   A. Banerjee *et al.*, "12.0% Efficiency on Large-Area, Encapsulated, Multijunction nc-Si:H-Based Solar Cells," *IEEE J. Photovoltaics*, vol. 2, no. 2, pp. 104–108, Apr. 2012, doi: 10.1109/JPHOTOV.2011.2181823.

[15] "What Factors Determine Solar Panel Efficiency? - Energy Informative," *Energy Informative.org*. 2013. [Online]. Available: https://energyinformative.org/solar-panel-efficiency/

[16] A. H. Trojnar, C. E. Valdivia, K. M. Azizur-Rahman, R. R. LaPierre, K. Hinzer, and J. J. Krich, "Optimization of GaAs nanowire solar cell efficiency via optoelectronic modeling," in *2015 IEEE 42nd Photovoltaic Specialist Conference (PVSC)*, Jun. 2015, pp. 1–6. doi: 10.1109/PVSC.2015.7355660.

[17] M. Feifel, D. Lackner, J. Ohlmann, J. Benick, M. Hermle, and F. Dimroth, "Direct Growth of a GaInP/GaAs/Si Triple-Junction Solar Cell with 22.3% AM1.5g Efficiency," *Sol. RRL*, vol. 3, no. 12, p. 1900313, 2019, doi: https://doi.org/10.1002/solr.201900313.

[18] W. Shockley and H. J. Queisser, "Detailed balance limit of efficiency of p-n junction solar cells," *J. Appl. Phys.*, vol. 32, no. 3, pp. 510–519, 1961, doi: 10.1063/1.1736034.

[19] C. S. Durganjali and R. Sudha, "PV Cell Performance with Varying Temperature Levels," *2019 Glob. Conf. Adv. Technol. GCAT 2019*, pp. 1–5, 2019, doi: 10.1109/GCAT47503.2019.8978302.

[20] S. Odeh and M. Behnia, "Improving photovoltaic module efficiency using water cooling," *Heat Transf. Eng.*, vol. 30, no. 6, pp. 499–505, 2009, doi: 10.1080/01457630802529214.

[21] S. A. Abdulgafar, O. S. Omar, and K. M. Yousif, "Improving The Efficiency Of Polycrystalline Solar Panel Via Water Immersion Method," *Int. J. Innov. Res. Sci. Eng. Technol. (An ISO Certif. Organ.*, 2007.

[22] Y.-K. Choi, N.-H. Lee, and K.-J. Kim, "Empirical Research on the efficiency of Floating PV systems compared with Overland PV Systems," *Ces-Cube 2013, Astl*, 2013.

[23] K. N. Sheeba, R. M. Rao, and S. Jaisankar, "A Study on the Underwater Performance of a Solar Photovoltaic Panel," *Energy Sources, Part A Recover. Util. Environ. Eff.*, vol. 37, no. 14, pp. 1505–1512, Jul. 2015, doi: 10.1080/15567036.2011.619632.

[24] Y.-K. Choi, "A Study on Power Generation Analysis of Floating PV System Considering Environmental Impact," *Int. J. Softw. Eng. Its Appl.*, vol. 8, no. 1, pp. 75–84, Jan. 2014, doi: 10.14257/ijseia.2014.8.1.07.

[25] S. Kalaiselvan, V. Karthikeyan, G. Rajesh, A. Sethu Kumaran, B. Ramkiran, and P. Neelamegam, "Solar PV Active and Passive Cooling Technologies-A Review," *7th IEEE Int. Conf. Comput. Power, Energy, Inf. Commun. ICCPEIC 2018*, pp. 166–169, 2018, doi: 10.1109/ICCPEIC.2018.8525185.

[26] K. Trapani and M. Redõn Santafé, "A review of floating photovoltaic installations: 2007-2013," *Progress in Photovoltaics: Research and Applications*. 2015. doi: 10.1002/pip.2466.

[27] M. Rosa-Clot, P. Rosa-Clot, G. M. Tina, and P. F. Scandura, "Submerged photovoltaic solar panel: SP2," *Renew. Energy*, 2010, doi: 10.1016/j.renene.2009.10.023.

[28] Z. A. A. Majid, M. H. Ruslan, K. Sopian, M. Y. Othman, and M. S. M. Azmi, "Study on performance of 80 watt floating photovoltaic panel," *J. Mech. Eng. Sci.*, 2014, doi: 10.15282/jmes.7.2014.14.0112.

[29] Y. G. Lee, H. J. Joo, and S. J. Yoon, "Design and installation of floating type photovoltaic energy generation system using FRP members," *Sol. Energy*, 2014, doi: 10.1016/j.solener.2014.06.033.

[30] G. M. Tina, M. Rosa-Clot, P. Rosa-Clot, and P. F. Scandura, "Optical and thermal behavior of submerged photovoltaic solar panel: SP2," *Energy*, 2012, doi: 10.1016/j.energy.2011.08.053.

[31] A. Holm, "Floating solar photovoltaics gaining ground." National Renewable Energy Lab, blog. Retrieved from httpswww. nrel. gov~…, 2017.

[32] M. R. Clot, P. Rosa-Clot, and G. M. Tina, "Submerged PV Solar Panel for Swimming Pools: SP3," *Energy Procedia*, vol. 134, pp. 567–576, 2017, doi: 10.1016/j.egypro.2017.09.565.

[33] R. Lanzafame *et al.*, "Field experience with performances evaluation of a single-crystalline photovoltaic panel in an underwater environment," *IEEE Trans. Ind. Electron.*, 2010, doi: 10.1109/TIE.2009.2035489.

[34] R. J. Walters *et al.*, "Multijunction organic photovoltaic cells for underwater solar power," *2015 IEEE 42nd Photovolt. Spec. Conf. PVSC 2015*, pp. 3–5, 2015, doi: 10.1109/PVSC.2015.7355644.

[35] A. A.Mol'kov and L. S.Dolin, "The Possibility of Determining Optical Properties of Water from the Image of the Underwater Solar Path," *Radiophys. Quantum Electron.*, vol. 58, no. 8, pp. 586–597, 2016, doi: 10.1007/s11141-016-9630-9.

[36] G. G. Hahn, L. A. Adoram-Kershner, H. P. Cantin, and M. W. Shafer, "Assessing Solar Power for Globally Migrating Marine and Submarine Systems," *IEEE J. Ocean. Eng.*, vol. PP, pp. 1–14, 2018, doi: 10.1109/JOE.2018.2835178.

[37] G. M. Tina, M. Rosa-Clot, V. Lojpur, and I. L. Validzic, "Numerical and Experimental Analysis of Photovoltaic Cells under a Water Layer and Natural and Artificial Light," *IEEE J. Photovoltaics*, vol. 9, no. 3, pp. 733–740, 2019, doi: 10.1109/JPHOTOV.2019.2896669.

[38] G. Wang, M. Ciobotaru, and V. G. Agelidis, "Power smoothing of large solar PV plant using hybrid energy storage," *IEEE Trans. Sustain. Energy*, vol. 5, no. 3, pp. 834–842, 2014, doi: 10.1109/TSTE.2014.2305433.

[39] S. Vavilapalli, U. Subramaniam, S. Padmanaban, and V. K. Ramachandaramurthy, "Design and real-time simulation of an AC voltage regulator based battery charger for large-scale PV-grid energy storage systems," *IEEE Access*, vol. 5, pp. 25158–25170, 2017, doi: 10.1109/ACCESS.2017.2768438.

[40] J. Malavatu, R. O'Born, P. Kepplinger, and B. Faessler, "Hybrid energy storage systems of energy- and power-dense batteries: A survey on modelling techniques and control methods," *Procedia CIRP*, vol. 105, pp. 794–798, 2022, doi: 10.1016/j.procir.2022.02.193.

[41] K. Shirinda and K. Kanzumba, "A review of hybrid energy storage systems in renewable energy applications," *Int. J. Smart Grid Clean Energy*, no. June, pp. 99–108, 2022, doi: 10.12720/sgce.11.2.99-108.

[42] T. Bocklisch, "Hybrid energy storage systems for renewable energy applications," in *Energy Procedia*, 2015, vol. 73, pp. 103–111. doi: 10.1016/j.egypro.2015.07.582.

[43] V. Bagalini, B. Y. Zhao, R. Z. Wang, and U. Desideri, "Solar PV-Battery-Electric Grid-Based Energy System for Residential Applications: System Configuration and

Viability," *Research*, vol. 2019, 2019, doi: 10.34133/2019/3838603.

[44]   A. Bhimaraju, A. Mahesh, and S. N. Joshi, "Techno-economic optimization of grid-connected solar-wind-pumped storage hybrid energy system using improved search space reduction algorithm," *J. Energy Storage*, vol. 52, no. PA, p. 104778, 2022, doi: 10.1016/j.est.2022.104778.

[45]   S. Mohseni and A. C. Brent, "Quantifying the effects of forecast uncertainty on the role of different battery technologies in grid-connected solar photovoltaic/wind/micro-hydro micro-grids: An optimal planning study," *J. Energy Storage*, vol. 51, no. March, p. 104412, 2022, doi: 10.1016/j.est.2022.104412.

[46]   K. Muchiri, J. N. Kamau, D. W. Wekesab, C. O. Saoke, J. N. Mutuku, and J. K. Gathua, "Institute of Energy and Environmental Technology , Jomo Kenyatta University of," *Sci. African*, p. e01599, 2023, doi: 10.1016/j.sciaf.2023.e01599.

[47]   A. Panda, A. K. Dauda, H. Chua, R. R. Tan, and K. B. Aviso, "Recent advances in the integration of renewable energy sources and storage facilities with hybrid power systems," *Clean. Eng. Technol.*, vol. 12, no. October 2022, p. 100598, 2023, doi: 10.1016/j.clet.2023.100598.

[48]   A. Shokri and M. Sanavi Fard, "A sustainable approach in water desalination with the integration of renewable energy sources: Environmental engineering challenges and perspectives," *Environ. Adv.*, vol. 9, no. August, p. 100281, 2022, doi: 10.1016/j.envadv.2022.100281.

[49]   M. Mimica, M. Perčić, N. Vladimir, and G. Krajačić, "Cross-sectoral integration for increased penetration of renewable energy sources in the energy system – Unlocking the flexibility potential of maritime transport electrification," *Smart Energy*, vol. 8, no. October, 2022, doi: 10.1016/j.segy.2022.100089.

[50]   K. Yamashita and S. M. Villanueva, "Integration of renewable energy sources, energy storages, and their impacts," in *Encyclopedia of Electrical and Electronic Power Engineering*, J. García, Ed. Oxford: Elsevier, 2023, pp. 36–44. doi: https://doi.org/10.1016/B978-0-12-821204-2.00130-6.

[51]   D. Zappalá, N. Sarma, S. Djurović, C. J. Crabtree, A. Mohammad, and P. J. Tavner, "Electrical & mechanical diagnostic indicators of wind turbine induction generator rotor faults," *Renew. Energy*, vol. 131, pp. 14–24, 2019, doi: 10.1016/j.renene.2018.06.098.

[52]   A. K. Verma, S. Radhika, and S. V. Padmanabhan, "Wavelet based fault detection and diagnosis using online MCSA of stator winding faults due to insulation failure in industrial induction machine," *2018 IEEE Recent Adv. Intell. Comput. Syst. RAICS 2018*, pp. 204–208, 2019, doi: 10.1109/RAICS.2018.8635058.

[53]   W. Touti, M. Salah, K. Bacha, and A. Chaari, "Condition monitoring of a wind turbine drivetrain based on generator stator current processing," *ISA Trans.*, vol. 128, pp. 650–664, 2022, doi: 10.1016/j.isatra.2021.10.014.

[54]   J. Hu, R. Harmsen, W. Crijns-Graus, E. Worrell, and M. van den Broek, "Identifying barriers to large-scale integration of variable renewable electricity into the electricity market: A literature review of market design," *Renew. Sustain. Energy Rev.*, vol. 81, no. September 2016, pp. 2181–2195, 2018, doi: 10.1016/j.rser.2017.06.028.

[55]   S. Karytsas and I. Choropanitis, "Barriers against and actions towards renewable energy technologies diffusion: A Principal Component Analysis for residential ground source heat pump (GSHP) systems," *Renew. Sustain. Energy Rev.*, vol. 78,

no. May 2016, pp. 252–271, 2017, doi: 10.1016/j.rser.2017.04.060.

[56]   A. Shivakumar, A. Dobbins, U. Fahl, and A. Singh, "Drivers of renewable energy deployment in the EU: An analysis of past trends and projections," *Energy Strateg. Rev.*, vol. 26, no. January 2018, p. 100402, 2019, doi: 10.1016/j.esr.2019.100402.

[57]   C. Kim, "A review of the deployment programs, impact, and barriers of renewable energy policies in Korea," *Renew. Sustain. Energy Rev.*, vol. 144, no. June 2020, p. 110870, 2021, doi: 10.1016/j.rser.2021.110870.

[58]   A. D. Owen, "Renewable energy: Externality costs as market barriers," *Energy Policy*, vol. 34, no. 5, pp. 632–642, 2006, doi: 10.1016/j.enpol.2005.11.017.

[59]   S. Reddy and J. P. Painuly, "Diffusion of renewable energy technologies-barriers and stakeholders' perspectives," *Renew. Energy*, vol. 29, no. 9, pp. 1431–1447, 2004, doi: 10.1016/j.renene.2003.12.003.

[60]   S. Sen and S. Ganguly, "Opportunities, barriers and issues with renewable energy development – A discussion," *Renew. Sustain. Energy Rev.*, vol. 69, no. May 2016, pp. 1170–1181, 2017, doi: 10.1016/j.rser.2016.09.137.

[61]   N. Anglani, S. R. Di Salvo, G. Oriti, and A. L. Julian, "Steps towards Decarbonization of an Offshore Microgrid: Including Renewable, Enhancing Storage and Eliminating Need of Dump Load," *Energies*, vol. 16, no. 3, pp. 3–5, 2023, doi: 10.3390/en16031411.

[62]   N. K. Roy, E. Hossain, and H. R. Pota, "Size optimization and sensitivity analysis of hybrid Wind / PV micro-grids- A case study for a tropical country," *IEEE Access*, vol. PP, p. 1, 2019, doi: 10.1109/ACCESS.2019.2945937.

[63]   P. P. Jenkins *et al.*, "High-bandgap solar cells for underwater photovoltaic applications," *IEEE J. Photovoltaics*, vol. 4, no. 1, pp. 202–206, 2014, doi: 10.1109/JPHOTOV.2013.2283578.

[64]   G. M. Tina, C. Ventura, S. Ferlito, and S. De Vito, "A state-of-art-review on machine-learning based methods for PV," *Appl. Sci.*, vol. 11, no. 16, 2021, doi: 10.3390/app11167550.

[65]   B. Carrera and K. Kim, "Comparison analysis of machine learning techniques for photovoltaic prediction using weather sensor data," *Sensors (Switzerland)*, vol. 20, no. 11, 2020, doi: 10.3390/s20113129.

[66]   Y. Zhou, J. Wang, Z. Li, and H. Lu, "Short-term photovoltaic power forecasting based on signal decomposition and machine learning optimization," *Energy Convers. Manag.*, vol. 267, no. April, p. 115944, 2022, doi: 10.1016/j.enconman.2022.115944.

[67]   M. Hamza Zafar, N. Mujeeb Khan, M. Mansoor, A. Feroz Mirza, S. Kumayl Raza Moosavi, and F. Sanfilippo, "Adaptive ML-based technique for renewable energy system power forecasting in hybrid PV-Wind farms power conversion systems," *Energy Convers. Manag.*, vol. 258, no. March, p. 115564, 2022, doi: 10.1016/j.enconman.2022.115564.

[68]   J. D. Osorio *et al.*, "Forecasting solar-thermal systems performance under transient operation using a data-driven machine learning approach based on the deep operator network architecture," *Energy Convers. Manag.*, vol. 252, no. November 2021, p. 115063, 2022, doi: 10.1016/j.enconman.2021.115063.

[69]   R. A. Rajagukguk, R. A. A. Ramadhan, and H. J. Lee, "A review on deep learning

models for forecasting time series data of solar irradiance and photovoltaic power," *Energies*, vol. 13, no. 24, 2020, doi: 10.3390/en13246623.

[70] H. Wang, Z. Lei, X. Zhang, B. Zhou, and J. Peng, "A review of deep learning for renewable energy forecasting," *Energy Convers. Manag.*, vol. 198, no. July, p. 111799, 2019, doi: 10.1016/j.enconman.2019.111799.

[71] M. Uddin, M. F. Romlie, M. F. Abdullah, S. Abd Halim, A. H. Abu Bakar, and T. Chia Kwang, "A review on peak load shaving strategies," *Renew. Sustain. Energy Rev.*, vol. 82, no. August, pp. 3323–3332, 2018, doi: 10.1016/j.rser.2017.10.056.

[72] A. Bhattacharjee, H. Samanta, A. Ghosh, T. K. Mallick, S. Sengupta, and H. Saha, "Optimized Integration of Hybrid Renewable Sources with Long-Life Battery Energy Storage in Microgrids for Peak Power Shaving and Demand Side Management under Different Tariff Scenario," *Energy Technol.*, vol. 9, no. 9, p. 2100199, Sep. 2021, doi: 10.1002/ente.202100199.

[73] A. K. Barnes, J. C. Balda, and A. Escobar-Mejia, "A Semi-Markov Model for Control of Energy Storage in Utility Grids and Microgrids With PV Generation," *IEEE Trans. Sustain. Energy*, vol. 6, no. 2, pp. 546–556, 2015, doi: 10.1109/TSTE.2015.2393353.

[74] A. K. Rohit, K. P. Devi, and S. Rangnekar, "An overview of energy storage and its importance in Indian renewable energy sector: Part I – Technologies and Comparison," *Journal of Energy Storage*, vol. 13. Elsevier Ltd, pp. 10–23, 2017. doi: 10.1016/j.est.2017.06.005.

[75] H. Zhang, K. Huys, J. Baeyens, J. Degrève, W. Kong, and Y. Lv, "Thermochemical Energy Storage for Power Generation on Demand," *Energy Technol.*, vol. 4, no. 2, pp. 341–352, 2016, doi: 10.1002/ente.201500261.

[76] T. M. Taylor, "Energy storage," in *EPJ Web of Conferences*, Oct. 2018, vol. 189, no. February, p. 00009. doi: 10.1051/epjconf/201818900009.

[77] J. Gustavsson, "Energy Storage Technology Comparison," *KTH Sch. Ind. Eng. Manag.*, p. 44, 2016, [Online]. Available: http://www.diva-portal.org/smash/get/diva2:953046/FULLTEXT01.pdf

[78] H. Li and C. Guedes Soares, "Assessment of failure rates and reliability of floating offshore wind turbines," *Reliab. Eng. Syst. Saf.*, vol. 228, no. August, 2022, doi: 10.1016/j.ress.2022.108777.

[79] J. Kang, L. Sun, and C. Guedes Soares, "Fault Tree Analysis of floating offshore wind turbines," *Renew. Energy*, vol. 133, pp. 1455–1467, 2019, doi: 10.1016/j.renene.2018.08.097.

[80] B. Rouabah, H. Toubakh, M. R. Kafi, and M. Sayed-Mouchaweh, "Adaptive data-driven fault-tolerant control strategy for optimal power extraction in presence of broken rotor bars in wind turbine," *ISA Trans.*, vol. 130, pp. 92–103, 2022, doi: 10.1016/j.isatra.2022.04.008.

[81] Z. Song, C. Xia, and T. Shi, "Assessing transient response of DFIG based wind turbines during voltage dips regarding main flux saturation and rotor deep-bar effect," *Appl. Energy*, vol. 87, no. 10, pp. 3283–3293, 2010, doi: 10.1016/j.apenergy.2010.04.009.

[82] Y. Amirat, M. E. H. Benbouzid, E. Al-Ahmar, B. Bensaker, and S. Turri, "A brief status on condition monitoring and fault diagnosis in wind energy conversion

systems," *Renew. Sustain. Energy Rev.*, vol. 13, no. 9, pp. 2629–2636, 2009, doi: 10.1016/j.rser.2009.06.031.

[83] B. Rouabah, H. Toubakh, M. R. Kafi, and M. Sayed-Mouchaweh, "Adaptive data-driven fault-tolerant control strategy for optimal power extraction in presence of broken rotor bars in wind turbine," *ISA Trans.*, vol. 130, pp. 92–103, 2022, doi: 10.1016/j.isatra.2022.04.008.

[84] O. Attallah, R. A. Ibrahim, and N. E. Zakzouk, "Fault diagnosis for induction generator-based wind turbine using ensemble deep learning techniques," *Energy Reports*, vol. 8, pp. 12787–12798, 2022, doi: 10.1016/j.egyr.2022.09.139.

[85] R. C. Bansal, T. S. Bhatti, and D. R. Kothari, "A Novel Mathematical Modelling of Induction Generator for Reactive Power Control of Isolated Hybrid Power Systems," *Int. J. Model. Simul.*, vol. 24, no. 1, pp. 1–7, 2004, doi: 10.1080/02286203.2004.11442280.

[86] Z. Gan, M. B. Zhao, and T. W. S. Chow, "Induction machine fault detection using clone selection programming," *Expert Syst. Appl.*, vol. 36, no. 4, pp. 8000–8012, 2009, doi: 10.1016/j.eswa.2008.10.058.

[87] Z. Song, C. Xia, and T. Shi, "Assessing transient response of DFIG based wind turbines during voltage dips regarding main flux saturation and rotor deep-bar effect," *Appl. Energy*, vol. 87, no. 10, pp. 3283–3293, 2010, doi: 10.1016/j.apenergy.2010.04.009.

[88] R. Benger, H. Wenzl, H. P. Beck, M. Jiang, D. Ohms, and G. Schaedlich, "Page 0342," *World Electr. Veh. J.*, vol. 3, no. EVS24, pp. 342–351, 2009.

[89] R. Kasim, A. R. Abdullah, N. A. Selamat, M. F. Baharom, and N. H. T. H. Ahmad, "Battery Parameters Identification Analysis Using Periodogram," in *Recent Trends in Power Engineering*, 2015, vol. 785, pp. 687–691. doi: 10.4028/www.scientific.net/AMM.785.687.

[90] P. Sathya and G. Aarthi, "Technology Modelling and Simulation of Solar Photovoltaic array for Battery charging Application using Matlab-Simulink," *Int. J. Eng. Sci. Res. Technol.*, vol. 2(11), pp. 3111–3115, 2013.

[91] N. Cheeweewattanakoon, G. Kaur, N. Chawla, and O. Bruno, "Residential battery energy storage systems (BESS) modeling and effect on the smart grid from the classroom point of view," *ASEE Annu. Conf. Expo. Conf. Proc.*, 2014, doi: 10.18260/1-2--22978.

[92] Energy information administration of US Department of Energy, "International energy outlook 2016-Natural gas," *Int. energy outlook 2016*, vol. 2016, pp. 37–60, 2016.

[93] S. Essig, J. Benick, M. Schachtner, A. Wekkeli, M. Hermle, and F. Dimroth, "Wafer-Bonded GaInP/GaAs//Si Solar Cells With 30% Efficiency Under Concentrated Sunlight," *IEEE J. Photovoltaics*, vol. 5, no. 3, pp. 977–981, 2015, doi: 10.1109/JPHOTOV.2015.2400212.

[94] J. A. Muaddi and M. A. Jamal, "Solar spectrum at depth in water," *Renew. Energy*, vol. 1, no. 1, pp. 31–35, 1991, doi: 10.1016/0960-1481(91)90100-4.

[95] United Nations Educational Scientific and Cultural Organisation, "The Properties and Availability of Water: A Fundamental Consideration for Life," *Water Civiliz. Int. Cent.*, p. 1, 2012, [Online]. Available:

http://www.unesco.org/new/fileadmin/MULTIMEDIA/FIELD/Venice/pdf/special_events/bozza_scheda_DOW02_1.0.pdf

[96]   P. Würfel, *Physics of Solar Cells: From Principles to New Concepts*. 2007. doi: 10.1002/9783527618545.

[97]   K. D. Smith, H. K. Gummel, J. D. Bode, D. B. Cuttriss, R. J. Nielsen, and W. Rosenzweig, "The Solar Cells and Their Mounting," *Bell Syst. Tech. J.*, vol. 42, no. 4, pp. 1765–1816, 1963, doi: 10.1002/j.1538-7305.1963.tb04050.x.

[98]   K. L. Kennerud, "Electrical Characteristics of Silicon Solar Cells at Low Temperatures," *IEEE Trans. Aerosp. Electron. Syst.*, vol. AES-3, no. 4, pp. 586–590, Jul. 1967, doi: 10.1109/TAES.1967.5408834.

[99]   M. B. Prince and M. Wolf, "New developments in silicon photovoltaic devices," *J. Br. Inst. Radio Eng.*, vol. 18, no. 10, pp. 583–594, 1958, doi: 10.1049/jbire.1958.0062.

[100] C. S. Durganjali and R. Sudha, "PV Cell Performance with Varying Temperature Levels," 2019. doi: 10.1109/GCAT47503.2019.8978302.

[101] W. Yin, X. Wang, F. Zhang, and L. Zhang, "19.6% cast mono-MWT solar cells and 268 W modules," *IEEE J. Photovoltaics*, vol. 3, no. 2, pp. 697–701, 2013, doi: 10.1109/JPHOTOV.2013.2239357.

[102] T. S. Böscke *et al.*, "Bifacial n-type cells with >20% front-side efficiency for industrial production," *IEEE J. Photovoltaics*, vol. 3, no. 2, pp. 674–677, 2013, doi: 10.1109/JPHOTOV.2012.2236145.

[103] J. Muller *et al.*, "Resistive power loss analysis of PV modules made from halved 15.6 × 15.6 cm2 silicon PERC solar cells with efficiencies up to 20.0%," *IEEE J. Photovoltaics*, vol. 5, no. 1, pp. 189–194, 2015, doi: 10.1109/JPHOTOV.2014.2367868.

[104] S. Zhang *et al.*, "335-W world-record p-type monocrystalline module with 20.6% efficient PERC solar cells," *IEEE J. Photovoltaics*, vol. 6, no. 1, pp. 145–152, 2016, doi: 10.1109/JPHOTOV.2015.2498039.

[105] W. Deng *et al.*, "20.8% PERC solar cell on 156 mm × 156 mm P-type multicrystalline silicon substrate," *IEEE J. Photovoltaics*, vol. 6, no. 1, pp. 3–9, 2016, doi: 10.1109/JPHOTOV.2015.2489881.

[106] Z.-W. Peng, T. Buck, L. J. Koduvelikulathu, V. D. Mihailetchi, and R. Kopecek, "Industrial Screen-Printed n -PERT-RJ Solar Cells: Efficiencies Beyond 22% and Open-Circuit Voltages Approaching 700 mV," *IEEE J. Photovoltaics*, vol. 9, no. 5, pp. 1166–1174, Sep. 2019, doi: 10.1109/JPHOTOV.2019.2919117.

[107] M. Taguchi *et al.*, "24.7% Record efficiency HIT solar cell on thin silicon wafer," *IEEE J. Photovoltaics*, vol. 4, no. 1, pp. 96–99, 2014, doi: 10.1109/JPHOTOV.2013.2282737.

[108] J. J. Wysocki, "Lithiu[1] J. J. Wysocki, 'Lithium-doped radiation resistant silicon solar cells,' in IEEE RANSACTIONS on NUCLEAR SCIENCE, 1966, vol. 13, no. 6, pp. 168–173. doi: 10.1109/iedm.1966.187649.m-doped radiation resistant silicon solar cells," in *IEEE RANSACTIONS on NUCLEAR SCIENCE*, 1966, vol. 13, no. 6, pp. 168–173. doi: 10.1109/iedm.1966.187649.

[109] R. R. Brown, "Surface effects in silicon solar cells," *IEEE Trans. Nucl. Sci.*, vol. NS-14, no. 6, pp. 260–265, 1967, doi: 10.1109/TNS.1967.4324805.

[110] R. J. Tallent and H. Oman, "Solar-cell performance with concentrated sunlight," *Trans. Am. Inst. Electr. Eng. Part II Appl. Ind.*, vol. 81, no. 1, pp. 30–33, 2013, doi: 10.1109/tai.1962.6371786.

[111] S. Krauter, "Increased electrical yield via water flow over the front of photovoltaic panels," *Sol. Energy Mater. Sol. Cells*, vol. 82, no. 1–2, pp. 131–137, May 2004, doi: 10.1016/j.solmat.2004.01.011.

[112] A. Royne, C. J. Dey, and D. R. Mills, "Cooling of photovoltaic cells under concentrated illumination: A critical review," *Sol. Energy Mater. Sol. Cells*, 2005, doi: 10.1016/j.solmat.2004.09.003.

[113] R. Kumar and M. A. Rosen, "A critical review of photovoltaic-thermal solar collectors for air heating," *Applied Energy*. 2011. doi: 10.1016/j.apenergy.2011.04.044.

[114] R. Daghigh, M. H. Ruslan, and K. Sopian, "Advances in liquid based photovoltaic/thermal (PV/T) collectors," *Renewable and Sustainable Energy Reviews*. 2011. doi: 10.1016/j.rser.2011.07.028.

[115] A. Makki, S. Omer, and H. Sabir, "Advancements in hybrid photovoltaic systems for enhanced solar cells performance," *Renewable and Sustainable Energy Reviews*. 2015. doi: 10.1016/j.rser.2014.08.069.

[116] M. K. Smith *et al.*, "Water Cooling Method to Improve the Performance of Field-Mounted, Insulated, and Concentrating Photovoltaic Modules," *J. Sol. Energy Eng.*, vol. 136, no. 3, Aug. 2014, doi: 10.1115/1.4026466.

[117] W. He, Y. Zhang, and J. Ji, "Comparative experiment study on photovoltaic and thermal solar system under natural circulation of water," *Appl. Therm. Eng.*, 2011, doi: 10.1016/j.applthermaleng.2011.06.021.

[118] J. K. Tonui and Y. Tripanagnostopoulos, "Improved PV/T solar collectors with heat extraction by forced or natural air circulation," *Int. J. Hydrogen Energy*, 2006, doi: 10.1016/j.ijhydene.2006.02.009.

[119] S. Nižetić, D. Čoko, A. Yadav, and F. Grubišić-Čabo, "Water spray cooling technique applied on a photovoltaic panel: The performance response," *Energy Convers. Manag.*, 2016, doi: 10.1016/j.enconman.2015.10.079.

[120] C. J. Smith, P. M. Forster, and R. Crook, "Global analysis of photovoltaic energy output enhanced by phase change material cooling," *Appl. Energy*, vol. 126, pp. 21–28, Aug. 2014, doi: 10.1016/j.apenergy.2014.03.083.

[121] X. Han, Y. Wang, and L. Zhu, "The performance and long-term stability of silicon concentrator solar cells immersed in dielectric liquids," *Energy Convers. Manag.*, vol. 66, pp. 189–198, Feb. 2013, doi: 10.1016/j.enconman.2012.10.009.

[122] A. N. Al-Shamani *et al.*, "Nanofluids for improved efficiency in cooling solar collectors - A review," *Renewable and Sustainable Energy Reviews*. 2014. doi: 10.1016/j.rser.2014.05.041.

[123] J. G. Webster, Y. G. GUREVICH, and J. E. VELAZQUEZ-PEREZ, "Peltier Effect in Semiconductors," *Wiley Encycl. Electr. Electron. Eng.*, no. November 2017, pp. 1–21, 2014, doi: 10.1002/047134608x.w8206.

[124] Z. Farhana, Y. M. Irwan, R. M. N. Azimmi, A. R. N. Razliana, and N. Gomesh, "Experimental investigation of photovoltaic modules cooling system," 2012. doi: 10.1109/ISCI.2012.6222687.

[125] B. Du, E. Hu, and M. Kolhe, "Performance analysis of water cooled concentrated photovoltaic (CPV) system," *Renewable and Sustainable Energy Reviews*. 2012. doi: 10.1016/j.rser.2012.09.007.

[126] H. Bahaidarah, A. Subhan, P. Gandhidasan, and S. Rehman, "Performance evaluation of a PV (photovoltaic) module by back surface water cooling for hot climatic conditions," *Energy*, 2013, doi: 10.1016/j.energy.2013.07.050.

[127] M. Rahimi, P. Valeh-E-Sheyda, M. A. Parsamoghadam, M. M. Masahi, and A. A. Alsairafi, "Design of a self-adjusted jet impingement system for cooling of photovoltaic cells," *Energy Convers. Manag.*, 2014, doi: 10.1016/j.enconman.2014.03.053.

[128] I. E. El-Seesy, T. Khalil, and M. H. Ahmed, "Experimental investigations and developing of photovoltaic/thermal system," *World Appl. Sci. J.*, 2012, doi: 10.5829/idosi.wasj.2012.19.09.2794.

[129] M. Chandrasekar, S. Suresh, T. Senthilkumar, and M. Ganesh Karthikeyan, "Passive cooling of standalone flat PV module with cotton wick structures," *Energy Convers. Manag.*, 2013, doi: 10.1016/j.enconman.2013.03.012.

[130] M. Moradgholi, S. M. Nowee, and I. Abrishamchi, "Application of heat pipe in an experimental investigation on a novel photovoltaic/thermal (PV/T) system," *Sol. Energy*, 2014, doi: 10.1016/j.solener.2014.05.018.

[131] M. Redón Santafé, J. B. Torregrosa Soler, F. J. Sánchez Romero, P. S. Ferrer Gisbert, J. J. Ferrán Gozálvez, and C. M. Ferrer Gisbert, "Theoretical and experimental analysis of a floating photovoltaic cover for water irrigation reservoirs," *Energy*, vol. 67, pp. 246–255, Apr. 2014, doi: 10.1016/j.energy.2014.01.083.

[132] J. J. F. Gozálvez, P. S. F. Gisbert, C. M. F. Gisbert, M. R. Santafé, J. B. T. Soler, and E. P. Puig, "Covering reservoirs with a system of floating solar panels: technical and financial analysis," 2012.

[133] C. Ferrer-Gisbert, J. J. Ferrán-Gozálvez, M. Redón-Santafé, P. Ferrer-Gisbert, F. J. Sánchez-Romero, and J. B. Torregrosa-Soler, "A new photovoltaic floating cover system for water reservoirs," *Renew. Energy*, 2013, doi: 10.1016/j.renene.2013.04.007.

[134] Y. Choi, "A case study on suitable area and resource for development of floating photovoltaic system," *Int. J. Electr. Comput. Energ. Electron. Commun. Eng.*, vol. 8, no. 5, pp. 828–832, 2014.

[135] G. M. Tina, M. Rosa-Clot, and P. Rosa-Clot, "Electrical behavior and optimization of panels and reflector of a photovoltaic floating plant," in *Proceedings of the 26th european photovoltaic solar energy conference and exhibition (EU PVSEC'11)*, 2011, pp. 4371–4375.

[136] C. J. Ho, W. L. Chou, and C. M. Lai, "Thermal and electrical performance of a water-surface floating PV integrated with a water-saturated MEPCM layer," *Energy Convers. Manag.*, 2015, doi: 10.1016/j.enconman.2014.10.039.

[137] C. J. Ho, B.-T. Jou, and C.-M. Lai, "Thermal and electrical performance of a PV module integrated with double layers of water-saturated MEPCM," *Appl. Therm. Eng.*, vol. 123, pp. 1120–1133, Aug. 2017, doi: 10.1016/j.applthermaleng.2017.05.166.

[138] and D. Sen P. Sharma, B. Muni, "Design Parameters of 10kw Floating Solar Power

Plant," 2015.

[139] A. Sahu, N. Yadav, and K. Sudhakar, "Floating photovoltaic power plant: A review," *Renewable and Sustainable Energy Reviews*. 2016. doi: 10.1016/j.rser.2016.08.051.

[140] Y.-K. Choi, N.-H. Lee, A.-K. Lee, and K.-J. Kim, "A study on major design elements of tracking-type floating photovoltaic systems," *Int. J. Smart Grid Clean Energy*, 2014, doi: 10.12720/sgce.3.1.70-74.

[141] Y. K. Choi and Y. G. Lee, "A study on development of rotary structure for tracking-type floating photovoltaic system," *Int. J. Precis. Eng. Manuf.*, 2014, doi: 10.1007/s12541-014-0613-5.

[142] Y. Ueda, T. Sakurai, S. Tatebe, A. Itoh, and K. Kurokawa, "Performance analysis of PV systems on the water," in *23rd European Photovoltaic Solar Energy Conference*, 2008, pp. 2670–2673.

[143] R. Cazzaniga, M. Rosa-Clot, P. Rosa-Clot, and G. M. Tina, "Floating tracking cooling concentrating (FTCC) systems," 2012. doi: 10.1109/PVSC.2012.6317668.

[144] K. Trapani and D. L. Millar, "The thin film flexible floating PV (T3F-PV) array: The concept and development of the prototype," *Renew. Energy*, 2014, doi: 10.1016/j.renene.2014.05.007.

[145] D. Mittal, B. K. Saxena, and K. V. S. Rao, "Floating solar photovoltaic systems: An overview and their feasibility at Kota in Rajasthan," *Proceedings of IEEE International Conference on Circuit, Power and Computing Technologies, ICCPCT 2017*, 2017.

[146] D. V. Pozdnyakov, A. V. Lyaskovsky, F. J. Tanis, and D. R. Lyzenga, "Modeling of apparent hydro-optical properties and retrievals of water quality in the great lakes for SeaWiFS: a comparison with in situ measurements," *Int. Geosci. Remote Sens. Symp.*, vol. 5, pp. 2742–2744, 1999, doi: 10.1109/igarss.1999.771637.

[147] F. T. Mackenzie, "Chemical And Physical Properties Of Seawater," *Seawater*, pp. 1–24, 2018.

[148] D. P. Morris, "Optical Properties of Water," *Encycl. Inl. Waters*, pp. 682–689, 2009, doi: 10.1016/B978-012370626-3.00069-7.

[149] C. D. Mobley, "Chapter 12: Terrestrial Optics," *Handb. Opt. V.1*, p. 1664, 1995, doi: https://doi.org/10.1016/B978-012370626-3.00069-7.

[150] E. Siegel, "This Is Why Earth's Oceans And Skies Are Blue - Starts With A Bang! - Medium." https://medium.com/starts-with-a-bang/this-is-why-earths-oceans-and-skies-are-blue-c408ce7d0d45

[151] J. A. Muaddi and M. A. Jamal, "Solar Energy At Various Depths Below," vol. 14, no. February, pp. 859–867, 1990.

[152] P. Balasubramanian and P. Karthickumar, "Indian energy crisis - A sustainable solution," *IEEE-International Conf. Adv. Eng. Sci. Manag. ICAESM-2012*, no. Goldemberg 1988, pp. 411–415, 2012.

[153] H. Y. B.Rengammal Sankari, Amit Rai, Ankur kumar Rai, "Effect od COVID-19 on Energy Sector in India," in *2021 International Conference on Advance Computing and Innovative Technologies in Engineering (ICACITE)*, 2021, vol. 7, pp. 726–729. doi: 10.1109/ICACITE51222.2021.9404590.

[154] L. Szabó, "The history of using solar energy," *Proc. - 2017 Int. Conf. Mod. Power*

Syst. MPS 2017, no. April, 2017, doi: 10.1109/MPS.2017.7974451.

[155] C. S. Durganjali, S. Bethanabhotla, S. Kasina, and D. S. Radhika, "Recent Developments and Future Advancements in Solar Panels Technology," *J. Phys. Conf. Ser.*, vol. 1495, no. 1, 2020, doi: 10.1088/1742-6596/1495/1/012018.

[156] E. Yin, Q. Li, and Y. Xuan, "A novel optimal design method for concentration spectrum splitting photovoltaic–thermoelectric hybrid system," *Energy*, vol. 163, pp. 519–532, 2018, doi: 10.1016/j.energy.2018.08.138.

[157] F. Almonacid, E. F. Fernández, B. Almonacid-Cruz, and P. M. Rodrigo, "Spectral-matching-ratio modelling based on ANNs and atmospheric parameters for the electrical characterization of multi-junction concentrator PV systems," *Energy*, vol. 156, pp. 409–417, 2018, doi: 10.1016/j.energy.2018.05.105.

[158] G. K. Singh, "Solar power generation by PV (photovoltaic) technology: A review," *Energy*, vol. 53, pp. 1–13, 2013, doi: 10.1016/j.energy.2013.02.057.

[159] M. Alonso-Abella, F. Chenlo, G. Nofuentes, and M. Torres-Ramírez, "Analysis of spectral effects on the energy yield of different PV (photovoltaic) technologies: The case of four specific sites," *Energy*, vol. 67, pp. 435–443, 2014, doi: 10.1016/j.energy.2014.01.024.

[160] D. J. Yang, Z. F. Yuan, P. H. Lee, and H. M. Yin, "Simulation and experimental validation of heat transfer in a novel hybrid solar panel," *Int. J. Heat Mass Transf.*, vol. 55, no. 4, pp. 1076–1082, 2012, doi: https://doi.org/10.1016/j.ijheatmasstransfer.2011.10.003.

[161] W. C. TURNER and S. DOTY, *ENERGY MANAGEMENT HANDBOOK:SIXTH EDITION*. The Fairmont Press, Inc., 2013.

[162] A. Richter, M. Hermle, and S. W. Glunz, "Reassessment of the limiting efficiency for crystalline silicon solar cells," *IEEE J. Photovoltaics*, vol. 3, no. 4, pp. 1184–1191, 2013, doi: 10.1109/JPHOTOV.2013.2270351.

[163] P. T. Chiu *et al.*, "Direct semiconductor bonded 5J cell for space and terrestrial applications," *IEEE J. Photovoltaics*, vol. 4, no. 1, pp. 493–497, 2014, doi: 10.1109/JPHOTOV.2013.2279336.

[164] P. T. Chiu *et al.*, "35.8% space and 38.8% terrestrial 5J direct bonded cells," *2014 IEEE 40th Photovolt. Spec. Conf. PVSC 2014*, pp. 11–13, 2014, doi: 10.1109/PVSC.2014.6924957.

[165] L. A. Granon and M. G. Coleman, "Flat plate vs. concentrator solar photovoltaic cells - a manufacturing cost analysis," *Conf. Rec. IEEE Photovolt. Spec. Conf.; (United States)*, [Online]. Available: https://www.osti.gov/biblio/6596737

[166] T. V. Ramachandra, G. Krishnadas, and R. Jain, "Solar Potential in the Himalayan Landscape," *ISRN Renew. Energy*, vol. 2012, pp. 1–13, 2012, doi: 10.5402/2012/203149.

[167] C. S. Durganjali, S. Radhika, R. N. Ponnalagu, and S. Goel, "A Study on the Performance of Solar Photovoltaic Systems in the Underwater Environment," in *Microelectronics and Signal Processing*, CRC Press, 2021, pp. 203–226.

[168] T. T. Chow, "A review on photovoltaic/thermal hybrid solar technology," *Appl. Energy*, vol. 87, no. 2, pp. 365–379, 2010, doi: 10.1016/j.apenergy.2009.06.037.

[169] E. Yin, Q. Li, and Y. Xuan, "One-day performance evaluation of photovoltaic-thermoelectric hybrid system," *Energy*, vol. 143, pp. 337–346, 2018, doi:

10.1016/j.energy.2017.11.011.

[170] "Planar silicon solar cell – Lumerical Support." [Online]. Available: https://support.lumerical.com/hc/en-us/articles/360042165534-Planar-silicon-solar-cell

[171] V. N. Vapnik, "An overview of statistical learning theory," *IEEE Trans. Neural Networks*, vol. 10, no. 5, pp. 988–999, 1999, doi: 10.1109/72.788640.

[172] N. I. Sapankevych and R. Sankar, "Time Series Prediction Using Support Vector Machines: A Survey," *IEEE Comput. Intell. Mag.*, vol. 4, 2009.

[173] P. Bhola and S. Bhardwaj, "Estimation of solar radiation using support vector regression," *J. Inf. Optim. Sci.*, vol. 40, no. 2, pp. 339–350, 2019, doi: 10.1080/02522667.2019.1578093.

[174] S. Theocharides, G. Makrides, E. George, and A. Kyprianou, "Machine Learning Algorithms for Photovoltaic System Power Output Prediction," *2018 IEEE Int. Energy Conf.*, pp. 1–6, 2018.

[175] M. W. Ahmad, M. Mourshed, and Y. Rezgui, "Tree-based ensemble methods for predicting PV power generation and their comparison with support vector regression," *Energy*, vol. 164, pp. 465–474, 2018, doi: 10.1016/j.energy.2018.08.207.

[176] G. B. Pant, P. P. Kumar, J. V. Revadekar, and N. Singh, *Climate change in the Himalayas*. 2017. doi: 10.1007/978-3-319-61654-4.

[177] IXYS Corporation, "IXOLAR High Efficiency SolarBIT KXOB-12X1L Datasheet," no. 408. pp. 1–6, 2011.

[178] T. H. Anderson, M. Faryad, T. G. Mackay, A. Lakhtakia, and R. Singh, "Combined optical–electrical finite-element simulations of thin-film solar cells with homogeneous and nonhomogeneous intrinsic layers," *J. Photonics Energy*, 2016, doi: 10.1117/1.jpe.6.025502.

[179] K.-T. Lee, J.-Y. Jang, J. Zhang, S.-M. Yang, S. Park, and H. J. Park, "Highly Efficient Colored Perovskite Solar Cells Integrated with Ultrathin Subwavelength Plasmonic Nanoresonators," *Sci. Rep.*, vol. 7, no. 1, p. 10640, Dec. 2017, doi: 10.1038/s41598-017-10937-3.

[180] A. Ghahremani and A. E. Fathy, "A three-dimensional multiphysics modeling of thin-film amorphous silicon solar cells," *Energy Sci. Eng.*, vol. 3, no. 6, pp. 520–534, 2015, doi: 10.1002/ese3.100.

[181] Comsol, "Si Solar Cell 1D." pp. 1–18. [Online]. Available: https://www.comsol.co.in/model/download/832041/models.semicond.si_solar_cell_1d.pdf

[182] A. Shang and X. Li, "Photovoltaic Devices: Opto-Electro-Thermal Physics and Modeling," *Adv. Mater.*, vol. 29, no. 8, pp. 1–8, 2017, doi: 10.1002/adma.201603492.

[183] P. i Cabarrocas, "Deposition Techniques and Processes Involved in the Growth of Amorphous and Microcrystalline Silicon Thin Films," in *Physics and Technology of Amorphous-Crystalline Heterostructure Silicon Solar Cells*, W. G. J. H. M. van Sark, L. Korte, and F. Roca, Eds. Berlin, Heidelberg: Springer Berlin Heidelberg, 2012, pp. 131–160. doi: 10.1007/978-3-642-22275-7_5.

[184] A. Benvenuti, W. M. Coughrau, and M. R. Pinto, "A thermal-fully hydrodynamic

model for semiconductor devices and applications to III-V HBT simulation," *IEEE Trans. Electron Devices*, vol. 44, no. 9, pp. 1349–1359, 1997, doi: 10.1109/16.622585.

[185] P. K. Nayak, S. Mahesh, H. J. Snaith, and D. Cahen, "Photovoltaic solar cell technologies: analysing the state of the art," *Nat. Rev. Mater.*, vol. 4, no. 4, pp. 269–285, 2019, doi: 10.1038/s41578-019-0097-0.

[186] M. Wang, J. Shen, Z. Pan, and D. Han, "An improved supported vector regression algorithm with application to predict aftershocks," *J. Seismol.*, vol. 23, 2019, doi: 10.1007/s10950-019-09848-9.

[187] M. Ojala and G. C. Garriga, "Permutation tests for studying classifier performance," *J. Mach. Learn. Res.*, vol. 11, pp. 1833–1863, 2010.

[188] F. Pedregosa *et al.*, "Scikit-learn: Machine Learning in {P}ython," *J. Mach. Learn. Res.*, vol. 12, pp. 2825–2830, 2011.

[189] L. Buitinck *et al.*, "{API} design for machine learning software: experiences from the scikit-learn project," in *ECML PKDD Workshop: Languages for Data Mining and Machine Learning*, 2013, pp. 108–122.

[190] S. Anuphappharadorn, S. Sukchai, C. Sirisamphanwong, and N. Ketjoy, "Comparison the economic analysis of the battery between lithium-ion and lead-acid in PV stand-alone application," *Energy Procedia*, vol. 56, no. C, pp. 352–358, 2014, doi: 10.1016/j.egypro.2014.07.167.

[191] F. Andrade, A. Borges, L. F. De Mello, L. C. Mathias, and J. Maurício, "Complete Development of an Battery Charger System With State-of-Charge Analysis," *Eur. Int. J. Sci. Technol.*, vol. 2, no. 6, pp. 182–197, 2013, [Online]. Available: https://www.eijst.org.uk/images/frontImages/gallery/Vol_2_No._6/20.pdf

[192] A. Panday, H. O. Bansal, and P. Srinivasan, "Thermoelectric Modeling and Online SOC Estimation of Li-Ion Battery for Plug-In Hybrid Electric Vehicles," *Model. Simul. Eng.*, vol. 2016, 2016, doi: 10.1155/2016/2353521.

[193] G. Gautham Prasad, N. Shetty, S. Thakur, Rakshitha, and K. B. Bommegowda, "Supercapacitor technology and its applications: A review," *IOP Conf. Ser. Mater. Sci. Eng.*, vol. 561, no. 1, pp. 0–11, 2019, doi: 10.1088/1757-899X/561/1/012105.

[194] C. Chukwuka and K. A. Folly, "Batteries and super-capacitors," *IEEE Power Energy Soc. Conf. Expo. Africa Intell. Grid Integr. Renew. Energy Resour. PowerAfrica 2012*, no. July, 2012, doi: 10.1109/PowerAfrica.2012.6498634.

[195] A. Vlad, N. Singh, J. Rolland, S. Melinte, P. M. Ajayan, and J. F. Gohy, "Hybrid supercapacitor-battery materials for fast electrochemical charge storage," *Sci. Rep.*, vol. 4, no. March, 2014, doi: 10.1038/srep04315.

[196] J. Shi, L. Wang, W. J. Lee, X. Cheng, and X. Zong, "Hybrid Energy Storage System (HESS) optimization enabling very short-term wind power generation scheduling based on output feature extraction," *Appl. Energy*, vol. 256, no. January, p. 113915, 2019, doi: 10.1016/j.apenergy.2019.113915.

[197] S. Podder and M. Z. R. Khan, "Comparison of lead acid and Li-ion battery in solar home system of Bangladesh," *2016 5th Int. Conf. Informatics, Electron. Vision, ICIEV 2016*, pp. 434–438, 2016, doi: 10.1109/ICIEV.2016.7760041.

[198] W. M. Seong *et al.*, "Abnormal self-discharge in lithium-ion batteries," *Energy Environ. Sci.*, vol. 11, no. 4, pp. 970–978, 2018, doi: 10.1039/c8ee00186c.

[199] X. P. Gao and H. X. Yang, "Multi-electron reaction materials for high energy density batteries," *Energy Environ. Sci.*, vol. 3, no. 2, pp. 174–189, 2010, doi: 10.1039/b916098a.

[200] A. Tomaszewska *et al.*, "Lithium-ion battery fast charging: A review," *eTransportation*, vol. 1, p. 100011, 2019, doi: 10.1016/j.etran.2019.100011.

[201] K. Liu, Z. Wei, C. Zhang, Y. Shang, R. Teodorescu, and Q. L. Han, "Towards Long Lifetime Battery: AI-Based Manufacturing and Management," *IEEE/CAA J. Autom. Sin.*, vol. 9, no. 7, pp. 1–27, 2022, doi: 10.1109/JAS.2022.105599.

[202] Z. Wei, Z. Quan, J. Wu, Y. Li, J. Pou, and H. Zhong, "Deep Deterministic Policy Gradient-DRL Enabled Multiphysics-Constrained Fast Charging of Lithium-Ion Battery," *IEEE Trans. Ind. Electron.*, vol. 69, no. 3, pp. 2588–2598, 2022, doi: 10.1109/TIE.2021.3070514.

[203] J. Hu, X. Bian, Z. Wei, J. Li, and H. He, "Residual Statistics-Based Current Sensor Fault Diagnosis for Smart Battery Management," *IEEE J. Emerg. Sel. Top. Power Electron.*, vol. 10, no. 2, pp. 2435–2444, 2022, doi: 10.1109/JESTPE.2021.3131696.

[204] Z. Wei, J. Hu, H. He, Y. Yu, and J. Marco, "Embedded Distributed Temperature Sensing Enabled Multi-State Joint Observation of Smart Lithium-Ion Battery," *IEEE Trans. Ind. Electron.*, vol. 0046, no. c, 2022, doi: 10.1109/TIE.2022.3146503.

[205] Y. Li, Z. Wei, B. Xiong, and D. M. Vilathgamuwa, "Adaptive Ensemble-Based Electrochemical–Thermal Degradation State Estimation of Lithium-Ion Batteries," *IEEE Trans. Ind. Electron.*, vol. 69, no. 7, pp. 6984–6996, 2022, doi: 10.1109/TIE.2021.3095815.

[206] M. Yilmaz and P. T. Krein, "Review of battery charger topologies, charging power levels, and infrastructure for plug-in electric and hybrid vehicles," *IEEE Trans. Power Electron.*, vol. 28, no. 5, pp. 2151–2169, 2013, doi: 10.1109/TPEL.2012.2212917.

[207] J. C. Gómez and M. M. Morcos, "Impact of EV battery chargers on the power quality of distribution systems," *IEEE Trans. Power Deliv.*, vol. 18, no. 3, pp. 975–981, 2003, doi: 10.1109/TPWRD.2003.813873.

[208] C. H. Dharmakeerthi, N. Mithulananthan, and T. K. Saha, "Impact of electric vehicle fast charging on power system voltage stability," *Int. J. Electr. Power Energy Syst.*, vol. 57, pp. 241–249, 2014, doi: 10.1016/j.ijepes.2013.12.005.

[209] G. Mauri, D. Bertini, E. Fasciolo, and S. Fratti, "The impact of EV's fast charging stations on the MV distribution grids of the Milan metropolitan area," *IET Conf. Publ.*, vol. 2013, no. 615 CP, pp. 6–8, 2013, doi: 10.1049/cp.2013.1149.

[210] M. J. Rutherford and V. Yousefzadeh, "The impact of electric vehicle battery charging on distribution transformers," *Conf. Proc. - IEEE Appl. Power Electron. Conf. Expo. - APEC*, pp. 396–400, 2011, doi: 10.1109/APEC.2011.5744627.

[211] A. Kuperman, U. Levy, J. Goren, A. Zafransky, and A. Savernin, "Traction Battery Switch Station," *IEEE Trans. Ind. Electron.*, vol. 60, no. 12, pp. 5391–5399, 2013.

[212] M. Etezadi-amoli, S. Member, K. Choma, J. Stefani, and S. Member, "Rapid-Charge Electric-Vehicle Stations," vol. 25, no. 3, pp. 1883–1887, 2010.

[213] T. Dragičević, S. Sučić, J. C. Vasquez, and J. M. Guerrero, "Flywheel-based distributed bus signalling strategy for the public fast charging station," *IEEE Trans. Smart Grid*, vol. 5, no. 6, pp. 2825–2835, 2014, doi: 10.1109/TSG.2014.2325963.

[214] T. Ise, M. Kita, and A. Taguchi, "A hybrid energy storage with a SMES and secondary battery," *IEEE Trans. Appl. Supercond.*, vol. 15, no. 2 PART II, pp. 1915–1918, 2005, doi: 10.1109/TASC.2005.849333.

[215] S. Wang *et al.*, "Design and advanced control strategies of a hybrid energy storage system for the grid integration of wind power generations," *IET Renew. Power Gener.*, vol. 9, no. 2, pp. 89–98, 2015, doi: 10.1049/iet-rpg.2013.0340.

[216] L. Huat Saw, Hiew Mun Poon, Wen Tong Chong, Chin-Tsan Wang, Ming Chian Yew, Ming Kun Yew, and Tan Ching Ng, "Numerical modeling of hybrid supercapacitor battery energy storage system for electric vehicles," *Energy Procedia*, vol. 158, pp. 2750–2755, Feb. 2019, doi: 10.1016/j.egypro.2019.02.033.

[217] M. Doyle, J. Newman, A. S. Gozdz, C. N. Schmutz, and J.-M. Tarascon, "Comparison of Modeling Predictions with Experimental Data from Plastic Lithium Ion Cells," *J. Electrochem. Soc.*, vol. 143, no. 6, pp. 1890–1903, Jun. 1996, doi: 10.1149/1.1836921.

[218] D. BATTERIES, "Ultra 123 Ultra 123 Lithium / Manganese Dioxide," pp. 6–7, 2000.

[219] C. S. Durganjali, H. Raghavan, and S. Radhika, "Modelling and Performance Analysis of Different Types of Li-Ion Battery," in *Volume 8: Energy*, Nov. 2020, vol. 8, pp. 2–8. doi: 10.1115/IMECE2020-24404.

[220] Y. Wang, L. Wang, M. Li, and Z. Chen, "A review of key issues for control and management in battery and ultra-capacitor hybrid energy storage systems," *eTransportation*, vol. 4, p. 100064, 2020, doi: 10.1016/j.etran.2020.100064.

[221] K. Naoi, S. Ishimoto, J. I. Miyamoto, and W. Naoi, "Second generation 'nanohybrid supercapacitor': Evolution of capacitive energy storage devices," *Energy Environ. Sci.*, vol. 5, no. 11, pp. 9363–9373, 2012, doi: 10.1039/c2ee21675b.

[222] J. Ding, W. Hu, E. Paek, and D. Mitlin, "Review of Hybrid Ion Capacitors: From Aqueous to Lithium to Sodium," *Chem. Rev.*, vol. 118, no. 14, pp. 6457–6498, 2018, doi: 10.1021/acs.chemrev.8b00116.

[223] M. S. E. Houache, C.-H. Yim, Z. Karkar, and Y. Abu-Lebdeh, "On the Current and Future Outlook of Battery Chemistries for Electric Vehicles—Mini Review," *Batteries*, vol. 8, no. 7, p. 70, 2022, doi: 10.3390/batteries8070070.

[224] X. Li, "Modeling and comparative analysis of a lithium-ion hybrid capacitor under different temperature conditions," no. January, pp. 3801–3820, 2020, doi: 10.1002/er.5168.

[225] S. Farhad, "Introducing the energy efficiency map of lithium - ion batteries," no. September 2018, pp. 931–944, 2019, doi: 10.1002/er.4332.

[226] H. Xu, "The control of lithium-ion batteries and supercapacitors in hybrid energy storage systems for electric vehicles : A review," no. July, pp. 20524–20544, 2021, doi: 10.1002/er.7150.

[227] S. K. Sharma, D. P. Sharma, M. K. Sharma, K. Gaur, and P. Manohar, "Trend Analysis of Temperature and Rainfall of Rajasthan, India," *J. Probab. Stat.*, vol. 2021, no. December, pp. 1–7, 2021, doi: 10.1155/2021/6296709.

[228] L. J. L. Stival, A. K. Guetter, and F. O. de Andrade, "The impact of wind shear and turbulence intensity on wind turbine power performance," *Espaço Energ.*, no. 27, pp. 11–20, 2017.

[229] M. Sanchez Gomez and J. K. Lundquist, "The effect of wind direction shear on turbine performance in a wind farm in central Iowa," *Wind Energy Sci.*, vol. 5, no. 1, pp. 125–139, 2020, doi: 10.5194/wes-5-125-2020.

[230] A. El Yaakoubi, A. Bouzem, R. El Alami, N. Chaibi, and O. Bendaou, "Wind turbines dynamics loads alleviation: Overview of the active controls and the corresponding strategies," *Ocean Eng.*, vol. 278, no. April, p. 114070, 2023, doi: 10.1016/j.oceaneng.2023.114070.

[231] M. A. Soliman, H. M. Hasanien, H. Z. Azazi, E. E. El-Kholy, and S. A. Mahmoud, "An adaptive fuzzy logic control strategy for performance enhancement of a grid-connected PMSG-Based wind turbine," *IEEE Trans. Ind. Informatics*, vol. 15, no. 6, pp. 3163–3173, 2019, doi: 10.1109/TII.2018.2875922.

[232] A. A. Kebede *et al.*, "A techno-economic optimization and performance assessment of a 10 kWP photovoltaic grid-connected system," *Sustain.*, vol. 12, no. 18, 2020, doi: 10.3390/su12187648.

[233] S. Singh and S. C. Kaushik, "Optimal sizing of grid integrated hybrid PV-biomass energy system using artificial bee colony algorithm," *IET Renew. Power Gener.*, vol. 10, no. 5, pp. 642–650, 2016, doi: 10.1049/iet-rpg.2015.0298.

[234] A. Jaiswal, "Lithium-ion battery based renewable energy solution for off-grid electricity: A techno-economic analysis," *Renew. Sustain. Energy Rev.*, vol. 72, no. August 2016, pp. 922–934, 2017, doi: 10.1016/j.rser.2017.01.049.

[235] NASA Langley Research Center, "Index @ Power.Larc.Nasa.Gov." 2021. [Online]. Available: https://power.larc.nasa.gov/

[236] A. Alem *et al.*, "Techno-economic analysis of lithium-ion and lead-acid batteries in stationary energy storage application," *J. Energy Storage*, vol. 40, no. May, p. 102748, 2021, doi: 10.1016/j.est.2021.102748.

[237] B. K. Das, N. Hoque, S. Mandal, T. Kumar, and A. Raihan, "A techno-economic feasibility of a stand-alone hybrid power generation for remote area application in Bangladesh," *Energy*, vol. 134, pp. 775–788, 2017, doi: 10.1016/j.energy.2017.06.024.

[238] S. Singh, M. Singh, and S. Chandra, "Feasibility study of an islanded microgrid in rural area consisting of PV , wind , biomass and battery energy storage system," *Energy Convers. Manag.*, vol. 128, pp. 178–190, 2016, doi: 10.1016/j.enconman.2016.09.046.

[239] S. Podder, "Comparison of Lead acid and Li-ion Battery in Solar Home System of Bangladesh," pp. 434–438, 2016.

[240] A. Jaiswal, "Lithium-ion battery based renewable energy solution for o ff -grid electricity : A techno-economic analysis," *Renew. Sustain. Energy Rev.*, vol. 72, no. December 2015, pp. 922–934, 2017, doi: 10.1016/j.rser.2017.01.049.

[241] R. Hemmati and H. Saboori, "Emergence of hybrid energy storage systems in renewable energy and transport applications – A review," *Renew. Sustain. Energy Rev.*, vol. 65, pp. 11–23, 2016, doi: 10.1016/j.rser.2016.06.029.

[242] U. S. Manual, "For Correct Use of SuperCapacitor," vol. 01, 2017, [Online]. Available: https://www.tokin.com/english/product/pdf_dl/supercap_manual.pdf

[243] S. S. Modules, "16V SCM Series 16V SCM Series Series-Connected SuperCapacitor Modules".

[244] C. Sing *et al.*, "Levelized cost of electricity for photovoltaic / biogas power plant hybrid system with electrical energy storage degradation costs," *Energy Convers. Manag.*, vol. 153, no. May, pp. 34–47, 2017, doi: 10.1016/j.enconman.2017.09.076.

[245] N. Djagarov, G. Enchev, and J. Djagarova, "Simulation of Broken Rotor Bar Fault by Asymmetric Induction Motor Model," *Diagnostika 2022 - 2022 Int. Conf. Diagnostics Electr. Eng. Proc.*, 2022, doi: 10.1109/Diagnostika55131.2022.9905121.

[246] S. Chen, "Induction Machine Broken Rotor Bar Diagnostics Using Prony Analysis," *Tese*, p. 127, 2008.

[247] M. R. Sarkar, S. Julai, C. W. Tong, O. Z. Chao, and M. Rahman, "Mathematical modelling and simulation of induction generator based wind turbine in MATLAB/SIMULINK," *ARPN J. Eng. Appl. Sci.*, vol. 10, no. 22, pp. 17276–17280, 2015.

[248] R. Mahalakshmi, J. Viknesh, and K. C. S. Thampatty, "Mathematical modelling of grid connected doubly fed induction generator based wind farm," *IEEE Int. Conf. Power Electron. Drives Energy Syst. PEDES 2016*, vol. 2016-Janua, 2017, doi: 10.1109/PEDES.2016.7914301.

[249] R. C. Bansal, T. S. Bhatti, and D. R. Kothari, "A Novel Mathematical Modelling of Induction Generator for Reactive Power Control of Isolated Hybrid Power Systems," *Int. J. Model. Simul.*, vol. 24, no. 1, pp. 1–7, 2004, doi: 10.1080/02286203.2004.11442280.

[250] O. M. Babatunde, J. L. Munda, and Y. Hamam, "Off-grid hybrid photovoltaic – micro wind turbine renewable energy system with hydrogen and battery storage: Effects of sun tracking technologies," *Energy Convers. Manag.*, vol. 255, no. February, p. 115335, 2022, doi: 10.1016/j.enconman.2022.115335.

[251] O. Attallah, R. A. Ibrahim, and N. E. Zakzouk, "Fault diagnosis for induction generator-based wind turbine using ensemble deep learning techniques," *Energy Reports*, vol. 8, pp. 12787–12798, 2022, doi: 10.1016/j.egyr.2022.09.139.

[252] M. Abdelouhab, A. Attar, A. Senhaji, R. Aboutni, and J. Bouchnaif, "Improved direct torque control on an induction machine with short circuit fault," *Mater. Today Proc.*, vol. 72, pp. 3820–3825, 2023, doi: https://doi.org/10.1016/j.matpr.2022.09.489.

[253] M. J. Jafarian and J. Nazarzadeh, "Employing neutral-voltage spectrum for internal turn-to-turn fault detection in the induction machine drives," *ISA Trans.*, vol. 81, no. July, pp. 306–317, 2018, doi: 10.1016/j.isatra.2018.07.027.

[254] Z. Gan, M. B. Zhao, and T. W. S. Chow, "Induction machine fault detection using clone selection programming," *Expert Syst. Appl.*, vol. 36, no. 4, pp. 8000–8012, 2009, doi: 10.1016/j.eswa.2008.10.058.

LIST OF PUBLICATIONS

International SCI Journals

- C. S. Durganjali, V. Chawla, H. Raghavan, and S. Radhika, "Design, development, and techno-economic analysis of extreme fast charging topologies using Super Capacitor and Li-Ion Battery combinations," *J. Energy Storage*, vol. 56, p. 106140, Dec. 2022,https://doi.org/10.1016/j.est.2022.106140. IF- 8.907

- C. S. Durganjali, G. Avinash, K. Megha, R. N. Ponnalagu, S. Goel, and S. Radhika, "Prediction of PV cell parameters at different temperatures via ML algorithms and comparative performance analysis in Multiphysics environment," *Energy Convers. Manag.*, vol. 282, p. 116881, 2023, doi: https://doi.org/10.1016/j.enconman.2023.116881. IF-11.533

- C. S. Durganjali, S. Bethanabhotla, S. Kasina, and D. S. Radhika, "Recent Developments and Future Advancements in Solar Panels Technology," in *Journal of Physics: Conference Series*, 2020, vol. 1495, no. 1. https://iopscience.iop.org/article/10.1088/1742-6596/1495/1/012018/meta - (Scopus indexed)

- C. S. Durganjali, and S. Radhika, "SSPV cell performance at different water depths in Multiphysics environment and prediction via ML algorithms". (Editing in process)

- C. S. Durganjali, G. Avinash, A. K. Verma and S. Radhika "Offshore microgrid system with/without DFIG BRB fault consideration". (Editing in process)

Book Chapters

- C. S. Durganjali, S. Radhika, R. N. Ponnalagu, and S. Goel, "A Study on the Performance of Solar Photovoltaic Systems in the Underwater Environment," in *Microelectronics and Signal Processing*, CRC Press, 2021, pp. 203–226

National or international conferences

- C. S. Durganjali and R. Sudha, "PV Cell Performance with Varying Temperature Levels," *2019 Glob. Conf. Adv. Technol. GCAT 2019*, pp. 1–5, 2019, doi: 10.1109/GCAT47503.2019.8978302.

➢ C. S. Durganjali, Sameer Bethanabhotla, Satwik Kasina, Sudha Radhika "Recent Developments and Future Advancements in Solar Panels Technology: A Review" in *International Conference on Multifunctional Materials (ICMM-2019)*-on December 19th, 2019.

➢ C. S. Durganjali, H. Raghavan, and S. Radhika, "Modelling and Performance Analysis of Different Types of Li-Ion Battery," in *Volume 8: Energy*, Nov. 2020, vol. 8, pp. 2–8. doi: 10.1115/IMECE2020-24404.

Poster Presentation

➢ Santhi Durganjali.C, Sudha Radhika, Ponnalagu R.N, Sanket Goel "Modelling of 3D Solar Cell With Finite Volume Discretization" *PVSEC-30 & GPVC 2020 Hybrid Conference* -November 8- 13, 2020- Proceedings- P3-T1-101- Pg.No-769.

BIOGRAPHY

<u>Biography of Candidate</u>

Challa Santhi Durganjali received the B.E degree in Electrical and Electronics Engineering from SDITW, JNTU Anantapur, India, in 2014, and the M.E degree in Electrical Power Engineering from AITS, Rajampet, JNTUA, India, in 2016. Currently, doing Ph.D. in the department of Electrical and Electronics Engineering (EEE), Birla Institute of Technology and Science (BITS), Pilani, Hyderabad Campus, Hyderabad, India. Her current research interests include Underwater PV cells, wind energy, battery design and management system, control systems, micro grid. Published two reputed core international SCI journals with impact factor of 11.533 and 8.907, and one book chapter in Taylor & Francis and attended 3 national/ international conferences. The research interest includes Robotics, Power Electronics, Power Systems, Control Systems, Micro-grid, Energy Storage Devices, Offshore energy generation, current signature analysis etc., but not limited.

Biography of Supervisor

Prof. Sudha Radhika, is currently working as Asst. Prof. in Electrical and Electronics Engineering Department in BITS Pilani, Hyderabad Campus. She had completed her Ph.D. from Tokyo Polytechnic University, Japan in the field of Wind Engineering. She is a recipient of Global COE (GCOE) funding from the Japan Government (2009-2012) for her Doctoral Studies. She has about 50 (Fifty) publications to her credits. She has 18 years of teaching experiences and 3+ years of research experiences at IIT-M, Chennai and Tokyo Polytechnic University, Japan together. She has completed a DRDO funded Project for Design of Underwater Solar Panel as a co-investigator and currently she is working in DST CRG Project of approximately 30 lakhs. In addition, she also has RIG and ACRG funded projects from BITS Pilani in the area of Online condition monitoring of Industrial machines and Wind Turbines. She had reviewed papers in IEEE Transactions on Sustainable Energy, Elsevier Journal, Journal of Wind Engineering and Industrial Aerodynamics, Journal of The Institution of Engineers (India): Series etc., and also gave invited talks at Texas Tech University, Lubbock, Texas, USA, Tongji University, Shanghai, China, Beijing Jiao tong University, Beijing, China. Her area of research includes Renewable energy (Solar and Wind), Micro-grid and Smart Grid, Machine condition monitoring, Remote Sensing, Medical image analysis.

Biography of Co-Supervisors

1) **Prof. Sanket Goel** received the B.Sc. (H-physics) degree from Ramjas College, Delhi University, the M.Sc. (physics) degree from IIT Delhi, and the Ph.D. (electrical engineering) degree from the University of Alberta, Canada, under the NSERC Fellowship. He headed the R&D Department and worked as an Associate Professor with the Electronics and Instrumentation Engineering Department, University of Petroleum and Energy Studies, Dehradun, India, from 2011 to 2015. He is currently an Associate Professor and Head, Electrical and Electronics Engineering Department, BITS–Pilani, Hyderabad Campus, Hyderabad, India. He has >60 publications, 6 patents (1 U.S. and 5 Indian) to his credits, delivered >50 invited talks, and guided 6 Ph.D. and 10 master's students. His current research interests are microfluidics and nanotechnology, materials and devices for energy (both conventional and renewable), and biomedical applications. He has won several awards during the course of his career, including the Prestigious Fulbright-Nehru Fellowship (2015), the Young Scientist Award (2013), the Best Students Paper Award (2005), and the Ph.D. Thesis Award (2005). Currently, he is the Associate Editor of IEEE Sensors Journal and IEEE Access, and holds visiting appointment with UiT, The Arctic University of Norway.

2) **Dr. R. N. Ponnalagu** received the B.E degree in Electrical and Electronics Engineering from Madurai Kamaraj University, India, in 2000, M.E degree in Electronics and Control from Sathyabama University, Chennai, India, in 2005, and the Ph. D degree in Electrical Engineering from the Indian Institute of Technology (IIT) Madras, Chennai, India in 2017. Currently, she is working as an Assistant Professor in the department of Electrical and Electronics Engineering (EEE), Birla Institute of Technology and Science (BITS), Pilani, Hyderabad Campus, Hyderabad, India. Her current research interests include sensors and instrumentation, signal conditioning, signal processing, IoT systems, biomedical applications and development of UAVs. She has published several research papers in international journals and peer reviewed conferences and also serves as reviewer for international journals.